

TRANSPORT-PROPERTY AND MASS SPECTRAL MEASUREMENTS
IN THE PLASMA EXHAUST PLUME OF A
HALL-EFFECT SPACE PROPULSION SYSTEM

by

Lyon Bradley King

A dissertation submitted in partial fulfillment
of the requirements for the degree of
Doctor of Philosophy
(Aerospace Engineering)
1998

Doctoral Committee

Associate Professor Alec Gallimore
Professor James Driscoll
Associate Professor Brian Gilchrist
Professor Tamas Gombosi

ACKNOWLEDGMENTS

Although the spine of this book bears my name, the work reported here would not have been possible without the help of a great number of people. First and foremost, I would like to thank my advisor, Prof. Alec Gallimore, for stepping forward when I required guidance, and stepping back when things were going well. Prof. Gallimore has created a research environment in which students are free to pursue their own unique interests and creativity flourishes. Additionally I would like to thank my dissertation committee comprised of Prof. Jim Driscoll, Prof. Brian Gilchrist, and Prof. Tamas Gombosi for their time in evaluating this thesis; any errors that remain are my own. I am also indebted to the talented students that I had the fortune to work alongside. I am richer for the many hours spent swearing, wiring, contemplating, fixing, taping (that's right, Sang, taping), and occasionally celebrating with Colleen, Frank, James, Matt, Sang, and more recently George and Shane.

A hardware-intensive endeavor, such as this research proved to be, required the assistance of skilled technicians. I would like to thank Warren Eaton, Terry Larrow, Tom Griffin, Gary Gould, and Dave McLean for assistance with all things metal.

Financially, this research benefited from the generous support of the Air Force Office of Scientific Research (AFOSR) represented by Dr. Mitat Birkan, the NASA-Lewis Research Center with equipment grants administered by Mr. John Sankovic, and support from the NASA-Johnson Space Center under the direction of Mr. Richard Barton. The unique opportunity to evaluate a state-of-the-art thruster was made available by a generous equipment loan from Mr. Mike Day of the Space Systems/Loral company. This support is gratefully acknowledged.

On a personal level I would like to thank my parents for emphasizing the importance of education in life. Moreover, the opportunities afforded to me as a result of their support and guidance were designed to produce nothing less than complete success in my every endeavor.

Finally, I would like to express my heartfelt thanks to my wife, who bore the brunt of my frustrations throughout my studies. Pursuit of the Ph.D. has consisted of months of pure boredom punctuated by moments of sheer panic; she was with me through every peak and valley. I would like to thank her for keeping faith in me and for being my biggest fan.

L.B.K.

May 13, 1998

PREFACE

This thesis represents a broad study to characterize the heavy-particle structure of the exhaust plume produced from a 1.5-kW-class Hall thruster. The goal of this study was to provide an extensive data base of plasmadynamic quantities to be used as an input to plasma-surface interaction models. Additionally, conclusions drawn from analysis of these quantities yielded insight regarding basic thruster performance mechanisms.

The plume characterization study employed the use of a variety of classic plasma diagnostic techniques including Langmuir probes, retarding potential analyzers (RPAs), and Faraday probes. Novel probes were also conceived of and tested to evaluate previously un-obtained information regarding the plasma components. These techniques included the development of a neutral particle flux probe (NPF) to quantify the existence of high-energy neutral atoms and the application of a heat-flux probe technique in the determination of ion and neutral densities.

To complement the in-situ probe data, a unique molecular beam mass spectrometer (MBMS) was designed and used to provide great insight into the plasma species and energy structure of the Hall thruster plume. This system provided simultaneous mass and energy measurement through the use of an electrostatic energy analyzer in a time-of-flight mode. The MBMS data enabled

the measurement of propellant ionization states and the construction of species-dependent ion energy distribution functions useful for evaluation of basic thruster acceleration mechanisms.

Through an evaluation of the probe-based data in addition to the MBMS results a collisional analysis of the ionic portion of the plasma plume was performed. Through models and concepts developed in this thesis the products of both elastic momentum transfer and inelastic charge-exchange collisions were directly identified within the measured ion energy distributions. These results confirmed the existence of both single- and multiple-electron transfers between plume ions and parasitic neutral gas due to ground-test facility interactions in addition to momentum transfer collisions between propellant ionic species.

TABLE OF CONTENTS

ACKNOWLEDGMENTS	ii
PREFACE.....	iv
LIST OF FIGURES	ix
LIST OF TABLES	xix
NOMENCLATURE.....	xx
CHAPTER	
1. INTRODUCTION.....	1
1.1. Overview of Electric Propulsion Concepts	1
1.2. Hall-effect Thrusters: Research History	6
1.3. Physics of Hall Thruster Operation	10
1.4. Contributions of Research.....	15
1.5. Description of Experimental Facilities.....	17
2. PRACTICAL THEORY OF IN-SITU PROBES	20
2.1. Introduction	20
2.2. Retarding Potential Analyzer	22
2.3. Langmuir Probe	25
2.4. Faraday Probe	25
2.5. Heat-Flux Probe	28
2.6. Neutral Particle Flux Probe	32
3. A PROBE-BASED STUDY OF THE HALL THRUSTER	37

3.1. Experimental Set-up and Apparatus	37
3.2. Probe Data and Results.....	40
3.2.1. Langmuir Probe.....	40
3.2.2. Retarding Potential Analyzer.....	42
3.2.3. Faraday Probe.....	48
3.2.4. Heat-Flux Probe.....	49
3.2.5. NPF Probe	52
3.3. Interpretation of Probe Results and Derived Quantities	55
3.3.1. Ion Energy Structure	55
3.3.2. Density Distribution	61
3.3.3. Neutral-Particle Properties.....	63
3.3.4. Ion-Neutral Charge Exchange Processes.....	66
 4. MOLECULAR BEAM MASS SPECTROMETER DESIGN	 70
4.1. Motivation Behind MBMS Research	70
4.2. Configuration of Apparatus.....	73
4.3. Electrostatic Energy Analyzer.....	79
4.3.1. Theory of Operation	79
4.3.2. Description of Apparatus	84
4.4. Time-of-flight Mass Analyzer	85
4.4.1. Theory of Operation	85
4.4.2. Design Principles	88
4.4.3. Practical Design Considerations	95
4.4.4. Description of Apparatus	100
 5. MBMS ENERGY DIAGNOSTICS.....	 106
5.1. Experimental Set-up	107
5.2. Ion Energy Measurements in an SPT-100 at 0.5 m.....	110
5.3. Ion Energy Measurements in an SPT-100 at 1.0 m.....	119
5.4. Discussion of Ion Voltage Distributions	131
5.4.1. Comparison with RPA.....	133
5.4.2. Ion Temperature.....	137
5.4.3. Most Probable Voltage.....	145
5.4.4. Two-stream Instability Analysis.....	151
5.4.5. Multiple Peak Structure	153
 6. MASS SPECTROMETRIC STUDIES.....	 154
6.1. Experimental Set-up	154
6.2. Measurements in an SPT-100	156

6.3. Discussion of Mass Spectral Measurements.....	162
6.3.1. Minor Species Analysis.....	162
6.3.2. Propellant Ionization.....	164
7. PLUME ION COLLISION ANALYSIS	172
7.1. Overview of Collision Processes	172
7.1.1. Ion Collision Probabilities.....	173
7.1.2. Elastic Collision Signatures	175
7.1.3. CE Collision Signatures.....	187
7.2. Collision Evidence in SPT-100 Plume	192
7.3. Ion-Electron Recombination	214
7.4. Discussion of Plume Collisions.....	216
8. CONCLUSIONS	224
8.1. Overall Hall Thruster Plume Structure.....	224
8.2. Ion Energy Structure.....	226
8.3. Facility Interaction Considerations.....	228
8.4. Plume Asymmetry	229
8.5. Suggestions for Future Work	230

LIST OF FIGURES

<p>FIGURE 1-1. FINAL NET MASS DELIVERED TO GEO AS A FUNCTION OF LEO-TO-GEO TRIP TIME FOR VARIOUS PROPULSION OPTIONS BASED ON A 1550 KG ATLAS IIAS-CLASS PAYLOAD WITH 10 KW ON-BOARD POWER.⁷</p>	5
<p>FIGURE 1-2. BASIC HALL THRUSTER COMPONENTS SHOWING LAYOUT OF ELECTRIC DISCHARGE BETWEEN ANODE AND CATHODE, APPLIED MAGNETIC FIELD CIRCUITRY, AND ORIENTATION OF DOMINANT ELECTRIC AND MAGNETIC FIELDS WITHIN DISCHARGE VOLUME.</p>	11
<p>FIGURE 1-3. SCHEMATIC OF HALL THRUSTER COMPONENTS SHOWING A COMPARISON BETWEEN THE MAGNET LAYER TYPE, SUCH AS THE SPT-100, AND THE ANODE LAYER TYPE, SUCH AS THE D-55.</p>	13
<p>FIGURE 1-4. SCHEMATIC OF THE 9 X 6 M VACUUM CHAMBER. THE POSITION OF THE THRUSTER FOR THE PROBE-BASED STUDY REPORTED IN CHAPTER 3 IS INDICATED ALONG WITH REPRESENTATIVE ARCS OF 0.5 M AND 1.0 M RADIUS SHOWN FOR PERSPECTIVE. ALSO SHOWN IS THE POSITION OF THE THRUSTER RELATIVE TO THE MOLECULAR BEAM MASS SPECTROMETER (MBMS) AS REPORTED IN CHAPTERS 5 AND 6.</p>	19
<p>FIGURE 2-1. SCHEMATIC OF THREE-GRID RPA UTILIZED TO OBTAIN ION ENERGY DISTRIBUTION FUNCTION.</p>	24
<p>FIGURE 2-2. FARADAY PROBE USED TO MEASURE THE ION CURRENT DENSITY.</p>	28
<p>FIGURE 2-3. HEAT-FLUX SENSOR SHOWING BOTH TOTAL- AND RADIANT-HEAT-FLUX TRANSDUCERS MOUNTED IN A WATER-COOLED PROBE HOUSING.</p>	31
<p>FIGURE 2-4. NEUTRAL PARTICLE FLUX PROBE SHOWING ELECTROSTATIC REPULSION GRIDS AND IONIZATION PRESSURE SENSOR USED AS A DETECTOR.</p>	34
<p>FIGURE 3-1. LAYOUT OF APPARATUS FOR IN-SITU PROBE BASED STUDY OF THE SPT-100 SHOWING PROBE MOUNTS TO AUTOMATED TRANSLATION SYSTEM AND COORDINATE SYSTEM SIGN CONVENTIONS.</p>	39
<p>FIGURE 3-2. TYPICAL LANGMUIR PROBE CURRENT-VOLTAGE CHARACTERISTIC. THIS TRACE WAS TAKEN AT 1.0 M FROM THE SPT-100 AT 20 DEGREES OFF THRUSTER CENTERLINE.</p>	41
<p>FIGURE 3-3. PLASMA POTENTIAL IN THE PLUME OF THE SPT-100 AT 0.5 M AND 1.0 M RADIUS FROM THE THRUSTER EXIT PLANE.</p>	41

FIGURE 3-4. RPA SAMPLE SWEEPS OF COLLECTOR CURRENT AS A FUNCTION OF ION REPELLING VOLTAGE IN THE PLUME OF THE SPT-100 AT 0.5 M RADIUS FROM THRUSTER EXIT. UNCERTAINTY IN CURRENT AND VOLTAGE IS LESS THAN 10%.	43
FIGURE 3-5. ION ENERGY DISTRIBUTION CURVES MEASURED WITH THE RPA IN THE PLUME OF THE SPT-100 AT 0.5 M RADIUS FOR POSITIONS WITHIN 35 DEGREES OF THRUSTER AXIS.....	45
FIGURE 3-6. ION ENERGY DISTRIBUTION FUNCTION MEASURED WITH THE RPA IN THE PLUME OF THE SPT-100 AT 0.5 M RADIUS FOR ANGLES BETWEEN 40 AND 55 DEGREES OFF THRUSTER CENTERLINE.....	46
FIGURE 3-7. ION ENERGY DISTRIBUTION MEASURED WITH THE RPA IN THE PLUME OF THE SPT-100 AT 0.5 M RADIUS AT A POSITION -60 DEGREES OFF THRUSTER CENTERLINE SHOWING HIGH LEVELS OF UNCERTAINTY DUE TO EXTREMELY LOW MEASURED ION CURRENT.	47
FIGURE 3-8. ION ENERGY DISTRIBUTION FUNCTION MEASURED WITH THE RPA IN THE PLUME OF THE SPT-100 AT 1.0 M RADIUS FROM THE THRUSTER FOR POSITIONS WITHIN 50 DEGREES OF THRUSTER CENTERLINE.	48
FIGURE 3-9. ION CURRENT DENSITY MEASUREMENTS IN THE SPT-100 AND D-55 AT RADIAL POSITIONS OF 0.5 M AND 1.0 M. UNCERTAINTY IN CURRENT DENSITY IS LESS THAN 10%; UNCERTAINTY IN ANGULAR POSITION IS 3 DEGREES.	49
FIGURE 3-10. RADIANT AND TOTAL HEAT FLUX MEASUREMENTS IN THE SPT-100 AT 0.5 M RADIUS FROM THE THRUSTER EXIT. UNCERTAINTY IN HEAT FLUX IS LESS THAN 10%; UNCERTAINTY IN ANGULAR POSITION IS 3 DEGREES.	51
FIGURE 3-11. RADIAL AND TOTAL HEAT FLUX MEASUREMENTS IN THE SPT-100 AT 1.0 M RADIUS FROM THE THRUSTER EXIT. UNCERTAINTY IN HEAT FLUX IS LESS THAN 10%; UNCERTAINTY IN ANGULAR POSITION IS 3 DEGREES.	52
FIGURE 3-12. NPF PROBE CHECK-OUT OPERATION IN THE PLUME OF THE SPT-100 AT 0.5 M RADIUS AND 15 DEGREES OFF THRUSTER CENTERLINE. PROBE WAS USED AS A TRADITIONAL RPA TO VERIFY OPERATION OF ION AND ELECTRON REPELLING GRID SYSTEM.	54
FIGURE 3-13. NEUTRAL PARTICLE FLUX PROBE MEASUREMENTS IN THE SPT-100 AT 0.5 M AND 1.0 M. UNCERTAINTY IN ANGULAR POSITION IS 3 DEGREES.	55

FIGURE 3-14. AVERAGE ION VELOCITY IN THE SPT-100 OBTAINED BY INTEGRATING THE ION ENERGY DISTRIBUTION FUNCTIONS MEASURED USING THE RPA. DATA ARE SHOWN FOR BOTH 0.5 M AND 1.0 M RADIAL DISTANCES FROM THE THRUSTER EXIT PLANE. A FEW SAMPLE ERROR BARS ARE SHOWN TO INDICATE THE MAGNITUDE OF THE UNCERTAINTY INHERENT TO ALL DATA POINTS..... 58

FIGURE 3-15. SCHEMATIC REPRESENTATION OF MECHANISM CAUSING HIGH-ENERGY ANNULUS AND LOW-ENERGY CORE IN THRUSTER PLUME. ION PRODUCTION REGION DENOTED AS ACCORDING TO BISHAEV AND KIM.¹¹ HIGH ENERGY IONS ARE FORMED CLOSEST TO THE ANODE..... 60

FIGURE 3-16. COMPARISON OF CALCULATED PARTICLE DENSITY IN THE PLUME OF THE SPT-100 AT 0.5 M RADIUS FROM THRUSTER EXIT PLANE. THE FARADAY-BASED VALUE IS CALCULATED ACCORDING TO EQN. 3-1 AND THE HEAT-FLUX BASED VALUE IS CALCULATED VIA EQN. 3-2. 62

FIGURE 3-17. COMPARISON OF CALCULATED PARTICLE DENSITY IN THE PLUME OF THE SPT-100 AT 1.0 M RADIUS FROM THRUSTER EXIT PLANE. THE FARADAY-BASED VALUE IS CALCULATED ACCORDING TO EQN. 3-1 AND THE HEAT-FLUX BASED VALUE IS CALCULATED VIA EQN. 3-2. 63

FIGURE 3-18. NEUTRAL PARTICLE FLUX IN THE PLUME OF THE SPT-100 MEASURED WITH THE NPF PROBE AT 0.5 M AND 1.0 M RADIUS FROM THE THRUSTER EXIT..... 64

FIGURE 3-19. CALCULATED NEUTRAL PARTICLE CONVECTIVE HEATING IN THE PLUME OF THE SPT-100 AT 0.5 M AND 1.0 M RADIAL POSITIONS FROM THE THRUSTER EXIT PLANE. 66

FIGURE 4-1. SCHEMATIC OF OVERALL CONFIGURATION OF MBMS APPARATUS SHOWING ORIENTATION TO MAIN VACUUM CHAMBER, THRUSTER MOUNT, AND SCALE SIZE. 75

FIGURE 4-2. TOP-VIEW PHOTOGRAPH OF MBMS INSTRUMENT SHOWING ELECTROSTATIC ANALYZER CHAMBER AND ELECTRON MULTIPLIER DETECTOR PORT. 76

FIGURE 4-3. SIDE-VIEW PHOTOGRAPH OF MBMS SHOWING OIL DIFFUSION PUMPS. 76

FIGURE 4-4. SCHEMATIC OF 45-DEGREE ELECTROSTATIC ION ENERGY ANALYZER. CONSTANT ELECTRIC FIELD IS FORMED BY APPLYING REPELLING VOLTAGE TO TOP PLATE WITH BOTTOM PLATE GROUNDED. FIELD CORRECTION PLATES ARE BIASED WITH A VOLTAGE DIVIDER TO FORCE BOUNDARY CONDITIONS AT MID-PLANES TO PREVENT FIELD DISTORTION DUE TO SURROUNDING GROUND POTENTIAL. 79

FIGURE 4-5. REPRESENTATION OF TYPICAL TIME-OF-FLIGHT SPECTRA ILLUSTRATING THE EFFECT OF THE GATE PULSE WIDTH AND FLIGHT TIME ON THE MASS RESOLUTION.	89
FIGURE 4-6. ILLUSTRATION OF TOF SPECTROMETER CONCEPTS SHOWING GATE REGION AND FIELD-FREE DRIFT REGION.....	89
FIGURE 4-7. ALLOWABLE GATE LENGTH TO DRIFT LENGTH RATIOS FOR TOF MASS SPECTROMETER.....	93
FIGURE 4-8. ELECTROSTATIC BEAM GATE LAYOUT FOR TOF ANALYSIS SHOWING RELEVANT PARAMETERS.	95
FIGURE 4-9. THE INCOMING ION BEAM IS CONSIDERABLY DIVERGENT AFTER PASSING THROUGH THE SAMPLING SKIMMER. THIS DIVERGENCE GREATLY INCREASES THE AMOUNT OF DEFLECTION REQUIRED TO STEER THE BEAM OUT OF THE COLLIMATING APERTURE DOWNSTREAM.....	97
FIGURE 4-10. DESIGN CURVE ILLUSTRATING ALLOWED VALUES OF T_{GATE} TO TRANSMIT AN ION WITH MASS OF 131 AMU AT FULL INTENSITY FOR $D_{GATE}=1.3$ CM.	99
FIGURE 4-11. ELECTRICAL SCHEMATIC OF CONTROLLING ELECTRONICS AND DATA SYSTEM FOR TOF SPECTROMETER.	102
FIGURE 4-12. TOF SYSTEM AMPLIFIER CIRCUIT DIAGRAM.....	104
FIGURE 5-1. EXPERIMENTAL SET-UP DIAGRAM SHOWING ROTARY THRUSTER MOUNT AND LASER ALIGNMENT OF BEAM LINE.....	107
FIGURE 5-2. PHOTOGRAPH SHOWING SPT-100 MOUNT TO ROTARY TABLE FOR MBMS CHARACTERIZATION.	108
FIGURE 5-3. ION CURRENT AS A FUNCTION OF ION VOLTAGE AT 0.5 M RADIUS FROM THE SPT-100 ALONG THE THRUST AXIS AND FOR POINTS AT 10, 20, AND 30 DEGREES OFF AXIS.....	111
FIGURE 5-4. ION CURRENT AS A FUNCTION OF ION VOLTAGE AT 0.5 M RADIUS FROM THE SPT-100 FOR POINTS AT 40, 50, 60, AND 70 DEGREES OFF THRUST AXIS.....	112
FIGURE 5-5. ION CURRENT AS A FUNCTION OF ION VOLTAGE AT 0.5 M RADIUS FROM THE SPT-100 FOR POINTS AT 80, 90, 100, AND 110 DEGREES OFF THRUST AXIS.....	113
FIGURE 5-6. ION CURRENT AS A FUNCTION OF ION VOLTAGE AT 0.5 M RADIUS FROM THE SPT-100 FOR POINTS AT 120, 130, 140, AND 150 DEGREES OFF THRUST AXIS.....	114
FIGURE 5-7. ION CURRENT AS A FUNCTION OF ION VOLTAGE AT 0.5 M RADIUS FROM THE SPT-100 FOR POINTS AT 160, 170, 180, AND -170 DEGREES OFF THRUST AXIS.....	115

FIGURE 5-8. ION CURRENT AS A FUNCTION OF ION VOLTAGE AT 0.5 M RADIUS FROM THE SPT-100 FOR POINTS AT -10, -20, -30, AND -40 DEGREES OFF THRUST AXIS.	116
FIGURE 5-9. ION CURRENT AS A FUNCTION OF ION VOLTAGE AT 0.5 M RADIUS FROM THE SPT-100 FOR POINTS AT -50, -60, -70, AND -80 DEGREES OFF THRUST AXIS.	117
FIGURE 5-10. ION CURRENT AS A FUNCTION OF ION VOLTAGE AT 0.5 M RADIUS FROM THE SPT-100 FOR POINTS AT -90, -100, -110, AND -120 DEGREES OFF THRUST AXIS.	118
FIGURE 5-11. ION CURRENT AS A FUNCTION OF ION VOLTAGE AT 0.5 M RADIUS FROM THE SPT-100 FOR POINTS AT -130, -140, -150, AND -160 DEGREES OFF THRUST AXIS.	119
FIGURE 5-12. ION CURRENT AS A FUNCTION OF ION VOLTAGE AT 1.0 M RADIUS FROM THE SPT-100 ON THE THRUST AXIS IN ADDITION TO POINTS AT 10, 20, AND 30 DEGREES OFF AXIS.	121
FIGURE 5-13. ION CURRENT AS A FUNCTION OF ION VOLTAGE AT 1.0 M RADIUS FROM THE SPT-100 FOR POINTS AT 40, 50, 60, AND 70 DEGREES OFF THRUST AXIS.	122
FIGURE 5-14. ION CURRENT AS A FUNCTION OF ION VOLTAGE AT 1.0 M RADIUS FROM THE SPT-100 FOR POINTS AT 80, 90, 100, AND 110 DEGREES OFF THRUST AXIS.	123
FIGURE 5-15. ION CURRENT AS A FUNCTION OF ION VOLTAGE AT 1.0 M RADIUS FROM THE SPT-100 FOR POINTS AT -10, -20, -30, AND -40 DEGREES OFF THRUST AXIS.	124
FIGURE 5-16. ION CURRENT AS A FUNCTION OF ION VOLTAGE AT 1.0 M RADIUS FROM THE SPT-100 FOR POINTS AT -50, -60, -70, AND -80 DEGREES OFF THRUST AXIS.	125
FIGURE 5-17. ION CURRENT AS A FUNCTION OF ION VOLTAGE AT 1.0 M RADIUS FROM THE SPT-100 FOR POINTS AT -90, -100, -110, AND -120 DEGREES OFF THRUST AXIS.	126
FIGURE 5-18. ION CURRENT AS A FUNCTION OF ION VOLTAGE AT 1.0 M RADIUS FROM THE SPT-100 FOR POINTS AT -130, -140, AND -150 DEGREES OFF THRUST AXIS.	127
FIGURE 5-19. EVOLUTION OF ION CURRENT TRACES AS A FUNCTION OF ANGULAR POSITION BETWEEN THRUST AXIS AND 20 DEGREES AT 1.0 M RADIUS FROM THE SPT-100.	128
FIGURE 5-20. EXPLODED VIEW OF ION CURRENT EVOLUTION BETWEEN 6 DEGREES AND 17 DEGREES OFF THRUST AXIS AT 1.0 M RADIUS FROM THE SPT-100.	129

FIGURE 5-21. ION CURRENT EVOLUTION BETWEEN -5 AND -7 DEGREES OFF THRUST AXIS AT 1.0 M RADIUS FROM SPT-100.....	130
FIGURE 5-22. ION CURRENT EVOLUTION BETWEEN -7 DEGREES AND -20 DEGREES OFF THRUST AXIS AT 1.0 M RADIUS FROM THE SPT-100.	131
FIGURE 5-23. COMPARISON BETWEEN RPA AND MBMS MEASUREMENTS OF THE ION VOLTAGE AT 0.5 M RADIUS FROM THE SPT-100. RPA TRACES ARE SHOWN AS DASHED LINES CORRESPONDING TO THE RIGHT VERTICAL AXES, WITH THE MBMS DATA SHOWN SOLID WITH UNITS ON THE LEFT AXES.	134
FIGURE 5-24. COMPARISON BETWEEN RPA AND MBMS MEASUREMENTS OF THE ION VOLTAGE AT 1.0 M RADIUS FROM THE SPT-100. RPA TRACES ARE SHOWN AS DASHED LINES CORRESPONDING TO THE RIGHT VERTICAL AXES, WITH THE MBMS DATA SHOWN SOLID WITH UNITS ON THE LEFT AXES.	135
FIGURE 5-25. VARIATION OF DEFINED ION TEMPERATURE, T_i , AS A FUNCTION OF ANGULAR POSITION AT 0.5 M RADIUS FROM THE SPT-100.	141
FIGURE 5-26. VARIATION OF DEFINED ION TEMPERATURE, T_i , AS A FUNCTION OF ANGULAR POSITION AT 1.0 M RADIUS FROM THE SPT-100.	142
FIGURE 5-27. NEUTRAL PROPELLANT DENSITY AND LOCAL PLASMA POTENTIAL WITHIN THE HALL THRUSTER ACCELERATION LAYER AS MODELED BY BARANOV, ET AL. ³¹	143
FIGURE 5-28. MOST PROBABLE ION VOLTAGE (ENERGY/Q) AS A FUNCTION OF ANGULAR POSITION IN THE PLUME OF THE SPT-100 AT 0.5 M AND 1.0 M RADIUS FROM THRUSTER EXIT.....	145
FIGURE 5-29. MEAN ELECTRIC FIELD COMPONENTS IN THE AZIMUTHAL AND RADIAL DIRECTIONS IN THE SPT-100 PLUME AT 0.5 M RADIUS AND 1.0 M RADIUS. POSITIVE E_r DENOTES THE DIRECTION POINTING BACK TOWARDS THE THRUSTER, WHILE POSITIVE E_θ REFLECTS A VECTOR POINTING IN THE DIRECTION OF INCREASING θ	147
FIGURE 5-30. MEAN ELECTRIC FIELD VECTORS AS A FUNCTION OF ANGULAR POSITION ABOUT THE SPT-100.	148
FIGURE 5-31. ILLUSTRATION OF FORMATION OF ACCELERATION LAYER WITHIN SPT-100 DISCHARGE CHAMBER.....	149
FIGURE 6-1. TYPICAL TOF SPECTRA FOR 280 V IONS AT 0.5 M RADIUS FROM THE SPT-100 FOR THE POINT 5 DEGREES OFF THRUSTER AXIS. THE DASHED LINE REPRESENTS THE BEAM GATE POTENTIAL AND	

CORRESPONDS TO THE RIGHT AXIS. THE SOLID LINE REFLECTS THE CEM OUTPUT CURRENT, WHICH IS SCALED ON THE LEFT AXIS.	156
FIGURE 6-2. TYPICAL MASS SPECTRA FOR 260 V IONS AT 0.5 M RADIUS 5 DEGREES OFF THRUST AXIS.	158
FIGURE 6-3. MINOR SPECIES IDENTIFICATION FOR 260 V IONS AT 0.5 M FROM THE SPT-100 FOR THE POINT 5 DEGREES OFF THRUST AXIS.	159
FIGURE 6-4. MASS SPECTRA FOR EVALUATION OF XENON IONIZATION STATES FOR IONS WITH 180, 280, AND 380 V ACCELERATION IN THE SPT-100 AT 0.5 M RADIUS, 5 DEGREES OFF THRUST AXIS.	161
FIGURE 6-5. NUMBER DENSITY FRACTIONS OF Xe^+ , Xe^{2+} , AND Xe^{3+} AS A FUNCTION OF ION ENERGY AT 0.5 M RADIUS AND 5 DEGREES OFF THRUST AXIS IN THE SPT-100. ALSO SHOWN IN THE TOP CURVE IS THE VALUE OF TOTAL ION CURRENT AS A FUNCTION OF ION VOLTAGE FOR COMPARISON OF TOTAL DENSITY.	166
FIGURE 6-6. THE ION VOLTAGE DISTRIBUTION FUNCTION FOR EACH PROPELLANT IONIZATION SPECIES IN THE SPT-100 AT 0.5 M RADIUS AND 5 DEGREES OFF THRUST AXIS.	168
FIGURE 6-7. RESULTS OF BARANOV MODEL ³¹ OF PLASMA PARAMETERS IN HALL THRUSTER DISCHARGE CHAMBER INCLUDING NEUTRAL ATOM DENSITY (LEFT AXIS), ELECTRON TEMPERATURE (LEFT AXIS), AND PLASMA POTENTIAL (RIGHT AXIS).	169
FIGURE 7-1. A COMPARISON OF THE RELATIVE PROBABILITIES OF CHARGE-EXCHANGE COLLISIONS, Σ_{CE} , TO ATOMIC IONIZATION COLLISIONS, Σ_p , AS A FUNCTION OF THE ENERGY BETWEEN COLLIDING PARTICLES. ³⁶	174
FIGURE 7-2. COMPARISON OF TOTAL, CE, AND ELASTIC COLLISION PROBABILITIES AS A FUNCTION OF INTER-PARTICLE ENERGY.	175
FIGURE 7-3. ILLUSTRATION OF TAIL FORMATION MECHANISM IN THE ENERGY DISTRIBUTION THROUGH ELASTIC COLLISIONS BETWEEN TWO MONO-ENERGETIC SPECIES.	178
FIGURE 7-4. PRE-COLLISION ENERGY OF A TWO-SPECIES FLOW HAVING SEPARATE GAUSSIAN DISTRIBUTIONS.	178
FIGURE 7-5. PRE-COLLISION ENERGY DISTRIBUTION OF SPECIES 1 SHOWN WITH THE PROBABILITY OF POST-COLLISION VELOCITIES FOR SPECIES 1 WITH A HIGHER ENERGY COLLISION PARTNER.	180
FIGURE 7-6. PRE-COLLISION ENERGY DISTRIBUTION OF SPECIES 2 PARTICLES SHOWN ALONG WITH THE PROBABILITY OF FINDING A SPECIES 1 PARTICLE WITH POST-COLLISION ENERGY OF E_1'	181

FIGURE 7-7. GRAPHICAL REPRESENTATION OF THE PRE-COLLISION ENERGY DISTRIBUTION OF THE REACTANTS AND THE ENERGY DISTRIBUTION OF THE POST-COLLISION PRODUCTS OF ELASTIC COLLISIONS.	182
FIGURE 7-8. ILLUSTRATION OF “TAIL” FORMATION ON PRE-COLLISION ENERGY DISTRIBUTION DUE TO ELASTIC COLLISIONS.	183
FIGURE 7-9. VOLTAGE DISTRIBUTIONS OF SINGLY AND DOUBLY CHARGED IONS FORMED BY IDENTICAL PROCESSES.	185
FIGURE 7-10. SIGNATURE OF ELASTIC COLLISIONS BETWEEN SINGLY AND DOUBLY CHARGED IONS AS SEEN IN THE ION VOLTAGE DISTRIBUTION FUNCTION.	186
FIGURE 7-11. POST-CE-COLLISION ENERGY DISTRIBUTIONS FOR THE INTERACTION OF DOUBLY CHARGED IONS (SPECIES 2) WITH SINGLY CHARGED IONS (SPECIES 1) OF THE SAME PRE-COLLISION VOLTAGE DISTRIBUTION.	188
FIGURE 7-12. TOTAL POST-CE-COLLISION VOLTAGE DISTRIBUTION FUNCTION ARISING FROM CE COLLISIONS BETWEEN DOUBLY CHARGED IONS (SPECIES 2) WITH SINGLY CHARGED IONS (SPECIES 1).	189
FIGURE 7-13. TOTAL ION VOLTAGE DISTRIBUTION MEASURED AT 0.5 M FROM THE SPT-100 AT 5 DEGREES OFF THRUSTER CENTERLINE WITH PROPOSED FORMS OF THE PRE-COLLISION DISTRIBUTIONS OF SINGLY AND DOUBLY CHARGED IONS.	194
FIGURE 7-14. CONVOLUTION OF ASSUMED PRE-COLLISION GAUSSIAN DISTRIBUTIONS OF Xe^+ AND Xe^{2+} INTO THEIR COMBINED POST-COLLISION SHAPE COMPARED WITH MBMS-MEASURED DATA AT 0.5 M RADIUS FROM THE SPT-100 AND 5 DEGREES OFF CENTERLINE.	195
FIGURE 7-15. COMPARISON OF MBMS DATA WITH CONVOLUTION OF PROPOSED PRE-COLLISION GAUSSIANS FOR Xe^+ AND Xe^{2+} AT 0.5 M FROM THE SPT-100, 5 DEGREES OFF CENTERLINE.	197
FIGURE 7-16. ILLUSTRATION OF COULOMB INTERACTION PREFERENCE FOR LOW ENERGY TRANSFER IN A BINARY ELASTIC COLLISION BETWEEN IONS.	201
FIGURE 7-17. ION VOLTAGE DISTRIBUTION AT 0.5 M FROM THE SPT-100 FROM 10 DEGREES TO 90 DEGREES OFF CENTERLINE SHOWING COLLISION SIGNATURE EVOLUTION FROM ELASTIC BEHAVIOR TO CE BEHAVIOR.	203

FIGURE 7-18. PROPOSED PRE-COLLISION GAUSSIAN DISTRIBUTIONS FOR Xe^+ AND Xe^{2+} FOR THE DATA AT 0.5 M FROM THE SPT-100, 90 DEGREES OFF AXIS. 205

FIGURE 7-19. POST-COLLISION DISTRIBUTION RESULT OF CE REACTION BETWEEN SINGLY AND DOUBLY CHARGED BEAM IONS BASED ON ASSUMED GAUSSIAN PRE-COLLISION DISTRIBUTION. 206

FIGURE 7-20. PROPOSED PRE-COLLISION DISTRIBUTION OF Xe^{2+} COMPUTED FROM THE MBMS DATA AT 0.5 M, 90 DEGREES OFF AXIS IN THE SPT-100. THE PROPOSED DISTRIBUTION WAS CALCULATED AS A FRACTION OF THE ORIGINAL DATA BETWEEN 0 AND 300 V. 208

FIGURE 7-21. ILLUSTRATION OF IDENTICAL SHAPE IN TAIL AND MAIN BODY OF VOLTAGE DISTRIBUTION DATA MEASURED AT 0.5 M RADIUS AND 90 DEGREES OFF CENTERLINE IN THE SPT-100..... 209

FIGURE 7-22. ION ENERGY DISTRIBUTION MEASURED AT 1.0 M RADIUS FROM THE SPT-100 FOR ANGLES AT -7, -9, AND -11 DEGREES OFF THRUST AXIS. CLEARLY EVIDENT ARE THE HIGH-VOLTAGE PEAKS AT $3V_B/2$, $2V_B$, AND $3V_B$ PRODUCED AS A RESULT OF CE COLLISIONS WITH NEUTRAL ATOMS. 213

FIGURE 7-23. ION VOLTAGE DISTRIBUTION AT 1.0 M RADIUS FROM THE SPT-100 PLUME AT 11 DEGREES OFF AXIS SHOWING PEAKS AT $4V_B/3$, $3V_B/2$, $2V_B$, AND $3V_B$ 213

FIGURE 8-1. HEAVY-PARTICLE STRUCTURE OF SPT-100 PLUME. THE SPT-100 BODY OUTLINE INCLUDING THE CATHODE AND SUPPORT STRUCTURE IS DRAWN TO SCALE WITH THE 0.5 M AND 1.0 M RADIUS ARCS SHOWN. AZIMUTHAL INCREMENTS OF 10 DEGREES ARE INDICATED. QUANTITIES LYING NEAR THE INNER CIRCLE DENOTE THOSE VALUES AT 0.5 M RADIUS, WHILE QUANTITIES ABOUT THE OUTER CIRCLE REPRESENT 1.0 M RADIUS VALUES. 225

LIST OF TABLES

TABLE 1-1. COMPARISON OF STATE-OF-THE-ART CHEMICAL THRUSTER WITH COMPETING ELECTRIC PROPULSION DEVICES.....	3
TABLE 4-1. PHYSICAL CHARACTERISTICS AND RESOLVING POWER OF 45-DEGREE ELECTROSTATIC ENERGY ANALYZER.	85
TABLE 4-2. PHYSICAL PARAMETERS OF MBMS TIME-OF-FLIGHT COMPONENTS.	101
TABLE 4-3. VALUE OF CIRCUIT ELEMENTS IN TOF AMPLIFIER. NOTATION REFERS TO FIGURE 4-12.....	104
TABLE 6-1. COMPARISON BETWEEN MBMS-MEASURED IONIZATION FRACTIONS WITH VALUES DERIVED FROM MANZELLA’S STUDY USING OPTICAL EMISSION SPECTROSCOPY. UNCERTAINTY IN MBMS VALUES IS APPROXIMATELY 5%.	167
TABLE 7-1. POSSIBLE REACTANT AND PRODUCT COMBINATIONS FOR CE COLLISIONS OCCURRING BETWEEN TWO HIGH-ENERGY BEAM IONS, EACH WITH VOLTAGE V_B	191
TABLE 7-2. POSSIBLE REACTANT-PRODUCT COMBINATIONS FOR THE CE COLLISION BETWEEN A BEAM ION WITH VOLTAGE V_B AND A STAGNANT BACKGROUND NEUTRAL.....	191

NOMENCLATURE

A_c	Area of current collector (m^2)
A	Arbitrary constant
b_0	Landau length (m)
c	Speed of light in vacuum (3.00×10^8 m/s)
d	Electrostatic energy analyzer plate separation (m)
d_{tof}	Time-of-flight path length (m)
d_m	Hard sphere collision diameter (m)
D_s	Diameter of MBMS sampling skimmer (m)
D_{coll}	Diameter of MBMS collimating skimmer
e	Elementary charge (1.6022×10^{-19} C)
E_i	Energy of ion (eV)
E_d	Bulk drift energy of ion distribution (eV)
E_{coll}	Relative interparticle collision energy (eV)
$E_{1,2}$	Pre-collision energy of atoms species 1, 2 (eV)
$E_{1,2}'$	Post-collision energy of species 1, 2 (eV)
$f(V)$	Ion voltage distribution function (s/m)
F_{esc}	Velocity distribution function of escaping particles (s/m)

$f(E)$	Pre-collision energy distribution function (s/m)
$f'(E)$	Post-collision energy distribution function (s/m)
G_{CEM}	Current gain of channel electron multiplier
h	Planck constant (6.63×10^{-34} J s)
I	Current (A)
I_{sp}	Specific impulse (sec)
I_{CEM}	Current output of channel electron multiplier (A)
k	Boltzmann constant (1.3807×10^{-23} J/kg K)
K_{45}	Spectrometer constant of 45-degree energy analyzer
$K_{1,2}$	Constants for evaluation of CE cross section
k_c	Coefficient of thermal conduction for heat-flux sensor
k_w	Wave number (m^{-1})
l	Inter-slit distance of 45-degree energy analyzer (m)
m_e	Electron mass (9.11×10^{-31} kg)
m_i	Mass of ion (kg)
m	Mass of particle (kg)
m_n	Mass of neutral (kg)
m_p	Mass of proton (1.6605×10^{-27} kg)
m^*	Reduced mass of two-particle system
M_i	Atomic weight of ion (amu)
M_{max}	Atomic weight of heaviest ion (amu)
n_b	Density of "bump" population (m^{-3})

n_e	Electron density (m^{-3})
n_i	Ion density (m^{-3})
n_n	Neutral density (m^{-3})
n_m	Measured density (m^{-3})
P_m	Measured pressure (Pa or torr)
P_{coll}	Probability of collision
$P_{1,2}'$	Post-collision distribution of products
q_{total}	Total heat-flux incident to probe (W/m^2)
$q_{ion\ conv}^{i,r}$	Incident/reflected ion convective heat-flux (W/m^2)
$q_{e\ conv}^{i,r}$	Incident/reflected electron convective heat-flux (W/m^2)
$q_{radiant}^{i,r}$	Incident/reflected radiant-heat-flux (W/m^2)
$q_{ion/elec\ recomb}$	Incident heat flux of ion-electron recombination (W/m^2)
$q_{ablative}$	Ablative heat-flux (W/m^2)
$q_{ion\ conv}^{net}$	Incident minus reflected ion convective heat-flux (W/m^2)
$q_{radiant}^{net}$	Incident minus reflected radiant heat-flux (W/m^2)
q_{ion}^{net}	Net heat flux due to ions (W/m^2)
$q_{neutral}$	Heat-flux due to neutrals (W/m^2)
q, q_i	Integer ion charge state
R	Mass spectrometer resolving power
S	Differential cross section (m^2)
s	Ion path length or inter-electrode spacing (m)
T_e	Electron temperature (K)

T_m	Measured temperature (K)
T_p	Surface temperature of heat-flux sensor (K)
T_n	Temperature of neutrals (K)
t	Time (s)
t_0	Initial time (s)
t_{tof}	Mass spectrometer time-of-flight (sec)
t_d	Ion residence time in gate region (sec)
t_{gate}	Duration of gate opening pulse (sec)
T_{eV}	Ion temperature (eV)
u_{coll}	Relative collision speed (m/s)
u_i	Ion velocity (m/s)
u_n	Neutral velocity (m/s)
u_m	Velocity of measured particles (m/s)
u_d	Bulk drift velocity of distribution (m/s)
V	Voltage (V)
$V_{x,y,z}$	Cartesian atomic velocity vectors (m/s)
V_p	Voltage of 45-degree analyzer repelling plate (V)
V_i	Ion voltage (V)
V_0	Drift velocity of “bump” distribution (m/s)
V_{gate}	Voltage applied to beam gate electrode (V)
V_m	Most-probable voltage of ion distribution (V)
V_b	Voltage of primary beam ions (V)

w	45-degree analyzer slit width (m)
x, y	Cartesian spatial coordinates (m)
y_d	Ion beam deflection at gate exit (m)
α	Ion-electron recombination coefficient (m^6/s)
α_c	Collisional recombination coefficient (m^6/s)
α_r	Radiative recombination coefficient (m^6/s)
$\alpha_n(V)$	Voltage-dependent fraction of Xe^{n+}
β	Constant equal to $m/2kT$
ϵ	Plasma dielectric function
ϵ_0	Permittivity constant (8.85×10^{-12} F/m)
θ	Divergence angle (deg), scattering angle (rad)
τ	Pre-amplifier time constant (sec)
τ_{TS}	Two-stream instability growth period (s)
τ_i	Mathematically defined ion temperature (V)
σ_c	General charge-exchange cross section (m^2)
σ_{CE}	Charge-exchange cross section between Xe^+ and Xe (m^2)
σ_p	Ionization cross section due to atomic collision (m^2)
ω	Plasma wave frequency (1/s)
ω_i	Ion plasma frequency (1/s)
ω_b	Ion plasma frequency of “bump” population (1/s)
λ	Mean-free-path (m)
Φ_n	Total ion fraction of flow

1. INTRODUCTION

The field of electric space propulsion has undergone a recent renaissance in the field of aerospace engineering. The renewed interest in this technology is a result of simultaneous increases in on-board electrical power with commercial demand for more efficient spacecraft. Many of the concepts which make EP attractive are unique to these systems. This chapter provides a comparison between EP and traditional propulsion, a brief discussion of the operating principles of EP devices, and an account of research history leading up to this study.

1.1. Overview of Electric Propulsion Concepts

Traditional space propulsion systems achieve thrust by accelerating heated propellant through a nozzle under the action of fluid pressure forces generated in the propellant. The energy to heat the propellant is stored within the chemical bonds of on-board fuel and oxidizer; this energy is released through chemical combustion of the reactants in the thrust chamber and transferred to the products. The fuel and oxidizer can take on a variety of forms

depending upon the specific device; these include solids, storable cryogenic gases, and hypergolic liquids. The amount of energy that can be delivered to the propellant to produce thrust is limited by that available in the chemical bonds of the reactants; hence traditional propulsion is referred to as Chemical Propulsion.

Electric Propulsion (E.P.) utilizes electrothermal, electrostatic, or electromagnetic forces to accelerate ionized propellant producing a reactive thrust. The energy required to produce the acceleration is obtained from on-board electrical systems in the form of batteries or solar arrays. The energy available for thrust is therefore de-coupled from the propellant and is limited only by the size and efficiency of the on-board electrical supply. Rather than paying to launch all of the required propellant and energy (in the form of fuel and oxidizer) from the Earth, an E.P. system can realize a mass savings by launching only the propellant, while obtaining the energy on orbit through solar arrays. Furthermore, E.P. systems typically achieve much higher propellant exhaust velocities than chemical systems, thereby increasing the available impulse from a given propellant mass. To realize a benefit over chemical systems the propellant mass savings must outweigh the added mass of the PPU that is required to condition and deliver the electrical power.

The fundamental operating principles of many current E.P. devices are outlined briefly in the text by Hill and Peterson.¹ Basically, E.P. systems can be classified as electrothermal (e.g. arcjet), electrostatic (e.g. gridded ion engine), or

electromagnetic (e.g. Hall thruster). Table 1-1 compares typical state-of-the-art thrusters from each category with a chemical bi-propellant rocket.

	<i>Chemical Bi-prop</i>	<i>2.4 kW Arcjet</i>	<i>1.5 kW Hall Thruster</i>	<i>2.5 kW Ion Engine</i>
<i>I_{sp}</i>	328 sec	600 sec	1600 sec	3000 sec
<i>Efficiency</i>	N/A	32%	50%	62%
<i>Thrust</i>	400 N	0.270 N	0.085 N	0.100 N
<i>Propellant</i>	N ₂ H ₄ /N ₂ O ₄	N ₂ H ₄	Xe	Xe

Table 1-1. Comparison of state-of-the-art chemical thruster with competing electric propulsion devices

As can be seen from Table 1-1, E.P. devices can be broadly classified as high I_{sp} , low thrust systems when compared with typical chemical thrusters. The *Efficiency* is defined as the ratio of input electrical power to usable thrust power (and is therefore not applicable to the chemical system); typical E.P. devices vary in efficiency from 30% to over 60%. The figure of merit in the above comparison is the specific impulse. Interpreted broadly as a "fuel efficiency rating," the inherent advantage of E.P. over chemical thrusters stems from their large achievable I_{sp} .

Due to their high I_{sp} , E.P. thrusters can be used to provide enhancing or enabling technology to many space missions. Several E.P. options have been found to provide specific benefit to missions encompassing the "New Millennium" program currently envisioned for solar system exploration.^{2,3,4}

These missions are characterized by small scientific payloads (10 kg to 50 kg) utilizing advanced technologies and relatively low cost ceilings. As an example, both Hall thrusters and ion engines were found to enable a Vesta main-belt asteroid rendezvous, which could not be performed by conventional chemical propulsion. Additionally, arcjets were found to provide significant net payload mass increase for a Nereus sample return mission. E.P. showed less significant net payload mass benefit to lower ΔV missions, such as Mars and Venus rendezvous missions where aerobraking is used to achieve final orbit, however, E.P. may be able to reduce the risk for these missions by eliminating the need for aerobraking.⁴

Although E.P. can benefit many solar system and deep space missions the most immediate interest in this technology has been generated by the commercial space industry for use in orbit-transfer and station-keeping of communications satellites. For this application, attention has been focused specifically on the Hall thruster and ion engine.^{5,6,7} Results of a study performed by Oleson, et al.,⁷ demonstrate the performance enhancements made possible through the application of E.P. systems to geostationary satellite missions. This study analyzed the use of E.P. systems for both orbit-raising and north/south station-keeping (NSSK) of geostationary communications payloads. By simply replacing the chemical NSSK system of a geocomsat with an E.P. system a net payload increase on the order of 15% can be realized. Due to the inherent low thrust levels associated with E.P., the transfer time required to raise a payload

from Low Earth Orbit (LEO) to Geostationary Earth Orbit (GEO) using E.P. is much greater than with a high-thrust chemical system. However, the study shows that if the mission is capable of tolerating a longer LEO-to-GEO trip time, some of the chemical propulsion apogee engine fuel can be reduced by supplementing the orbit-raising duties with E.P. systems. The net result is an increase in payload delivered to GEO at the expense of trip time. These results are summarized in Figure 1-1. As evidenced in the graph, if a 60 to 90 day trip time to GEO is tolerable, the use of a Hall thruster to supplement the chemical orbit raising engine in addition to NSSK can deliver 30% more payload to GEO than state-of-the-art chemical systems alone.

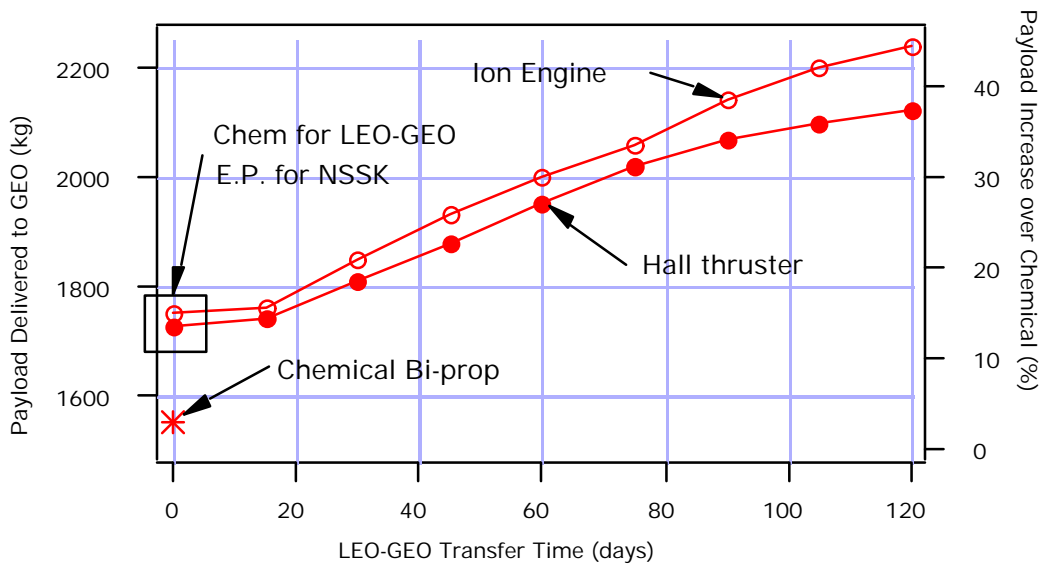


Figure 1-1. Final net mass delivered to GEO as a function of LEO-to-GEO trip time for various propulsion options based on a 1550 kg Atlas IIAS-class payload with 10 kW on-board power.⁷

1.2. Hall-effect Thrusters: Research History

The field of electric space propulsion began during the 1960-70 time period. Based on interest in interplanetary travel and projections of future availability of light-weight electrical power supplies, the goal was to produce devices with specific impulse in the range of 5,000-10,000 sec. At this value of I_{sp} , electrothermal devices (such as arcjets) become unfeasible due to excessive excitation and ionization losses. The Hall-effect thruster, although identified as a possible candidate for such use, demonstrated anomalously high electron diffusion to the anode when operated at such high values of I_{sp} . This electron backflow caused excessive anode heating and, compared to the gridded ion engines of this same period, much lower efficiencies. As a result much of the early work on Hall thrusters ceased in the western hemisphere around 1970; effort was instead focused on the development of gridded ion engines.⁸

During this time, however, Hall thruster research in the Soviet Union flourished.^{9,10,11,12} The best documentation for Hall thruster technology in the Soviet Union during the 1970's and 80's can be found in the proceedings of the All-Union Conferences on Accelerators and Ion Injectors.¹³ The first operation of a Hall thruster in space occurred in February 1972 on board the Soviet *Meteor* spacecraft.¹⁴ Following this initial operation approximately 100 Hall thrusters were used operationally on Soviet satellites.

After the collapse of the Soviet Union in the early 90's the Russian Hall thruster technology was made available to western spacecraft manufacturers in

the form of the SPT-100 (Stationary Plasma Thruster), a thruster built by the Russian firm Fakel.¹⁵ Driven by commercial interest and the potential benefit to U.S. industry, the Ballistic Missile Defense Organization (BMDO) sponsored a team comprised of electric propulsion specialists from three U.S. government facilities; this team traveled to Russia and evaluated the performance of the SPT-100 at two Russian test facilities. The results of these tests confirmed and documented the Russian claims on thruster performance and efficiency.¹⁶ Buoyed by the preliminary results, the BMDO acquired an SPT-100 for independent evaluation at two U.S. facilities: the Jet Propulsion Laboratory (JPL) and NASA-Lewis Research Center (LeRC). These tests further verified the performance parameters of $I_{sp} = 1,600$ sec, thrust = 83 mN, and efficiency = 50% for the SPT-100.^{17,18} Further tests performed at JPL established the operating life of the thruster as greater than 5,000 hrs (the test was voluntarily terminated with no thruster failure),¹⁹ which is sufficient to supply the total impulse of 1.5 million Newton-seconds required by the large long-lived spacecraft that would most benefit from the SPT.²⁰ These operating parameters of the SPT-100 were nearly ideal for its application as a station-keeping thruster on western geostationary communications satellites with increased payload masses, extended mission lifetimes, and reduced launch vehicle costs as the potential benefits of using the SPT rather than chemical thrusters.

With the operational parameters and thruster lifetime of the SPT-100 established, the next step towards application of this device to western

spacecraft was a study of the interaction between this fundamentally new thruster and existing satellite designs. Although the Russian manufacturers had performed spacecraft interaction characterization previously, more extensive testing was required due to longer lifetimes of western spacecraft and differing spacecraft configuration design philosophies which increase the criticality of accurate exhaust plume characterization relative to Russian spacecraft.²⁰

Of primary concern with the use of the Hall thruster was the effect of the highly energetic plasma exhaust plume on spacecraft surfaces. Specific issues included the erosion of solar array material due to incident high energy propellant ions,^{21,22,23} coating and contamination of solar arrays and other surfaces due to efflux of thruster self-erosion material, heating of sensitive spacecraft components, and uneven spacecraft charging due to impinging propellant ions. In order to fully quantify and understand these phenomena extensive characterization of the plasma plume was necessary.

The initial effort towards characterizing the Hall thruster plume was undertaken by a joint industry team comprised of Russian and U.S. researchers.²⁴ This test utilized a set of sample slides representative of spacecraft surfaces placed in the plume flow to model erosion and contamination in addition to the use of a Faraday probe to measure ion current density and a gridded Retarding Potential Analyzer (RPA) to measure the ion energy distribution. Due to the rapid decay in ion density with increasing distance from the thruster centerline (thrust vector), these diagnostics were limited to

points lying within 60 degrees of the thrust vector. Within this volume, however, the RPA data demonstrated some intriguing trends: although the thruster discharge voltage was set to 300 V, the ion energy distribution curve showed a significant "tail" representing ions accelerated through potentials as great as 350 to 400 V. Possible reasons for the existence of this anomalous high-energy population were not addressed. More plume characterization testing followed: Myers and Manzella performed additional measurements using an RPA, but the data was limited to very few spatial locations within the plume and again was confined to points within 60 degrees of the axis.²⁵ These data, as well, suggested the existence of ions with voltages greater than that supplied by the applied discharge. The region of with plume with the greatest interest for spacecraft designers was the far off-axis region (angles greater than 60 degrees from centerline) due to the probable location of spacecraft surfaces; the ion current density in this region (out to 100 degrees) was probed by Manzella and Sankovic,²⁶ however the low signal-to-noise levels present in the RPA at such angles prevented the recording of ion energy. Continued studies of plume-induced erosion and contamination were performed utilizing more extensive test matrices comprising a wide array of representative spacecraft materials exposed to a large volume of the plasma plume, including the far off-axis region.^{27,28} For the most part, these studies were addressed not at deepening the knowledge of the plasma properties within the plume, instead they documented the erosion/contamination problem from a top-level perspective by simply

measuring the net effects of the plume on representative spacecraft materials. For near-term applications of the SPT-100 these top-level studies provided sufficient data bases to enable integration of the Hall thruster with western satellites. However, in order to prevent the need for further extensive sample testing to accommodate new spacecraft materials or design configurations in the future, it was apparent that a more thorough understanding of the underlying physics and properties of the plasma plume was required. To this end Manzella approached the problem of characterizing the plume using optical diagnostics: through emission spectroscopy of the self-luminous plume estimates of propellant ionization fractions were made,²⁹ while a Laser-induced Fluorescence (LIF) technique was employed to measure the propellant ion velocity distribution function.³⁰ When compared with previous indications of ion velocity derived from RPA data, the LIF data displayed striking dissimilarities. The LIF data did not indicate any population of anomalous high-energy ions as seen with previous RPA studies. Furthermore, the width of the velocity distribution as measured through LIF was an order of magnitude narrower than that measured using RPA probes. An explanation to account for these discrepancies was not attempted.

1.3. Physics of Hall Thruster Operation

The closed-drift Hall thruster, known as a CDT or simply a Hall thruster, is a coaxial device in which a magnetic field that is produced by an

electromagnet is channeled between an inner ferromagnetic core (pole piece) and outer ferromagnetic ring. A schematic showing the basic components of a Hall thruster is presented as Figure 1-2.

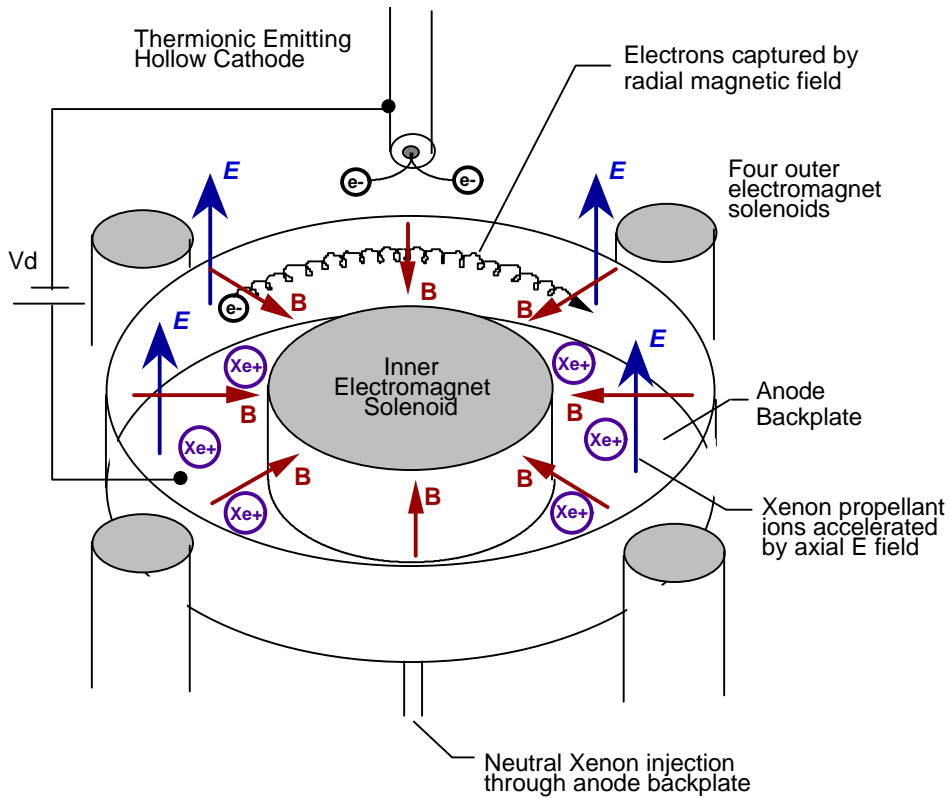


Figure 1-2. Basic Hall thruster components showing layout of electric discharge between anode and cathode, applied magnetic field circuitry, and orientation of dominant electric and magnetic fields within discharge volume.

This configuration results in an essentially radial magnetic field with a peak strength of a few hundred gauss. This field strength is such that the heavy ions experience negligible influence due to the magnetic field, while the trajectory of the much lighter electrons is significantly affected. In addition to the applied magnetic field, an axial electric field is provided by applying a voltage between

the annular anode backplate and the downstream cathode. As the electrons proceed from the cathode to the anode under the action of the applied electric field, the magnetic field configuration results in an $E \times B$ drift (Hall current) in the azimuthal direction impeding their progress to the anode. The electrons are effectively trapped in a closed-drift azimuthal orbit with only collisions between electrons, ions, neutral particles, and the channel walls permitting a slow diffusion back to the anode. Due to the highly suppressed axial mobility of the electrons the plasma can support a very large axial electric field with a potential difference close to the applied voltage between the electrodes. Propellant atoms (usually xenon) are introduced to the discharge volume through small holes in the annular anode. Through collisions with the trapped electrons, these atoms are ionized shortly after entering the discharge; the ionized propellant is then accelerated through the large axial electric field producing a reactive thrust. For more detail regarding the Hall thruster operation the reader is referred to the literature.^{8,31,32,33,34}

Hall thrusters (of the closed-drift variety discussed above) essentially come in two variations: magnetic layer types and anode layer types. An excellent discussion of the subtle but important differences between these thrusters has been given by Kaufman⁸ and Zhurin, et al.³⁴ A comparison between the two types of thrusters is shown in Figure 1-3.

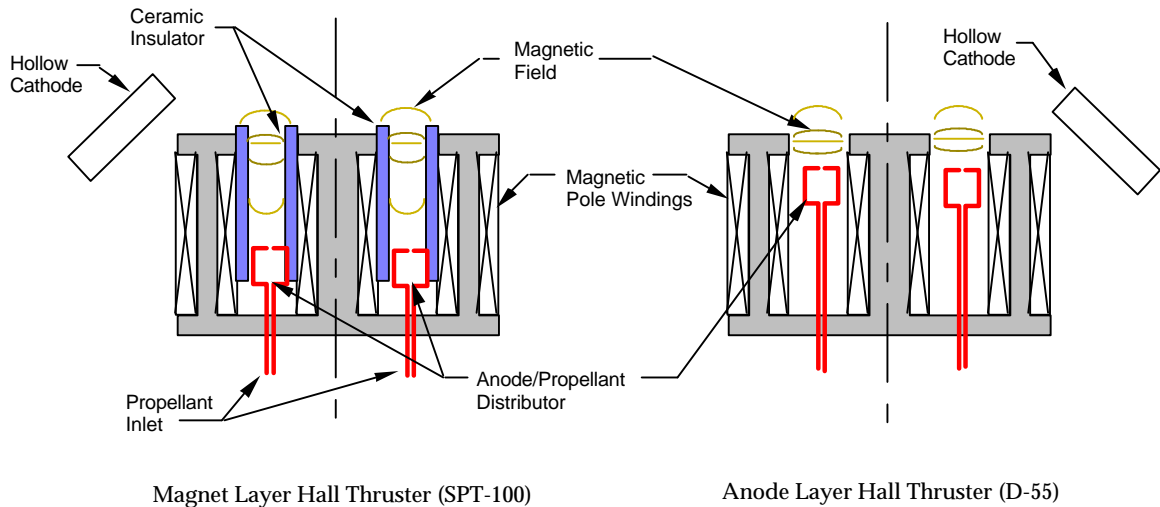


Figure 1-3. Schematic of Hall thruster components showing a comparison between the Magnet Layer type, such as the SPT-100, and the Anode Layer Type, such as the D-55.

The fundamental difference between the two thruster types lies in the length of the acceleration channel and the material comprising the channel walls. The magnet layer type, such as the SPT-100, utilizes an extended acceleration channel with length comparable to or longer than the channel width. This channel is coated with dielectric walls; the main purpose of which is to minimize plasma erosion of the ferromagnetic pole pieces. The anode layer type, such as the D-55, has a very short acceleration channel; consequently the discharge plasma occupies a volume downstream of the thruster exit plane and dielectric protection for the magnetic circuitry is not necessary.

Although very similar in layout and principle, the materials and configurations used in the acceleration channels of the magnet layer type and anode layer type have profound effects on the underlying operational physics.

The dielectric material used to protect the walls of the magnet layer thruster has a secondary electron emission coefficient due to impacting electrons of approximately unity. Due to the high electron re-supply rate from secondary emission the potential drop across the plasma sheath adjacent to the wall is very small and a considerable number of discharge electrons are capable of reaching the wall. The net effect of the dielectric material is to limit the temperature of the confined electrons within the discharge chamber: as trapped electrons diffuse toward the anode they undergo an increase in temperature driven by the applied electric field. When one of these hot electrons impacts the dielectric wall it is absorbed and a much colder secondary electron is emitted; the result is that the dielectric wall serves to "trade" hot electrons for cold electrons. By limiting the discharge electron temperature, a smooth continuous variation in plasma potential results between the anode and the cathode. The anode layer thruster, on the other hand, does not employ dielectric walls. Instead, the discharge chamber walls in this thruster are made of a conducting metal with a much lower secondary electron yield; furthermore, these walls are maintained at cathode potential greatly reducing the incidence of electron impact with the walls. As the electrons diffuse towards the anode their temperature increases significantly. At a given location near the anode the electrons become hot enough that the upstream thermal diffusion (back towards the cathode) becomes equal to the applied electric field diffusion towards the anode. At this point a

very abrupt, discontinuous potential jump occurs in the plasma over a very thin layer near the anode, thus the term anode layer thruster.

1.4 Contributions of Research

The research reported in this volume has been motivated by the need to fully characterize the plasma exhaust plume of a Hall thruster to facilitate spacecraft interaction studies. The goal of this research has been to combine a broad array of diagnostic techniques to both directly measure and indirectly derive properties associated with the transport of propellant ions and neutral atoms. Whereas previous research has utilized classic plasma diagnostic techniques over a very limited spatial volume of the plasma plume, this research extends these techniques to a much broader volume of plasma creating complete, self-consistent data sets with which to characterize the Hall thruster plume properties. In addition to a broad array of proven classic techniques, this research developed diagnostics and data interpretation schemes enabling the quantitative analysis of heretofore un-obtained plasma quantities. Specifically, this research provided the following contributions.

- A probe-based study greatly extended the data archive of ion current density and RPA-measured ion energy distribution over an expansive volume of the SPT-100 plume.

- A new probe technique was designed and developed to provide the first ever direct measurement and documentation of the existence of high-energy neutrals resulting from charge-exchange collisions between plume ions and neutrals.
- A new diagnostic technique and data interpretation scheme involving measurement of the heat-flux was developed to quantify both ionic and neutral particle properties within the plasma.
- The first spatial map of the local electric fields within the plasma plume was constructed based on probe data enhancing the understanding of the plume structure.
- A custom molecular beam mass spectrometer was constructed and used to measure the ion energy distribution structure with unprecedented accuracy and resolution. Furthermore, this diagnostic produced the first ever measurements of the ion energy at large angles off centerline including the region directly behind the thruster due to backflow.
- Mass spectral measurements produced the first direct measurements of the propellant ionization state and species fractions. This research produced the first (and only) evidence of the existence of triply and quadruply ionized propellant atoms, suggesting elevated electron temperatures within the thruster discharge.
- A comprehensive collisional model was developed which provides the first explanation of the heretofore anomalous high-voltage tail of previous

ion energy distribution measurements. This collisional analysis revealed direct evidence of elastic collisions between multiply charged plume ions in addition to evidence of multiply charged ion charge-exchange collisions with ambient neutral particles involving both single and double electron transfer.

1.5. Description of Experimental Facilities

An extensive description of the facility used for the reported research can be found in Gallimore, et al.;³⁵ for convenience this description is reproduced in this section. All experiments reported were performed in a 9-m-long by 6-m-diameter stainless-steel vacuum chamber. A schematic of this chamber is shown in Figure 1-4. The facility is supported by six 81-cm-diameter oil diffusion pumps (with water-cooled coldtraps) rated each at 32,000 l/s on nitrogen, backed by two 2000-cfm blowers, and four 400-cfm mechanical pumps. These pumps give the facility an overall pumping speed of over 180,000 l/s at 10^{-5} torr. In addition, a Polycold PFC-1100 closed-loop water cryopump doubles the water pumping speed of the facility to over 150,000 l/s, greatly reducing the required pumpdown time.

Chamber pressure is measured with MKS model 919 hot-cathode ionization gauges, that were corrected for xenon, located on vacuum ports on either side of the chamber. Chamber base pressure is roughly 2×10^{-5} torr. Background chamber pressure was maintained at less than 5×10^{-5} torr when the

Hall thrusters under evaluation were operating on approximately 5 mg/s of xenon.

Propellant is supplied to the Hall thrusters from compressed gas bottles (99.999% purity) through stainless-steel feed lines. Xenon propellant flow is controlled and monitored with MKS 1159B mass flow controllers specifically calibrated for xenon. The system is capable of providing up to 120 SCCM of xenon with an accuracy of 1%. Through the use of multiple propellant feed lines and valves it was possible to monitor and control both main discharge (anode) flow and cathode flow of a Hall thruster separately and simultaneously. The flow controllers were periodically calibrated with an apparatus that measures gas pressure and temperature as a function of time in an evacuated chamber of known volume.

A Macintosh computer-based data acquisition system was used to record and analyze all data. Analog voltage signals were read through a 16-bit A/D card manufactured by National Instruments (model NB-MIO-16XH) utilizing adjustable filtering and signal amplification through external signal conditioning modules. High-speed data signals were recorded on a 1 GHz digitizing oscilloscope (Tektronix model TDS-540) and transferred to computer via IEEE-488.2 (GPIB) interface.

Many of the plume diagnostics were performed through the use of a custom-made probe positioning system. This remotely-controlled table contains two rotary platforms on a 1.8-m-long linear translation stage mounted radially

on a 0.9-m-travel axial stage allowing data to be obtained over an extensive volume of the plume. The system allows for sweeps of over 60 cm/s with an absolute position accuracy of 0.15 mm.

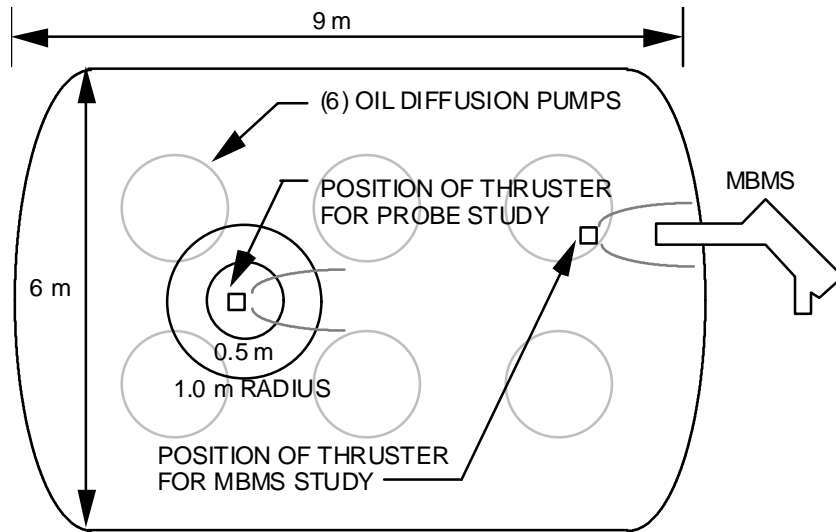


Figure 1-4. Schematic of the 9 x 6 m vacuum chamber. The position of the thruster for the probe-based study reported in Chapter 3 is indicated along with representative arcs of 0.5 m and 1.0 m radius shown for perspective. Also shown is the position of the thruster relative to the Molecular Beam Mass Spectrometer (MBMS) as reported in Chapters 5 and 6.

2. PRACTICAL THEORY OF IN-SITU PROBES

Much information regarding plasma properties can be obtained by interrogating a local volume of plasma using a probe sensitive to some property of the particle flux. Numerous techniques exist for such measurements. This chapter provides a discussion of the various techniques applied in this research along with practical considerations relevant to their use in a Hall thruster plume.

2.1. Introduction

Historically, the most widely used method of diagnosing plasma properties has been to insert a probe in the plasma region of interest. These probes come in many varieties and are, for the most part, sensitive to some property based on the plasma particle flux. As an example, one of the most successfully utilized techniques in plasma research has been the electrostatic probe developed by Irving Langmuir which bears his name. The limitations to such techniques lie in the fact that in-situ probes can only be used to diagnose plasma regions in which the probe itself can survive and are, therefore, limited to cool plasmas. The benefit of in-situ probes is the realization of directly measured values of localized plasma quantities. Fortunately the plasma plume

region of interest to this research comprised a plasma in which probe techniques were successfully applied.

A variety of probe-based plasma diagnostic techniques were utilized to characterize the energetic heavy-particle (ionic and neutral) transport properties within the Hall thruster plume. From a transport-property perspective, any gas quantity of interest can be determined if a full set of the moments of the velocity distribution function is known; thus the goal was to directly measure various moments of the distribution function and attempt to derive secondary transport properties based on these values. To this effort, a Retarding Potential Analyzer (RPA) was used to measure the ion energy distribution function, which is closely related to the velocity distribution function, a planar Faraday probe measured the ion current flux, or the first moment, and a heat-flux sensor was used to measure the third moment of the distribution function. Due to practical instrument considerations it was not feasible to measure the second moment of the distribution function, represented by the plasma pressure. In conjunction with the RPA, Faraday probe, and heat-flux sensor, various other probes were utilized to quantify other plasma properties of interest. This chapter introduces the various probe techniques, derives the relations necessary for data interpretation, and presents practical considerations for their use.

2.2. Retarding Potential Analyzer

The most fundamental quantity from a gaskinetic standpoint for any flow is the velocity distribution function of the flow constituents. This function, when combined with the particle density, can be theoretically used to calculate any flow property of interest.

For this investigation a gridded Retarding Potential Analyzer (RPA) was used to determine the ion energy distribution in the plume. This well-known technique uses a series of electrostatic grids upstream of a current-collecting surface to selectively repel plasma constituents. An account of RPA operational theory can be found in most plasma-diagnostic texts.³⁶ By removing all plasma electrons from the flow and selectively filtering out all ions with energies less than a value determined by the ion retarding grid, the ion current incident on the collector is given as

$$I(V) = A_c q_i e n_i \int_{u_{\min}(V)}^{\infty} u_i f(u_i) du_i$$

or, transforming variables

$$u_i = \sqrt{\frac{2q_i e V}{m_i}} \Rightarrow du_i = \frac{1}{2} \sqrt{\frac{2q_i e}{m_i}} V^{-1/2} dV$$

the collected current becomes

$$I(V) = A_c q_i e n_i \int_V^{\infty} \sqrt{\frac{2q_i e V'}{m_i}} \frac{1}{2} \sqrt{\frac{2q_i e}{m_i}} V'^{-1/2} f(V') dV'$$

Eqn. 2-1

$$I(V) = \frac{q_i^2 e^2 n_i A_c}{m_i} \int_V^{\infty} f(V') dV'$$

Differentiating both sides of Eqn. 2-1 in terms of the repelling voltage, V , yields

$$\text{Eqn. 2-2} \quad -\frac{dI}{dV} = \frac{q_i^2 e^2 n_i A_c}{m_i} f(V).$$

Data are obtained by varying the ion retarding grid potential and recording the collected ion current as $I(V)$ vs V . For a single species flow, i.e. $q_i = \text{constant}$ and $m_i = \text{constant}$, Eqn. 2-2 shows that the negative derivative of these data is directly proportional to the ion voltage distribution function, $f(V)$. Since $V = E_i / q_i$, where E_i is the ion kinetic energy, and we have assumed constant q_i the function $f(V) = f(E_i / q_i)$ is identical to the ion energy distribution function. It must be emphasized here, however, that interpretation of the RPA data as ion energy distribution is only valid in the case of same species (mass and charge) ions. In the more realistic case of ions with the same mass but different charge states the numerical differentiation of Eqn. 2-2 yields only the ion voltage distribution function, e.g. doubly-charged ions with energy E_i appear indiscernible from singly-charged ions with energy $E_i / 2$. Furthermore, the magnitude of the dI/dV curve must be moderated by a value of q^2 for each ionic species.

The RPA used in this investigation employed three grids: the first grid (and probe body) was electrically isolated and allowed to float, thus minimizing disturbance to the plasma from the strong electric fields generated within the probe. The second grid was biased at a constant negative potential of sufficient strength to repel all plasma electrons from the collector. The third grid was an ion-retarding grid connected to a variable high voltage power supply. The

potential of the ion-retarding grid was varied from zero to 500 V; this grid repelled all plume ions with voltages less than that set by the power supply voltage from reaching the collector and being recorded as current.

A schematic of the probe used in this study is shown as Figure 2-1. The probe body, grids, and collector were fashioned from stainless steel. The insulators between grids were made of Teflon and ceramic. The entire probe was approximately 2.5 cm in diameter and 1 cm in depth from first grid to collector. The grid mesh sizes were as follows. Floating grid: 0.112 mm-dia.-wire spaced at 0.266 mm on center; electron retarding grid: 0.028 mm-dia.-wire spaced at 0.056 mm on center; and ion retarding grid: 0.042 mm-dia.-wire spaced at 0.225 mm on center.

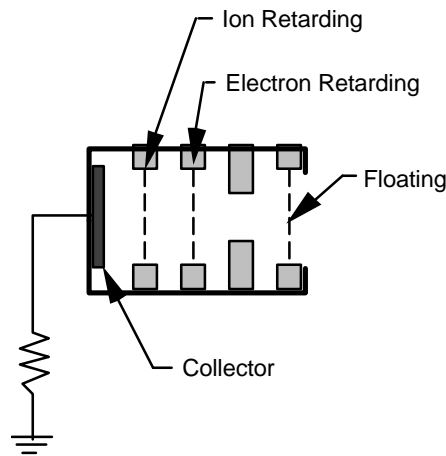


Figure 2-1. Schematic of three-grid RPA utilized to obtain ion energy distribution function.

2.3. Langmuir Probe

The Langmuir probe is one of the most widely used, and therefore widely documented plasma diagnostic techniques.³⁶ Such a probe consists of a biased conductor (wire) inserted in the plasma. The potential of the conductor is varied while monitoring the current induced on the probe by the surrounding electrons and ions. Quantities available from this technique include plasma density as well as electron temperature.

For the Hall thruster plasma a single cylindrical probe technique was used. The probe size was chosen such that it was much larger than the local debye length of the plasma, enabling the use of thin-sheath theory for data interpretation. The Hall thruster discharge employs magnetic fields to achieve propellant acceleration, however the region of plume probed in this study was between 0.5 and 1.0 m from the thruster discharge region; thus, the magnetic field at these locations is insignificant and the plasma can be considered unmagnetized.

2.4. Faraday Probe

The ion current density, which comprises the first moment of the ion velocity distribution function since $j_i = \langle q_i e n_i u_i \rangle / A_c$, can be measured in a straightforward manner through the use of a simple planar probe known as a Faraday probe. In essence, the Faraday probe is a planar conducting surface exposed to the plasma; the current incident on this collector due to the

impinging ions is recorded and divided by the total collector surface area to provide a measure of current density, j_i . In practice, however, there are some subtle points that must be considered and corrected in order to obtain accurate ion current flux data.

The plasma flow of interest to this research contained a very energetic stream of ions which provide an easily measurable current on the probe. However, the electrons are much more mobile and hence the negative electron current incident to the probe surface will significantly obscure the current due to the ions. The electron current, therefore, must be eliminated from the probe. This is accomplished by biasing the probe to a suitably large negative potential with respect to the local plasma to repel all plume electrons. At the same time, this potential will attract ions from regions in space immediately surrounding the collecting surface; this effective ion current collection area, which is now larger than the actual surface area of the collecting electrode, induces an uncertainty to the value of calculated current density. To correct for this field-enhanced ion collection a shield electrode surrounds the edges of the collector electrode. This shield is biased at the same potential as the collector, but is electrically isolated from the ion collection circuitry. The effect of the shield is to create a uniform, planar electric field upstream of the collector electrode such that ion current is drawn only from an area equal to the collector surface area.

Additional complications to the Faraday technique arise due to the high energy of the plume ions. When a high-energy ion strikes a conducting surface

it will cause the conductor to emit a secondary electron into free space in addition to the electron pulled from the conductor by the ion for recombination. This effectively makes “one” ion appear as “two” ions when the net current to the collector is measured. The probability of producing a secondary electron per incident ion is a function of the conductor metal and is known as the secondary electron yield. In order to minimize this uncertainty a conductor with a very low secondary electron yield must be used for the Faraday probe.

The Faraday probe used in this research had a circular collector electrode fashioned from stainless steel with diameter of 2.4 cm. This collector was spray-coated with tungsten, which has a very low secondary electron yield. This disk was mounted flush with the end of a stainless steel cylindrical body which served as a shield electrode, eliminating edge collection effects. A schematic of the probe is shown in Figure 2-2. The collector and body of the Faraday probe were biased with a negative voltage of sufficient strength to repel all plasma electrons so only ions were collected.

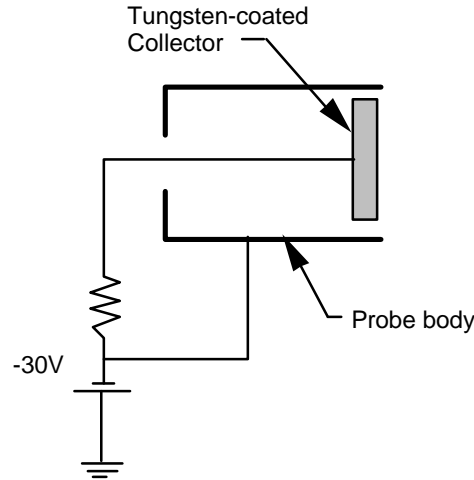


Figure 2-2. Faraday probe used to measure the ion current density.

2.5. Heat-Flux Probe

The convective heat-flux, or power density, is related to the third moment of the particle velocity distribution function, however, measurement of this mode of energy transfer to a surface contains other complicating phenomena. For an isolated surface exposed to the plasma flow of interest to this research the heat transfer can be modeled as

Eqn. 2-3

$$Q_{\text{total}} = Q_{\text{ion conv}}^i - Q_{\text{ion conv}}^r + Q_{\text{e conv}}^i - Q_{\text{e conv}}^r + Q_{\text{radiant}}^i - Q_{\text{radiant}}^r + Q_{\text{ion/elec recomb}} - Q_{\text{ablative}}$$

where a superscript “i” represents incident quantities and “r” denotes reflected quantities. The first two terms of Eqn. 2-3 represent the net convective (kinetic) heat flux due to impacting ions, the next two terms represent the net convective heat flux due to impacting electrons, q_{radiant} represents the radiant energy due to

the hot plasma and thruster components, $q_{\text{ion/elec recomb}}$ denotes the energy deposited to the surface due to recombination of the incident ion with a surface electron, and q_{ablative} is the energy carried away from the surface due to ablated (sputtered) surface material.

For this investigation considerable simplifications to Eqn. 2-3 are possible. Among the heat-transfer phenomena, convective and radiant heating dominate the transport of energy due to the high exhaust velocity of the thruster in addition to the intense radiation produced by both the plasma and the hot thruster body. For ion-electron recombination heating, each ion deposits energy equal to the Xe⁺ ionization energy (12 eV) to the surface as it recombines with an electron from the probe. Calculations show that this mode of probe heating comprises approximately 2% of the convective heating and is therefore ignored in this analysis. Elimination of electron current heating is achieved by biasing the probe to ground potential, which was found to be between 5 and 8 volts lower than plasma potential. Previous studies have measured the electron temperature to be close to 3 eV in the plume;²⁵ the grounded probe therefore collected negligible electron current while inducing only a very small energy addition of 5 volts on the high-energy (200-300 V) ions. The ablative cooling is assumed to be insignificant in this model. Under this simplified model, Eqn. 2-3 becomes

Eqn. 2-4
$$Q_{\text{total}} = Q_{\text{ion conv}}^{\text{net}} + Q_{\text{radiant}}^{\text{net}} \cdot$$

Furthermore, the ion convective heat flux can be written in terms of the flow properties as

Eqn. 2-5
$$q_{\text{ion}}^{\text{net}} = n_i \left[\frac{1}{2} m_i \int_0^{\infty} u_i^3 f(u_i) du_i - 2kT_p \int_0^{\infty} u_i f(u_i) du_i \right].$$

A heat-flux sensor was constructed based on commercially-available transducers. The probe is shown in Figure 2-3. The probe consisted of a water-cooled housing containing two identical heat-flux transducers placed 5 mm apart. The transducer chosen was a Schmidt-Boelter thermopile type device, where the flat surface of a plate is exposed to a heat source. The heat is then conducted in a direction normal to the exposed surface through the plate. The heat flux to the face is then given by $q_{\text{total}} = k_c \Delta T / t$ where k_c is the coefficient of heat conduction for the plate material, ΔT is the temperature difference between the front and back face, and t is the plate thickness. The housing was instrumented with a thermocouple to provide a measurement of probe surface temperature. Each transducer was coated with optical black to minimize reflected radiation. One transducer was exposed directly to the environment to obtain a measure of total heat-flux. The second identical transducer was covered by a sapphire window; this window shielded the device from convective heat-flux. The useful transmission-wavelength range of sapphire is 200-5,500 nm. Previous research has shown the plasma emissions in the SPT-100 plume to be confined mostly to 400-700 nm,^{29,37} while the black-body radiation from the hot

thruster has an expected peak between 1,000 and 5,000-nm. It follows that the sapphire window is effectively transparent to the dominant forms of radiated energy within the plume and provides an effective measure of radiant-heat-flux. Calibration of these transducers, including the sapphire window configuration, was performed by the manufacturer to NIST-traceable standards over the heating and wavelength values expected in this test.

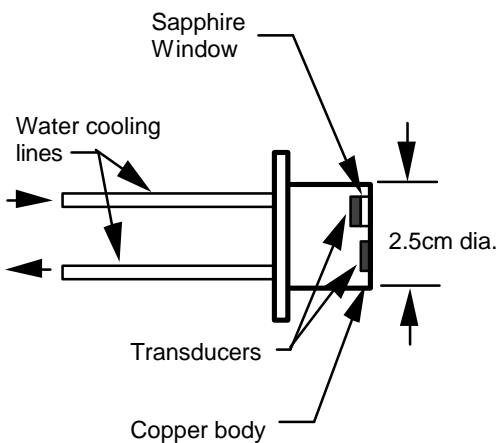


Figure 2-3. Heat-flux sensor showing both total- and radiant-heat-flux transducers mounted in a water-cooled probe housing.

By subtracting the measured radiant-heat-flux from the measured total heat-flux and approximating the heat transfer as in Eqn. 2-4, the net ion convective heating can be calculated. As shown in Eqn. 2-5 a measurement of the net ion convective heating combined with known values for the first and third moments of the ion velocity distribution function and the probe body temperature can be used to solve for the ion density.

It is important to note that the heat-flux probe employs no retarding electrostatic fields, nor does it rely on charge-carrying particles for detection.

Therefore, even though Eqn. 2-4 is written solely in terms of ion properties, the measured convective heat flux is actually due to both ions and neutral particles. It is possible (as will be shown in Chapter 3) to calculate information about the neutral plasma component by comparing the heat flux-derived ion density to the Faraday probe-derived ion density.

2.6. Neutral Particle Flux Probe

Electrostatic probes have widespread application in plasma diagnostics. These probes, such as Langmuir probes and Retarding Potential Analyzers (RPA's), rely on the electric charge of ions and electrons for both energy filtering and particle detection. Neutral particles, however, are unaffected by electric or magnetic fields and are difficult to detect.

Although neutral particles are very elusive, they play an important role in many plasma processes. In E.P. devices such as the Hall thruster neutral propellant is ionized and accelerated by electromagnetic fields. Any propellant that is not ionized will therefore not be accelerated and will be unavailable for electromagnetic thrust production. Optimizing the efficiency of such thrusters requires knowledge of the neutral propellant distribution. In addition to thruster optimization, neutral particle analysis is required to determine the exhaust plume distortion due to ground-based test facilities. In any ground-based vacuum facility there will exist a low density background neutral gas that is due to pump limitations. These neutral particles may collide with energetic

plume particles through charge exchange collisions; such a collision produces an energetic neutral and a slow ion.

The only directly detectable properties carried by neutral particles are momentum and energy. The momentum of the particles, represented by the particle flux, can be detected with a highly sensitive vacuum pressure gauge. However, the plasma flow of interest may have a very large ratio of charged-to-neutral particles. These charged particles also carry momentum and energy in addition to charge. The ions must therefore be filtered out by an electrostatic field prior to particle detection.

The Neutral Particle Flux probe, or NPF, is essentially a hybrid between a vacuum pressure sensor and a traditional gridded RPA. An off-the-shelf MKS tubulated hot cathode ionization gauge was used as the detector for this probe. Affixed to the inlet of the gauge tube was a set of four grids. By varying the potential on these grids, charged particles could be selectively admitted or denied access to the tube collector. A schematic of the probe is shown in Figure 2-4.

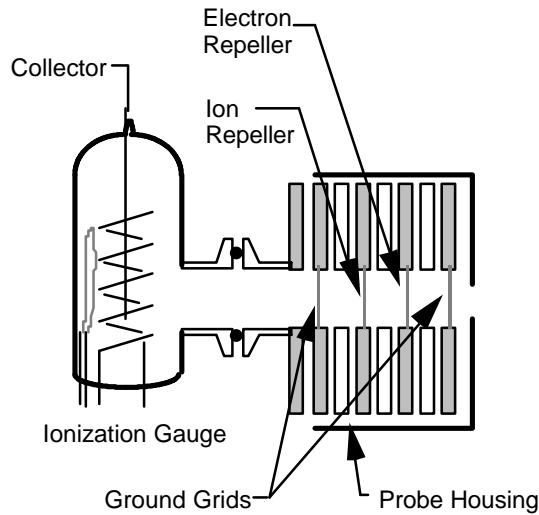


Figure 2-4. Neutral particle flux probe showing electrostatic repulsion grids and ionization pressure sensor used as a detector.

The operation of the grid system in the NPF is identical to that in a traditional RPA as discussed in Section 2.2: an electron retarding grid is used to scrub plasma electrons from the inlet flow and an ion retarding grid is used to remove the ions. A slight change to the RPA configuration involved grounding the first grid of the NPF to eliminate electromagnetic noise generated in the plume from entering the ionization gauge and also placing a grounded grid between the ion retarding grid and the sensing gauge to prevent the strong fields generated by the grids from interacting with operation of the ionization pressure gauge. By dialing the ion retarding grid to a suitably large positive voltage all plume ions will be repelled from the sensing volume; thus only neutral particles will pass unimpeded through the electrostatic grids and will

enter the sensing gauge volume appearing as a rise in pressure on the ionization pressure sensor.

As an output, the NPF probe measures the neutral pressure within the ionization gauge tube. In order to glean useful information from this a relation must be derived relating the measured pressure to the free stream neutral particle flux. This can be accomplished by using free molecular theory to establish a flux balance.

At equilibrium conditions, the total flux of neutral particles entering the ionization gauge tube must be equal to the total flux of particles exiting the tube. Specifically,

Eqn. 2-6
$$n_n \langle u_n \rangle_{in} = n_m \langle u_m \rangle_{out}$$

The flux of particles leaving the tube can be analytically evaluated. In order to do this we assume the ionization gauge tube can be modeled as a gas reservoir containing a macroscopically stagnant equilibrium gas. Additionally we neglect the effects of the finite length entrance to the tube and model it as an ideal orifice. If the mean free path of the gas within the tube is larger than the dimensions of the inlet orifice, then intermolecular collisions can be neglected. This is an accurate approximation: at a measured pressure of 1×10^{-4} torr within the tube the mean free path is greater than 10 cm while the inlet orifice has a diameter of 1 cm. The escaping molecules, therefore, move through the entering molecules without interaction, and the quantities can be evaluated separately.

Denoting the positive z direction exiting the orifice and assuming the gas in the ion gauge tube to be Maxwellian, the velocity distribution of molecules escaping from the ideal orifice is

Eqn. 2-7
$$F_{\text{esc}} = n_m \left(\frac{m}{2pkT_m} \right)^{3/2} e^{-m(v_x^2 + v_y^2 + v_z^2)/2kT_m}$$

for $v_z > 0$, and $F_{\text{esc}} = 0$ otherwise. The escape flux of particles is then integrated as

Eqn. 2-8
$$n_m \langle u_m \rangle_{\text{out}} = \int_{-\infty}^{\infty} dv_x \int_{-\infty}^{\infty} dv_y \int_0^{\infty} dv_z v_z F_{\text{esc}}(v).$$

Combining Eqn. 2-6, Eqn. 2-7, and Eqn. 2-8 yields

Eqn. 2-9
$$n_n \langle u_n \rangle_{\text{in}} = n_m \sqrt{\frac{kT_m}{2pm}}.$$

Finally, using the ideal gas law to relate the measured pressure within the gauge volume to the density closes the relationship between NPF sensor output and neutral particle flux

Eqn. 2-10
$$n_n \langle u_n \rangle_{\text{in}} = \frac{P_m}{\sqrt{2pmkT_m}}.$$

It is apparent from Eqn. 2-10 that if the temperature of the measurement volume, T_m , remains constant then the measured pressure is directly proportional to the flux of neutral particles entering the probe.

3. A PROBE-BASED STUDY OF THE HALL THRUSTER

The Hall thruster plume plasma was characterized using numerous different in-situ probing techniques, many of which were discussed in Chapter 2. These diagnostics were performed at distances of 0.5 m and 1.0 m from the SPT-100, representing the mid- to far-field of the exhaust plume. The data obtained from these diagnostics reveals the underlying plume structure as well as providing insight to processes occurring within the thruster discharge chamber. This chapter presents the results of these probe-based diagnostics and discusses the implications of these data.

3.1. Experimental Set-up and Apparatus

The probe investigations were performed in the University of Michigan Plasmadynamics and Electric Propulsion Laboratory's (PEPL) large vacuum chamber as described in Section 1.5. For each test, three probes were mounted simultaneously to a rotating boom apparatus on a computerized remote positioning system. An overview of the set up is shown as Figure 3-1. The instruments were positioned 0.5-m from the boom pivot point. By positioning the pivot point directly beneath the thruster exit plane it was possible to obtain probe data at various angles off thruster centerline at a constant radial distance

of 0.5-m by simply rotating the boom. As indicated in Figure 3-1, positive angles off centerline indicate measurements taken on the cathode side of the thruster, while negative angles denote the non-cathode half plane. This convention will be followed throughout this thesis. By translating the pivot point of the instrument boom in addition to rotation, data were collected at a radius of 1.0 m from the thruster exit plane while ensuring that the probes remained normal to the flow. Angular resolution of the traversing mechanism was better than 0.1 deg.; however initial alignment of the probes with the “zero” point (thruster axis) could only be confidently performed to within 3 deg. The relative uncertainty in angular position between data points is thus 0.1 deg., but the 3 deg. absolute offset has been conservatively indicated as an error bar for all data points.

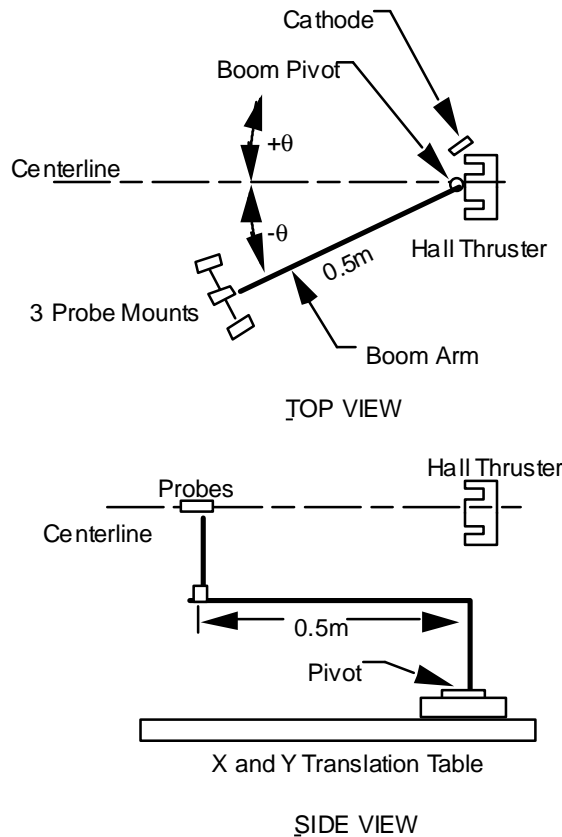


Figure 3-1. Layout of apparatus for in-situ probe based study of the SPT-100 showing probe mounts to automated translation system and coordinate system sign conventions.

The thruster used for all experiments was a flight model SPT-100 magnet layer Hall-effect thruster manufactured by the Fakel Design Bureau of Russia. Nominal operating conditions of 300 V discharge at 4.5 A were used for the SPT-100 thrusters. The thruster electrical discharge and magnetic field circuitry was controlled by a power processing unit (PPU) manufactured by Space Systems/Loral.²⁰ For the SPT-100 a total xenon flow rate of 56 SCCM was supplied to the propellant distribution system on the thruster which split 7% of this flow through the cathode. Main vacuum tank pressure was maintained at

less than 5×10^{-5} torr true Xe pressure during all testing as determined by two hot-cathode ionization gauges.

3.2. Probe Data and Results

3.2.1. Langmuir Probe

Plasma potential was investigated using a single cylindrical Langmuir probe technique for an unmagnetized plasma.³⁶ The probe was constructed of a 0.42-cm-diameter by 5.1-cm-long cylindrical molybdenum mandrel which was vapor-coated with rhenium. Compared with the local debye length this probe dimension allowed a thin-sheath analysis of the data. Langmuir probe I(V) traces were obtained at 0.5-m and 1.0-m radius from the SPT-100 for angular positions within 120 degrees of the thrust axis. These traces were used to calculate the plasma potential as a function of angular position. A typical probe trace is shown as Figure 3-2, with the resultant compiled distribution of plasma potential shown in Figure 3-3.

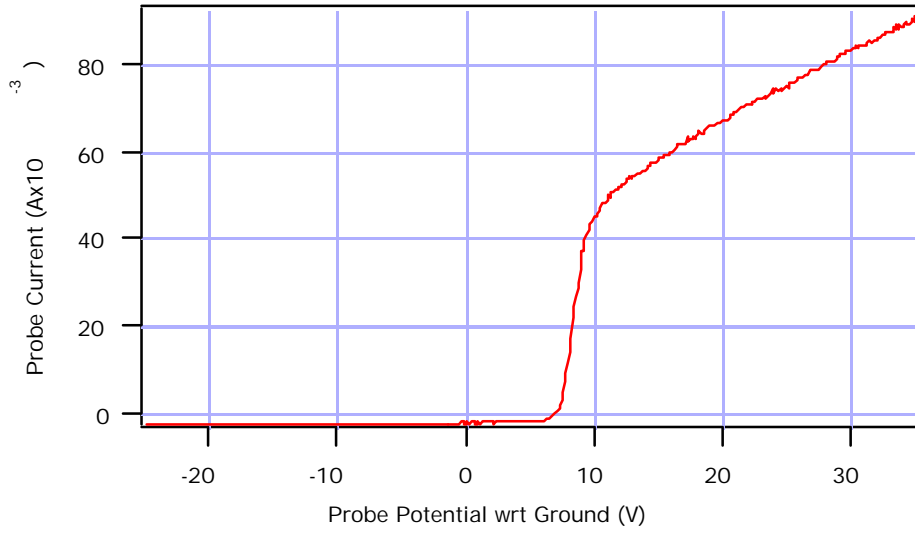


Figure 3-2. Typical Langmuir probe current-voltage characteristic. This trace was taken at 1.0 m from the SPT-100 at 20 degrees off thruster centerline

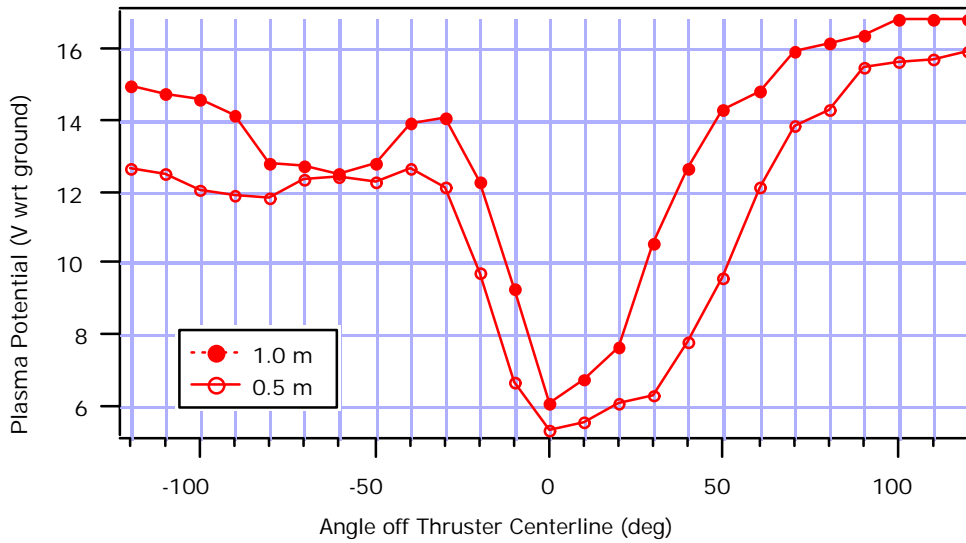


Figure 3-3. Plasma potential in the plume of the SPT-100 at 0.5 m and 1.0 m radius from the thruster exit plane.

3.2.2. Retarding Potential Analyzer

RPA data were collected in the negative half-plane (non-cathode side) of the SPT-100 from centerline out to -60 deg. Beyond 60 deg. off axis the collected current fell to levels for which the numerical differentiation required for data reduction produced unacceptably large error-to-measurement ratios. The electron retarding grid was biased to 30 V below local plasma; this potential was sufficient to repel all plasma electron current from the probe collector.²⁵ For the 0.5-m data set, sweeps of ion current vs. retarding voltage were recorded every five deg., with sweeps every ten deg. for the 1.0-m data. Peak ion current values were in the range of tens of mA near centerline down to hundreds of nA far off centerline for both 0.5-m and 1.0-m sweeps. Examples of these sweeps are shown as Figure 3-4 for the 0.5-m data set. The 10% measurement error represents uncertainties in the collected current. These uncertainties were then propagated through all plume analyses incorporating integrated values based on RPA measurements.

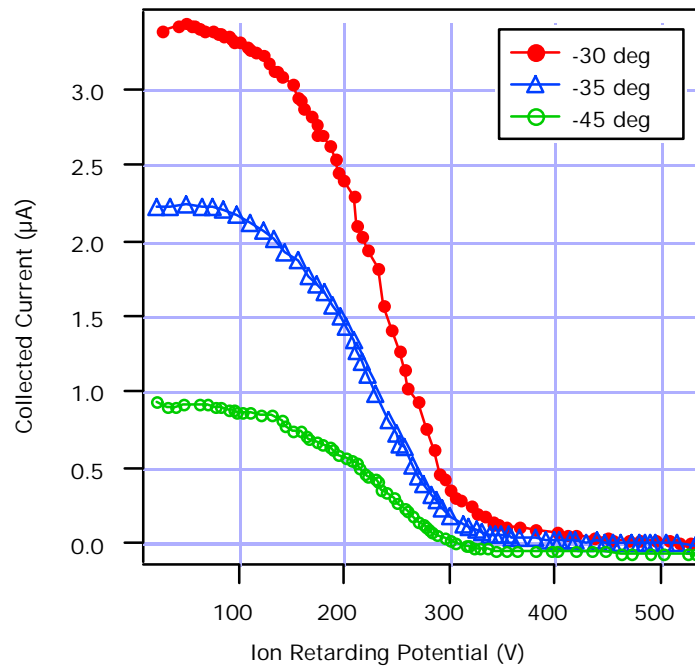


Figure 3-4. RPA sample sweeps of collector current as a function of ion repelling voltage in the plume of the SPT-100 at 0.5 m radius from thruster exit. Uncertainty in current and voltage is less than 10%.

In order to ensure the accuracy of the ion energy distribution a discrete but important correction must be applied to the RPA data. In the plots of Figure 3-4 the ion current is recorded as a function of ion repelling potential with respect to facility ground. As can be seen in Figure 3-3 the local potential of the plasma is above facility ground; the ions thus experience an imposed energy shift as they fall from the undisturbed local potential of the plume to the reference ground potential of the RPA. The magnitude of this shift must be accounted for by subtracting the value of plasma potential as measured by the Langmuir probe from the $I(V)$ vs. V data.

The corrected ion energy distribution curves as derived from data shown in Figure 3-4 according to the technique outlined by Eqn. 2-2 are shown as Figure 3-5 through Figure 3-8.

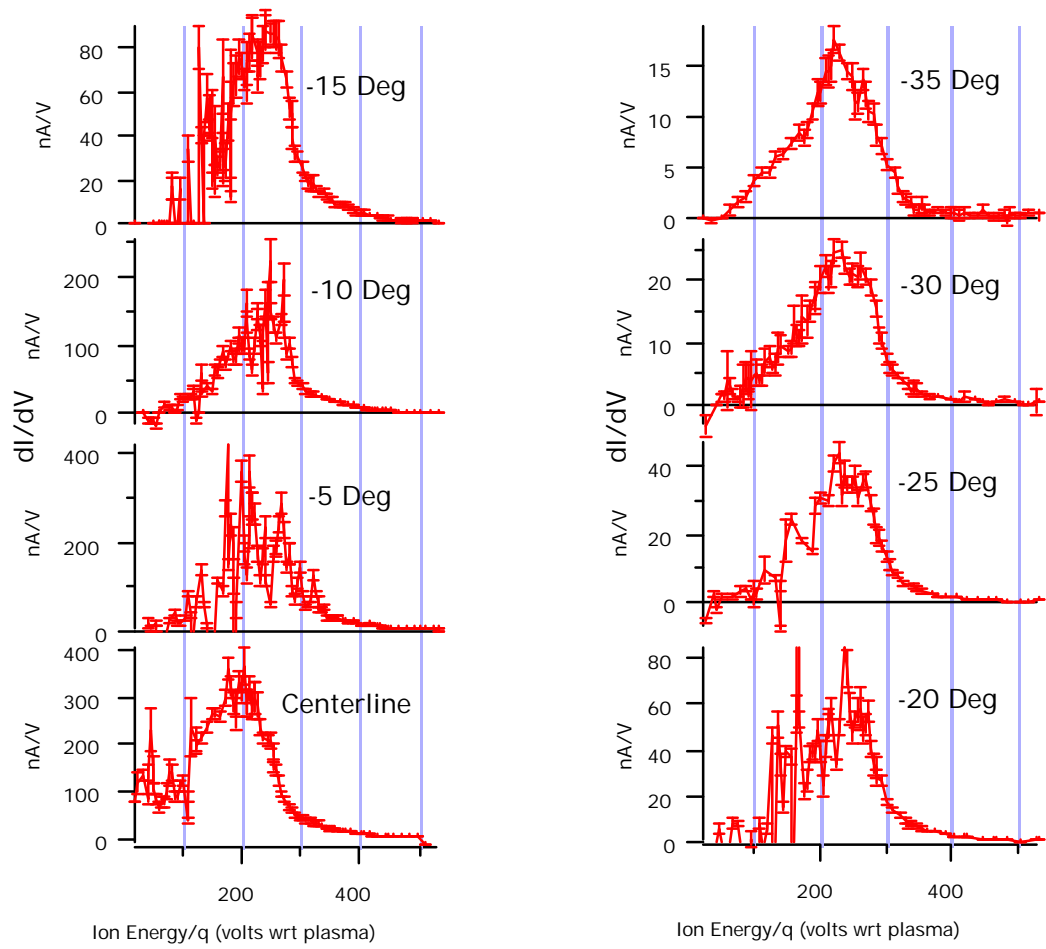


Figure 3-5. Ion energy distribution curves measured with the RPA in the plume of the SPT-100 at 0.5 m radius for positions within 35 degrees of thruster axis.

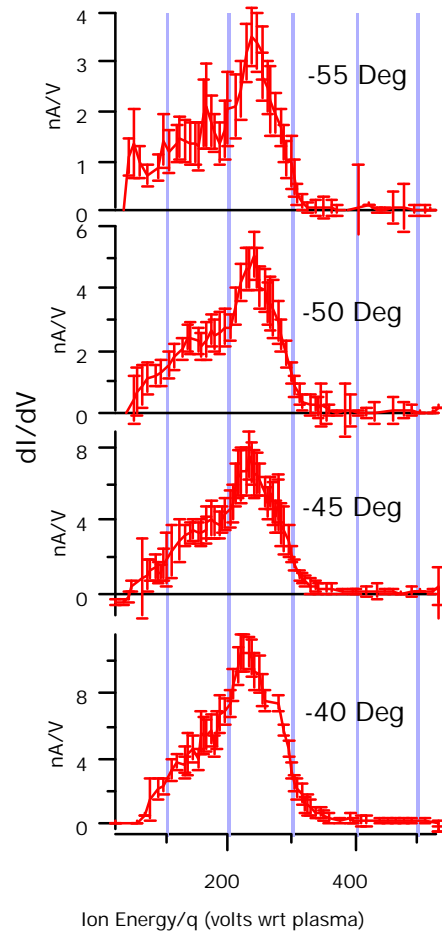


Figure 3-6. Ion energy distribution function measured with the RPA in the plume of the SPT-100 at 0.5 m radius for angles between 40 and 55 degrees off thruster centerline.

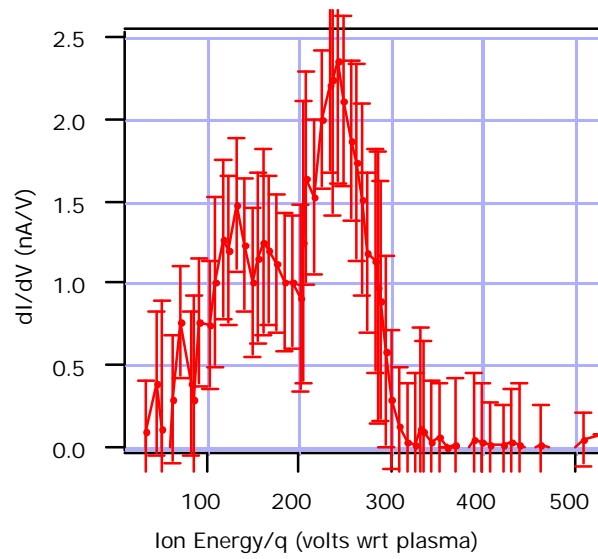


Figure 3-7. Ion energy distribution measured with the RPA in the plume of the SPT-100 at 0.5 m radius at a position -60 degrees off thruster centerline showing high levels of uncertainty due to extremely low measured ion current.

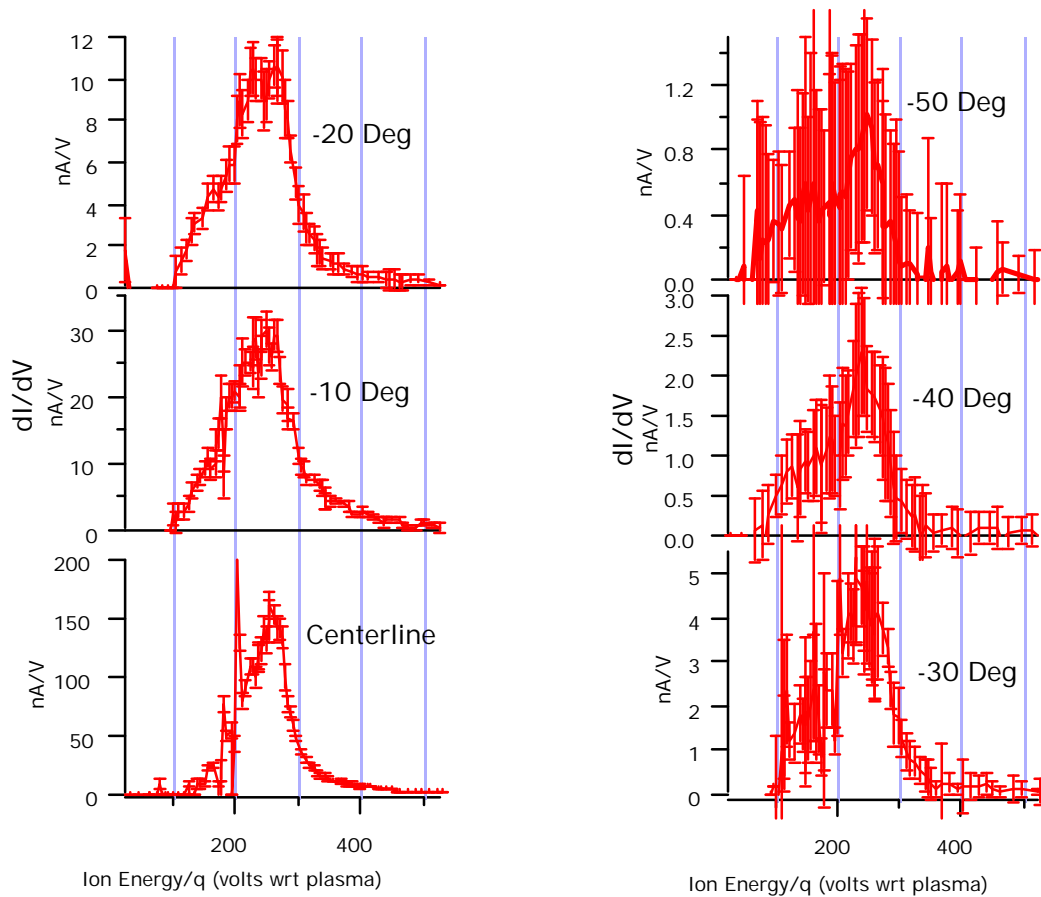


Figure 3-8. Ion energy distribution function measured with the RPA in the plume of the SPT-100 at 1.0 m radius from the thruster for positions within 50 degrees of thruster centerline.

3.2.3. Faraday Probe

The Faraday probe as discussed in Section 2.4 was used to probe the ion current density in both the SPT-100 and the D-55 thruster. The probe collector and shield electrode were biased to 30 V below plasma potential; this value was sufficient to repel all plasma electron current from the probe ensuring collection of ions only.²⁵ By using a sensitive picoammeter (Keithley 486) these data were successfully measured for points located 360 degrees about the SPT-100 at radial

positions of 0.5 m and 1.0 m. The results of the Faraday probe survey are shown in Figure 3-9.

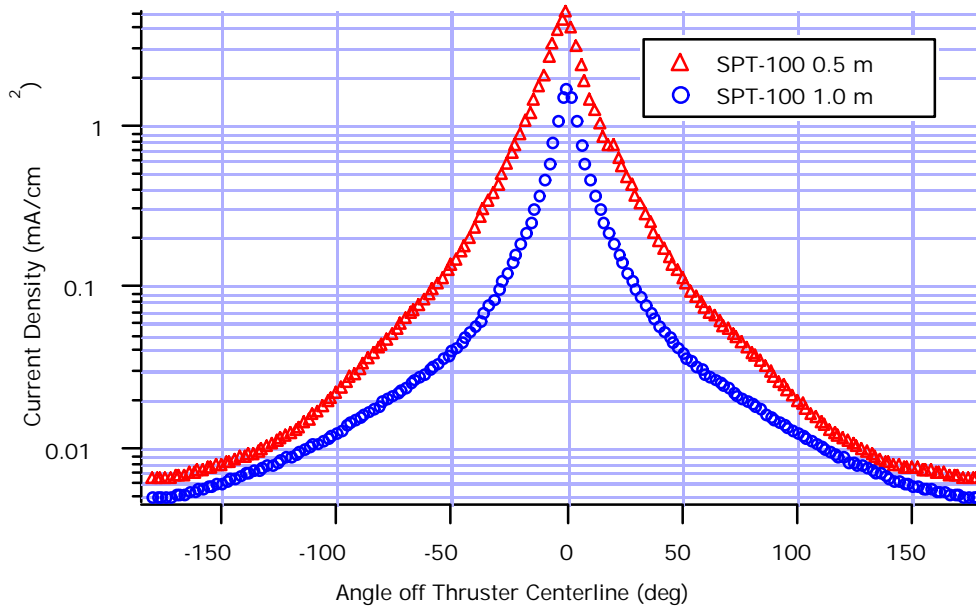


Figure 3-9. Ion current density measurements in the SPT-100 and D-55 at radial positions of 0.5 m and 1.0 m. Uncertainty in current density is less than 10%; uncertainty in angular position is 3 degrees.

3.2.4. Heat-Flux Probe

Data were obtained with the heat flux probe in the SPT-100 at 2-deg. increments from -60 deg. to 60 deg. at 0.5-m radius from thruster exit and five deg. increments at 1.0 m. The heat-flux probe water-cooling lines were connected to a closed-loop thermostatically controlled refrigeration system. The probe body maintained a temperature of between 5 and 6 deg. C for all test points. For the positions of -2, 0, and 2 deg. at 0.5 m, the measured total heat-flux exceeded the calibrated range of the sensor. Total heat-flux data are

therefore unavailable for these points. The radiant- and total-heat-flux data are shown in Figure 3-10 and Figure 3-11. Due to plasma sputtering, the surface texture and therefore the transmission properties of the sapphire window are expected to change over time. However, the entire data set reported required the heat-flux probe to be exposed to the plasma for less than 60 seconds. Over this short period no appreciable variation in the window surface was expected; post-test visual inspection confirmed the absence of window damage. The 10% error indicated in Figure 3-10 and Figure 3-11 represents uncertainties in calibration as reported by the transducer manufacturer over the measurement range of interest, with an additional 2% error to reflect neglect of ion-electron surface recombinative heating (see Section 2.5 for discussion of heat transfer model).

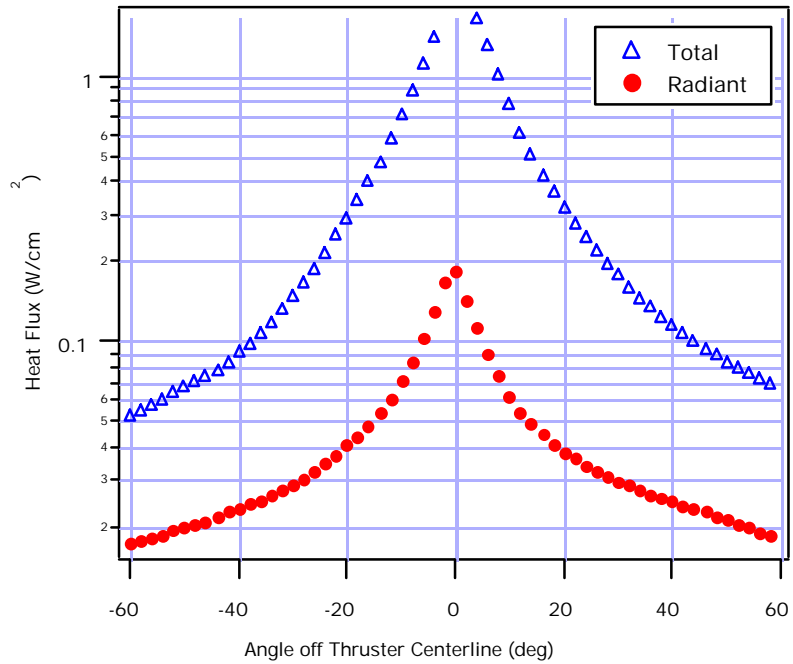


Figure 3-10. Radiant and total heat flux measurements in the SPT-100 at 0.5 m radius from the thruster exit. Uncertainty in heat flux is less than 10%; uncertainty in angular position is 3 degrees.

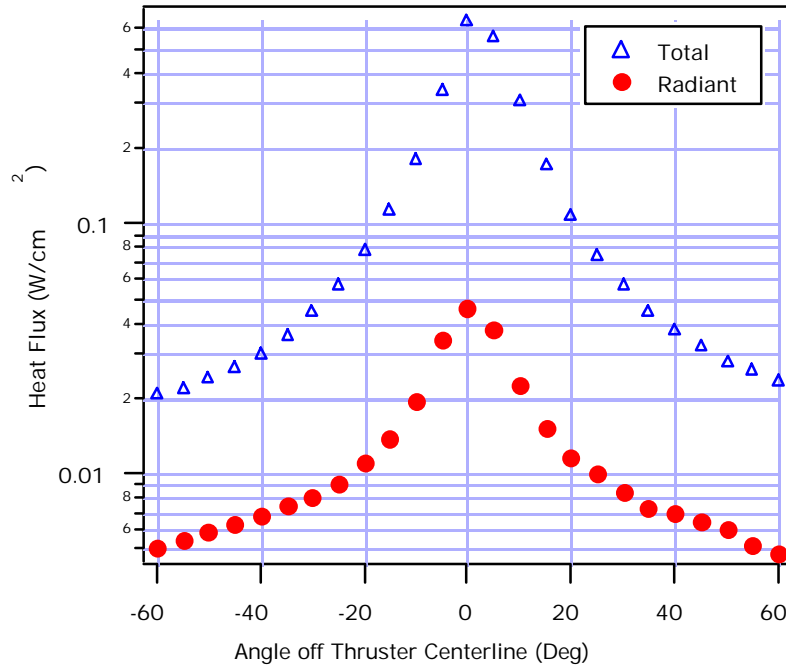


Figure 3-11. Radial and total heat flux measurements in the SPT-100 at 1.0 m radius from the thruster exit. Uncertainty in heat flux is less than 10%; uncertainty in angular position is 3 degrees.

3.2.5. NPF Probe

Since the NPF probe represented a new design initial troubleshooting was performed to assess such aspects as cable design, EMI minimization, and thruster thermal impacts. In order to allow remote positioning of the NPF probe within the volume of the vacuum chamber a custom set of power cables was constructed to operate the vacuum pressure sensor used as a detector. These cables, fed through the vacuum chamber wall, had an overall length of approximately 20 m. The NPF probe ionization gauge operation was verified by simply comparing the pressure measured at stagnant vacuum (no plasma flow) to the pressure measured by existing ionization gauges on the tank. During this

initial verification it was discovered that the NPF probe ionization gauge indicated a measured pressure of around 3×10^{-7} torr while the tank pressure was actually at 4×10^{-5} torr. The cause of this was identified as signal power loss in the lengthy cables. This problem was remedied by shortening the cables to approximately 10 m. After this configuration change the NPF ionization gauge confirmed the pressure measured by the tank gauges. Pressure measured by the ionization gauge showed absolutely no change when voltage was applied to either ion or electron retarding grids in the absence of plasma.

The effectiveness of the retarding grids in removing charged particles was investigated by operating the NPF as a traditional RPA; in this mode of operation the electron retarding grid was set to a constant negative potential of sufficient strength to repel plasma electrons. By adjusting the potential of the ion retarding grid ions were permitted to enter the ionization gauge tube according to Eqn. 2-1. The ion current was incident upon the collector wire of the ionization gauge; the gauge controller interpreted this ion current as an equivalent “pressure” which was directly proportional to the ion current. Thus, a curve of pressure (current) vs. retarding potential was obtained identically to the technique used for the RPA. This current was then numerically differentiated according to Eqn. 2-2 to provide an estimate of the ion energy distribution to verify operation of the repelling grid system. A plot showing a typical check-out trace of the NPF probe operated in this RPA mode is shown as Figure 3-12. By comparing Figure 3-12 with Figure 3-4 and Figure 3-5 it is

apparent that the NPF probe operation was very similar to that of the RPA as expected. Although the energy distribution obtained with the NPF probe is slightly different than that obtained using the RPA (which was specifically designed for such measurements) it is apparent from Figure 3-12 that an ion repelling potential of 500 V applied to the retarding grid of the NPF was sufficient to repel all plasma ions from the sensing volume.

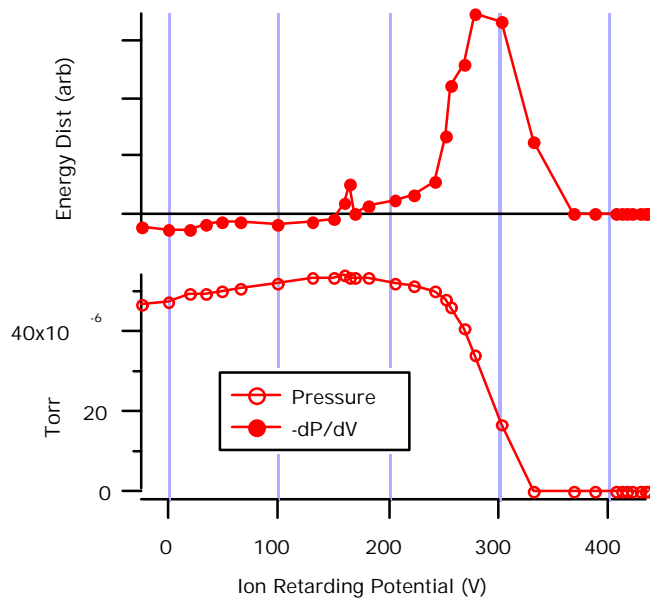


Figure 3-12. NPF probe check-out operation in the plume of the SPT-100 at 0.5 m radius and 15 degrees off thruster centerline. Probe was used as a traditional RPA to verify operation of ion and electron repelling grid system.

With the electron retarding grid set to 30 V below plasma potential and the ion retarding grid set to 500 V, NPF probe data were obtained in the plume of the SPT-100 at 2-deg. increments in the half plane from -60 deg. to 0 deg. at 0.5 m and at 5-deg. increments at 1.0 m. The over-pressure protect set point for the hot-cathode tube was set for 6×10^{-3} torr. Above this pressure, the tube de-

energized in order to prevent damage to the filament. Because of this, data within 10 deg. of centerline could not be obtained at either 0.5 m or 1.0 m. The raw output of the NPF probe is shown in Figure 3-13. Error bars reflect uncertainty in calibration of total pressure gauge as supplied by the manufacturer.

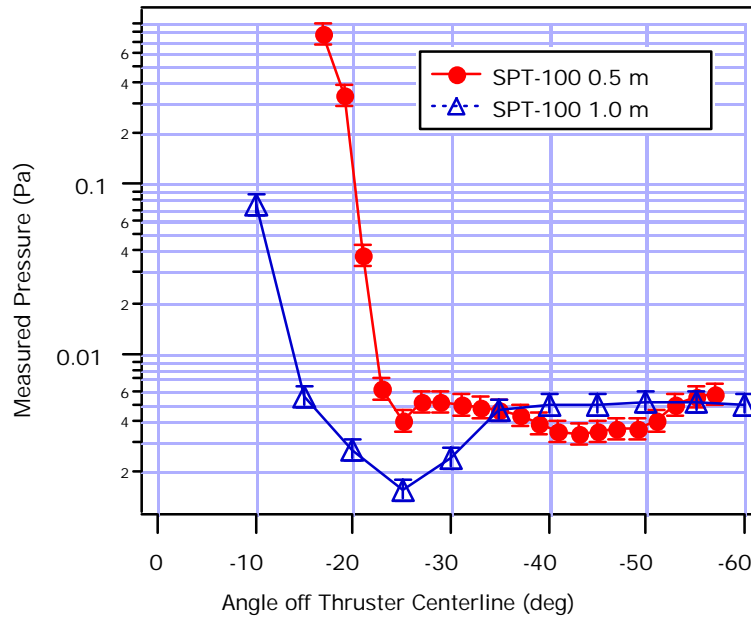


Figure 3-13. Neutral particle flux probe measurements in the SPT-100 at 0.5 m and 1.0 m. Uncertainty in angular position is 3 degrees.

3.3. Interpretation of Probe Results and Derived Quantities

3.3.1. Ion Energy Structure

As derived in Section 2.2 interpretation of the RPA data as the ion energy distribution requires that the flow consist of a single species of ion (i.e. identical

charge and mass). Although the plume of the SPT-100 is comprised entirely of one ionic mass species (xenon) the distribution of ionic charge states likely includes ions with $q=1+$, $2+$, etc. Indeed, using an emission spectroscopic technique Manzella²⁹ estimated the plume to be comprised of nearly 90% Xe^+ with Xe^{2+} occupying approximately 10% of the total flow. Based on the spectroscopic study, the data reduction procedure utilized for the research reported here simplifies the physics by assuming the flow to consist entirely of Xe^+ . Although technically the derivative of the RPA I-V characteristic is the voltage ($E_i/q_i e$) distribution, it has been assumed here that $q=1$ so that dI/dV is equal to the ion energy distribution. This assumption presents considerable limitations to the data analysis which will be discussed more fully in Chapters 5 and 6, however the simplification achieved permits valuable knowledge of the plasma properties to be obtained through simple probes without requiring the use of complicated emission or mass spectrometric diagnostics.

For angles near centerline of the SPT-100 the ion energy distribution is sharply peaked near a most probable energy of around 230 V, with a full-width-at-half-max (fwhm) of 100 V at -30 deg. off centerline. For larger angles, the distribution becomes much broader due to the appearance of a population of lower energy ions. Although the most probable ion energy remains 230 V, the fwhm is increased to more than 150 V at -45 deg. This broadening of the energy distribution for large angles was evident in all data points for both 0.5-m and 1.0-m data sets, however the most probable ion energy remains very near 230 V

for each trace. The discharge voltage of 300 V was applied to the thruster between the anode and the cathode; the cathode itself floated about 22 V below facility ground and the local plasma potential for points in the plume at 0.5 m and 1.0 m radius was approximately 7 V above ground (see Figure 3-3). This represents an available accelerating voltage of about 270 V for the propellant ions. However, a high energy “tail” representing ions accelerated through potentials greater than 270 V can be seen in all RPA traces (see Figure 3-5 through Figure 3-8). The size of this tail was largest for angles near thruster centerline and decreased with increasing angle. Furthermore, the tail was smaller in the 1.0-m data sets than for corresponding angles in the 0.5-m data. The existence of this tail has been documented previously by other researchers and has been the subject of much controversy,^{24,25,38,39} however, an explanation and account for the phenomena has not been attempted prior to this study. Chapters 5 and 6 of this volume contain a detailed explanation for the physical processes responsible for this tail.

Quantitatively, the ion energy distribution curves can be better understood by numerically evaluating the first few moments. Taking advantage of the assumption that the plume is entirely composed of singly ionized xenon, it is trivial to convert the ion energy distributions, $f(E_i/q_i)$, to ion velocity distributions, $f(u_i)$. The moments of these velocity distributions can then be evaluated and utilized to calculate ionic transport properties. The first moment, or average ion velocity, was computed numerically and is shown in Figure 3-14

for both 0.5 m and 1.0 m radius. The error bars of Figure 3-14 represent the propagation of original measurement uncertainties through the numerical integration.

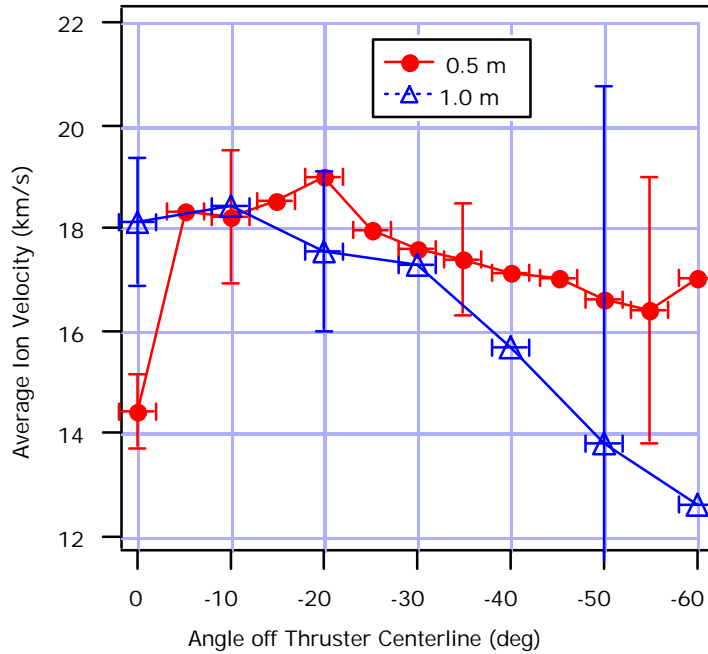


Figure 3-14. Average ion velocity in the SPT-100 obtained by integrating the ion energy distribution functions measured using the RPA. Data are shown for both 0.5 m and 1.0 m radial distances from the thruster exit plane. A few sample error bars are shown to indicate the magnitude of the uncertainty inherent to all data points.

A striking result of this analysis was the discovery of a very narrow low-energy core surrounded by a slightly higher-energy annulus with a peak at -20 deg. in the plume at 0.5-m radius from thruster exit. Although such a topology would be expected in the near field of the thruster due to the annular shape of the discharge chamber, it was believed that the divergence of the ion beam would smear out this configuration very rapidly. On the contrary, the average

ion velocity on centerline at 0.5-m is less than the velocity computed for any other point measured in the 0.5-m data set. This low-energy core is very narrow, limited to a region in space with a half angle of 5 deg. about thruster centerline. It should be noted, however, that this annulus structure was not uncovered in the Faraday probe data (see Figure 3-9). Since the Faraday probe measures $q_i e n_i \langle u_i \rangle / A_c$, the rapidly increasing ion density near centerline overwhelms the dip in $\langle u_i \rangle$ and a monotonically increasing ion current density results. The high-energy annulus/low-energy core structure is not present in the 1.0-m data set. At this downstream location the beam divergence has completely filled in the core. In addition to the smearing of the spatial energy structure, the ion velocity for large angles (greater than 30 deg.) is less at 1.0 m than at 0.5 m.

The existence of a high-energy plasma annulus with low spatial divergence is consistent with thruster discharge chamber geometry and field topology. The high-energy ions are formed closer to the anode and hence, further back inside the discharge chamber. These ions, in order to escape the discharge chamber without colliding with the wall, must have their velocity vectors geometrically contained within a defined solid angle. Those ions formed near the end of the discharge chamber farther from the anode will have lower energy as a consequence of the field topology, and will also have their velocity vectors distributed about a larger allowed solid angle.

The low-energy core in the mid-to-near field is most likely due to the distribution of ion production within the discharge chamber. According to data

obtained by Bishaev and Kim,¹¹ the majority of the ionization within the thruster occurs very near the inner wall of the discharge chamber. In order for these ions to escape the discharge chamber without colliding with a wall and being neutralized, their velocity vectors must be directed largely away from thruster centerline. Such a distribution of velocity vectors would produce a depletion of high-energy ions on thruster centerline until a considerable distance downstream. Such a scenario is depicted conceptually in Figure 3-15, with the high-ion-formation region of Bishaev and Kim¹¹ indicated.

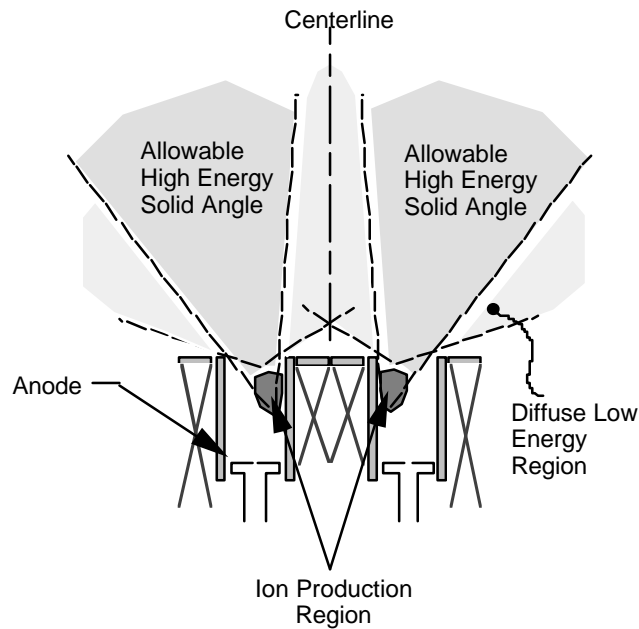


Figure 3-15. Schematic representation of mechanism causing high-energy annulus and low-energy core in thruster plume. Ion production region denoted as according to Bishaev and Kim.¹¹ High energy ions are formed closest to the anode.

3.3.2. Density Distribution

With the broad inter-related suite of data obtained in this study, it was possible to calculate two measures of particle density. In the first method, the Faraday probe-measured ion current density, j_i , is combined with the RPA-derived first moment of the ion velocity distribution function, $\langle u_i \rangle$, and used to predict the ion density according to

Eqn. 3-1
$$n_i = \frac{j_i}{q_i e \langle u_i \rangle}.$$

The second method is based on the heat-flux-probe data: by subtracting the measured radiant heat-flux from the measured total heat-flux, the value of particle convective heating, q_{conv} , is obtained. Combining q_{conv} with numerically calculated values of $\langle u_i \rangle$ and $\langle u_i^3 \rangle$, and recalling that the heat-flux probe is sensitive to both neutrals and ions, the total particle density (ion and neutral) can be calculated according to

Eqn. 3-2
$$n_{\text{total}} = \frac{q_{\text{conv}}}{\frac{1}{2} m_i \langle u_i^3 \rangle - 2kT_p \langle u_i \rangle}.$$

Based on the methods outlined above, two separate values of particle density are presented in Figure 3-16 for the 0.5-m data, and

Figure 3-17 for the 1.0-m data. The error bars in Figure 3-16 and

Figure 3-17 represent the propagation of all original measurement uncertainties. As can be seen in the figures, both methods of calculating particle

density produce comparable results indicating that neutrals represent only a small fraction of the flow. The maximum difference between the values at 0.5 m is approximately 25% at -5 deg., with a somewhat larger discrepancy of 40% on centerline at 1.0 m.

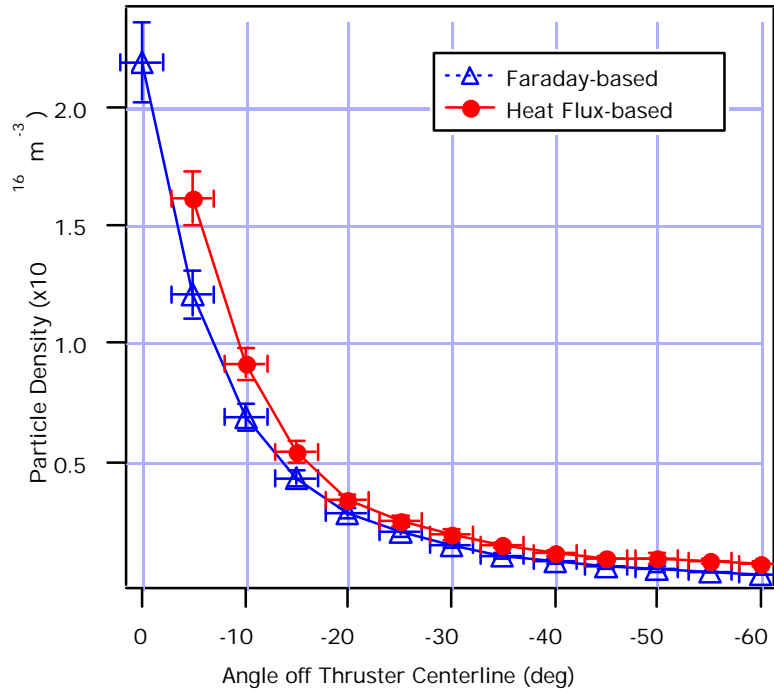


Figure 3-16. Comparison of calculated particle density in the plume of the SPT-100 at 0.5 m radius from thruster exit plane. The Faraday-based value is calculated according to Eqn. 3-1 and the heat-flux based value is calculated via Eqn. 3-2.

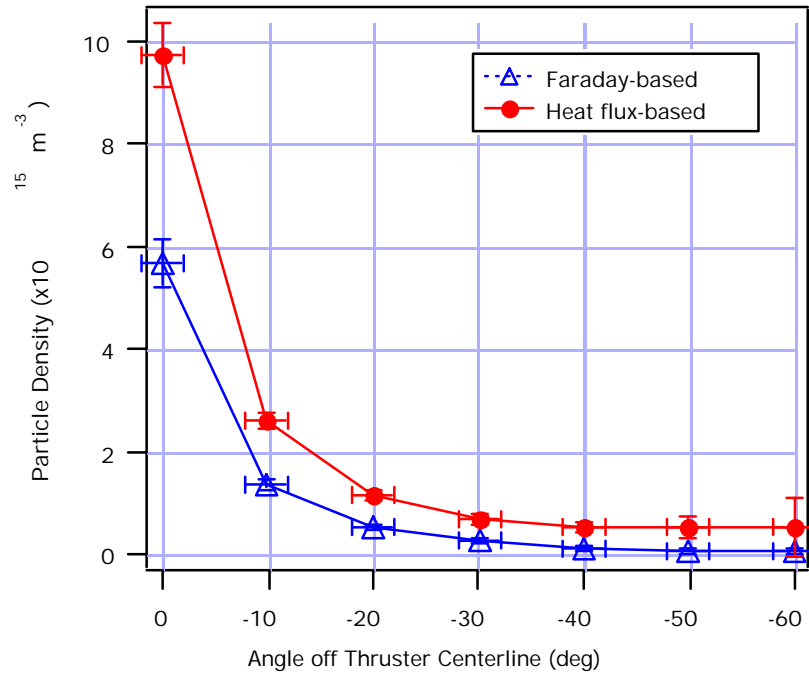


Figure 3-17. Comparison of calculated particle density in the plume of the SPT-100 at 1.0 m radius from thruster exit plane. The Faraday-based value is calculated according to Eqn. 3-1 and the heat-flux based value is calculated via Eqn. 3-2.

3.3.3. Neutral-Particle Properties

The neutral component of the plume was evaluated in this investigation using two methods: direct measurement of neutral particle flux using the NPF probe, and calculation of neutral particle properties based on the inter-relation of other probe data. The measured neutral pressure within the NPF probe displayed as Figure 3-13 can be converted via Eqn. 2-10 to provide a measure of neutral particle flux. This quantity is plotted in Figure 3-18 for both the 0.5-m and 1.0-m data sets.

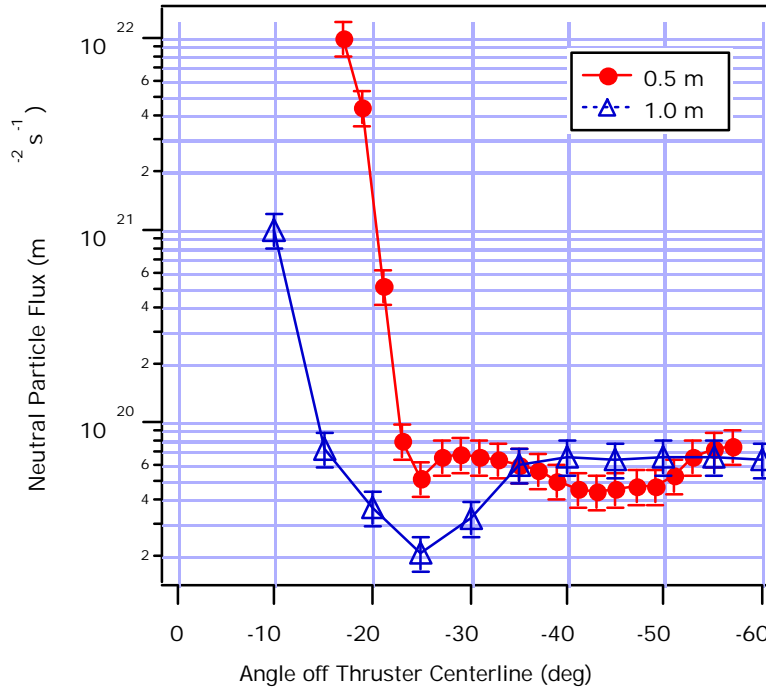


Figure 3-18. Neutral particle flux in the plume of the SPT-100 measured with the NPF probe at 0.5 m and 1.0 m radius from the thruster exit.

The NPF data suggest a region of high neutral particle flux near plume centerline. Although the data sets are limited to angles larger than 10 deg., it is evident that a well defined core of neutral particles is present in the plume. This core is surrounded by a region of depressed neutral flux bottoming out at about -25 deg., followed by a subsequent rise to ambient background pressure outside of about -40 deg. The region of depleted neutrals near -25 deg. corresponds loosely with the high-energy ionic annulus shown in Figure 3-14 at 0.5 m. The relationship between the depressed neutral flux and elevated ion energy is not fully understood at this writing.

The second method of determining neutral properties stems from the inherent difference between the Faraday probe and the heat-flux probe. By subtracting values calculated on the basis of Faraday data from values calculated from the heat flux data, it is possible to quantify the contribution of the neutral flow. This method was used to evaluate the neutral particle heat-flux. The value of convective heat flux, q_{conv} , due to both neutrals and ions was calculated from the heat-flux probe data by subtracting the measured radiant heat-flux from the measured total heat-flux. The ionic contribution to the convective heat flux was derived according to Eqn. 2-5 with the ion density calculated from the Faraday probe and RPA data via Eqn. 3-1. Subtracting the derived ionic heat-flux from the measured convective (ion and neutral) heat-flux yields the value of neutral particle heating

Eqn. 3-3
$$q_{\text{neutral}} = q_{\text{conv}} - n_i \left[\frac{1}{2} m_i \langle u_i^3 \rangle - 2kT_p \langle u_i \rangle \right].$$

This quantity is plotted in Figure 3-19 for both 0.5-m and 1.0-m data sets, with error bars representing the propagation of all measurement uncertainties. As expected, the neutral particle heating is greater at 0.5 m than at 1.0 m. Furthermore, the neutral heating is confined to a region within 25 deg. of thruster centerline falling off to negligible values sharply for larger angles. This corroborates the NPF data which also showed the neutral flux to be contained within a well-defined region with a half angle of 25 deg.

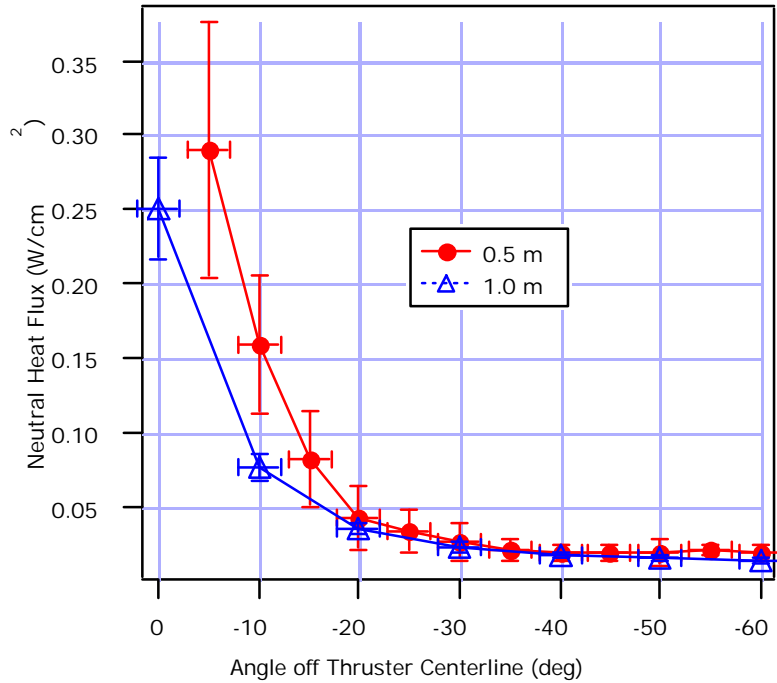
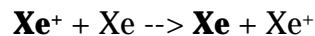


Figure 3-19. Calculated neutral particle convective heating in the plume of the SPT-100 at 0.5 m and 1.0 m radial positions from the thruster exit plane.

3.3.4. Ion-Neutral Charge Exchange Processes

The neutral and ionic portions of the plasma flow are linked through the process of resonant charge exchange (CE). In this process a high energy ion interacts with a low energy neutral of the same species. On a quantum mechanical level this interaction causes the transfer of an electron from the slow atom to the fast ion. The net result is a slow ion and fast neutral atom. In equation form this can be represented as



where bold face is used to indicate the high energy particle. The process is termed to be resonant since the energy liberated by the electron-ion

recombination is equal to the first ionization potential of the neutral; no third body is required. This process can occur within the thruster acceleration region due to entrained ambient background gas or un-ionized propellant, or it can occur downstream of the acceleration zone due to ambient background gas. There are basically two approaches that can be used to detect CE: one can either look for the slow ion products or the fast neutral products since their production rates are one-to-one. In this investigation both methods of detecting CE products were attempted.

Analysis of the neutral component of the plasma is missing one vital piece of information to close the CE analysis: the value of the neutral particle velocity distribution function. However, some insight to the neutral component can be derived from available quantities. From a top level perspective, it would be valuable to know whether the neutrals detected by the NPF are "slow" ambient background particles, or "fast" CE products. If we assume that the neutrals are slow, macroscopically stagnant Maxwellian particles at temperature T_n , then the free molecular convective heating to the water cooled probe is computed as

Eqn. 3-4
$$q_{\text{neutral}} = \frac{1}{4} n_n \langle u_n \rangle k (T_n - T_p)$$

where

Eqn. 3-5
$$\langle u_n \rangle = \sqrt{\frac{8kT_n}{m_n}}$$

Since the flow has been assumed to be stagnant, the pressure measured by the NPF probe would be the true ambient neutral pressure; this can be converted via the ideal gas law to obtain n_n . Evaluating Eqn. 3-4 for the sample point at -15 deg. from centerline at 0.5 m where $P_m = 0.8$ Pa (6×10^{-3} torr from Figure 3-13), and assuming a neutral background temperature $T_n=300$ K yields a value of neutral particle convective heating of 3.2×10^{-4} W/cm². This is 250 times lower than the value of 0.08 W/cm² derived from the data for the neutral heating at this location (see Figure 3-19). Even if the assumed background neutral temperature is increased in order to agree with the data-obtained heating, the neutrals would have to have an unrealistically high temperature of over 100,000 K (8.6 eV) at this sample point to account for the 0.08 W/cm² measured neutral heating. It is apparent that a distribution of slow neutrals cannot account for the measured neutral convective heating and that the neutrals measured with the NPF probe are most likely highly-energetic CE products.

The appearance of CE products is supported by a statistical collision analysis of the plume/background gas interaction. The charge exchange collision cross section for Xe⁺-Xe can be computed according to⁴⁰

Eqn. 3-6
$$\sigma_c = (K_1 \ln C_r + K_2)^2 \times 10^{-20} \text{ m}^2$$

with $K_1=-0.8821$ and $K_2=15.1262$. For this investigation, with an average relative interparticle speed $C_r = 17$ km/s and a tank background pressure of 6×10^{-3} Pa (5×10^{-5} torr), the CE mean free path is approximately 1.5 m. Although

this mean free path is longer than the largest path length in this investigation (1.0 m), examination of the collision statistics reveals that the effect of CE is not negligible. The fraction of particles which undergo a collision within a path length "s" is given by the well-known survival equation as

Eqn. 3-7
$$P_{\text{coll}}(s) = (1 - e^{-s/\lambda}).$$

Eqn. 3-7 shows that at 0.5 m from the thruster exit, almost 30% of the emitted plume ions have suffered a CE collision; this increases to a value of almost 50% of the ions undergoing a CE collision by 1.0 m. In reality, the tank background pressure of 6×10^{-3} Pa is not composed entirely of neutral Xe. Due to facility base-pressure limitations, a portion of this background pressure is residual air. Although accounting for this lower background Xe density would increase the computed Xe⁺-Xe mean free path, other non-resonant collisions between particles of dissimilar masses must be accounted for; these collisions would likely affect the plume ions similarly to the ideal case considered here.

4. MOLECULAR BEAM MASS SPECTROMETER DESIGN

Very little research has been performed to date to characterize the species constitution of the Hall thruster plasma plume. The only study to attempt to identify plasma species was an emission spectroscopic investigation that utilized a complicated equilibrium model to estimate flow fractions from data. Based on this lack of data, and the insensitivity of probe-based techniques to plasma species, an effort was undertaken to construct an instrument to make direct measurements of the mass and charge composition of the Hall thruster plume. This chapter reports on the design of the instrument used in this research and discusses general principles that may be valuable to future investigations.

4.1. Motivation Behind MBMS Research

As discussed in Chapters 2 and 3, in-situ plasma probes constitute a simple method through which detailed plasma properties can be evaluated. However, these probes provide no insight to plasma species (charge state and mass) composition. Indeed, the RPA technique of measuring the ion energy distribution function is not merely insensitive to flow species, rather its interpretation is only valid for a single species. Although RPAs enjoy

widespread use in plasma diagnostics it must be recognized that in a multiple-species flow differentiation of the I(V) vs V data does not produce a function directly proportional to the energy distribution as widely accepted, instead

Eqn. 4-1
$$\frac{dI}{dV} \propto \frac{q_i^2}{m_i} f(E/q_i).$$

The non-trivial relationship between the RPA data and the ion energy places a limitation on the rigor with which the resultant quantities can be applied.

Further complicating the understanding of RPA data has been the extensive documentation of a high-energy “tail” of ions with accelerating voltages much greater than that applied between the anode and cathode of the Hall thruster. This tail has been the subject of much controversy and confusion of late; postulates to explain its existence included plasma instability-driven turbulence within the thruster discharge as well as recombinative or charge-changing collisions within the exhaust plume. Exploration of these hypotheses required species-dependent analysis of the plasma. In addition to the data interpretation issues, the numerical differentiation required with the RPA technique produced unavoidably “noisy” distribution functions (as can be seen in Figure 3-5 through Figure 3-8) that impose further uncertainties in data analysis.

As a means of quantifying the plasma species constitution and to obtain a verification of the puzzling ion energy distribution, Manzella utilized spectroscopic techniques to interrogate the Hall thruster plasma. In these studies

emission spectroscopy was used to measure the xenon ionization fractions²⁹ while a laser-induced fluorescence (LIF) technique was used to obtain the Xe^+ velocity distribution function.³⁰ The emission study suggested that the fraction of Xe^+ was between 76% and 89% of the total flow while Xe^{2+} comprised between 19% and 12%. However, the author acknowledged that the Boltzmann equilibrium model used to derive these values from the data was not suited to the Hall thruster plasma. Although the correct model was identified as a collisional-radiative equilibrium (CRE) model, no such model was developed for several reasons attributed to the complicated atomic energy structure of xenon coupled with a lack of experimental data regarding various excitation rates; the accuracy and uncertainty of the derived ionization fractions is therefore unknown. The LIF investigation produced accurate values of the average ion velocity. Additionally, the shape of the fluorescence excitation spectrum was evaluated to assess other plasma parameters. However, the results implied by this shape analysis were in striking disagreement with the RPA data: the LIF study implied a width in the distribution function corresponding to a 3 eV spread in ion energy while the RPA data implied a spread on the order of 100-150 eV. Again, although the uncertainty in the ion velocity measured with the LIF technique was excellent, interpretation of the spectral shape required a complicated equilibrium model based on a large number of individual atomic transitions; many constants required to model these transitions were unavailable and had to be estimated.

The state of research preceding the study reported here reflected conflicting and poorly understood information regarding the ionic composition and energy within the Hall thruster plume: the only species analysis performed required the use of a complex and admittedly inappropriate model to achieve estimates of propellant ionization fraction, while the two existing measurements of ion energy distribution were in disagreement. It was apparent that a technique was required to (1) provide a direct measure of the propellant ionization fraction independent of a model regarding the plasma equilibrium state and (2) directly measure the energy distribution function of each species using a method that is sensitive to ionic charge and mass. Based on this need the construction of a custom-built molecular beam mass spectrometer for Hall thruster plume studies was initiated.

4.2. Configuration of Apparatus

There are three fundamental methods by which atomic and molecular particles can be filtered and analyzed according to mass. A discussion of these methods and their development histories can be found in the text by Duckworth, et al.⁴¹ and the collection edited by Reed.⁴² The first and possibly earliest developed method is known as magnetic sector mass spectroscopy. In this technique a strong magnetic field is used to separate ions into mass-dependent semi-circular trajectories for subsequent ion collection. Another method which is currently enjoying great popularity among commercial instrument

manufacturers is quadrupole mass analysis (QMA). QMA instruments utilize a set of four conducting rods with hyperbolic or circular cross sections to establish a quadrupole electrostatic field. A combination of DC and RF electric potentials are applied to the quadrupole lens such that a stable rectilinear trajectory from the instrument entrance to the current detector is possible only for a single ionic mass species. The third type of mass analysis is referred to as time-of-flight (TOF) spectroscopy. Although the basic operating principles of this technique have been known and discussed since the beginning of atomic physics it is only recently that high-speed, high-sensitivity electronics have matured sufficiently to make TOF techniques feasible; as a result the field of TOF mass spectroscopy has experienced a period of rapid growth of late.^{43,44,45} TOF spectroscopy relies on the principle that ions of equal energy but different mass will travel at different velocities. By timing the trajectory of an ion with known energy over a known path length it is possible to calculate the ion velocity and, therefore, the ionic mass.

In the initial effort to construct an MBMS for Hall thruster plume studies an attempt was made to incorporate a commercially available QMA to accomplish the ionic mass filtering. This effort, however, was unsuccessful due largely to incompatibility between the ion energy in the Hall thruster plume and the ion energy required by the QMA for mass analysis. The technique chosen for the custom-built Hall thruster MBMS was the TOF method with an instrument configuration similar to that developed by Pollard for analysis of

gridded electrostatic ion thrusters.⁴⁶ A detailed discussion of the components of this system will be presented in Sections 4.3 and 4.4, however, an overview of the system configuration is shown schematically in Figure 4-1 with photographs of the actual system in Figure 4-2 and Figure 4-3.

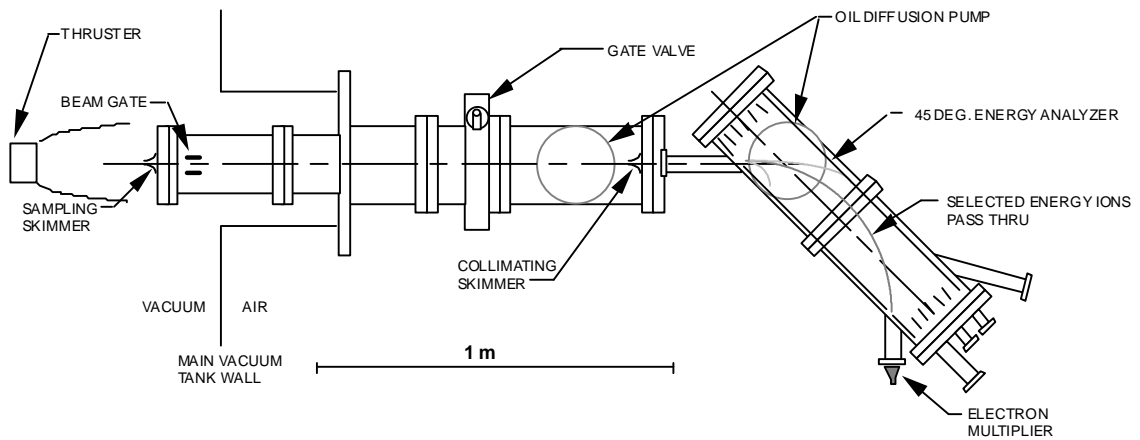


Figure 4-1. Schematic of overall configuration of MBMS apparatus showing orientation to main vacuum chamber, thruster mount, and scale size.

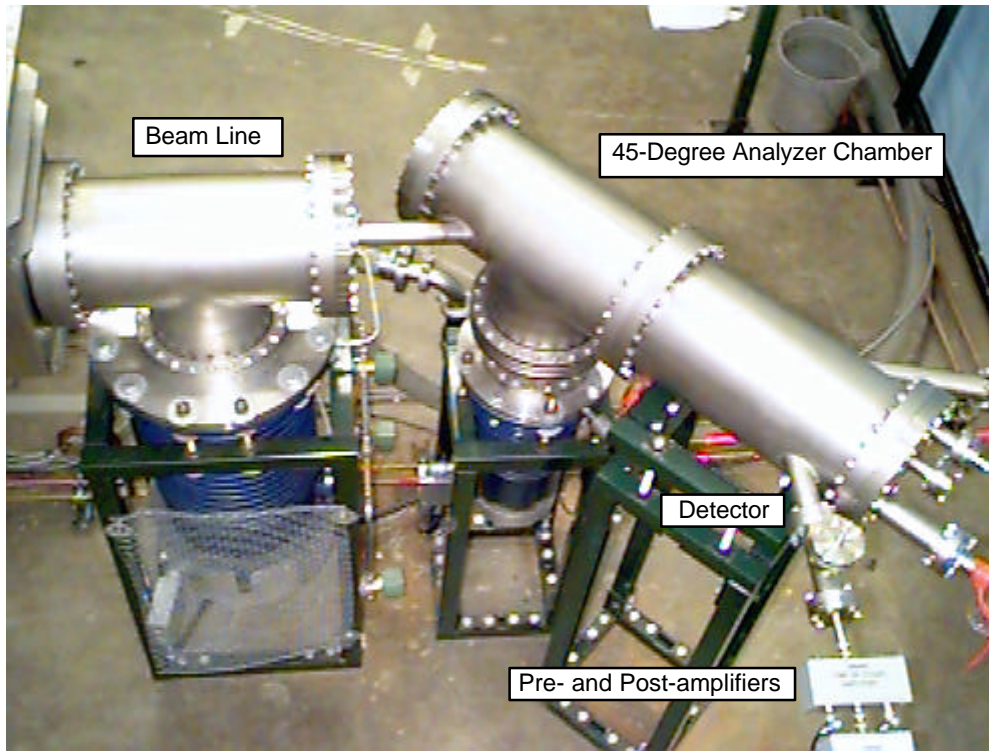


Figure 4-2. Top-view photograph of MBMS instrument showing electrostatic analyzer chamber and electron multiplier detector port.

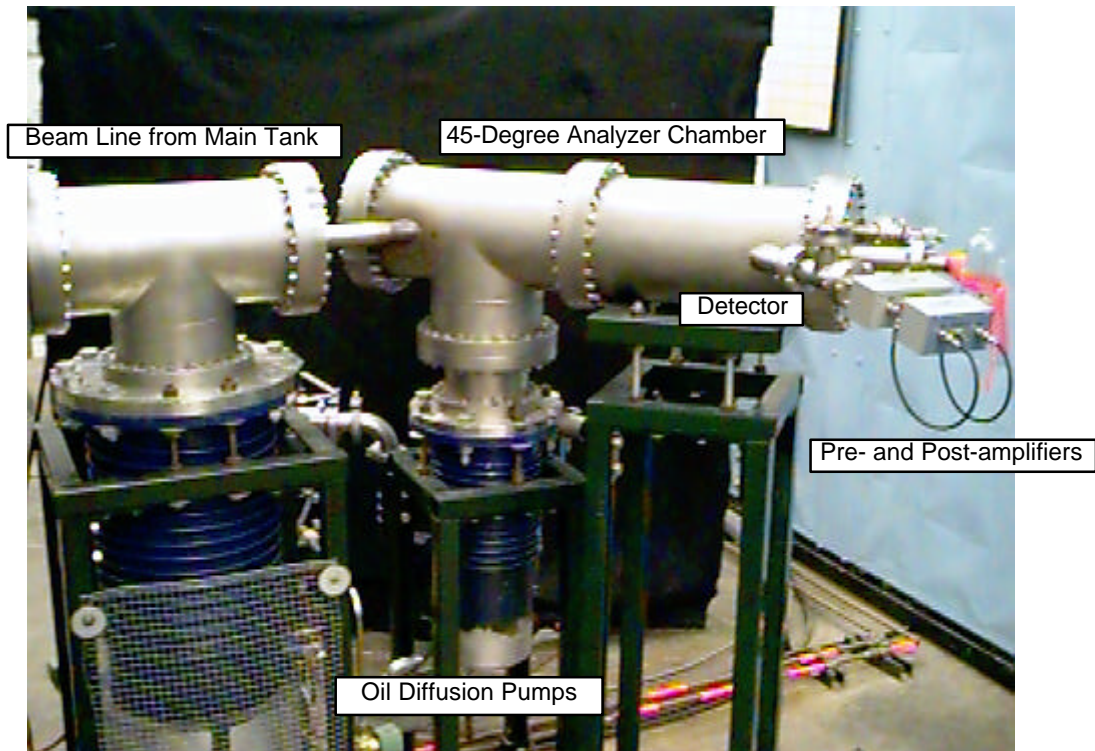


Figure 4-3. Side-view photograph of MBMS showing oil diffusion pumps.

The MBMS system used a set of orifice skimmers to admit a beam of plume ions from the main vacuum chamber into an array of differentially pumped sub-chambers. The sub-chambers were maintained at high vacuum to minimize and effectively eliminate collisions involving ions within the beam. A sampling skimmer orifice was mounted on the upstream end of the MBMS; this orifice skimmed off a small diameter ion beam into the first sub-chamber. This beam was then collimated by a second orifice at the downstream end of the first sub-chamber. The collimated beam then passed through the entrance slit of a 45-degree electrostatic energy analyzer. This analyzer employed a constant electric field such that only ions with a pre-selected energy have a trajectory which permits them to traverse the exit slit and impinge upon a detector. By recording the output current of the detector as a function of the electric field strength within the 45-degree analyzer the ion energy distribution function was evaluated. This system will be discussed in detail in Section 4.3. Mass analysis was obtained by using an electrostatic beam gate to “chop” the ion beam immediately downstream of the inlet skimmer and record the time required for an ion to pass from the gate to the detector: since the 45-degree analyzer admits only ions with a pre-selected value of $m_i u_i^2/2$ to the detector, ions of different mass but the same energy will have different velocities and, hence, will arrive at the detector at different times. Through the TOF principle discussed thoroughly in Section 4.4 the ionic mass can be distinguished.

Both the sampling and collimating skimmers were fashioned from 304 SS plates drilled and countersunk from the downstream face. This created a very thin-edged orifice to minimize skimmer wall effects. The sub-chambers were constructed from standard conflat vacuum hardware composed of eight-inch-inner-diameter 304 SS tubing, with the exception of the portion of the beam forming chamber lying within the main vacuum tank which was constructed of six-inch-I.D. tubing. The first sub-chamber was evacuated by a ten-inch-diameter oil diffusion pump (Varian model HS-10) operating on Dow-Corning 705 vacuum fluid and the chamber housing the electrostatic energy analyzer was evacuated using a six-inch-diameter oil diffusion pump (Varian model M6) also operating on Dow-Corning 705. Both oil diffusion pumps were fitted with conductively cooled “halo” baffles at the inlet to reduce oil backstreaming into the MBMS volume. The two diffusion pumps were backed by an 80-cfm rotary mechanical pump (Kinney model KDH-80). The MBMS vacuum was monitored by one thermocouple pressure sensor and two hot-cathode ionization pressure gauges; this system enabled an internal base pressure within the MBMS system of 3×10^{-7} torr which was achievable after approximately one hour of pumping. A large diameter (eight-inch) stainless-steel gate valve was placed between the energy analyzer chamber and the main vacuum tank enabling rapid venting and re-pumping of the MBMS for configuration adjustments without compromising the main tank vacuum.

4.3. Electrostatic Energy Analyzer

4.3.1. Theory of Operation

The 45-degree electrostatic energy analyzer is a flexible, robust method for particle energy filtering that has been used widely in beam physics research.^{46,47,48,49} A schematic of the system utilized in the MBMS is shown in Figure 4-4 with coordinate system and relevant dimensions defined.

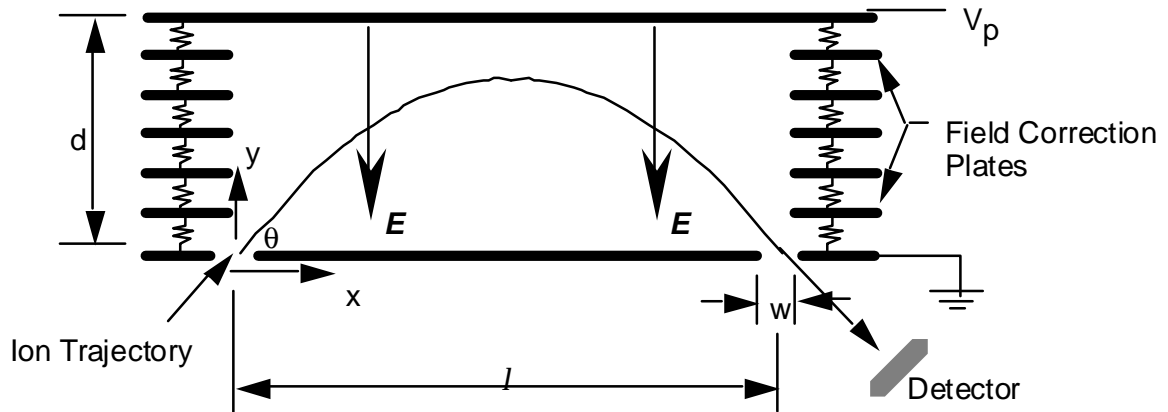


Figure 4-4. Schematic of 45-degree electrostatic ion energy analyzer. Constant electric field is formed by applying repelling voltage to top plate with bottom plate grounded. Field correction plates are biased with a voltage divider to force boundary conditions at mid-planes to prevent field distortion due to surrounding ground potential.

The ion beam is admitted through the entrance slit of the analyzer and immediately enters a region of constant electric field of magnitude V_p/d oriented at an angle θ to the direction of travel. The ions thus experience a constant acceleration in the negative y -direction such that the spatial equation of their trajectory is

Eqn. 4-2

$$y = x - \frac{q_i e V_p}{2 d m_i u_i^2 \sin^2 \theta} x^2.$$

Since $\theta = 45$ degrees and $u_i^2 = 2E_i/m_i$ Eqn. 4-2 becomes

Eqn. 4-3

$$y = x - \frac{1}{2d} \frac{V_p}{\left(\frac{E_i}{q_i e}\right)} x^2.$$

In order for an ion to pass through the analyzer and escape through the exit slit to the detector it must intersect the point $y=0, x=l$; this pass constraint is defined as the spectrometer constant, K_{45} , and is given by

Eqn. 4-4

$$K_{45} \equiv \frac{V_p}{\left(\frac{E_i}{q_i e}\right)} = \frac{2d}{l}.$$

The analyzer thus performs the function of an energy-per-charge filter, $E_i/q_i e$. Since the beam ions within the Hall thruster plume experienced a discharge acceleration according to $q_i e V_i = 1/2 m_i u_i^2$, the value of energy-per-charge for an ion is equivalent to the acceleration voltage, V_i . For a given value of repelling plate voltage, only ions with

Eqn. 4-5

$$V_i = \frac{1/2 m_i u_i^2}{q_i e} = \frac{V_p}{K_{45}}$$

will reach the collector and be recorded as ion current.

The current detector employed by the MBMS was a ceramic channel electron multiplier (CEM) capable of amplifying the input ion current by a factor greater than 1×10^8 (K-M Electronics model 7550m) with a maximum output current of approximately $5 \mu\text{A}$. The multiplier operates by applying a large negative potential (on the order of -2 kV) to the inlet of a semi-conducting channel while monitoring the current at the grounded exit of the channel. The material coating the channel walls has a high secondary electron impact yield due both to impacting ions and electrons. The high negative voltage input bias serves to efficiently collect incoming ions and draw them into the channel at high energies. These ions impinge on the channel walls and eject a number of secondary electrons. The electrons climb through the applied field towards the grounded channel exit, impacting the walls and ejecting more secondary electrons, thus greatly amplifying the current. The gain of the instrument can be adjusted by varying the applied high voltage potential on the inlet between -1.6 kV and -2 kV .

An important consideration was necessary when using the CEM in a multi-component ion beam: the initial “charge event” starting the electron cascade was due to secondary electrons ejected from an ion-wall collision. The number of electrons ejected per ion impact is a function of the material properties of the channel coating. Therefore an ion of charge $q=2$ does not cause twice as much electron current as a singly charged ion (as is the case in a

conducting metal collector such as an electrostatic probe). Therefore the CEM serves essentially as an ion counter rather than a charge counter.

For a single species flow the 45-degree electrostatic analyzer technique produces an ion current vs. repelling voltage trace which is directly proportional to the ion energy distribution function, analogous to the RPA technique. However, unlike the RPA technique, the 45-degree analyzer requires no numerical differentiation of raw data to obtain the distribution and the resultant curves are therefore much more precise and smooth. Unfortunately, like the RPA, the existence of multiple ion species in the beam considerably complicates interpretation of the data. This can be demonstrated by analyzing the output of the CEM. Since the CEM produced a current proportional to the number of ions incident on the collector, the current output can be written as

Eqn. 4-6
$$I_i = G_{\text{CEM}} A_c n_i \langle u_i \rangle.$$

According to Eqn. 4-5 only ions with a discrete voltage, V_i , will be detected by the CEM such that

Eqn. 4-7
$$\langle u_i \rangle = \left\langle \sqrt{\frac{2q_i e V_i}{m_i}} \right\rangle = \sqrt{\frac{2q_i e V_i}{m_i}}$$

so that now the current output of the CEM for a single value of ion voltage is written as

Eqn. 4-8
$$I_i(V_i) = G_{\text{CEM}} A_c n_i(V_i) \sqrt{\frac{2q_i e V_i}{m_i}}$$

where $n_i(V_i)$ is the number density of ions with voltage V_i which is precisely the ion voltage distribution function, $n_i(V_i) = f(V_i) = f(E_i/q_i e)$. Realizing this fact it is apparent from Eqn. 4-8 that the ion current vs. voltage is not directly proportional to the ion energy distribution function as is widely accepted. Rather, in a multi-component ion beam the 45-degree energy analyzer yields data which is related to the voltage distribution function according to

Eqn. 4-9
$$f(V_i) \propto \frac{I_i(V_i)}{\sqrt{q_i e V_i}}.$$

Even with the complications imposed on the data interpretation scheme by the effects of a multi-component flow, the 45-degree electrostatic energy analyzer yields great insight to the ion dynamics. Of considerable interest to this research is the ion voltage: by analyzing the ion voltage distribution information is gained regarding the acceleration of ions within the thruster discharge chamber. Eqn. 4-9 shows that by dividing the recorded ion current by the square root of the ion pass voltage a function very nearly equal to $f(V_i)$ is obtained; the existence of multiply charged ions only weakly affects the interpretation of these data for most flows. For example, the Hall thruster plasma has been estimated to consist of roughly 10% ions with $q=2$. The results of Eqn. 4-9 would then dictate that for a given value of measured ion current, a 10% fraction of the total current magnitude should be moderated by a factor of 0.707 (corresponding to $2^{-1/2}$). This constitutes a very small correction and thus,

the measured ion current vs. voltage curve is very nearly equal to the voltage distribution function, $f(V_i)$. A more detailed discussion of the proper data interpretation will be presented in Chapter 5.

4.3.2. Description of Apparatus

The 45-degree electrostatic energy analyzer was constructed of 1.5-mm-thick aluminum plates. In order to eliminate field distortion within the analyzer due to the surrounding ground potential of the vacuum chamber walls and to ensure a homogeneous electric field a set of seven centrally slotted field correction plates were mounted intermediate to the repelling plate and the entrance ground plate. These correction plates were biased using a resistor string voltage divider to force the field equipotentials at the mid-planes and minimize field leakage. The entire plate system was supported on a frame constructed of 3/16-inch-diameter nylon threaded rods to ensure electrical isolation of each plate.

The resolving power of the analyzer is dictated by geometric parameters and is given by

Eqn. 4-10
$$\frac{\Delta V_i}{V_i} = \frac{w \sin \theta}{l}$$

The desired voltage resolution was used to select the proper values for l and w . The depth of the analyzer, d , was then dictated by the parabolic trajectory of the

ions which pass through the analyzer to the exit slit: the apex of this trajectory must not intersect the repelling back plate. Manipulation of Eqn. 4-3 yields the necessary condition that $d > l/4$. The pertinent parameters of the 45-degree electrostatic energy analyzer used in the MBMS for this research are presented in Table 4-1.

Parameter	Value
d	160 mm
l	584 mm
w	3 mm
K_{45}	0.549
$\Delta V_i/V_i$	0.004

Table 4-1. Physical characteristics and resolving power of 45-degree electrostatic energy analyzer.

4.4. Time-of-flight Mass Analyzer

4.4.1. Theory of Operation

Time-of-flight mass spectrometry is based on the principle that particles with the same energy but different mass travel at different velocities and, hence, will take a different amount of time to traverse a known path length. Specifically,

Eqn. 4-11
$$t_{\text{tof}} = \frac{d_{\text{tof}}}{u_i} .$$

With u_i given as

Eqn. 4-12

$$u_i = \sqrt{\frac{2q_i e V_i}{M_i m_p}}$$

where M_i indicates the ionic atomic mass number and m_p is the mass of a proton it follows that

Eqn. 4-13

$$\frac{M_i m_p}{2q_i e V_i} = \frac{d_{\text{tof}}^2}{t_{\text{tof}}^2}$$

This relation is in general, however, the MBMS employs a 45-degree electrostatic energy analyzer to filter out all ions with the exception of those having a pre-selected value of V_i from detection. Therefore, by combining Eqn. 4-5 with Eqn. 4-13 a relation is derived relating the mass of the collected ions to their flight time through the MBMS:

Eqn. 4-14

$$\frac{M_i}{q_i} = \frac{2eV_p}{m_p K_{45}} \frac{t_{\text{tof}}^2}{d_{\text{tof}}^2}$$

In Eqn. 4-14 e and m_p are fundamental physical constants, K_{45} is the spectrometer constant of the 45-degree analyzer, V_p is the voltage applied to the repelling plate of the analyzer, and d_{tof} is the path length traveled by the ion through the MBMS which can easily be measured. It is apparent, then, that the time required for an ion to travel through the MBMS and reach the collector can be used to directly determine the ion mass-to-charge ratio.

Mass spectra is obtained in TOF mode by “chopping” the ion beam within the MBMS. Immediately downstream of the inlet skimmer is located an

electrostatic beam gate. This gate, which will be discussed more thoroughly in Section 4.4.2, creates a strong electric field transverse to the ion beam direction which deflects the ion beam uselessly into the wall, effectively closing the gate. For a brief instant on the order of 1 μ sec the gate is opened by negating the electric field and a burst of ions of all energies are sent towards the CEM detector; this gate opening sets the zero time for the ion “stopwatch” and denotes the beginning of the flight path. The 45-degree electrostatic energy analyzer then removes all ions with the exception of those having a single value of accelerating voltage which it transmits to the CEM detector. The temporal current output of the CEM detector is monitored to record the ion arrival; ions of the same voltage arrive at the detector “bunched” in time according to their atomic mass-to-charge ratio via Eqn. 4-14, therefore the form of the CEM output current is that of a zero current baseline punctuated by well-defined current peaks representing the arrival of different ionic mass species. This current vs. time spectra is easily converted to a current vs. mass-to-charge spectra where the current is directly proportional to the species density.

The flexible design of the MBMS used in this research enabled an energy-dependent analysis of plasma mass composition through the simultaneous measurement of ion energy and mass. The desired ion voltage was selected via the 45-degree analyzer and the TOF technique was then used to take a “snapshot” of the mass composition of ions with this pre-selected voltage. Thus,

individual mass spectra could be evaluated for ions with any desired acceleration voltage by varying the pass energy of the 45-degree analyzer.

4.4.2. Design Principles

The details of the TOF design can be best understood by examining the representation of the time-of-flight spectra shown in Figure 4-5 along with the concepts defined in Figure 4-6. The electrostatic gate of Figure 4-6 consists of two planar electrodes of length d_{gate} placed on opposing sides of the ion beam. A large voltage difference is applied between the plates creating a strong electric field perpendicular to the ion beam line. This field deflects all ions such that their trajectories intersect the chamber wall and they are lost. At time $t = 0$ in Figure 4-5 this electric field is removed for a period of time lasting t_{gate} , opening the gate and admitting a pulse of ions to the field-free drift region of length d_{tof} . According to the ionic mass-to-charge ratio, each ion species arrives at the detector a time t_{tof} after the start of the gate pulse.

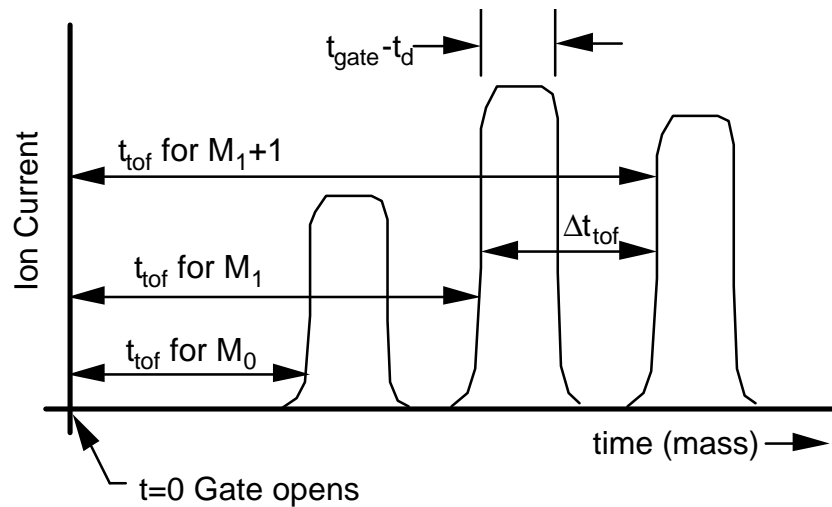


Figure 4-5. Representation of typical time-of-flight spectra illustrating the effect of the gate pulse width and flight time on the mass resolution.

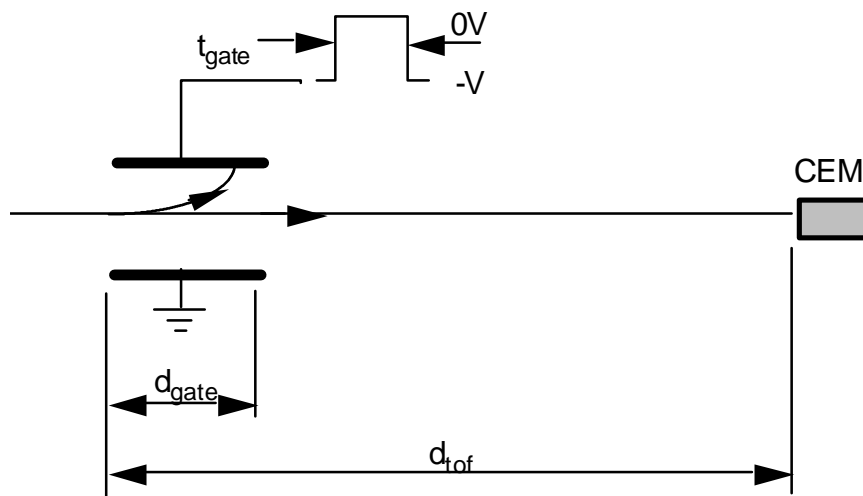


Figure 4-6. Illustration of TOF spectrometer concepts showing gate region and field-free drift region.

The length of the gate region and the duration of the gate pulse have a strong effect on the TOF spectra. When the gate field is removed at time $t = 0$, all

ions lying within the gate region of length d_{gate} have already been deflected somewhat and will not reach the collector; therefore the leading edge of the ion pulse begins its journey from the entrance of the gate region and travels a distance d_{tof} . When the field is re-applied and the gate closes at time $t = t_{\text{gate}}$ all ions lying within the gate region will be deflected and removed from the pulse, so that the trailing edge of the ion pulse has only to travel from the end of the gate region to the detector for a flight distance of $d_{\text{tof}} - d_{\text{gate}}$. Thus the width of the ion pulse arriving at the detector is the width of the gate pulse, t_{gate} , minus the length of time it takes an ion to travel through the gate region, $t_d = d_{\text{gate}}/u_i$. In the case where $t_{\text{gate}} \gg t_d$ the ion pulse is transmitted at full intensity and the TOF peak reflects the true density of the ion species. However, if the gate pulse is too short (or the ion is too slow) such that $t_{\text{gate}} < t_d$ then the ion will not have sufficient time to travel from the entrance of the gate region to the exit before the gate is closed again; in this case the ion will not be detected. For cases where t_{gate} is just slightly longer than t_d the leading edge of the ion pulse will successfully traverse the gate region, however the trailing edge of the ion pulse will be “clipped” and the resultant ion current peak at the detector will not reflect the true density of the species.

Although the use of a long gate pulse is desired to achieve a measure of the true intensity of an ionic species, the mass resolution of the MBMS is inversely proportional to the length of the gate pulse and, thus, a trade-off exists. This can be easily seen from Figure 4-5. In this figure Δt_{tof} represents the

difference in time between the arrival of ions with equivalent mass M_i/q_i and ions with mass $(M_i+1)/q_i$. When the peak width of the lighter ion, which is equal to $t_{\text{gate}}-t_d$, becomes greater than Δt_{tof} the trailing edge of the light ion peak will merge with the arrival time of the next heaviest ion and the peaks will become unresolvable. It follows, then, that the best mass resolution is achieved by employing a very short gate pulse such that the ion mass peaks are narrow.

The concepts affecting ion pulse throughput and mass peak resolution can be evaluated quantitatively. As discussed previously, the duration of the gate pulse must be much longer than the time it takes the slowest (heaviest) ion of interest in the spectra to traverse the gate region:

Eqn. 4-15
$$t_{\text{gate}} \gg d_{\text{gate}} \sqrt{\frac{M_{\text{max}} m_p}{2q_i e V_i}}.$$

However, the competing criteria for mass resolution requires the gate pulse to be shorter than the difference in arrival times between two adjacent mass species, $t_{\text{gate}} < \Delta t_{\text{tof}}$:

Eqn. 4-16
$$\Delta t_{\text{tof}} = d_{\text{tof}} \sqrt{\frac{M_1 m_p}{2q_1 e V_i}} - d_{\text{tof}} \sqrt{\frac{M_2 m_p}{2q_2 e V_i}}$$

where $M_1=M_2+1$ for adjacent mass species, so that

Eqn. 4-17
$$\Delta t_{\text{tof}} = d_{\text{gate}} \sqrt{\frac{m_p}{2eV_i}} \left(\sqrt{\frac{M_1}{q_1}} - \sqrt{\frac{M_1}{q_1} - 1} \right).$$

Apparent from Eqn. 4-17 is the fact that the smallest difference between adjacent species arrival times will occur for the heaviest ions such that $M_1/q_1 \approx M_1/q_1 - 1$.

It follows that the design constraint for well-resolved mass peaks will be most difficult to achieve for the heaviest ions of interest in the mass spectra. Thus, the minimum time interval between adjacent peaks is given as

$$\text{Eqn. 4-18} \quad \Delta t_{\text{tof},\text{min}} = d_{\text{tof}} \sqrt{\frac{m_p}{2eV_i}} \left(\sqrt{\frac{M_{\text{max}}}{q_i}} - \sqrt{\frac{M_{\text{max}}}{q_i} - 1} \right).$$

Combining Eqn. 4-15 and Eqn. 4-18 places an upper and lower limit on the gate pulse duration

$$\text{Eqn. 4-19} \quad d_{\text{gate}} \sqrt{\frac{M_{\text{max}} m_p}{2q_i eV_i}} \ll t_{\text{gate}} \ll d_{\text{tof}} \sqrt{\frac{m_p}{2eV_i}} \left(\sqrt{\frac{M_{\text{max}}}{q_i}} - \sqrt{\frac{M_{\text{max}}}{q_i} - 1} \right).$$

The criteria defined by Eqn. 4-19 effectively places a design constraint on the geometry of the TOF system in the MBMS; in order to transmit full intensity ion pulses with the ability to resolve 1 amu at the heaviest species of interest in the flow the gate and drift regions in the MBMS must satisfy the relation that

$$\text{Eqn. 4-20} \quad \frac{d_{\text{gate}}}{d_{\text{tof}}} \ll 1 - \sqrt{\frac{M_{\text{max}}/q_i - 1}{M_{\text{max}}/q_i}}.$$

As an illustration of this constraint Figure 4-7 shows a design curve representing the allowed MBMS geometry as a function of the maximum resolvable mass peak in the flow.

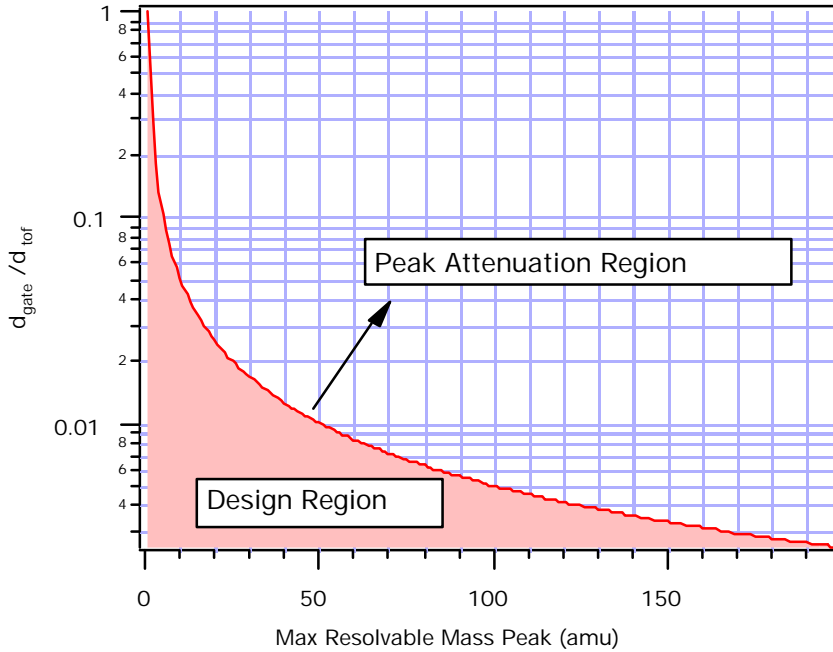


Figure 4-7. Allowable gate length to drift length ratios for TOF mass spectrometer.

The geometry of the TOF system is therefore dictated by the heaviest ion in the flow that must be resolved to within 1 amu. Once this geometry is chosen, the duration of the gate pulse can be determined as a function of the ion voltage under consideration. It follows from the constraint imposed by Eqn. 4-19 that the optimal gate pulse duration lies halfway between the lower bound, t_d , and the upper bound, $\Delta t_{\text{tof},\text{min}}$:

Eqn. 4-21
$$t_{\text{gate,opt}} = \frac{1}{2} \sqrt{\frac{m_p}{2eV_i}} \left[d_{\text{tof}} \left(\sqrt{\frac{M_{\text{max}}}{q_i}} - \sqrt{\frac{M_{\text{max}}}{q_i} - 1} \right) + d_{\text{gate}} \sqrt{\frac{M_{\text{max}}}{q_i}} \right].$$

Once the geometric ratio of the TOF system is determined the value of the required gate voltage can be calculated by analyzing the effect of the constant electric field in the gate region on the ion beam. A schematic of the electrostatic gate design employed for this research is shown in Figure 4-8. The equation relating the beam deflection at the exit of the gate region to the applied voltage is

Eqn. 4-22
$$V_{\text{gate}} = \frac{4s y_d V_i}{d_{\text{gate}}^2}.$$

In order to “close” the gate such that the ion beam is not detected by the CEM the beam deflection must be approximately equal to the diameter of the collimating orifice at the inlet of the 45-degree electrostatic analyzer. It is apparent from examining Eqn. 4-22 that the magnitude of the beam deflection is independent of ion mass and varies only as a function of ion energy.

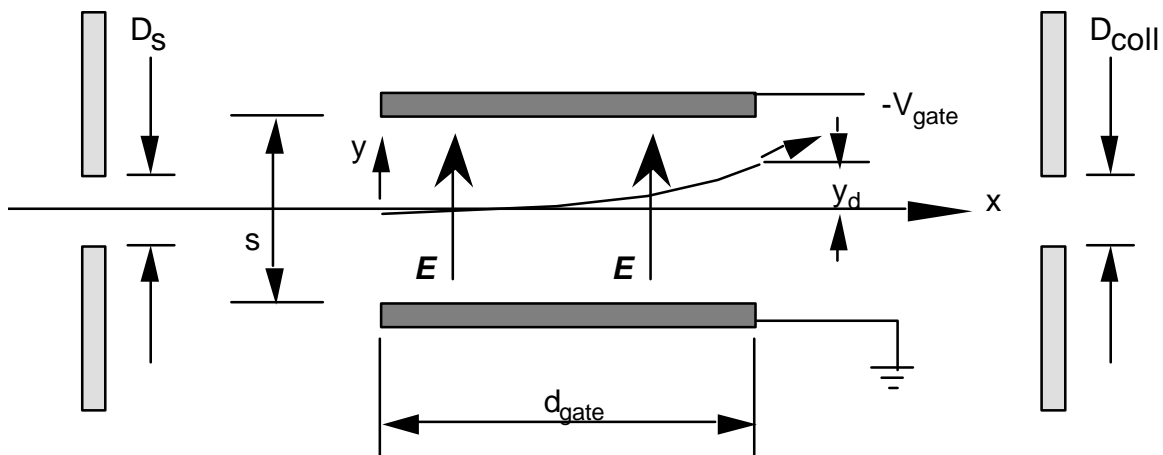


Figure 4-8. Electrostatic beam gate layout for TOF analysis showing relevant parameters.

4.4.3. Practical Design Considerations

Selection of the TOF path length and overall instrument size for this research was based on practical considerations involved in measuring the high-frequency, low amplitude TOF signal. Based on available instrumentation, a baseline flight time of approximately 100 μ sec for the heaviest ion species was chosen as the design target; since the main component of the flow to be analyzed was xenon (amu 131) accelerated through roughly 300 V the beam ions would have velocities approaching 20 km/s. This necessitated a path length on the order of 2 m. Due to available vacuum hardware the final instrument had a flight path length of $d_{\text{tof}}=2.35$ m.

By defining xenon as the heaviest ion mass to be analyzed the relations derived in Section 4.4.2 can, in principle, be used to select the optimum geometry for the MBMS. From Figure 4-7 and Eqn. 4-20 for $M_{\text{max}} = 131$ the ideal

geometric ratio of gate length to drift length must be less than $d_{\text{gate}}/d_{\text{tof}} = 3.8 \times 10^{-3}$. With the drift length set to $d_{\text{tof}} = 2.35$ m the gate length is fixed to be smaller than 0.9 cm. This length sets the starting point for the gate design. The diameter of the beam passing through the gate electrodes was defined by the diameter of the sampling skimmer orifice, which was 5 mm; this dimension set a minimum on the inter-electrode spacing of the gate, s , such that the gate electrodes did not obscure the beam line. A value of $s = 1$ cm was chosen to minimize the required gate voltage without interfering with the beam. The diameter of the collimating orifice at the inlet of the 45-degree analyzer was 3 mm; therefore, for a 300 V ion to be deflected 3 mm within the gate region Eqn. 4-22 mandates a gate electric field strength of approximately $V_{\text{gate}}/s = 50$ kV/m; this suggested a required gate repelling voltage of $V_{\text{gate}} = 500$ V. However, in practice the beam passing through the gate region was not cylindrical and collimated as the deflection voltage calculation assumed. Instead, the beam experienced a considerable divergence upon passing through the sampling skimmer, as illustrated in Figure 4-9. This greatly increased the repelling voltage required to completely divert all of the ion beam from entering the 45-degree analyzer.

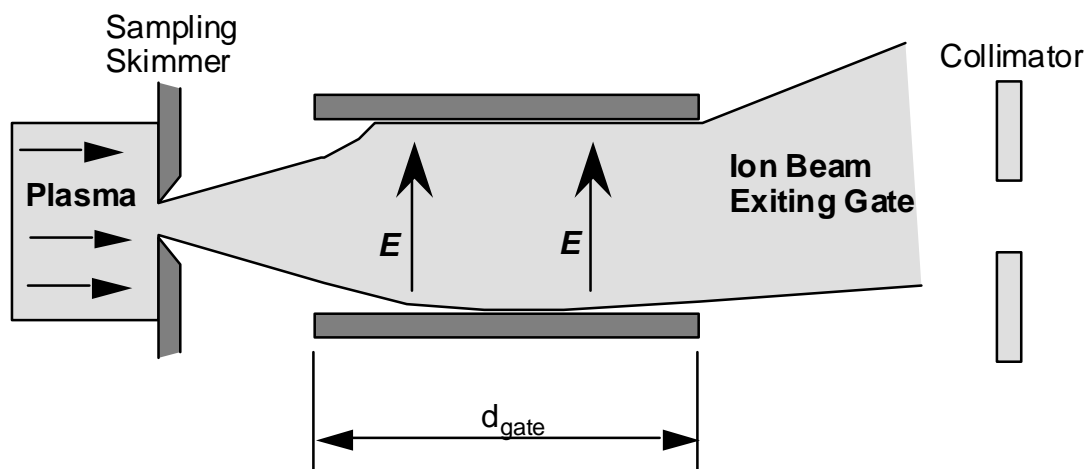


Figure 4-9. The incoming ion beam is considerably divergent after passing through the sampling skimmer. This divergence greatly increases the amount of deflection required to steer the beam out of the collimating aperture downstream.

Because of this divergence, experimental evaluation showed that the gate repelling plate voltage had to be greater than -2 kV in order to completely divert the beam. This high voltage caused an electrical breakdown between the gate electrodes and interfered with the normal operation of the MBMS. It was realized that in order to reduce the required repelling voltage the length of the gate region, d_{gate} , would have to be increased beyond the optimal value set by Eqn. 4-20.

Through trial and error a final gate length of 1.3 cm was chosen; this set the ratio of $d_{\text{gate}}/d_{\text{tof}}$ to 5.5×10^{-3} . As can be inferred from Figure 4-7 this implies a maximum resolvable mass peak of approximately 92 amu. Although this seems to be unacceptable since the primary species of interest to this research is xenon with $M_i=131$ amu, the results of this compromise have little impact on the

goals of this study. The optimum criteria of Eqn. 4-20 define the geometric ratio necessary to resolve the heaviest species of interest to within 1 amu while transmitting the peak at full intensity. By exceeding the optimum ratio of $d_{\text{gate}}/d_{\text{tof}}$ the TOF system will resolve the heaviest species within 1 amu, however, the peak will not be transmitted at full intensity since the gate pulse duration was too brief (or equivalently the gate region was too long). By simply relaxing the resolution criteria of the heaviest species of interest to greater than 1 amu, the gate pulse duration can be increased such that the peak is transmitted at full intensity; the result is that the peak will still arrive at the detector at the same time, t_{tof} , however the width of the peak will now be wider than 1 amu. Since the heaviest mass species of interest to this flow had a molecular weight of 131 amu and there were no other flow constituents with comparable masses, allowing the 131 peak to spread wider than several amu posed no difficulty in spectra analysis; arrival of the leading edge of the ion current peak determined the particle mass-to-charge ratio, while the peak width was limited to a few amu.

Of primary interest to this research was the quantitative measurement of propellant ionization fractions; this goal required that all ionization states of the primary species, xenon, be transmitted through the spectrometer at full intensity such that the current output of the CEM detector was representative of the true ion density fraction. As previously discussed, the mass resolution criteria for the MBMS was relaxed to greater than 1 amu since no isotopic analysis was desired.

Therefore, in order to ensure full transmission of all of the xenon ions, Eqn. 4-15 was applied as the criteria for choosing the gate pulse duration with 131 amu representing the slowest species. This set a lower limit on the gate pulse as a function of ion voltage as illustrated in Figure 4-10. For example, from Figure 4-10 it is apparent that for analyzing a 100 V Xe⁺ ion the gate pulse must be longer than 1 μsec in order to avoid clipping the ion pulse and recording an artificially low current peak.

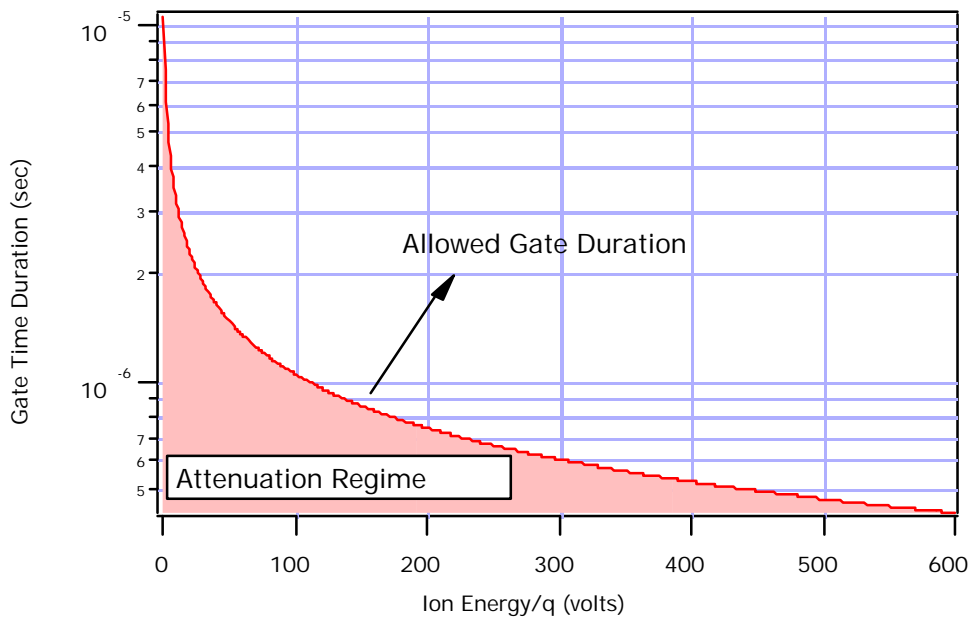


Figure 4-10. Design curve illustrating allowed values of t_{gate} to transmit an ion with mass of 131 amu at full intensity for $d_{\text{gate}}=1.3$ cm.

If the constraint illustrated in Figure 4-10 is satisfied, Eqn. 4-14 can be used to derive the mass resolving power of the MBMS for a given t_{gate} and d_{tof} . Defining the resolving power, R , as

Eqn. 4-23

$$R \equiv \frac{\Delta\left(\frac{M_i}{q_i}\right)}{\frac{M_i}{q_i}}$$

and employing Eqn. 4-14, the resolving power is derived as

Eqn. 4-24

$$R = \frac{2t_{\text{gate}}}{d_{\text{tof}}} \sqrt{\frac{2q_i eV_i}{M_i m_p}}$$

Although the resolving power is a measure of the width of any given mass species peak, it does not necessarily represent an uncertainty in determining the ionic mass: the leading edge of the ion mass current peak is used to set the value of t_{tof} to provide an unambiguous calculation of M_i/q_i , and R simply describes the width of the peak after the arrival of the leading edge. It is only in the case where t_{gate} is of sufficient duration that the trailing edge of one current peak runs into the leading edge of the next heaviest peak that the value of R represents the uncertainty in evaluating the ion M_i/q_i .

4.4.4. Description of Apparatus

As a result of the previously discussed practical considerations in the TOF system design (Section 4.4.3) Table 4-2 presents the final instrument configuration.

Parameter	Value
d_{tof}	2.35 m
d_{gate}	1.3 cm
s	1 cm
D_s	5 mm
D_{coll}	3 mm

Table 4-2. Physical parameters of MBMS time-of-flight components.

The keystone of the TOF system was the high-speed electronics used to control the flight timing and analyze and record the low-level ion current pulses. A schematic of the controlling instrument set-up is shown as Figure 4-11. The gate repelling voltage was supplied by a high-voltage pulser (Directed Energy, Inc. GRX-3) controlled by a low-voltage pulse generator. This pulser was capable of producing up to 3 kV square output pulses with a rise time of 20 nsec and settling time of 40 nsec. The low-voltage pulse generator was used to program the pulse duration and duty cycle of the high-voltage pulser. The leading edge of the high-voltage gate pulse triggered a 1-GHz digitizing oscilloscope (Tektronix TDS-540) and began the TOF waveform timing acquisition sequence.

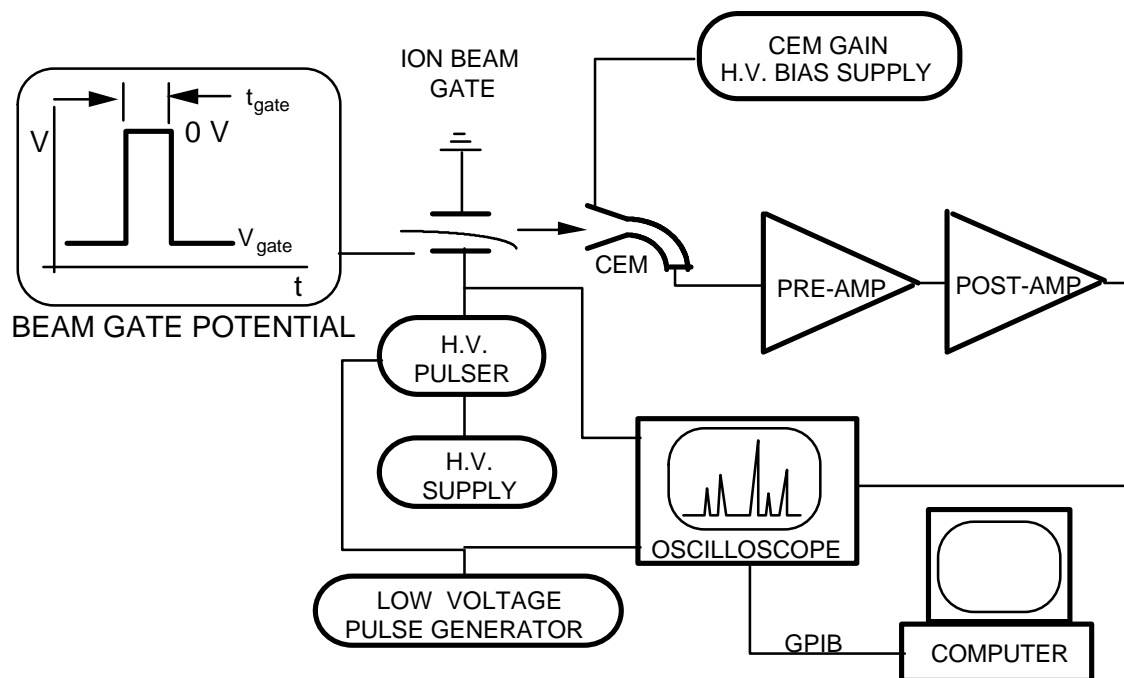


Figure 4-11. Electrical schematic of controlling electronics and data system for TOF spectrometer.

The output current of the CEM detector was input to a set of two amplifiers performing a high-speed current-to-voltage conversion; the output voltage of the post-amplifier was then sent to the oscilloscope which recorded the transient current peaks corresponding to the ion species arrival times. The oscilloscope waveform was transferred via GPIB protocol to a data acquisition computer. The computer applied the physical parameters of the MBMS system to the raw TOF data and converted the current vs. time waveform into a spectra of current vs. mass-to-charge for data archive.

The design of the pre- and post-amplifiers for the CEM were critical for overall system performance and hence were the subject of considerable analysis. The output current pulses of the CEM ranged from 1 nA to about $1\text{ }\mu\text{A}$

maximum; these low-level current pulses had durations of approximately 1 μ sec with rise and fall times of approximately 20 nsec. Utilization of high-speed, low-noise electronics was paramount to the acquisition of clean data; fundamental principles of high-speed amplifier design can be found in a number of texts.^{50,51} The overall amplifier circuit chosen is shown in Figure 4-12 with the values of the circuit components given in Table 4-3.

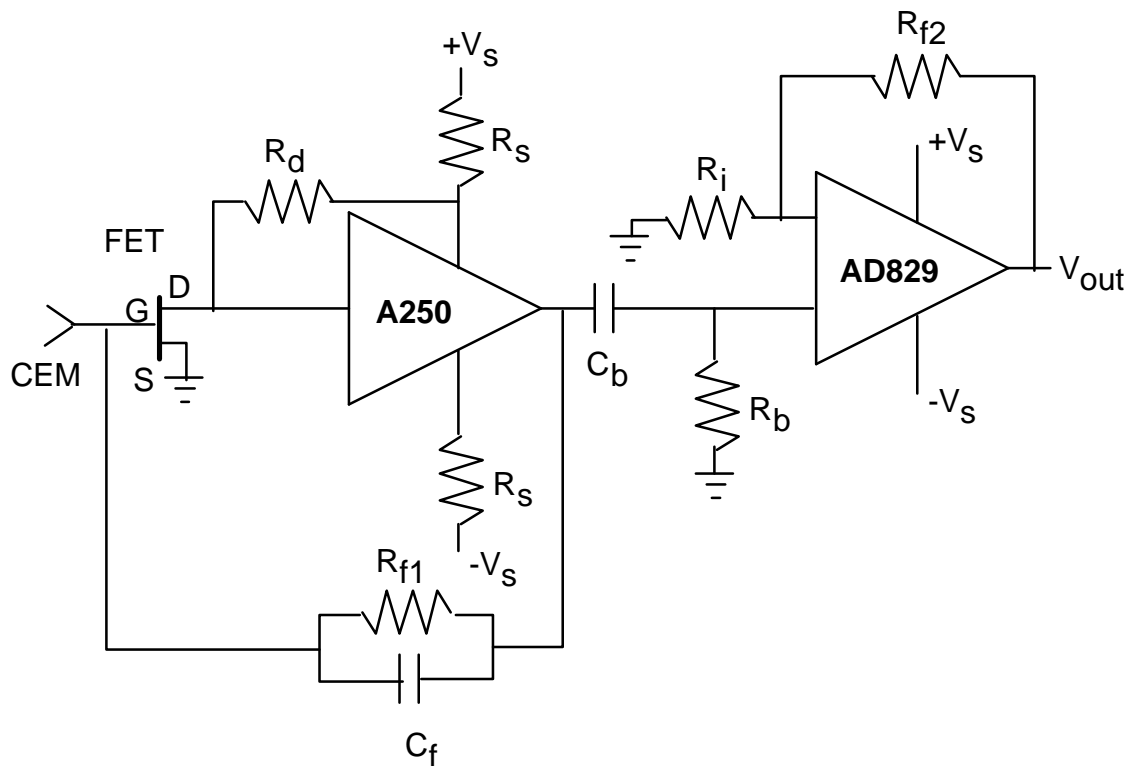


Figure 4-12. TOF system amplifier circuit diagram.

Component	Value
FET	2SK152
R_d	1 k Ω
R_s	50 Ω
$+V_s$	6 V
$-V_s$	-6 V
R_{f1}	50 k Ω
C_f	2 pF
C_b	0.1 μ F
R_b	1 k Ω
R_i	1 k Ω
R_{f2}	50 k Ω

Table 4-3. Value of circuit elements in TOF amplifier. Notation refers to Figure 4-12.

The pre-amplifier chosen for this system was an Amptek model A250. The A250 is a hybrid, ultra-low noise, high-frequency charge sensitive

preamplifier with a fast rise time of 2.5 nsec; this represents the current state-of-the-art in amplifier design. By suitable choice of feedback components the A250 was configured as a transimpedance (current-to-voltage) preamplifier. In this configuration the voltage output is determined by the input current according to $V=I_{cem}R_{f1}$; use of the feedback capacitor, C_f , is required to prevent unstable oscillation of the amplifier, however this combination of feedback capacitor and resistor sets the time constant of the output pulse such that $\tau=R_{f1}C_f$. Thus, increasing the gain of the A250 simultaneously decreases the amplifier frequency response. For this reason, the A250 circuit could not provide the gain required of the TOF detection system while simultaneously preserving the high-frequency of the spectra. A post-amplifier was therefore needed to perform a voltage-to-voltage amplification of the A250 output. The post-amplifier chosen was an AD829 manufactured by Analog Devices. This device is a low-noise, high-speed op-amp designed for use in video applications. The AD829 had a noise level of less than 2 nV/Hz^{1/2} with a gain-bandwidth-product of 750 MHz with feedback components as indicated in Figure 4-12 and Table 4-3.

The A250 pre-amplifier, as constructed with feedback components, had a current-to-voltage conversion factor of 50 mV/ μ A; similarly, the AD829 had a closed-loop gain of 50 for an overall conversion of 2.5 V/ μ A. Combined with the gain of the CEM this circuit comprised an amplification of the true ion current to a level of 2.5×10^{14} V/A.

5. MBMS ENERGY DIAGNOSTICS

For acquiring and analyzing ion energy distributions within the plume of the SPT-100 the MBMS was operated in a quasi-steady mode: the ion beam gate required by the TOF system was completely de-energized such that a continuous beam of ions was admitted to the 45-degree electrostatic energy analyzer. The electric field within the analyzer was varied slowly, while the ion current incident on the CEM was monitored. This chapter describes experiments performed to measure the ion energy distribution within the plume of the SPT-100 at distances of 0.5 m and 1.0 m from the thruster exit plane.

As discussed in Chapter 3 previous ion energy diagnostics were limited to angular positions lying within 60 degrees of the thruster plume centerline due to low ion densities at larger angles. A goal of the MBMS energy diagnostics was to measure the ion energy at very large angles from the plume centerline including and exceeding 90 degrees. These regions, representing oblique- and back-flow from the thruster, will be critical for spacecraft designers in evaluating the effects of thruster ion impingement of surrounding spacecraft surfaces.

5.1. Experimental Set-up

The SPT-100, discussed in Section 3.1, was mounted to a rotary table such that the rotation axis coincided with the center of the exit plane of the thruster. Therefore, by rotating the thruster relative to the fixed MBMS skimmer inlet the plasma plume could be sampled as a function of angular position at a fixed radial distance, r , from the exit plane. This set-up is illustrated schematically in Figure 1-4 and Figure 5-1 with a photograph of the setup shown in Figure 5-2.

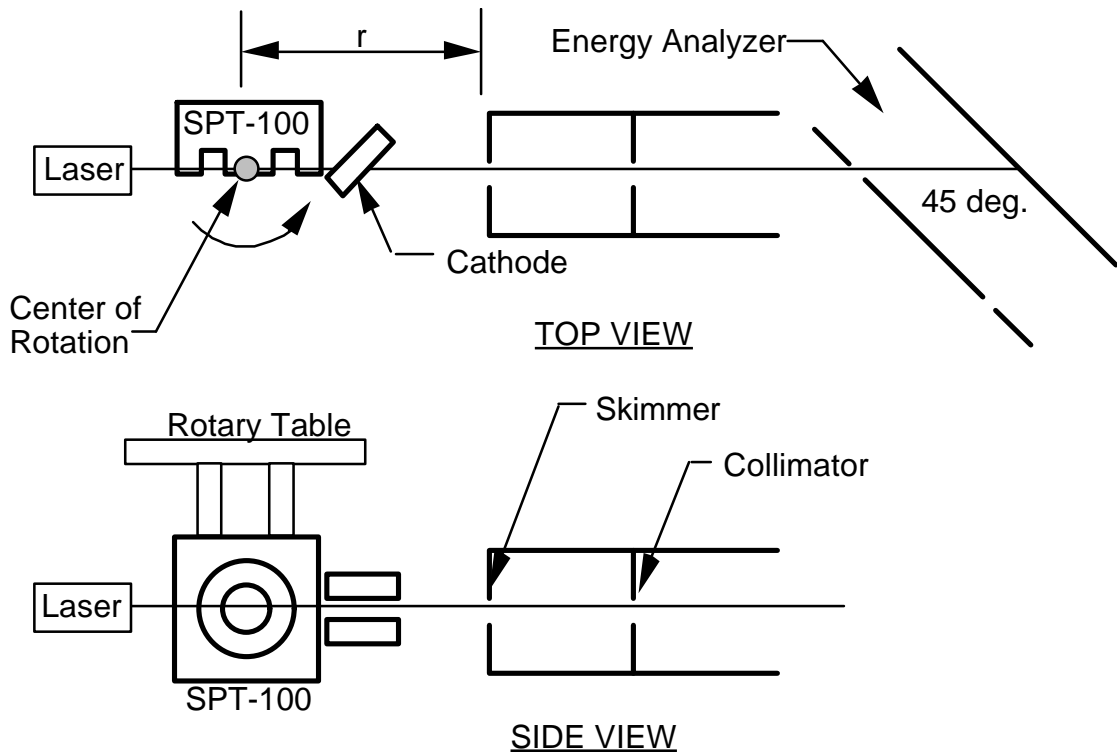


Figure 5-1. Experimental set-up diagram showing rotary thruster mount and laser alignment of beam line.

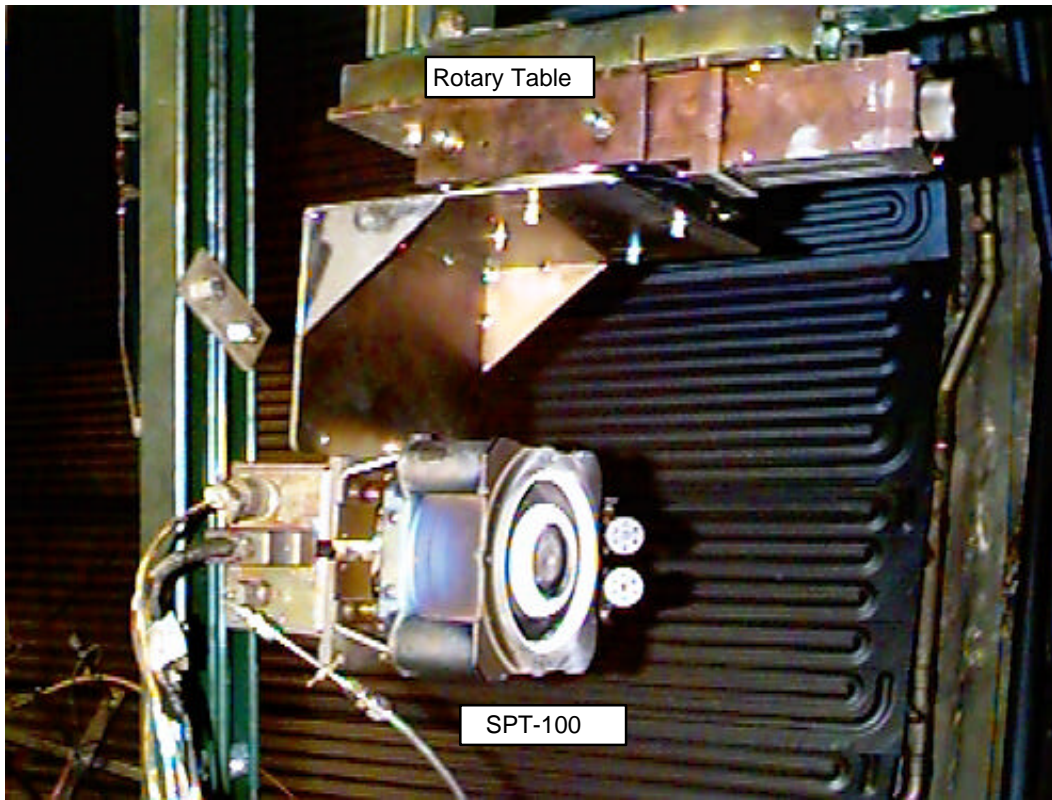


Figure 5-2. Photograph showing SPT-100 mount to rotary table for MBMS characterization.

The centerline (thrust axis) of the thruster was denoted as zero degrees, with positive theta values representing points in the cathode half-plane of rotation (the angular position shown in Figure 5-1 represents $\theta=+90$ degrees). The angular alignment of the thruster and MBMS was achieved by using a laboratory laser to establish the MBMS beam line. The laser beam line was used to verify the angular orientation of the 45-degree electrostatic analyzer to within 0.5 degrees; similarly, the thruster was rotated such that the laser beam line was precisely aligned with the center of the exit plane of the thruster, as shown in Figure 5-1, establishing the 90 degree position of the SPT-100 to better than 0.5 degrees. Since the relative uncertainty in angular position of the rotary table was 0.1 degrees, the uncertainty in position for all data points is ± 0.5 degrees due to initial alignment uncertainty. By re-locating the rotary table mount between tests, data were obtained as a function of angular position for radial distances from the thruster of $r = 0.5$ m and $r = 1.0$ m.

The 45-degree analyzer repelling voltage was supplied slowly varying the output of a high-precision sourcemeter (Keithley 2410). The sourcemeter provided regulated voltage with better than 0.012% accuracy over a range of zero to 1100 V. Since ion current sweeps were obtained in a very low speed acquisition the fast amplifier circuit as discussed in Section 4.4.4 was not necessary to monitor the output current of the CEM. Instead, the current was measured with a sensitive picoammeter (Keithley 486) and recorded as a

function of 45-degree analyzer pass voltage. By utilizing the picoammeter, the high-gain CEM, and long sampling times true ion currents as low as 1×10^{-19} A could be accurately measured; this represents an ion flux on the order of 1 ion per second incident on the CEM.

5.2. Ion Energy Measurements in an SPT-100 at 0.5 m

The ion current incident on the CEM was recorded as a function of ion voltage by varying the repelling potential on the 45-degree energy analyzer. In this fashion curves were obtained at a radial distance of 0.5 m from the thruster exit plane as a function of angular position about the thrust axis in 10-degree intervals. The high-gain attributed to the picoammeter and CEM enabled data to be obtained in a complete 360-degree envelope about the SPT-100. Peak ion current values fell as low as 1×10^{-18} A for points directly behind the thruster. These sweeps are shown in Figure 5-3 through Figure 5-11. The abscissa of the ion current curves have been corrected for the energy imparted to the ions as they fell from ambient plasma potential through the skimmer inlet to ground potential; the magnitude of the required correction was measured as discussed in Section 3.2.

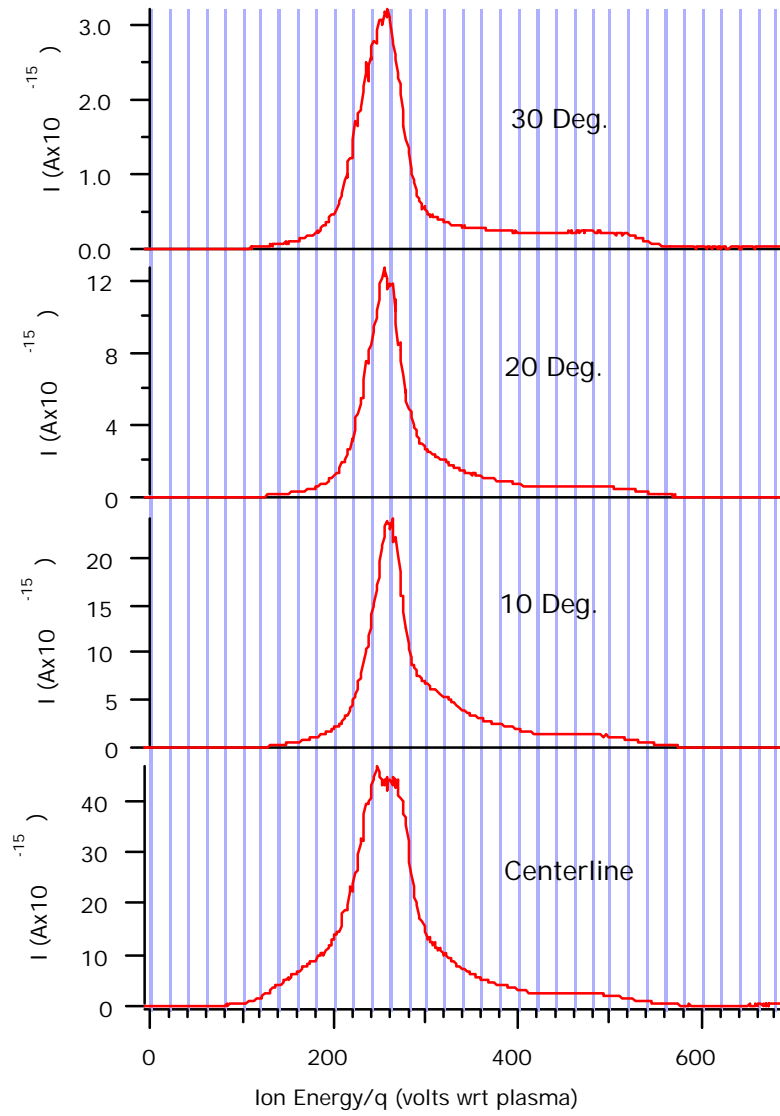


Figure 5-3. Ion current as a function of ion voltage at 0.5 m radius from the SPT-100 along the thrust axis and for points at 10, 20, and 30 degrees off axis.

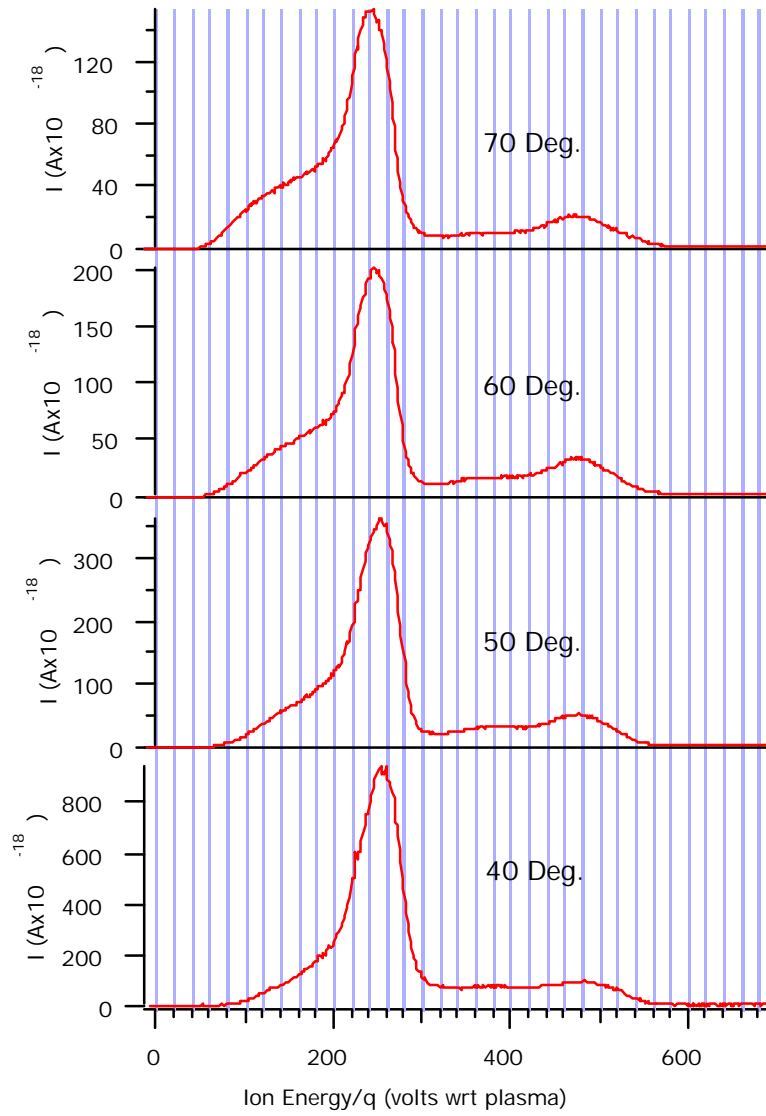


Figure 5-4. Ion current as a function of ion voltage at 0.5 m radius from the SPT-100 for points at 40, 50, 60, and 70 degrees off thrust axis.

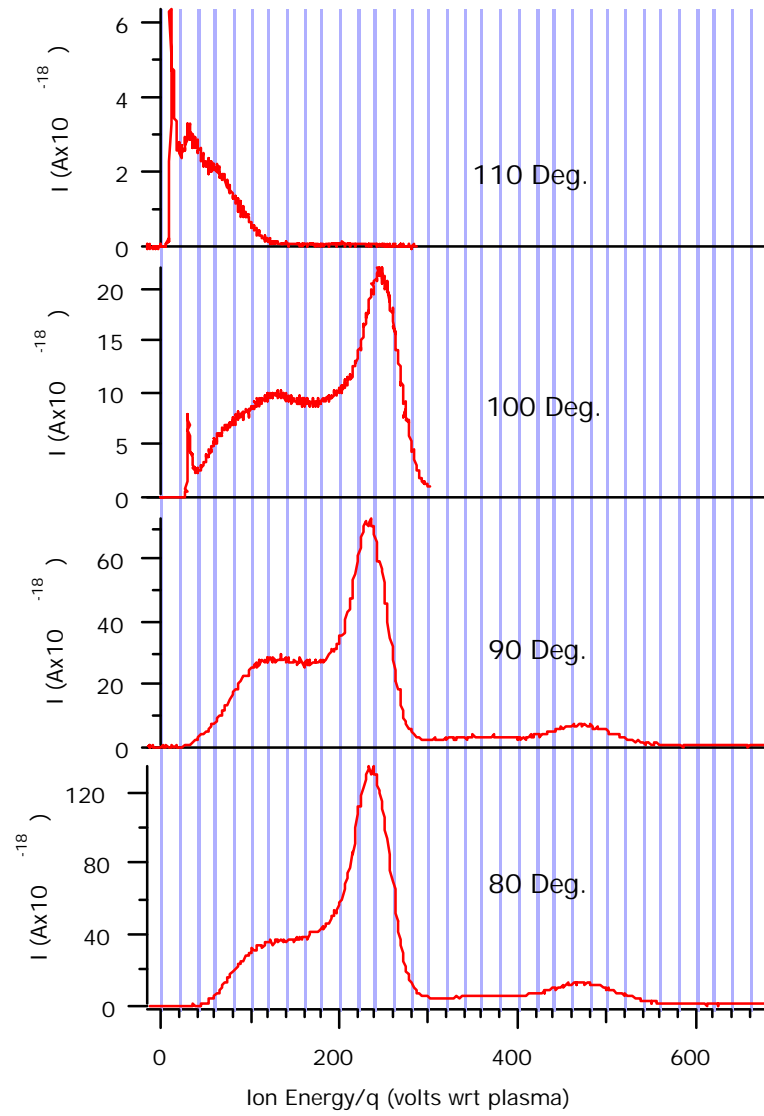


Figure 5-5. Ion current as a function of ion voltage at 0.5 m radius from the SPT-100 for points at 80, 90, 100, and 110 degrees off thrust axis.

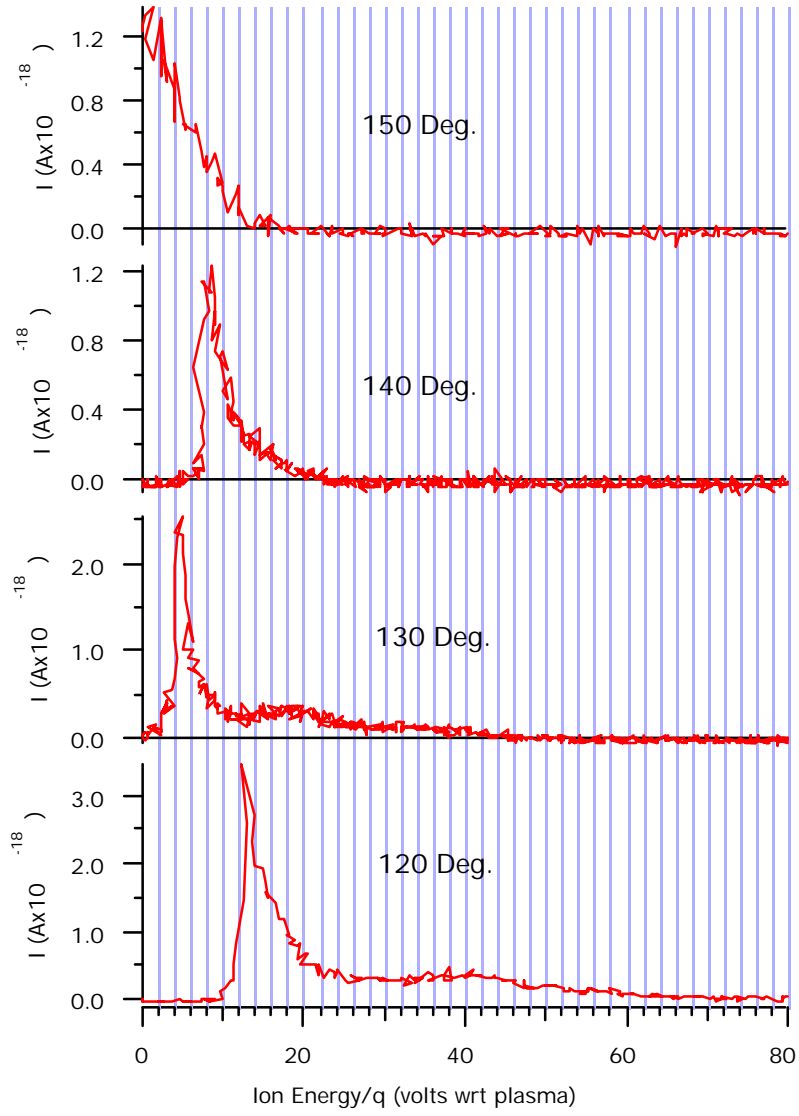


Figure 5-6. Ion current as a function of ion voltage at 0.5 m radius from the SPT-100 for points at 120, 130, 140, and 150 degrees off thrust axis.

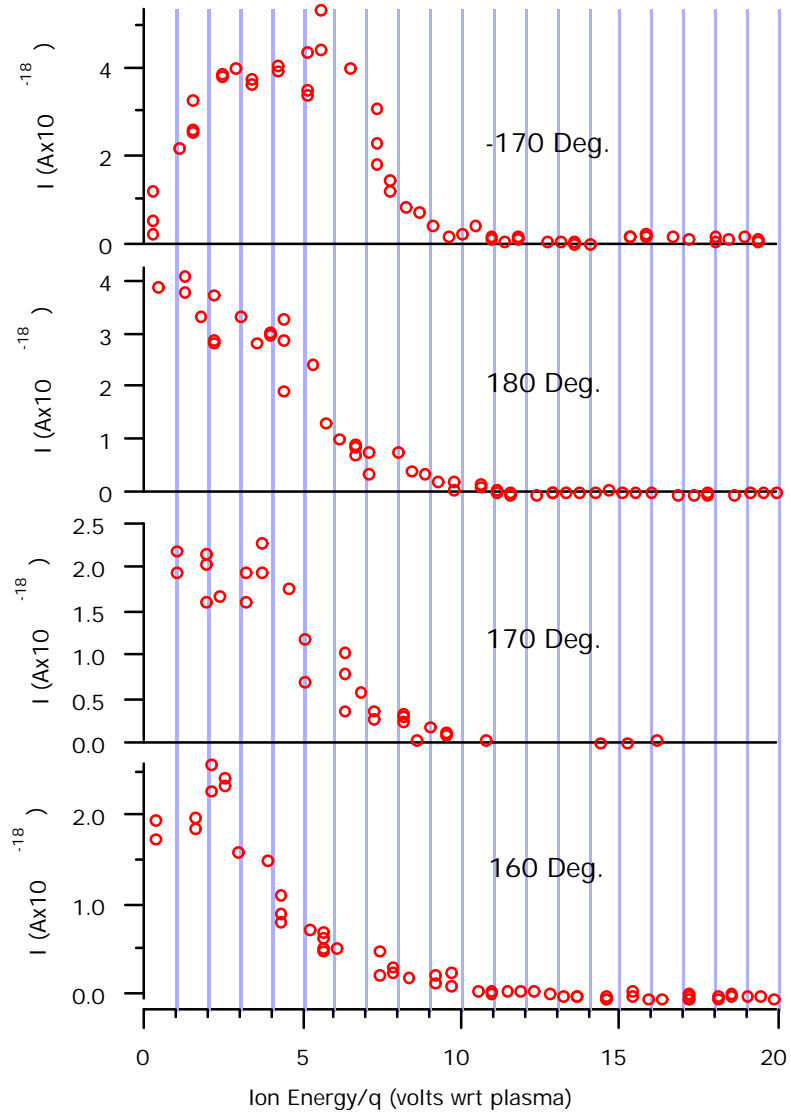


Figure 5-7. Ion current as a function of ion voltage at 0.5 m radius from the SPT-100 for points at 160, 170, 180, and -170 degrees off thrust axis.

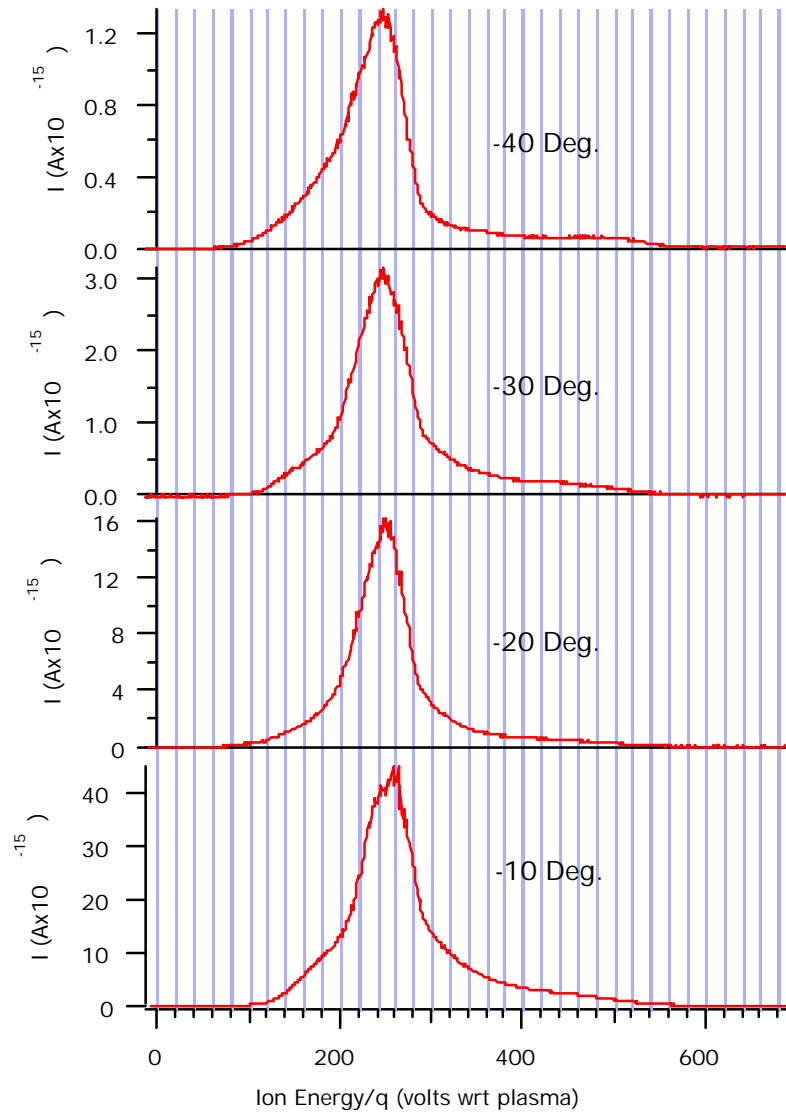


Figure 5-8. Ion current as a function of ion voltage at 0.5 m radius from the SPT-100 for points at -10, -20, -30, and -40 degrees off thrust axis.

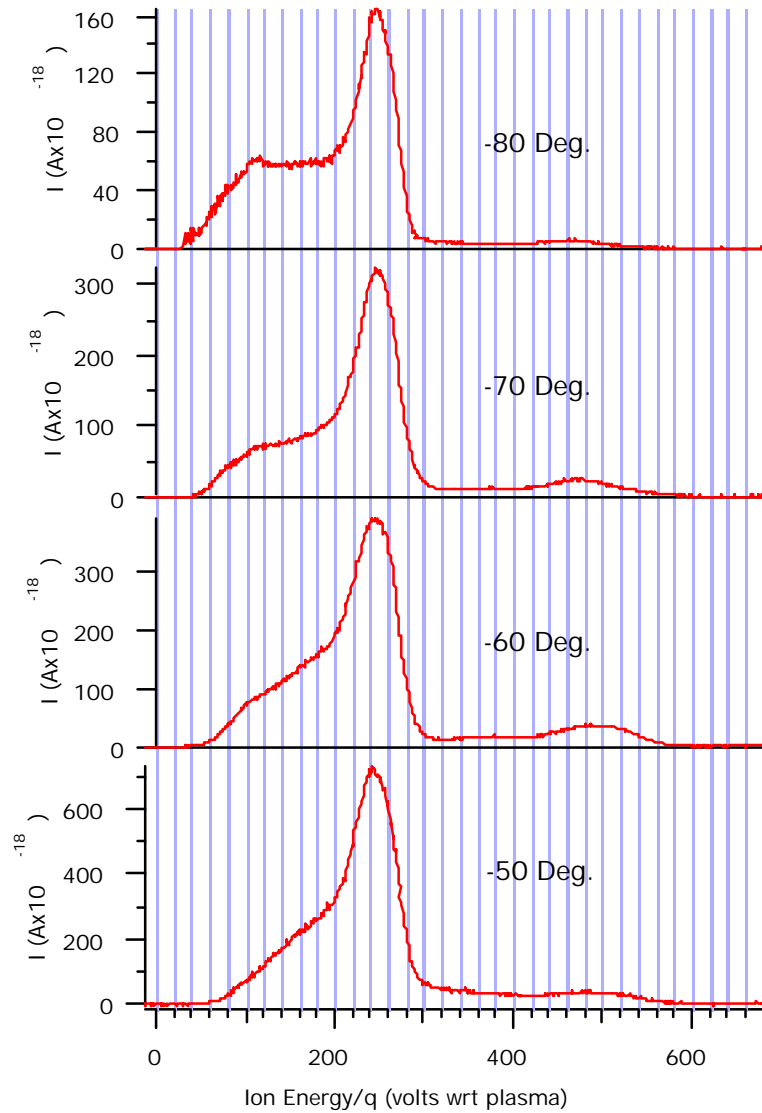


Figure 5-9. Ion current as a function of ion voltage at 0.5 m radius from the SPT-100 for points at -50, -60, -70, and -80 degrees off thrust axis.

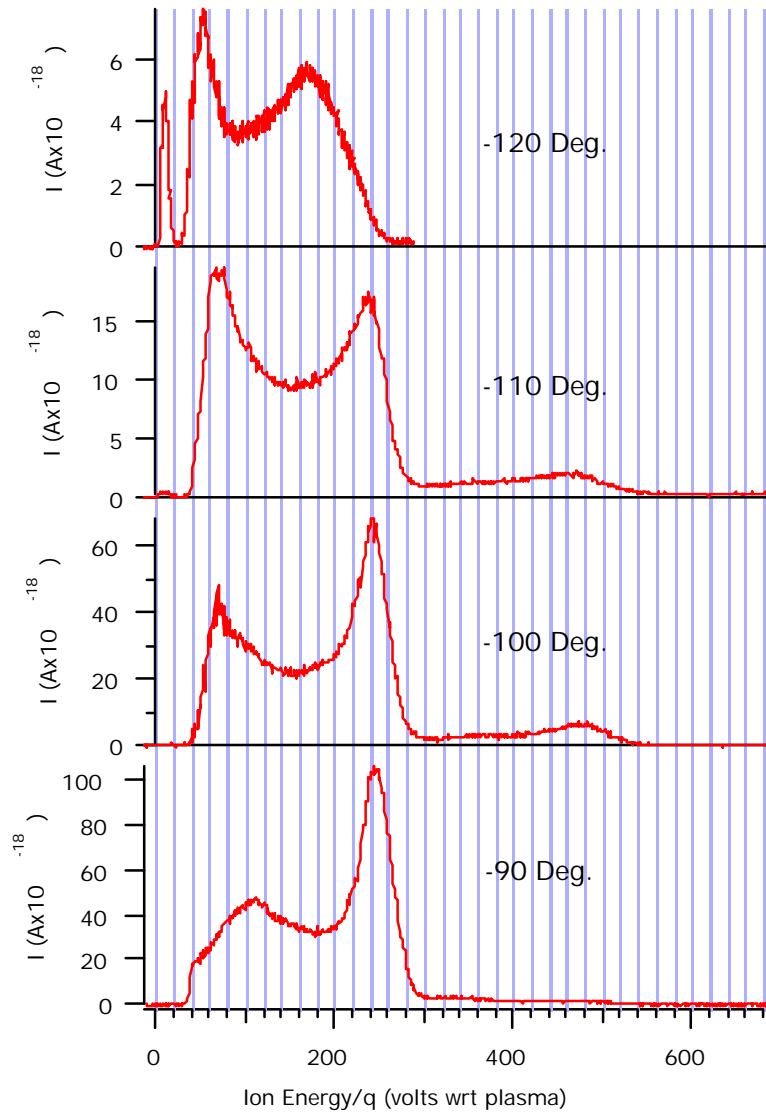


Figure 5-10. Ion current as a function of ion voltage at 0.5 m radius from the SPT-100 for points at -90, -100, -110, and -120 degrees off thrust axis.

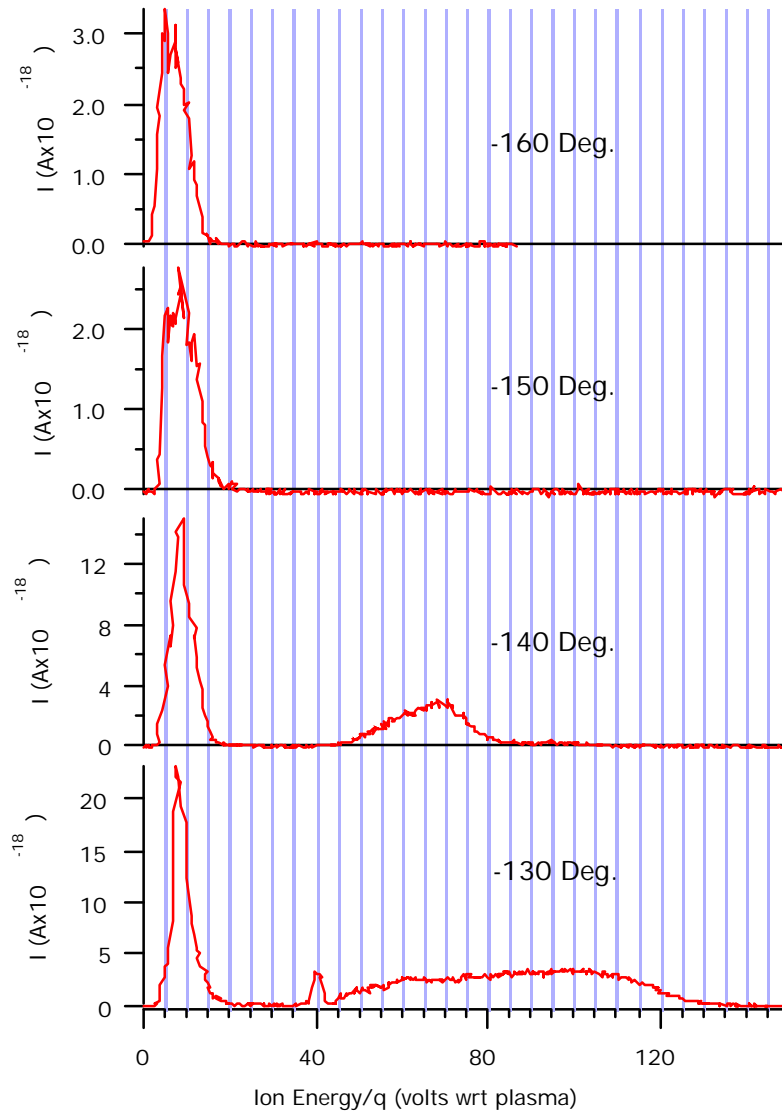


Figure 5-11. Ion current as a function of ion voltage at 0.5 m radius from the SPT-100 for points at -130, -140, -150, and -160 degrees off thrust axis.

5.3. Ion Energy Measurements in an SPT-100 at 1.0 m

The ion energy distribution function was evaluated at a radial distance of 1.0 m from the thruster exit plane by repositioning the thruster/rotary table mount relative to the MBMS inlet skimmer. At this distance curves were

obtained as a function of angular position about the SPT-100 thrust axis. Due to the much lower ion densities at 1.0 m as compared with those at 0.5 m, data could not be obtained in a complete 360-degree arc about the thruster. The region behind the thruster at positive angles greater than 110 degrees and negative angles of magnitude greater than -150 degrees represented ion currents less than 5×10^{-19} A; due to the low currents this region could not be evaluated. The resulting data are shown in Figure 5-12 through Figure 5-18. These curves have been corrected for the parasitic energy addition imposed to the ions as they fell from local plasma potential through the inlet skimmer to ground potential.

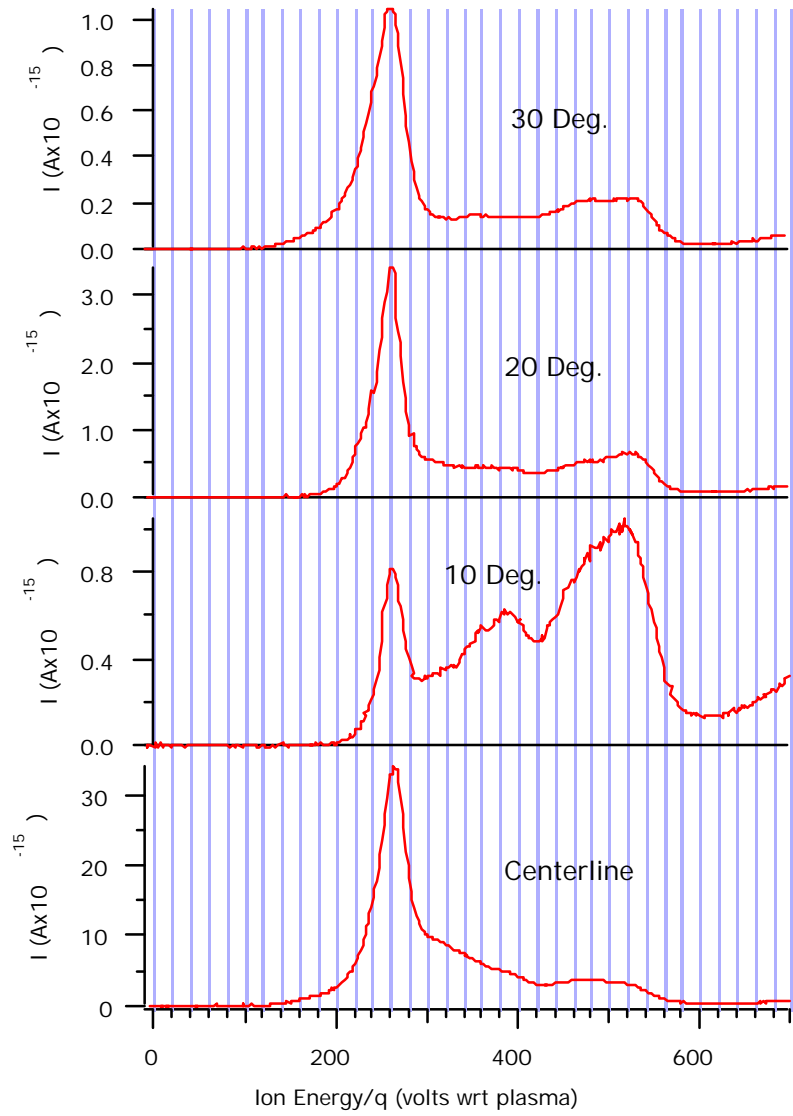


Figure 5-12. Ion current as a function of ion voltage at 1.0 m radius from the SPT-100 on the thrust axis in addition to points at 10, 20, and 30 degrees off axis.

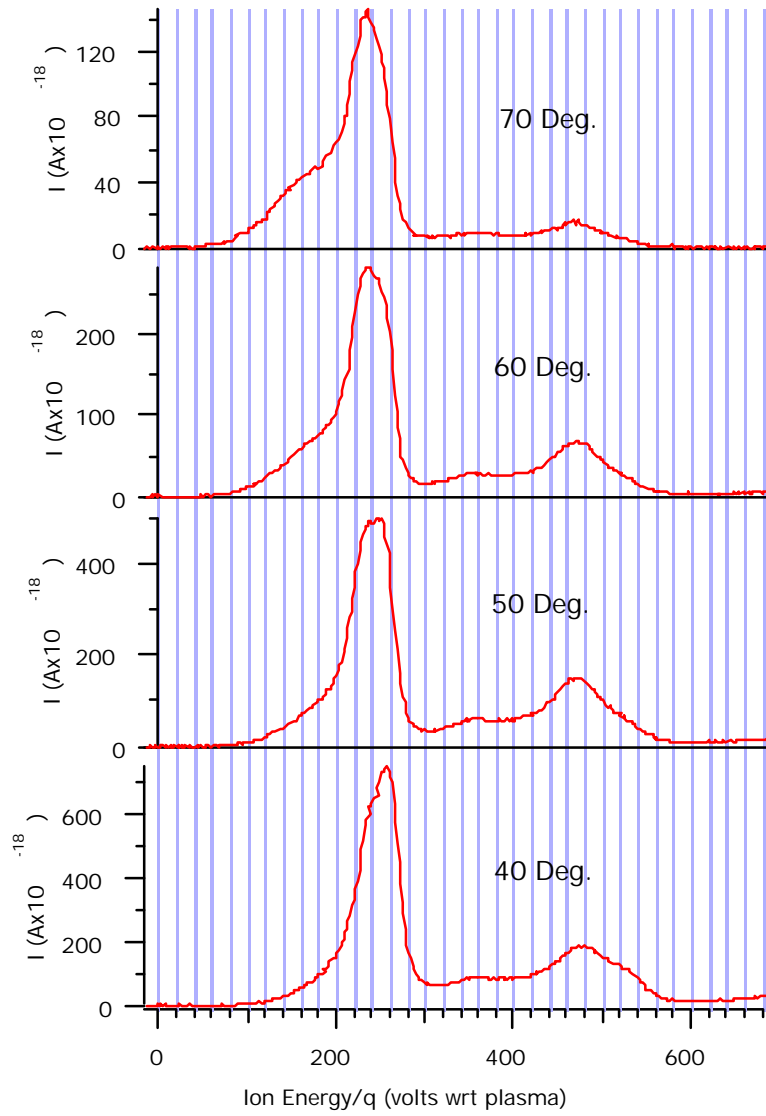


Figure 5-13. Ion current as a function of ion voltage at 1.0 m radius from the SPT-100 for points at 40, 50, 60, and 70 degrees off thrust axis.

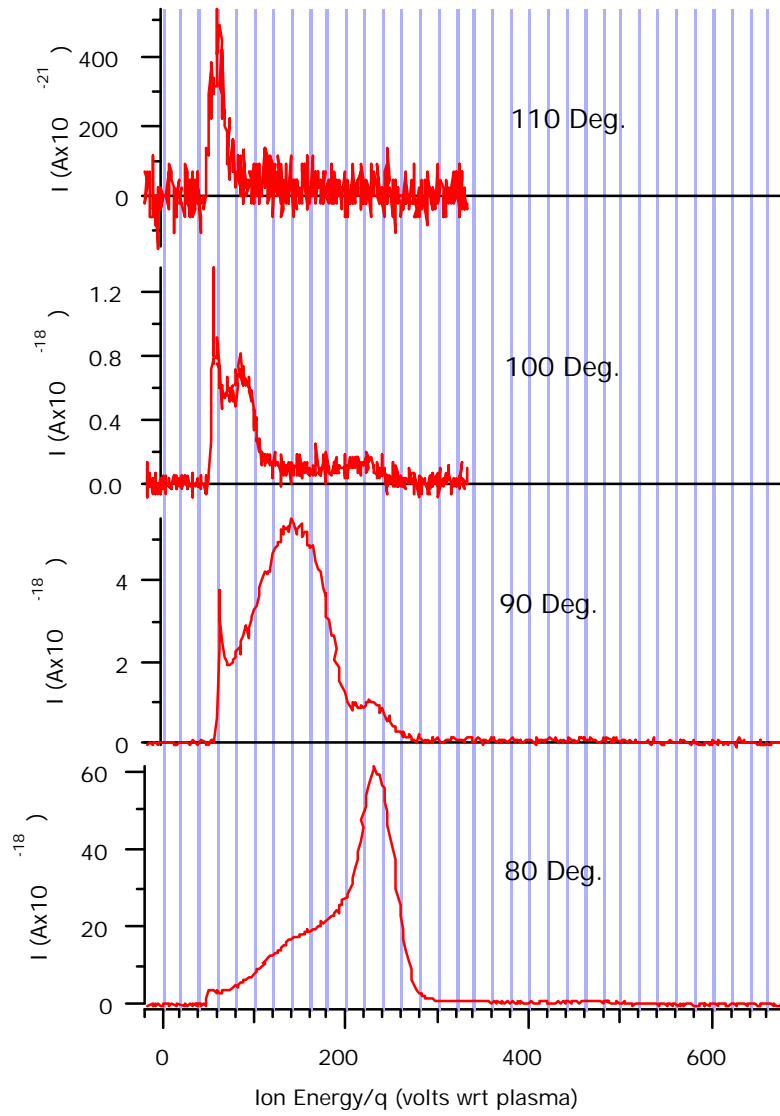


Figure 5-14. Ion current as a function of ion voltage at 1.0 m radius from the SPT-100 for points at 80, 90, 100, and 110 degrees off thrust axis.

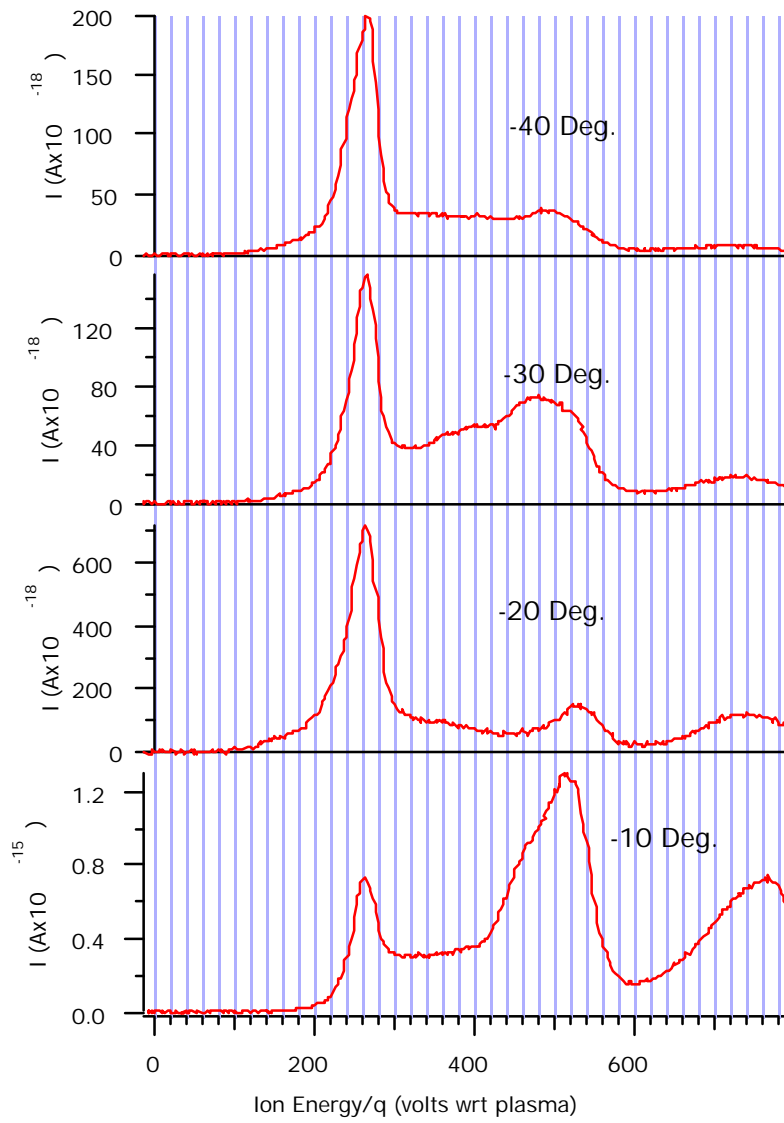


Figure 5-15. Ion current as a function of ion voltage at 1.0 m radius from the SPT-100 for points at -10, -20, -30, and -40 degrees off thrust axis.

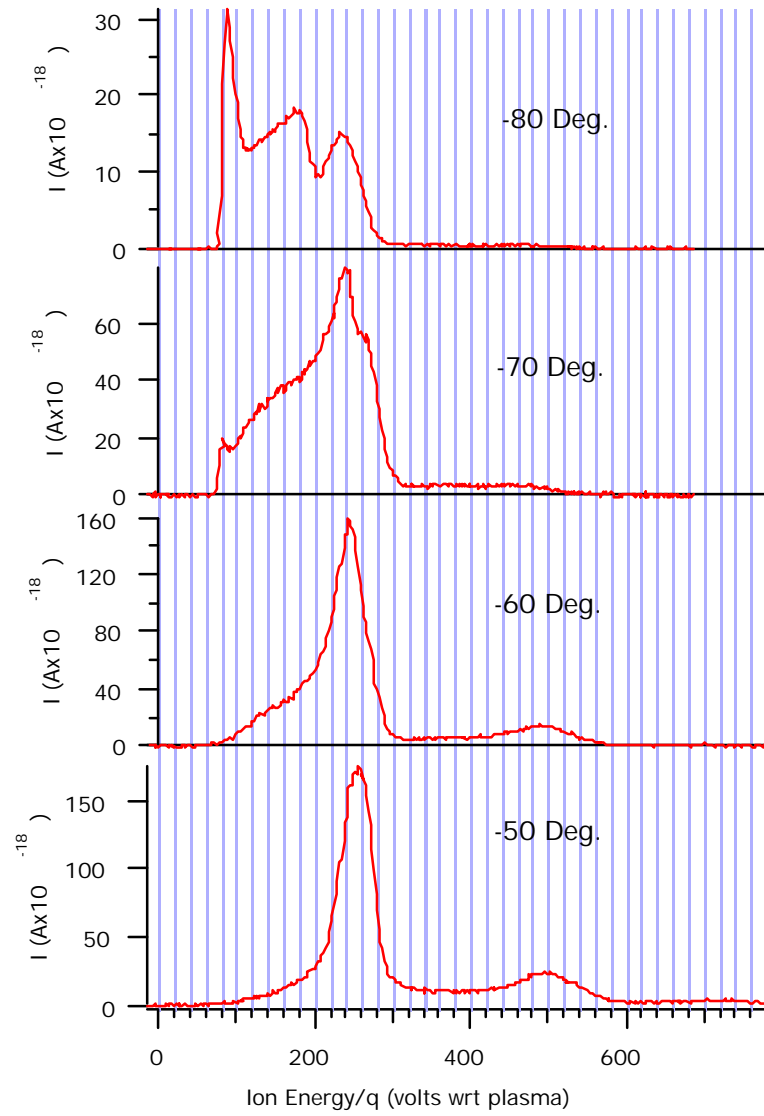


Figure 5-16. Ion current as a function of ion voltage at 1.0 m radius from the SPT-100 for points at -50, -60, -70, and -80 degrees off thrust axis.

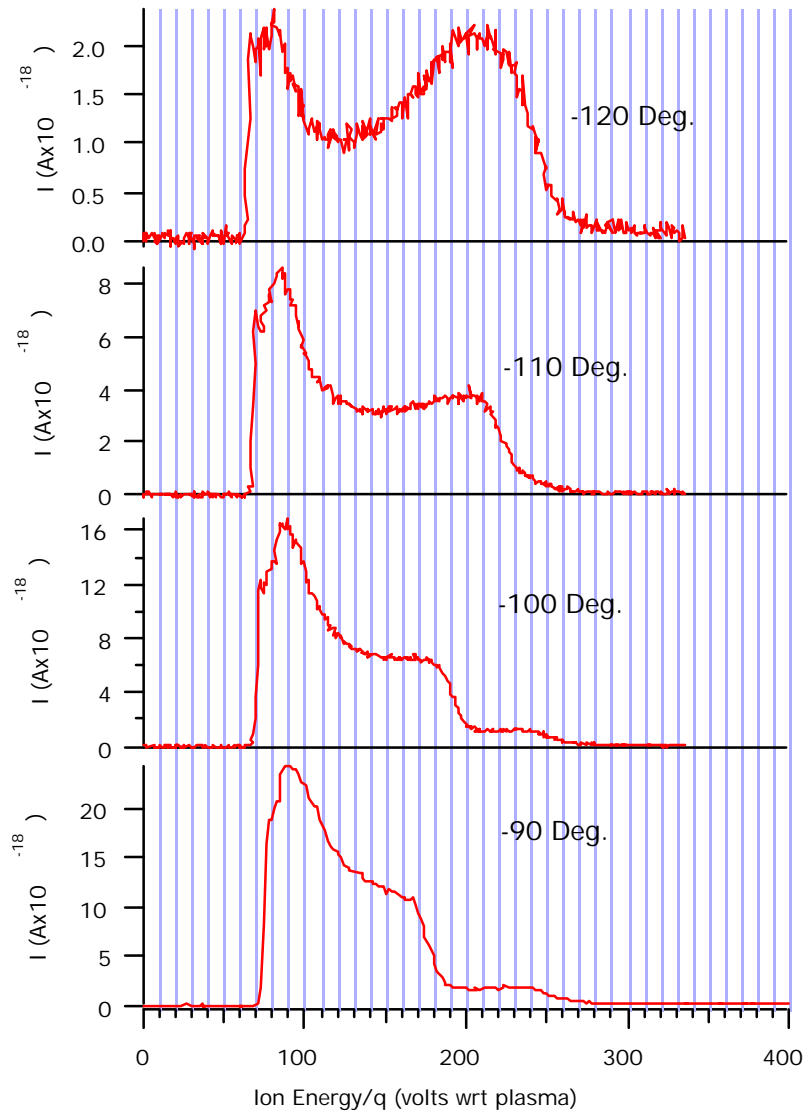


Figure 5-17. Ion current as a function of ion voltage at 1.0 m radius from the SPT-100 for points at -90, -100, -110, and -120 degrees off thrust axis.

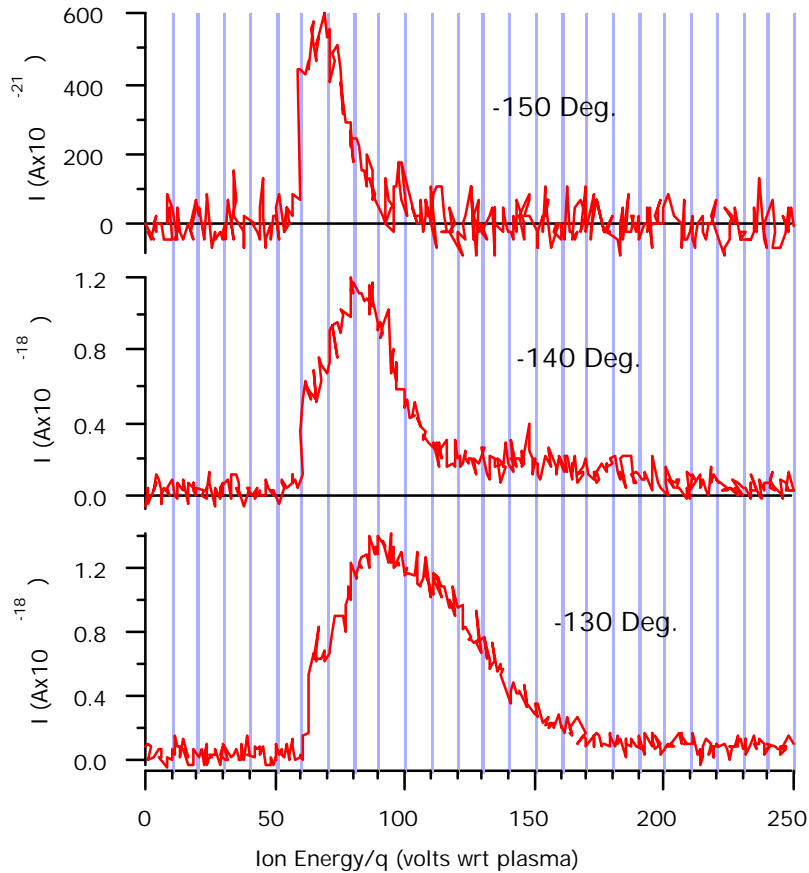


Figure 5-18. Ion current as a function of ion voltage at 1.0 m radius from the SPT-100 for points at -130, -140, and -150 degrees off thrust axis.

The ion current traces obtained for the points at 10 degrees and -10 degrees were strikingly dissimilar to the overall trends exhibited as a function of angular position. This contrast is easily seen by examining Figure 5-12 and Figure 5-15. In order to more fully interrogate this region of the plume data were obtained with much finer angular resolution for points within 20 degrees of the axis. Figure 5-19 illustrates the overall trend in ion current between the thrust axis and 20 degrees, with Figure 5-20 included as an expanded view of the

evolution between 6 degrees and 17 degrees. Figure 5-21 and Figure 5-22 present the ion current evolution for the positions between -5 degrees and -20 degrees.

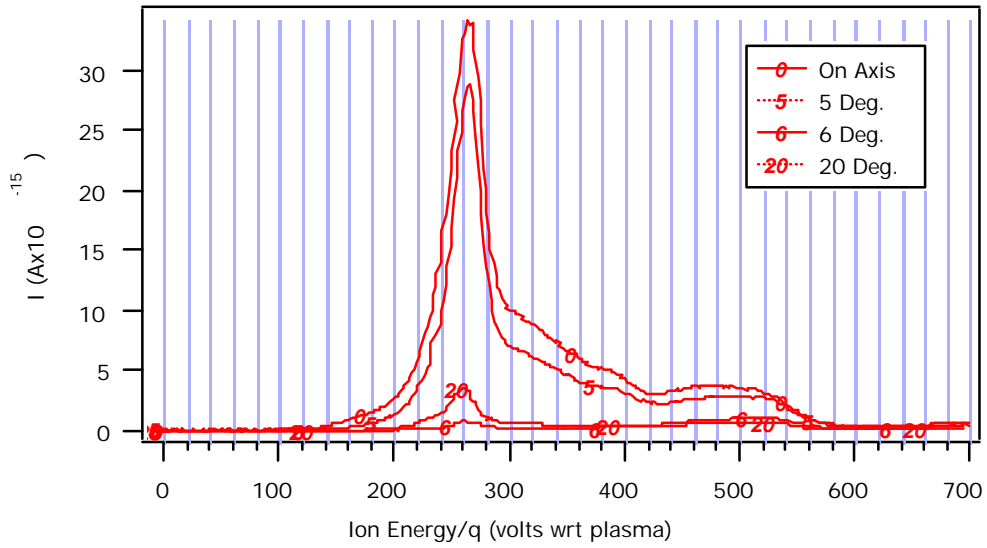


Figure 5-19. Evolution of ion current traces as a function of angular position between thrust axis and 20 degrees at 1.0 m radius from the SPT-100.

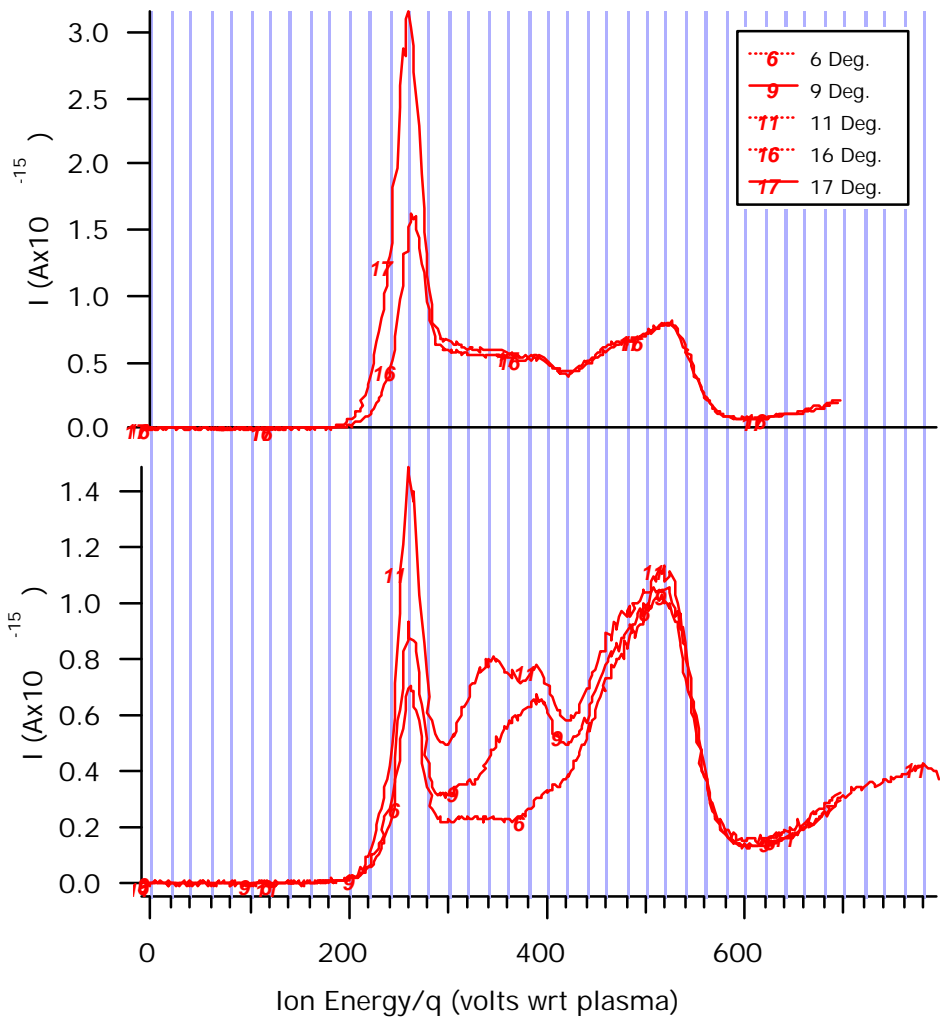


Figure 5-20. Exploded view of ion current evolution between 6 degrees and 17 degrees off thrust axis at 1.0 m radius from the SPT-100.

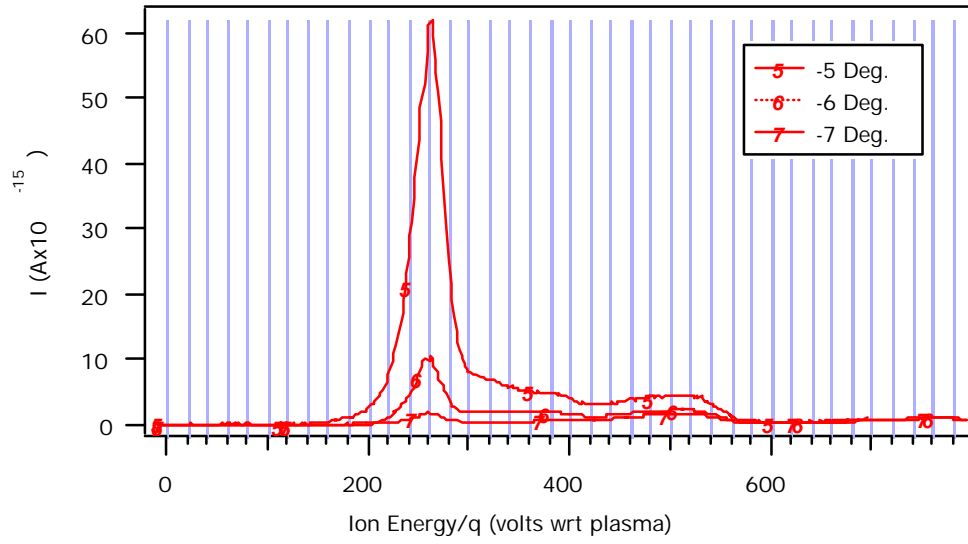


Figure 5-21. Ion current evolution between -5 and -7 degrees off thrust axis at 1.0 m radius from SPT-100.

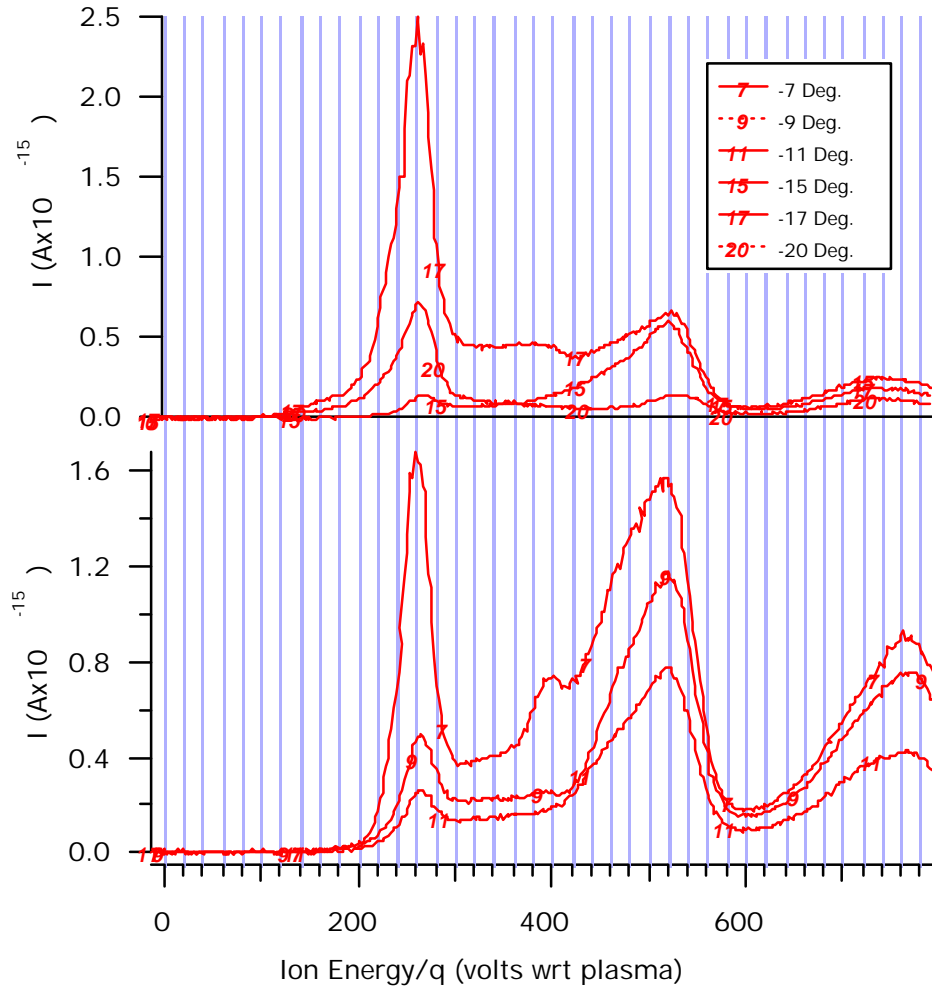


Figure 5-22. Ion current evolution between -7 degrees and -20 degrees off thrust axis at 1.0 m radius from the SPT-100.

5.4. Discussion of Ion Voltage Distributions

The relation linking the I(V) curve to the ion voltage distribution function was derived previously: as evidenced by Eqn. 4-9 calculation of the voltage distribution in a multi-species flow requires knowledge of the ionization-state-dependent current as a function of voltage. Specifically,

Eqn. 5-1

$$f(V) \propto \frac{1}{\sqrt{V}} \left(\frac{I(V, q_1)}{\sqrt{q_1}} + \frac{I(V, q_2)}{\sqrt{q_2}} + \dots \right)$$

where $I(V, q_n)$ denotes the current due to ions with voltage V and charge q_n . Since ion velocity increases with q , a population of high- q ions will produce a larger current than an equal number of low- q ions: The inclusion of $q^{-1/2}$ in Eqn. 5-1 is therefore required to account for the disproportional contribution of high- q ions to the total ion current. The data reported in Section 5.2 and 5.3 reflect the total current due to all ion charge states as a function of ion voltage, therefore they cannot be directly manipulated to yield $f(V)$. If the flow under consideration was composed almost entirely of one species of ion ($q = 1$) then it would be possible to obtain a good approximation of $f(V)$ by neglecting the contribution due to the higher charge states. This approximation has previously been applied to the RPA technique allowing valuable estimations of ion density and velocity to be made in the region of the plume near thruster centerline (see Section 3.3). However, as will be discussed in Chapter 6 and 7, investigations of the plume at extremely large angles off axis (60 degrees to 180 degrees) enabled by the high gain of the MBMS showed the assumption of a majority charge state to be possibly inappropriate.

Although the $I(V)$ curve is not directly proportional to $f(V)$ for reasons discussed above, it should be kept in mind that these two functions are very closely related. For example, if a portion of the $I(V)$ curve was known to result entirely from ions with $q = 2$, attenuation of this portion of the curve by a factor

of 0.707 would yield the value of $f(V)$. Allowing for the existence of ions with charge states up to $q = 4$ in the flow ensures that the value of $I(V)$ is never more than a factor of two larger than $f(V)$. Therefore, although it may be inappropriate to substitute $I(V)$ for $f(V)$ in detailed calculations, when discussing the overall shape and data trends it is reasonable to speak of the two functions interchangeably.

5.4.1. Comparison with RPA

A cursory examination of the $I(V)$ traces presented in Section 5.2 and 5.3 reveal a much improved resolution over the widely used RPA technique. The RPA data reduction process required numerical differentiation and hence produced very noisy distribution curves. The inherently different 45-degree analyzer technique required no differentiation and therefore produced much smoother, more accurate results. Additionally, the uncertainties associated with measuring the ion current in the RPA experiment combined with the noisy differentiation yielded data with unacceptable signal-to-noise ratios for angular positions exceeding 60 degrees from the thrust axis. The high gain of the CEM/picoammeter detector circuitry enabled measurement of the ion energy at points up to 180 degrees off thrust axis (directly behind the thruster). These far off-axis regions of the plume are especially critical in evaluating plume impingement on surrounding spacecraft surfaces.

A direct comparison between the MBMS and RPA data demonstrates a disagreement in the measured ion energy. Figure 5-23 shows a comparison of the two techniques at 0.5 m radius, while Figure 5-24 represents the points at 1.0 m radius.

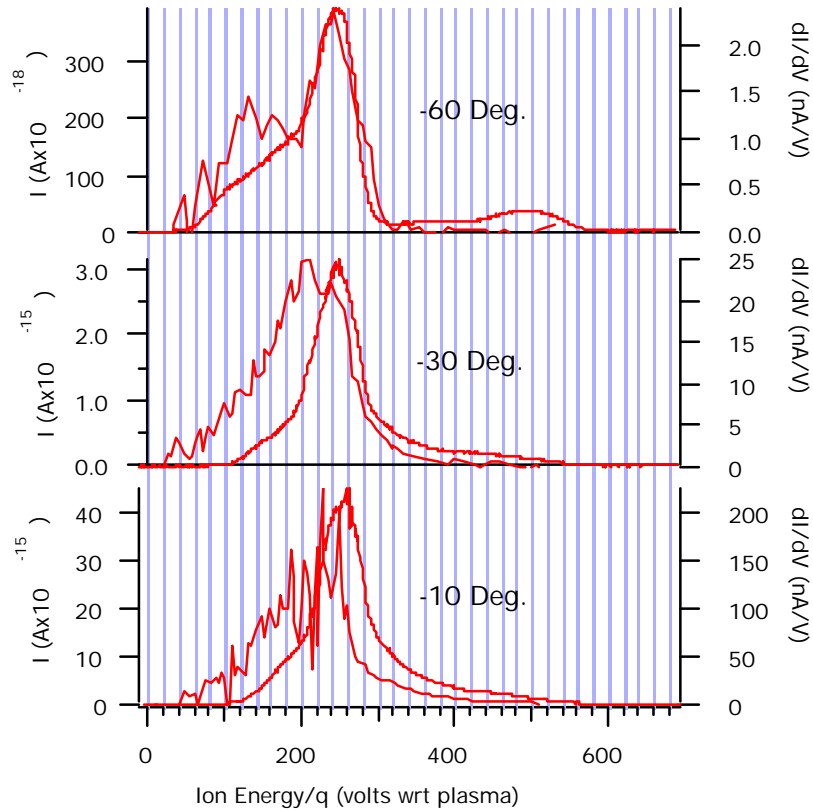


Figure 5-23. Comparison between RPA and MBMS measurements of the ion voltage at 0.5 m radius from the SPT-100. RPA traces are shown as dashed lines corresponding to the right vertical axes, with the MBMS data shown solid with units on the left axes.

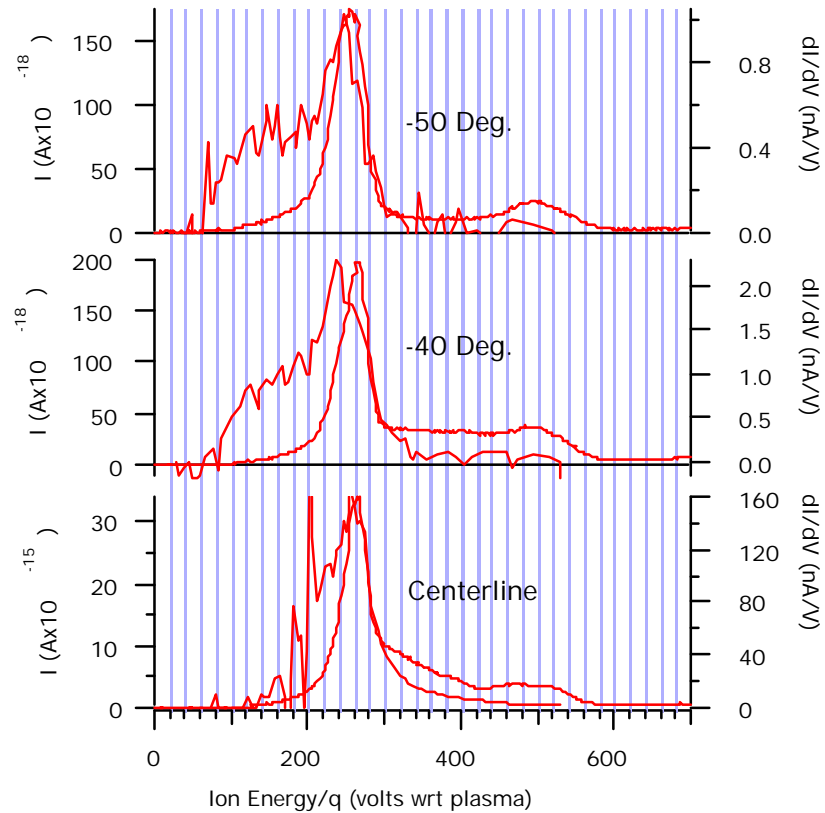


Figure 5-24. Comparison between RPA and MBMS measurements of the ion voltage at 1.0 m radius from the SPT-100. RPA traces are shown as dashed lines corresponding to the right vertical axes, with the MBMS data shown solid with units on the left axes.

The difference between the MBMS-obtained energy distributions and the in-situ RPA probe data exposed a shortcoming in the probe technique as applied to a high-density, high-velocity plasma such as the Hall thruster plume. Physically, the RPA probe resembled a cylinder closed on one end by a current collector, with the open end exposed to the flowing plasma (see Figure 2-1). Gate grids were located along the axis of the cylinder to selectively repel and filter out charged particles of both signs, while admitting a select energy range

of ion current to the collector at the back of the probe. The problem with this technique arises when the plasma flow velocity and density increase sufficiently to “choke” the closed internal volume of the probe. It was shown using a neutral particle flux probe in Chapter 3 that the internal pressure due to neutral Xe within the probe can exceed 10 or 20 mTorr in the SPT-100 plume near centerline at 0.5 m. This stagnation pressure rise was due to the ram effect of the flowing high density plasma entering the probe and being neutralized by collisions with the probe walls or current collector forming a high-density trapped gas volume. This relatively dense target gas scatters the incoming plume ions through both charge exchange (CE) and momentum transfer collisions. Any collision involving a plume ion and a stagnant target particle results in energy loss for the plume ion; the net effect is an attenuation of the energy peak and a broadening of the distribution in the direction of lower ion energy.

Although detailed cross sections for all collisions likely to occur within the RPA volume were not available, an estimation of the effect of ram gas build-up was made based on those that were. For example, the dominant collision mechanism is likely to be CE between singly ionized xenon plume ions and background xenon neutrals; the cross section for this reaction can be calculated according to Eqn. 3-6. Assuming that the internal probe pressure is 20 mTorr with a temperature near that of the probe walls (300 K), an incoming 300 V Xe^+ ion experiences a CE mean free path on the order of 3 mm. The RPA probe had a path length from inlet to collector of approximately 2 cm: this would cause

over 90% of the plume ions to suffer a CE collision prior to detection as calculated from Eqn. 3-7. On the other hand, differential pumping allowed the MBMS to maintain an internal vacuum of approximately 1×10^{-6} torr during operation; this equates to a mean-free-path on the order of 70 m for the CE collision. For ions traveling the 2.35 m path from the MBMS inlet to the detector this equates to a collision probability of approximately 3%. It is therefore justified to assume that collisional broadening of the ion energy within the MBMS is negligible.

The collisional broadening and attenuation within the RPA should be greatest for regions of high density and high velocity. From an examination of Figure 5-23 and Figure 5-24 this is seen to be true. The energy shift between the RPA and MBMS data was of greatest magnitude for the near centerline traces where the ion density was highest. Furthermore, the shift in the near centerline data is more severe for the data taken at 0.5 m from the thruster than for the 1.0 m data set

5.4.2. Ion Temperature

Since the I(V) traces obtained with the 45-degree analyzer very closely approximate the ion voltage distribution function it is perhaps instructive to describe their shape in terms of an ion temperature. However, the driving mechanism defining the shape of the I(V) curves is due to an overlap between the ionization region and acceleration region within the SPT-100 discharge

chamber: ions are created throughout a region in space over which the potential varies greatly, thus the spread in the I(V) curve reflects the fact that ions are “born” in regions of different potential and therefore experience different acceleration voltages. This spread is in no way equal to the traditional thermal variation in ion energy. The definition of ion temperature to be used in this report is therefore strictly mathematical and in no way implies any form of thermal equilibrium.

The ion temperature will be defined analogous to that of a traditional Maxwellian thermal distribution. The one-dimensional Maxwellian distribution written in terms of ion velocity is

Eqn. 5-2
$$f(u_i) = \sqrt{\frac{b}{p}} \exp(-bu_i^2)$$

with $\beta = m_i/2kT_i$. For a distribution imposed on a macroscopic bulk drift velocity, u_d , Eqn. 5-2 must be written in terms of the peculiar velocity, $u_i - u_d$:

Eqn. 5-3
$$f(u_i) = \sqrt{\frac{b}{p}} \exp(-b(u_i - u_d)^2).$$

written in terms of energy the peculiar velocity is

Eqn. 5-4
$$u_i - u_d = \left(\frac{2\sqrt{(E_i - E_d)^2}}{m_i} \right)^{\frac{1}{2}}$$

so that now

Eqn. 5-5
$$f(E_i) = \sqrt{\frac{b}{p}} \exp\left(\frac{-2b}{m_i} \sqrt{(E_i - E_d)^2}\right).$$

Substituting for β and recognizing that kT_i/e is the equivalent temperature in electron-volts, T_{eV} , yields the final result

Eqn. 5-6
$$f(E_i) = \sqrt{\frac{b}{p}} \exp\left[-\sqrt{\frac{\left(\frac{(E_i - E_d)}{qe}\right)^2}{T_{eV}^2}}\right].$$

According to Eqn. 5-6 for a Maxwellian energy distribution, the ion temperature in eV represents the half-width of $f(E_i)$ at the point where $f(E_i)$ has a value of e^{-1} times the peak value (where $E_i = E_d$ at the peak). Mathematically,

Eqn. 5-7
$$\frac{\left(\frac{(E_i - E_d)}{qe}\right)}{T_{eV}} = 1$$

where $f(E_i) = 0.37 f(E_d)$.

In the context of the Maxwellian analysis, the temperature of the $I(V)$ distributions obtained with the 45-degree analyzer will be defined as the half width of the $I(V)$ distribution at the point in the curve where $I(V)$ is equal to 0.37 times $I(V_m)$, where V_m represents the most probable voltage such that $I(V_m)$ is a maximum. This value of ion “temperature” will be denoted as τ_i , but, as stated earlier, usage of the term does not imply any type of equilibrium. Instead, τ_i

simply reflects an indication of the width-to-height aspect ratio of the I(V) distribution.

With this in mind trends in the extensive I(V) data sets were evaluated. In order to define a unique temperature the definition of τ_i requires the I(V) distribution to be symmetric about the drift energy, E_d . Since the curves obtained in this research were non-symmetric the definition of τ_i implied two distinct temperatures corresponding to the $0.37x_f(E_d)$ point on either side of the peak. For reasons that will be made clear in Chapter 7 the temperature was defined as the $0.37x_f(E_d)$ point such that $E > E_d$ (to the right of the peak).

The 0.5-m I(V) data sets exhibited interesting general trends in ion temperature. The interpretation of τ_i was somewhat confused by the existence of multiple peaks for the angular positions centered around 90 and -90 degrees; for these traces it was unclear which peak defined the main distribution. However, for many of the angular positions the distribution was characterized by a single dominant peak which was used to calculate τ_i . Figure 5-25 shows a plot of τ_i as a function of angular position for points lying 0.5 m away from the SPT-100 exit plane. Values of τ_i were not calculated for points in which the choice of dominant distribution peak was unclear.

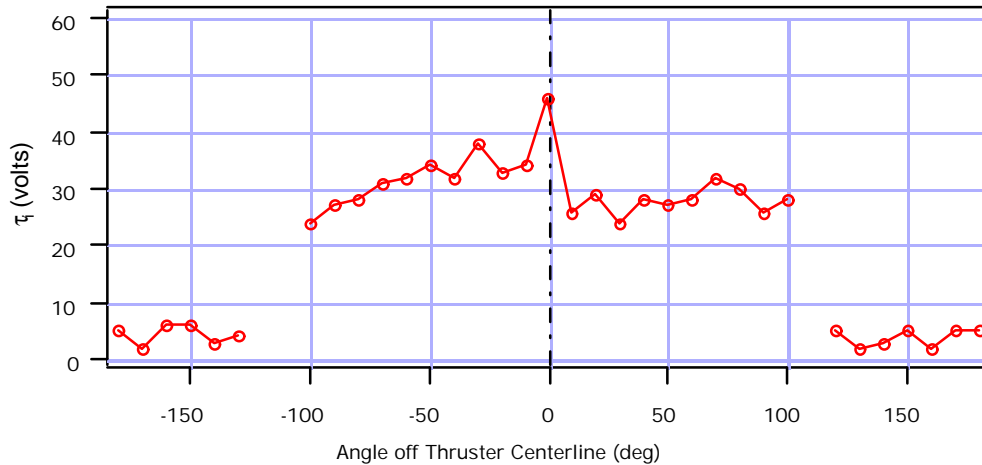


Figure 5-25. Variation of defined ion temperature, τ_i , as a function of angular position at 0.5 m radius from the SPT-100.

Variation in the ion temperature for points lying along the 1.0 m radius was also analyzed. However, the anomalous distributions found between 5 degrees and 20 degrees of thrust axis prevented calculation of a meaningful τ_i for these points: the distribution in this regime consisted of multiple current peaks with comparable magnitudes such that the choice of a dominant distribution was not clear. This fact created “gaps” in the τ_i vs θ plot shown as Figure 5-26 and hindered the identification of trends.

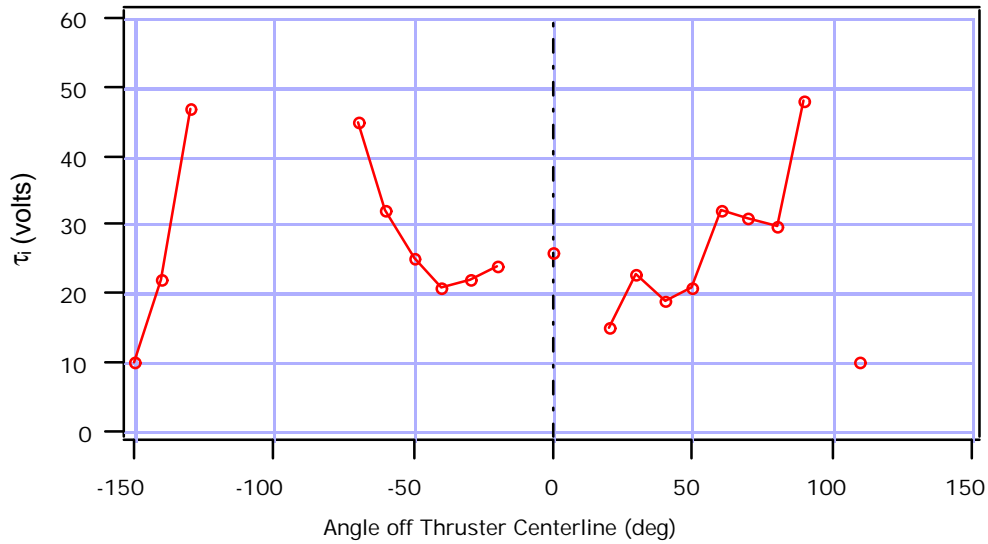


Figure 5-26. Variation of defined ion temperature, τ_i , as a function of angular position at 1.0 m radius from the SPT-100.

The calculated values for τ_i shown in Figure 5-25 and Figure 5-26 demonstrate excellent agreement with the currently accepted structure of the ionization and acceleration regions within the SPT-100 discharge chamber. Baranov, et al.³¹ have recently developed a comprehensive model of the acceleration layer formation within the Hall thruster. This model was used to predict plasma parameters such as electron temperature, plasma density, collision frequencies, and electric field within the acceleration region of a Hall thruster very similar to the SPT-100. The neutral atom density and plasma potential predictions resulting from this model are reproduced as Figure 5-27.

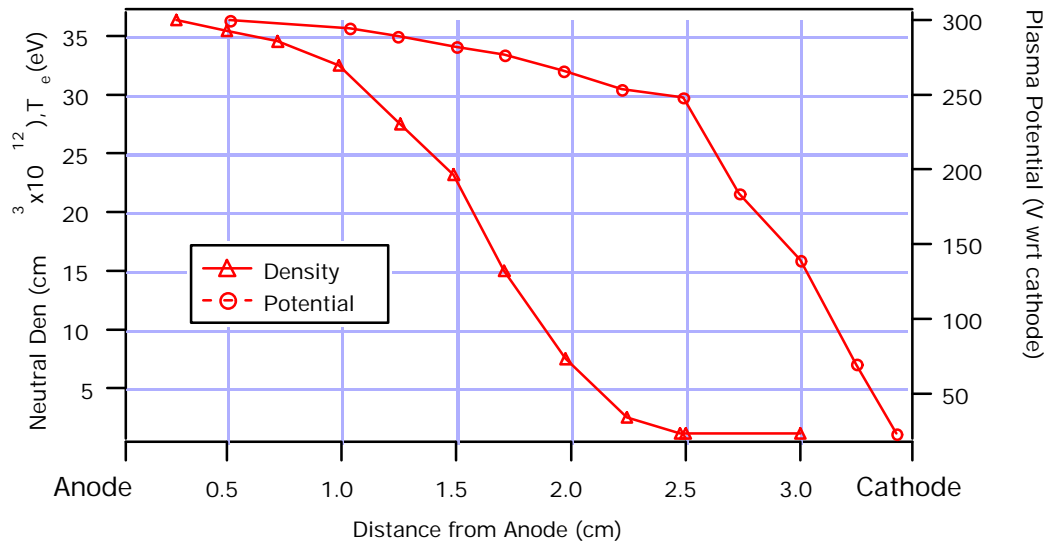


Figure 5-27. Neutral propellant density and local plasma potential within the Hall thruster acceleration layer as modeled by Baranov, et al.³¹

In this model, as in actual Hall thruster operation, neutral propellant is injected through the anode. This propellant is then ionized by electron collisions as the neutral atoms travel towards the cathode. The decay in neutral atom density with distance from the anode therefore corresponds to the disappearance of neutrals due to ionization. As can be seen from the model, most of the propellant is ionized within a region extending 2.5 cm from the anode. Within this ionization region the local plasma potential varies from 300 to 250 V; thus the ions that are “born” within this region will have a voltage spread of approximately 50 V upon exiting the discharge chamber. This agrees well with the measured values of τ_i (half-width) of approximately 20 to 40 V for the main discharge ion beam within 90 degrees of thrust axis shown in Figure 5-25 and Figure 5-26. Furthermore, many of the ions formed within the first 2.5 cm of the

anode will suffer a neutralizing collision with the discharge chamber wall downstream, followed by a second (or even third) ionizing electron collision; these ions will increase the spread in the exhaust voltage distribution beyond that induced by the 2.5 cm ionization zone.

The population of ions behind the thruster (at angles greater than about 100 degrees) possess considerably lower temperature than the main beam ions as expected. However, this backflow plasma still has a value of τ_i ranging between 2 and 5 V. Although no investigations of the Hall thruster backflow regions were performed prior to this study, it was widely accepted that this region most likely consisted of macroscopically stagnant plasma arising from charge-exchange collisions between plume ions and background facility gas due to vacuum chamber pumping limitations; thus the distribution would have a width on the order of the local ambient neutral temperature (300 K, or about 0.03 eV). However, it is very unlikely that the high temperature implied by the width of the measured voltage distribution in the backflow (of roughly 58,000 K) represents a true thermal spread within a macroscopically stagnant plasma as would be expected to exist behind the thruster. The physical mechanism producing such a wide energy spread in the backflow ions is unknown as of this writing. Further characterization of the backflow region is thus necessary.

5.4.3. Most Probable Voltage

As another measure of the ion energy structure the most probable ion voltage was compiled as a function of angular position. This voltage was easily defined and identifiable on all plots as the voltage (energy/ q) corresponding to the maximum in the $I(V)$ vs V curve. This quantity is plotted for both 0.5 m and 1.0 m in Figure 5-28.

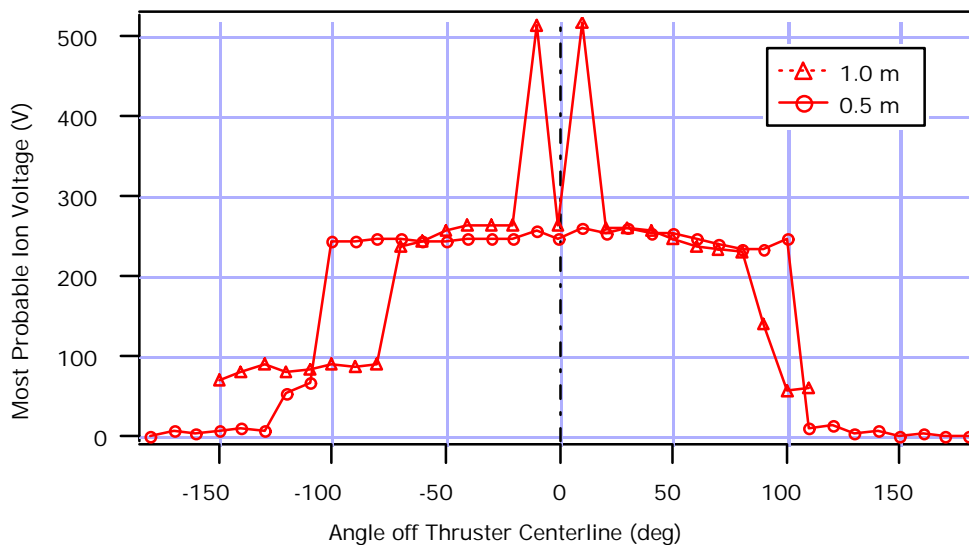


Figure 5-28. Most probable ion voltage (energy/ q) as a function of angular position in the plume of the SPT-100 at 0.5 m and 1.0 m radius from thruster exit.

The angular energy structure displayed in Figure 5-28 exhibits some intriguing qualities, the most striking of which is the existence of high-energy ions at angles exceeding 90 degrees from the thrust axis: ions with V_m on the order of 250 V persist out to 100 degrees, while particles with V_m nearly 100 V extend to nearly 130 degrees at 0.5 m. Although the 1.0 m data show high

energy ions up to 100 V at angles of 100 degrees, the extent of the 250 V ions is narrower at 1.0 m than at 0.5 m, with these high-energy ions decreasing at 70 to 80 degrees off axis. In general, the trends in angular evolution of most probable ion energy at 1.0 m appears to be a “pinched” version of that at 0.5 m.

This pinching effect corresponds to the trend in plasma electric field. The plasma potential was presented as a function of angular position earlier as Figure 3-3. Based on this plot the component of mean azimuthal electric field was computed for each radial position, while the potential difference between the 0.5 m and 1.0 m data sets were used to calculate the mean radial electric field. These quantities are shown in Figure 5-29.

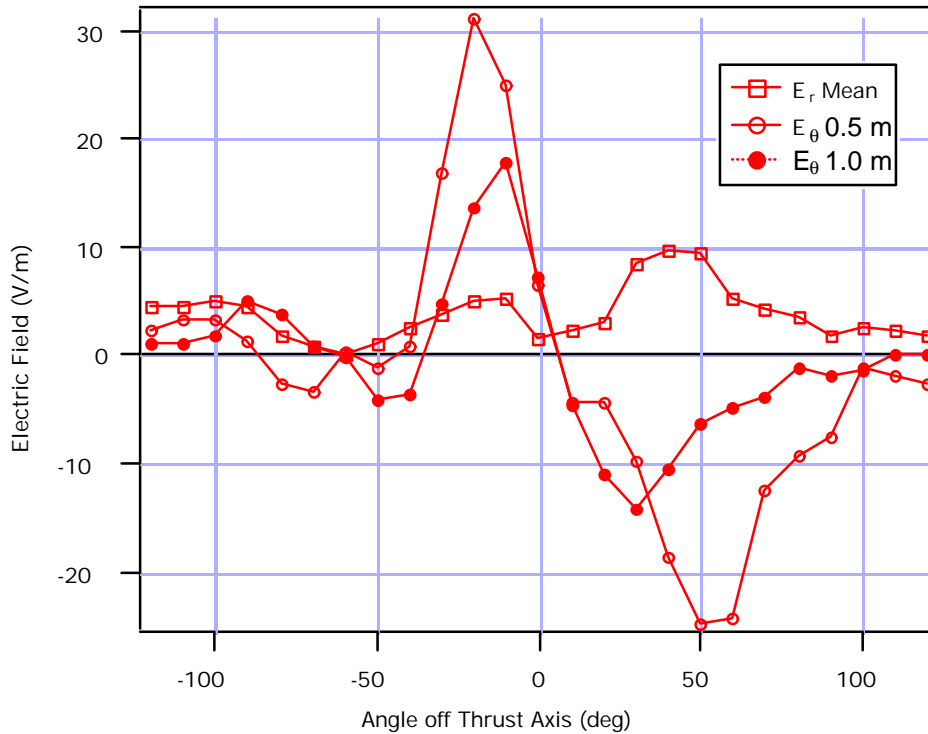


Figure 5-29. Mean electric field components in the azimuthal and radial directions in the SPT-100 plume at 0.5 m radius and 1.0 m radius. Positive E_r denotes the direction pointing back towards the thruster, while positive E_θ reflects a vector pointing in the direction of increasing θ .

Based on the calculated components of electric field a diagram has been constructed as Figure 5-30 indicating the magnitude and direction of the electric field about the SPT-100. This diagram is based on the value of E_θ at 0.5 m radius and the mean value of E_r . Since the azimuthal trends in E_θ for the 1.0 m radial position are nearly identical to those at 0.5 m a single figure provides an acceptable visualization of the field structure in the 0.5-to-1.0-m range.

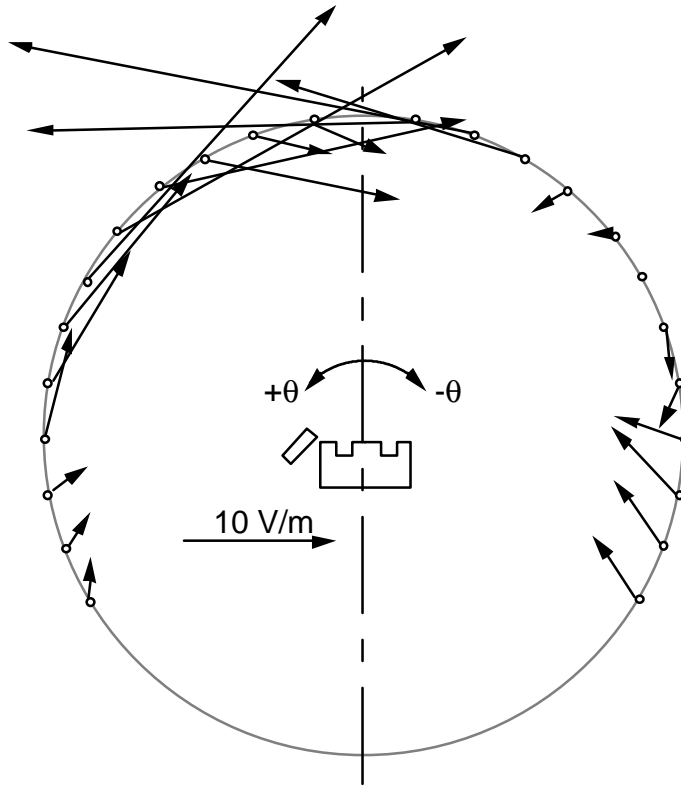


Figure 5-30. Mean electric field vectors as a function of angular position about the SPT-100.

It is apparent from the field diagram that the plasma electric field represents a “pinching” of the ion trajectories toward thruster centerline. Therefore, ions emitted in a purely radial direction will experience a push in the azimuthal direction towards centerline creating a slightly curved trajectory. The MBMS skimmer system only samples ions with purely radial trajectories, with an acceptance cone of half-angle 95 mrad, thus the slight curvature imposed by the mild plume electric fields curves the high energy ions out of the MBMS acceptance cone by 1.0 m radius.

Although the plasma electric field explains the narrowing of the highly divergent ions between 0.5 m and 1.0 m, the existence of such high-energy ions at angles exceeding 90 degrees off axis is still puzzling. Ions with acceleration voltages on the order of the discharge voltage of 300 V must be formed near the upstream end of the thruster acceleration layer and, thus, well upstream of the thruster exit plane. In order for these ions to be emitted at angles near and exceeding 90 degrees off axis they would have to undergo a considerable curvature in their trajectory upon exiting the thruster since there is no direct line-of-sight from these points to the inside of the discharge chamber. Such a scenario is depicted in Figure 5-31.

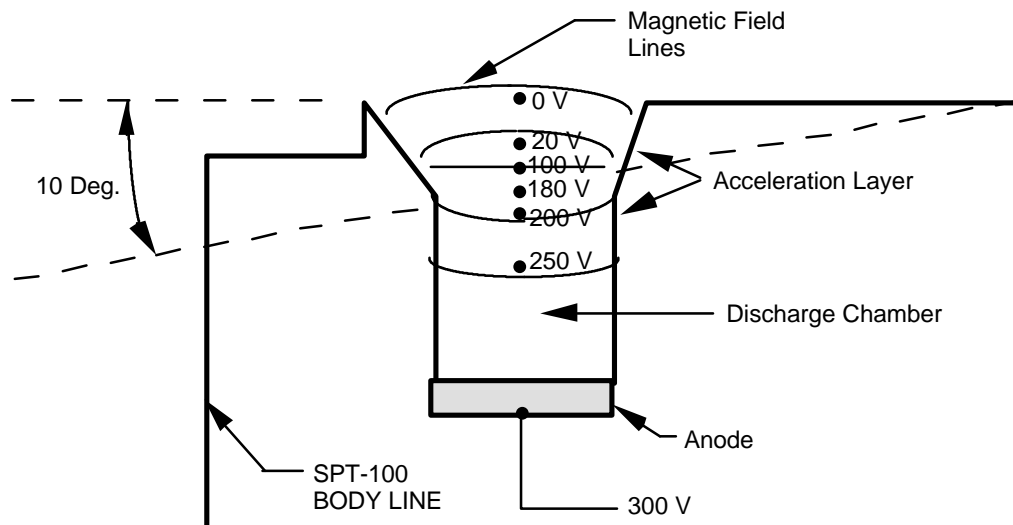


Figure 5-31. Illustration of formation of acceleration layer within SPT-100 discharge chamber.

With this picture of the acceleration layer formation it is apparent that a significant force would be required to deflect high-energy ions originating from

deep in the discharge chamber out to trajectories approaching and exceeding 90 degrees off axis. The existence of such a force is improbable. It is more plausible that a small amount of propellant ionization and radial acceleration occurs downstream of the discharge chamber exit, external to the thruster. Since the electron mobility is very large along magnetic field lines within the discharge chamber these magnetic field lines represent electric equipotentials. Thus ions are formed and accelerated into trajectories normal to the magnetic field line at the ion formation point. Bending of the magnetic field lines further outward from the exit plane than shown in Figure 5-31 would produce a magnetic field fringe with a normal approaching 90 degrees. Ions formed within this downstream region would experience an acceleration force perpendicular to the thrust vector and would therefore appear at large angles. However, although conceptually this scenario seems plausible, previous modeling and experimental probing of the near-exit-plane region in Hall thrusters has not documented electric and magnetic fields downstream of the discharge chamber of sufficient strength to produce ions with radial voltages on the order of the applied discharge voltage. It is clearly apparent that this phenomenon is poorly understood and requires further investigation.

The most-probable voltage at 1.0 m radius exhibits peaks of approximately $V_m = 520$ V at 10 degrees on either side of centerline. These peaks are believed to stem from CE collisions between the plume ions and background

ambient neutral atoms. A detailed discussion of this structure is postponed to Chapter 7

5.4.4. Two-stream Instability Analysis

The measured ion energy distribution function displays a prominent “bump-on-tail” structure in many of the points interrogated using the MBMS (see Figure 5-4). Such a structure represents a “two-stream” plasma instability. In this unstable normal mode, a plasma wave travelling with phase velocity near the “bump” velocity will interact strongly with the ions in the “bump” population. These ions will lose energy to the plasma wave, and thus the wave energy will grow. For large times, the ion energy available to “feed” the wave will deplete and the result is a disappearance of the bump population and a smoothing of the distribution tail.

Denoting the bulk drift velocity of the bump distribution as V_0 the dielectric function for this two-stream system is

Eqn. 5-8
$$\epsilon(k_w, \omega) = 1 - \frac{\omega_i^2}{\omega^2} - \frac{\omega_b^2}{(\omega - k_w V_0)}$$

where ω_i represents the ion-plasma frequency of the main distribution and ω_b is the same quantity for the bump distribution. The normal modes of the plasma are given as the zeros of the dielectric function. The unstable wave numbers of

interest to the two-stream instability are those for which $k_w V_0 = \omega_b$.⁵² The dispersion relation then becomes

Eqn. 5-9
$$\omega^3 = -\frac{1}{2} \omega_i^2 \omega_b.$$

Since the wave energy will evolve according to $e^{-i\omega t}$, any roots with $\text{Im}(\omega) > 0$ will grow like $e^{\text{Im}(\omega)t}$ and will be unstable. The instability growth period, τ_{TS} , is defined as the time for the wave amplitude to reach e^1 times its initial value. Since Eqn. 5-9 contains an unstable root at

Eqn. 5-10
$$\omega = \frac{1}{2} \left(\frac{\omega_i^2 \omega_b}{2} \right)^{1/3} + i \frac{\sqrt{3}}{2} \left(\frac{\omega_i^2 \omega_b}{2} \right)^{1/3}$$

the instability growth period is described by

Eqn. 5-11
$$\frac{1}{\tau_{\text{TS}}} = \frac{\sqrt{3}}{2} \left(\frac{\omega_i^2 \omega_b}{2} \right)^{1/3}.$$

Expressing the ion-plasma frequencies in terms of the ion densities yields the following form for the growth period

Eqn. 5-12
$$\frac{1}{\tau_{\text{TS}}} = \frac{\sqrt{3}}{2} \left(\frac{1}{2} \right)^{1/3} \left(\frac{4pe^2}{m_i} \right)^{1/2} n_i^{1/3} n_b^{1/6}.$$

It is apparent that the two-stream instability will grow fastest in regions of highest density. As an estimate of this process the point at 0.5 m radius on the thrust axis is considered, where $n_i = 2 \times 10^{16} \text{ m}^{-3}$. As an approximation the bump

density is estimated as one-fifth of the main density, so that $n_b=4 \times 10^{15} \text{ m}^{-3}$. This implies an instability growth period of 11 ms. As compared with the ion transit time in the region of the plume studied in this report (17 km/s over 0.5 m yields $t=30 \text{ } \mu\text{s}$) this growth period is very long. Thus, over the plasma volume covering the region within about 1.0 m radius of the thruster the two-stream instability will experience only negligible growth and the bump-on-tail distribution can be considered stable.

5.4.5. Multiple Peak Structure

Possibly the most striking feature uncovered in the analysis of the ion energy distribution function as approximated by $I(V)$ curves was the existence of multiple current peaks suggesting discrete distributions for many angular positions. As can be seen from examining these structures these peaks always occurred at discrete multiples of voltage, e.g. a primary peak at V_i , with secondary peaks at $V_i/3$, $V_i/2$, $3V_i/2$, $2V_i$, and $3V_i$. The explanation for this structure is based on the hypothesis of charge-exchange collisions occurring within the plume plasma. However, since the concepts required to discuss such a collisional analysis involve the existence of multiple ion charge states, an explanation for and discussion of this phenomenon has been postponed until Chapter 7.

6. MASS SPECTROMETRIC STUDIES

The MBMS instrument constructed for this research was capable of simultaneously measuring ion mass composition and energy. Mass diagnostics were performed through a time-of-flight principle with a 45-degree electrostatic energy analyzer functioning as an energy filter. This chapter discusses the technique used to quantify the mass species within the SPT-100 plume and presents the results of the species characterization.

6.1. *Experimental Set-up*

The MBMS was configured for operation in TOF mode as discussed in Chapter 4. In this mode a low-voltage pulse generator was used to program the gate width and duty cycle of the high-voltage pulser driving the electrostatic beam gate. The ion current bursts were measured by the CEM and amplified using the pre- and post-amplifier circuitry shown in Figure 4-12. The thruster was mounted and laser-aligned in the same manner as described in Section 5.1 such that the angular uncertainty was 0.5 degrees.

Although the extremely high gain attainable with the CEM/amplifier detection circuitry allowed the analysis of ion energy distributions to be made in

regions of extremely low ion density (and hence, ion current) the basic operating principles of the TOF system greatly limited the spatial extent of the plume that could be interrogated using mass spectrometry. As an illustration of this limitation consider the ion energy curves obtained near thruster centerline at 0.5 m radius (see Figure 5-3). The peak ion current recorded at this point is approximately 1×10^{-14} A. In energy analysis mode this current was nearly steady state and was therefore easily measured using the high-gain CEM and picoammeter. However, on an atomic level, this current represents a flux of only about 62,000 singly charged ions per second. The gate pulse durations utilized in TOF mode were on the order of 3 μ sec (see Figure 4-10), therefore a single gate opening admits, on the average, approximately 0.2 ions toward the CEM. Thus it required 5 gate opening/closing sequences to obtain a single ion for current measurement. Measurement of a meaningful TOF current spectra required the CEM output current waveform to be averaged over a large number of gate opening and closing sequences (up to 10,000) repeated over a fast duty cycle.

With the low-current limitation driving the TOF signal acquisition it was only possible to obtain mass spectra for points very near the thruster centerline at 0.5-m radius. The point at 5 degrees off thrust axis was chosen for species evaluation. The spectra reported at this location represent a signal that was waveform averaged by the digitizing oscilloscope over 10,000 acquisitions with a duty cycle of approximately 5 kHz. For all values of ion voltage analyzed Figure

4-10 was used to determine the proper gate pulse duration, t_{gate} . As an additional verification that the ion current peaks were transmitted at full intensity representative of the species density the gate pulse duration was varied while the heaviest species peak was monitored to ensure that the peak height was not affected by increasing t_{gate} .

6.2. Measurements in an SPT-100

As a demonstration of the data interpretation principles for the TOF system Figure 6-1 shows a typical TOF spectra obtained for a 45-degree analyzer ion pass voltage of 280 V at a position of 0.5 m radius and 5 degrees off axis.

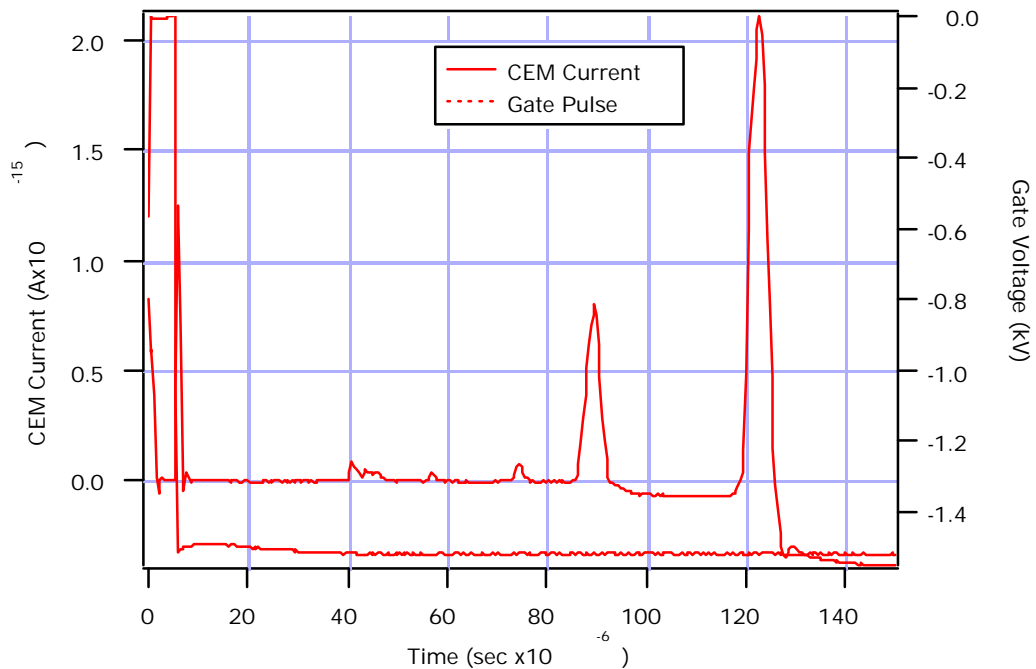


Figure 6-1. Typical TOF spectra for 280 V ions at 0.5 m radius from the SPT-100 for the point 5 degrees off thruster axis. The dashed line represents the beam gate potential and corresponds to the right axis. The solid line reflects the CEM output current, which is scaled on the left axis.

The potential difference across the gate electrodes was maintained at 1.5 kV nominally. At time $t = 0$ this potential difference was removed with a rise time of 40 nsec, opening the ion gate for a time $t_{\text{gate}} = 5 \mu\text{sec}$. This high-voltage transient induced “shot noise” into the facility ground plane which appeared as a noise burst in the CEM amplifier circuitry; this noise rapidly decayed after the pulse returning to a zero-current baseline. The transient current peaks appearing in the CEM output signal represent the arrival of different ion species at the detector. For example, from Eqn. 4-13 for 280 V ions, singly ionized xenon with $M_i/q_i = 131 \text{ amu}$ would take 120 μsec to travel the 2.35 m path and arrive at the detector; this species is seen as the dominant peak. Doubly ionized xenon has $M_i/q_i = 65.5$ and therefore corresponds to the peak seen at $t = 85 \mu\text{sec}$. Since the spectrometer was operated such that $t_{\text{gate}} \gg t_d$ the current peaks have a width very close to t_{gate} . The conversion between time and amu can be performed yielding a mass spectra as shown in Figure 6-2. In this figure the baseline offset displayed after an intense current peak was due to pre-amplifier undershoot.

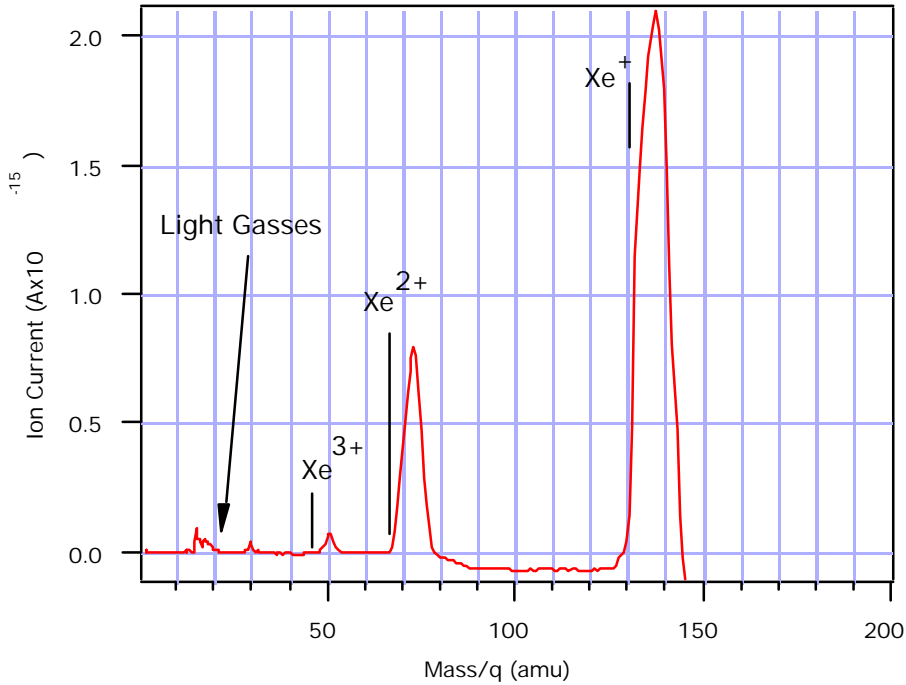


Figure 6-2. Typical mass spectra for 260 V ions at 0.5 m radius 5 degrees off thrust axis.

This mass spectra shows the first three ionization states of the propellant, xenon, along with a small population of light gasses with amu less than 30. Many of the characteristics illustrated in this spectra are typical of all data points. As a result of the quadratic conversion between arrival time and species mass the heavier mass peaks, although equal width in time, are wider in terms of amu than the lighter masses. Although the peak widths are on the order of 10 amu, this width does not impose any difficulty with mass identification or propellant ions: the leading (left) edge of the mass peak marks the arrival time of the species and, therefore, the species mass.

In an attempt to better identify the light gasses evidenced in Figure 6-2 the gate pulse was narrowed and the oscilloscope was configured to obtain better resolution for these minor species. The resultant minor species spectra is shown in Figure 6-3.

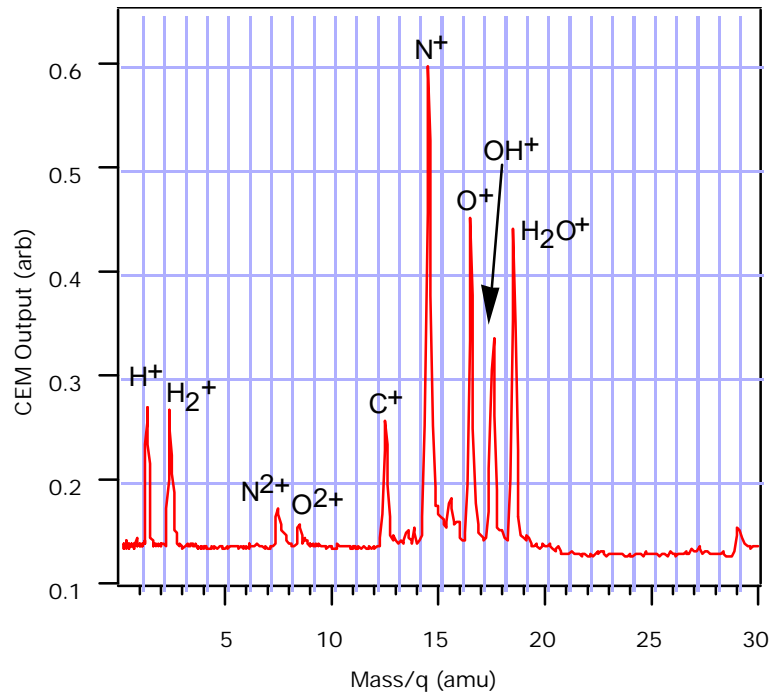


Figure 6-3. Minor species identification for 260 V ions at 0.5 m from the SPT-100 for the point 5 degrees off thrust axis.

Through the use of a very narrow gate pulse this spectra allows excellent species identification for the light gasses. However, the extremely short t_{gate} necessary to obtain this degree of mass resolution was insufficient to transmit these peaks at full intensity; therefore no quantitative assessment based on current peak height was possible.

Based on the problems involved with deriving quantitative information for light gas species it was decided to limit all quantitative analysis to the

ionization states of the heavy propellant, xenon. Thus, mass spectra were obtained at the fixed position of 0.5 m, 5 degrees, as a function of ion voltage with the gate pulse duration sufficient to resolve the ionization states of xenon with full transmission of current peaks. This was accomplished by using the 45-degree analyzer to define the pass voltage and taking a TOF mass spectra for only ions with this voltage. In order to avoid possible confusion it is emphasized that the thruster operation parameters of 300 V applied discharge at 4.5 A were not changed during testing; the voltages indicated for the TOF spectra correspond to the ion energy/q being analyzed in the MBMS for the fixed thruster discharge. Figure 6-4 illustrates the mass spectra obtained for ions with voltages of 180, 280, and 380 V.

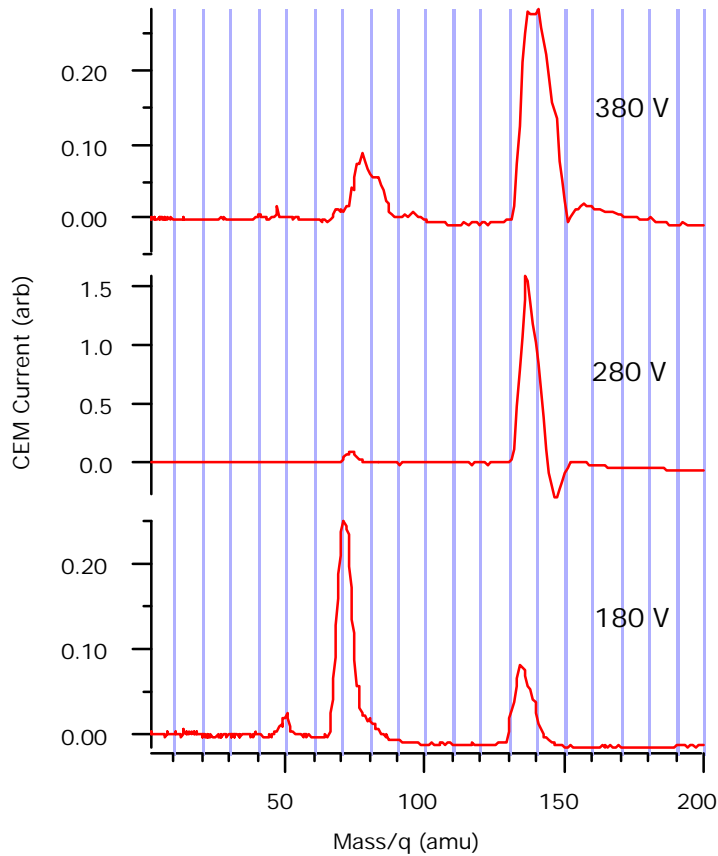


Figure 6-4. Mass spectra for evaluation of xenon ionization states for ions with 180, 280, and 380 V acceleration in the SPT-100 at 0.5 m radius, 5 degrees off thrust axis.

It should be noted that in Figure 6-4 no attempt was made to obtain narrow peaks of high mass resolution; on the contrary, the gate pulse duration was set excessively long in order to ensure the full transmission of the ion current pulses such that the peak height indicated a true measure of ion density fraction.

6.3. Discussion of Mass Spectral Measurements

6.3.1. Minor Species Analysis

The spectra obtained for identification of the minor species, shown in Figure 6-3, shows results consistent with previous investigations. In an emission spectroscopic study Manzella documented clear evidence of the ingestion and ionization of background gas from the vacuum facility within the SPT-100 discharge.²⁹ Due to facility pumping imperfections a trace amount of parasitic background gas exists within the chamber during testing. This gas consists mainly of atmospheric components, i.e. nitrogen and oxygen, with a disproportionate amount of hydrogen and water vapor owing to pumping difficulties with these gasses. The neutral background gas diffuses into the thruster discharge chamber where it is ionized and accelerated back out with the propellant ions. Manzella estimated a quantity of entrained background ions equivalent to 2% of the main propellant flow.

The minority species evaluation reported here supports the finding of ingested facility gasses. Due to the molecular “cracking” signature of the water molecule, electron impact ionization of this species produces dissociated peaks at $M/q = 18$ (H_2O^+), 17 (OH^+), and 1 (H^+). Likewise, an electron impact ionization reaction involving molecular nitrogen and oxygen would most likely produce atomic ions: the reason for this is that the bond energy of the diatom (5 eV for O_2 and 9 eV for N_2) is much less than the ionization potential of the molecule (12 eV for O_2 and 15.6 eV for N_2).⁵³ Thus electron impacts are much more likely to

dissociate the diatom into constituent neutral atoms (which are subsequently ionized) than direct ionization of the molecule. The existence of singly ionized carbon in the plume signature arises from facility effects, as well. In order to prevent material damage to the vacuum chamber walls immediately behind the MBMS inlet skimmer due to impacting high-energy ions these surfaces were extensively coated with low-sputter-yield flexible graphite sheets. Evidence of substantial ablative sputtering of the graphite was apparent as a thin gray film deposited on metallic facility surfaces during post-test inspections and re-configurations; this graphite is the likely source of the $M/q = 12$ signature in the minority spectrum.

It is important to note that the spectroscopic study by Manzella found no evidence of singly ionized nitrogen in the emission spectra, although clear evidence of N_2^+ was documented. This is contrary to the mass spectra obtained in this study showing a substantial peak at $M/q = 14$ with a negligible signature at $M/q = 28$. There are two possible explanations for this disagreement: (1) the facility background pressure in the Manzella study was an order of magnitude lower than the pressure in the study reported here possibly causing trace amounts of N^+ to be below the optical detection limit; and (2) the gate pulse duration utilized to obtain the minority spectra reported here may have too short to permit the heavy $M/q = 28$ ion to successfully be detected, while allowing the lighter N^+ ion to pass through the MBMS.

6.3.2. Propellant Ionization

Analysis of the propellant ionization state was accomplished by recording individual mass spectra for ion voltages ranging from 100 V up to 650 V at 10 V increments. Such a data set enabled the ionization fraction of each xenon species to be calculated as a function of ion voltage. The ion species current peaks are related to their respective ion densities through the value of ion charge state: the current output of the CEM for a given ion voltage and charge state ion is

Eqn. 6-1
$$I_i(V_i, q_i) = G_{\text{CEM}} e n_i u_i(V_i, q_i)$$

noting that although u_i is a function of q_i , the CEM acts as an ion counter rather than a charge counter so that I_i is not directly proportional to q_i (see Section 4.3.1). Expressing the ion velocity in terms of ion charge state and voltage yields

Eqn. 6-2
$$I_i(V_i, q_i) = G_{\text{CEM}} e n_i \sqrt{\frac{2q_i e V_i}{m_i}}.$$

Thus for a given species current peak the density and the current are related according to

Eqn. 6-3
$$n_i(q_i) \propto \frac{I_i(q_i)}{\sqrt{q_i}}.$$

Defining the number density fraction of Xe^{n+} having energy/ $q = V_i$ as $\alpha_n(V_i)$ yields

Eqn. 6-4

$$a_n(V_i) = \frac{I(V_i, n) / \sqrt{n}}{\sum_q I(V_i, q) / \sqrt{q}}$$

In the analysis of the propellant mass spectra xenon ions up to $q = 3$ were readily measured, with no conclusive evidence of Xe^{4+} exhibited in the spectra; complicating the search for Xe^{4+} was the fact that the mass-per-charge of this ion is 32.2 amu, which is very close to the 32 amu attributable to singly ionized O_2 present due to parasitic facility gasses. Therefore the mass spectra were inconclusive in identifying quadruply ionized xenon. The values of α_n were calculated from an assembly of mass spectra obtained at 10 V intervals of ion voltage (such as those shown in Figure 6-4 for ion voltages of 180, 280, and 380 V); the results are compiled as Figure 6-5, which shows a plot of the number density fraction of the first three ionization states of xenon plotted as a function of ion voltage. Compared with this plot is the total (species independent) ion voltage distribution function.

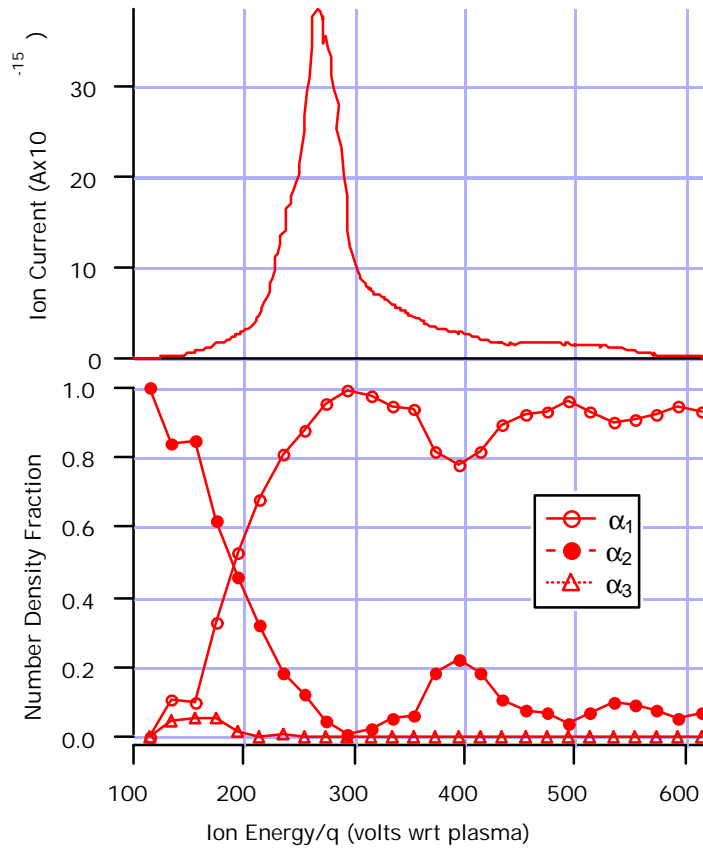


Figure 6-5. Number density fractions of Xe⁺, Xe²⁺, and Xe³⁺ as a function of ion energy at 0.5 m radius and 5 degrees off thrust axis in the SPT-100. Also shown in the top curve is the value of total ion current as a function of ion voltage for comparison of total density.

Figure 6-5 indicates that the majority of the plume ions have undergone accelerations through approximately 270 V; of these ions almost 90% are singly ionized. Although the ion density decreases for voltages less than 270 V, a greater fraction of these low-voltage ions are multiply charged with nearly 100% of the 110 V ions consisting of Xe²⁺. The number fraction of Xe³⁺ peaks at about 6% of the ions having voltages of 150 V. For voltages greater than the most probable voltage the fraction of multiply charged ions experiences a slight increase over the composition at 270 V.

The total number density fractions for all ions in the plume can be obtained by integrating the voltage-dependent flow fractions over all voltages. Denoting the overall fraction of ions with charge $q_i = n+$ as Φ_n ,

Eqn. 6-5

$$\Phi_n = \frac{\int_0^{\infty} a_n(V)I(V)dV}{\int_0^{\infty} I(V)dV}.$$

The total flow fractions computed from the MBMS data according to Eqn. 6-5 and the data of Figure 6-5 are compared with the fractions calculated by Manzella using an optical emission spectroscopic technique at the thruster exit plane; this comparison is shown in Table 6-1.

Species	Φ_n from MBMS	Φ_n from Manzella²⁹
Xe ⁺	0.888	0.89
Xe ²⁺	0.110	0.119
Xe ³⁺	0.002	(not measured)

Table 6-1. Comparison between MBMS-measured ionization fractions with values derived from Manzella's study using optical emission spectroscopy. Uncertainty in MBMS values is approximately 5%.

The agreement between the two techniques demonstrated in the table is excellent, exhibiting only negligible differences. Additionally, the MBMS system provided the first ever documentation of the existence of Xe³⁺ within the Hall thruster plume.

Further insight into the propellant ionization and acceleration mechanism is possible through analysis of the TOF spectra. As discussed earlier and evidenced by Eqn. 4-9 the existence of multiple ion species presents considerable difficulty in determining the ion energy distribution function using a method insensitive to ion charge state. However, by compiling the species current peak heights in the TOF spectra as a function of ion voltage it is possible to construct true ion energy distribution functions independently for each ion species in the flow. These data are shown in Figure 6-6.

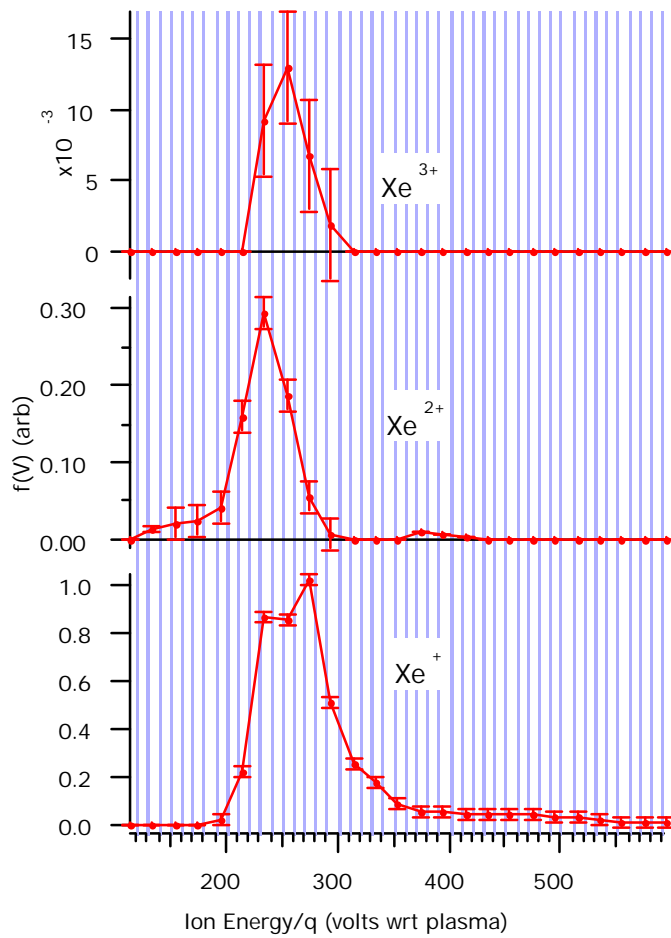


Figure 6-6. The ion voltage distribution function for each propellant ionization species in the SPT-100 at 0.5 m radius and 5 degrees off thrust axis.

The species-dependent energy distributions display some subtle, yet remarkable features. The highest most-probable voltage is displayed by Xe⁺, with $V_m = 274$ V, with the peaks in the multiple ions at lower voltages. This finding is consistent with the ionization and acceleration processes within the thruster discharge chamber. It has been widely documented that the electron temperature within the discharge chamber attains a maximum in the region of highest magnetic field strength, which occurs very near the thruster exit plane.^{11,31} Indeed, this behavior was displayed in the model by Baranov; Figure 6-7 shows the trends in neutral density and electric field that were previously shown as Figure 5-27 with the addition of electron temperature.

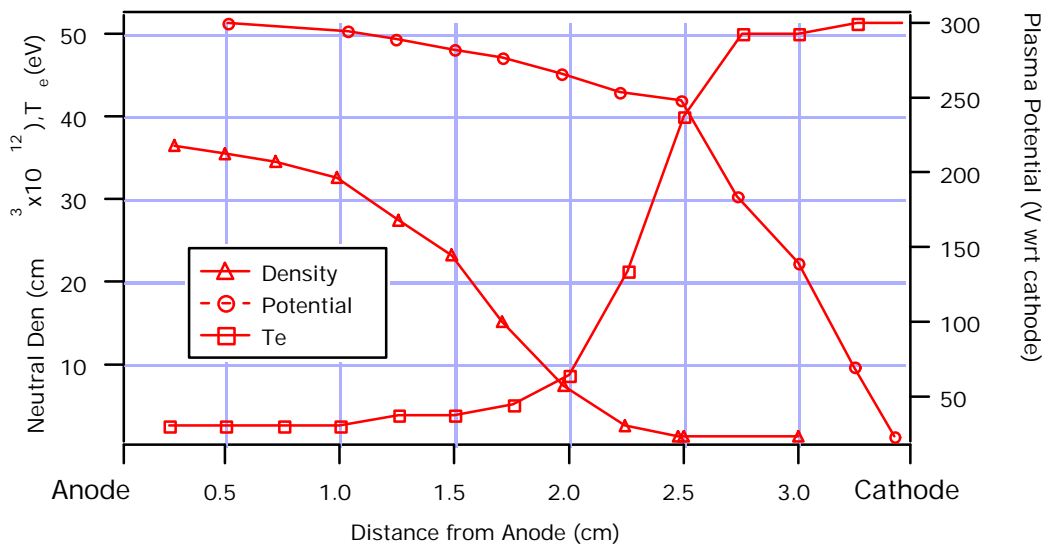


Figure 6-7. Results of Baranov model³¹ of plasma parameters in Hall thruster discharge chamber including neutral atom density (left axis), electron temperature (left axis), and plasma potential (right axis).

The energy required for the first ionization of neutral xenon is 12.1 eV, while the second ionization potential is 21.21 eV.⁵³ Therefore, as the neutral atoms travel from the anode towards the exit plane the initial electron collisions will have sufficient energy for single ionization, but insufficient energy to form a multiple ion; formation of the multiply charged ions will occur further downstream where the electrons are hotter and, as a result of the distribution of plasma potential, experience less accelerating voltage. The ionization potential of Xe³⁺ is 32.1 eV.⁵³ This would imply that the most-probable voltage of the triple ion should be less than that of the double. However, Figure 6-6 shows the distribution peak for the triple ion to be 255 V while the double exhibits a peak at 235 V. This behavior is contrary to the ionization and acceleration mechanism described above. The reason for this anomaly is believed to stem from uncertainty in determining the peak heights corresponding to Xe³⁺ in the TOF spectra compiled as Figure 6-6: since the triply charged xenon ion represented only 0.2 % of the total mass flow the current peaks were extremely small and, occasionally difficult to resolve in the TOF spectra. Combined with the 20 V resolution obtained by acquiring TOF spectra in 20 V intervals, this uncertainty could be responsible for a 20 V uncertainty in most-probable voltage location for the f(V) curve. Due to the larger, more easily resolved current peaks associated with Xe⁺ and Xe²⁺ TOF signatures, the uncertainty in most-probable voltage location for these species is estimated at roughly 10 V.

Consistent with the species ionization fraction analysis, Figure 6-6 demonstrates that almost all of the ions with voltages less than 200 V are doubly charged. The high-voltage spectra are equally intriguing. The applied discharge voltage between thruster anode and cathode was 300 V, while the cathode was allowed to float with respect to plasma; measurements showed the cathode potential to be approximately 20 V below plasma potential. This equates to a maximum available acceleration potential of 280 V for all ions. The species voltage spectra show that there exists a small tail of Xe^{2+} with voltages greater than 280 V along with a small, discrete population centered around 350 to 360 V. The Xe^+ distribution displays a long, low magnitude tail of ions with voltages greater than 280 V. It is noteworthy that the Xe^{3+} distribution shows no evidence of ions with voltages greater than 280 V. An explanation for the existence of these high-voltage “tails” and “bumps” will be the subject of Chapter 7.

7. PLUME ION COLLISION ANALYSIS

Interaction between the heavy propellant atoms in the flow has been difficult to quantify experimentally. Many of the cross-sections required to predict the extent of collisional events are not available for the ion-ion and ion-neutral reactions important in the Hall thruster, i.e. xenon gas at impact energies on the order of 100-300 eV. However, evidence of collisions can be observed as distinct signatures in the mass and energy spectra of the exhaust constituents. This chapter provides a discussion of possible collisions and their relative probability in the Hall thruster plume, along with an analysis and discussion of possible collision evidence found in this study.

7.1. *Overview of Collision Processes*

There are a number of possible collisions that may occur between propellant atoms, both ionized and neutral, within the Hall thruster plasma. Each reaction produces products which may or may not be directly measurable. Identifying the most probable collision reactions aids in the search for their products.

7.1.1. Ion Collision Probabilities

The two types of collisions which can occur between heavy propellant species in the plasma are (1) elastic collisions in which the total kinetic energy is conserved and (2) inelastic collisions involving some transfer of kinetic energy to an alternate mode. In an elastic collision momentum is transferred between the reactants resulting in products with changed velocities.

Possible inelastic collisions occurring between heavy particles within the Hall thruster plasma that would significantly affect the ion kinetic energy are ionizing collisions and charge-exchange (CE) collisions. Ionizing collisions require the ejection of an electron from one reactant due to the impact of another reactant. Although this type of collision-induced ionization is very efficient for electron-atom collisions at moderate impact energies, the two-atom collision requires a large amount of energy between the heavy species to remove an electron. On the contrary, CE collisions are most efficient when the reactant atoms have nearly equal velocities such that their interparticle energy approaches zero. This reaction involves a quantum-mechanical transfer of a bound electron from one atom to the other with no appreciable transfer of momentum; the electron transfer is most likely to occur when the reactant interaction time is long, therefore the CE cross section decreases with increasing interparticle energy. The probability of each of these reactions as a function of relative atomic impact energy is shown as Figure 7-1. It is apparent that the

dominant form of inelastic collision in the Hall thruster plume, which contains atoms with inter-particle energies on the order of 100-500 eV, is the CE reaction.

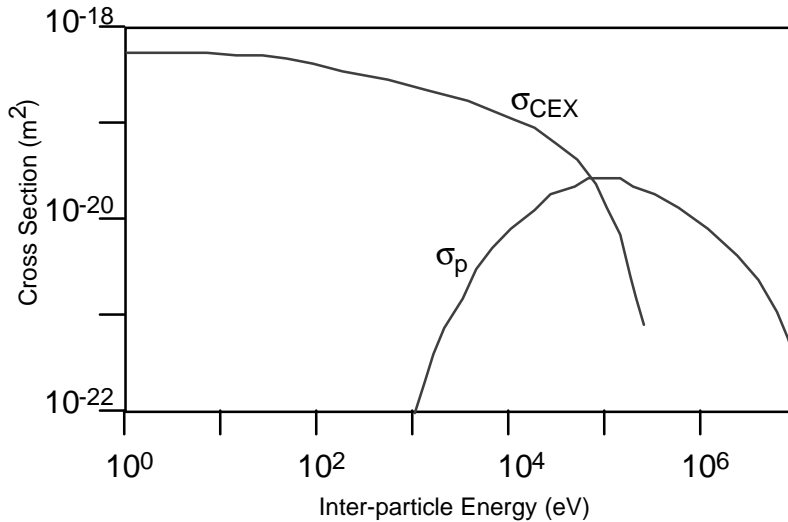


Figure 7-1. A comparison of the relative probabilities of charge-exchange collisions, σ_{CE} , to atomic ionization collisions, σ_p , as a function of the energy between colliding particles.³⁶

It is further instructive to compare the dominant inelastic CE collision with the probability of elastic collisions within the plasma. In the data compiled by Brown this comparison is made in terms of the probability of collision and shown as Figure 7-2.⁵⁴ For the energy range of the Hall thruster plasma the probability of CE collision is approximately an order of magnitude greater than that for an elastic collision.

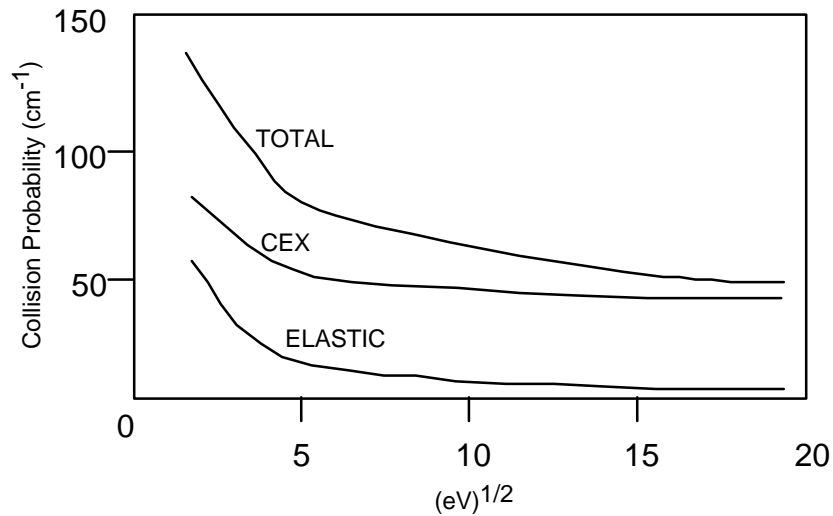


Figure 7-2. Comparison of total, CE, and elastic collision probabilities as a function of inter-particle energy.⁵⁴

Based on these evaluations it seems that the most common collision within the plasma will be CE collisions, with elastic collisions accounting for approximately 1 in 10 total collisions. Numerical cross sections are available for singly charged ion-neutral CE (see Eqn. 3-6) as well as Xe⁺-Xe⁺ elastic collisions. However, cross sections involving multiply charged xenon ions have not been found in the literature; these reactions include single- and double-electron CE as well as elastic momentum transfer collisions. Therefore an evaluation of these collisions must rely on alternate means of detecting the collision evidence.

7.1.2. Elastic Collision Signatures

Knowledge of species densities along with all possible collision cross sections would permit a detailed evaluation of collision probabilities and

unambiguous determination of dominant collision processes. Unfortunately, many cross sections relevant to this study are unavailable. The collision dynamics within the plasma can be evaluated, though, by searching for evidence of their occurrence within the mass and energy spectra. In order to provide a framework within which the collision signatures can be evaluated this section discusses the effect of the two types of collisions expected on the overall energy and mass spectra.

For the sake of simplicity, the elastic collisions are approximated as hard-sphere interactions. The differential cross section for a hard-sphere collision is $d_m^2/4$, where d_m is the effective hard-sphere diameter. Considering only binary collisions and denoting the collision scattering angle as θ , the fact that the differential cross section is constant stipulates that all values of θ are equally possible in a hard-sphere collision. Therefore hard-sphere collisions produce atoms with post-collision trajectories randomly distributed over all directions.

The energy lost by a particle of “type 1” due to an elastic collision with a particle of “type 2” is a function of the scattering angle, θ according to

Eqn. 7-1
$$\Delta E = E_{\text{coll}} \frac{m_1}{m_2} \sin^2 \frac{\theta}{2}$$

where m_1 and m_2 denote the particle masses and E_{coll} is the energy of the collision. The interactions of relevance to this study involve particles of identical masses, such that $m_1 = m_2$. Using E_1 and E_2 to represent the pre-collision kinetic energies, and E_1' and E_2' representing the post-collision energies yields

Eqn. 7-2
$$E_1' = E_1 + (E_2 - E_1) \sin^2 \frac{\theta}{2}.$$

The effects of such an interaction can be easily envisioned by analyzing the extreme cases: for glancing collisions in which $\theta = 0$, $E_1' = E_1$ and the particles are unaffected; for head-on collisions in which $\theta = 180$ degrees (complete backscattering) $E_1' = E_2$ and therefore $E_2' = E_1$. It follows that since the collisions will occur with equal probability for all values of θ between 0 degrees and 180 degrees the post-collision energy of particles "1" will be equally distributed between E_1 and E_2 . Similarly, since the collisions are elastic particles "2" will be equally distributed over the same range of post-collision energies.

The effect of an elastic momentum transfer collision on the energy distribution is most easily conceived through the analysis of the most simple flow: collisions between two mono-energetic species. Figure 7-3 demonstrates the evolution of the energy distribution function for the interaction between such particles. The energy distribution of the entire two-species flow is shown at the far left with mono-energetic particles of species 1 and 2. Allowing a fraction of these particles to undergo elastic collisions produces the post-collision energy distributions of each species shown to the right. As evidenced by this figure the momentum transfer collision produces "tails" on the original pre-collision distributions filling the energy regime between the two species. The relative amplitude of these tails would be determined by the species density and

collision cross section; in general the height of these tails will be much less than the height of the original pre-collision distribution.

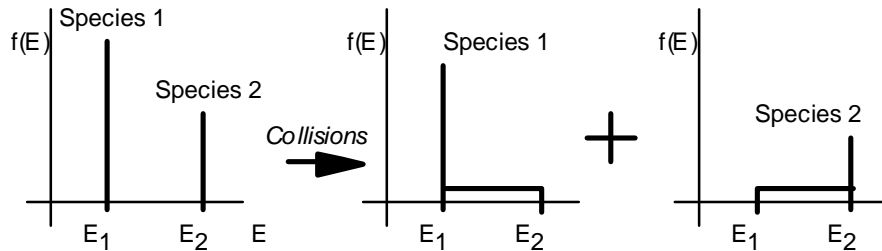


Figure 7-3. Illustration of tail formation mechanism in the energy distribution through elastic collisions between two mono-energetic species.

Interactions between two species having finite distributions of energy is more difficult to envision than the pedagogical case between mono-energetic species. For example, consider the interaction between two species with gaussian energy distributions as shown in Figure 7-4.

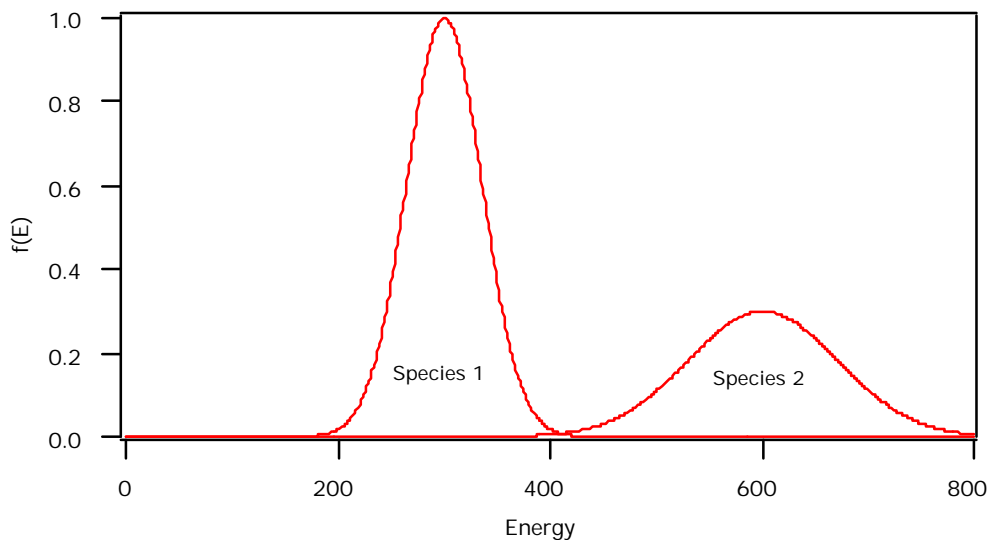


Figure 7-4. Pre-collision energy of a two-species flow having separate gaussian distributions.

A particle 1 with energy E_1 that has collided with a particle 2 with energy E_2 will have a post-collision energy somewhere between E_1 and E_2 ; therefore E_1' must be greater than E_1 (primed quantities denote post-collision values). Since a collision product of species 1 having energy E_1' must have originated as a particle with pre-collision energy $E_1 < E_1'$, the probability of finding a post-collision species 1 particle with energy E_1' is equal to the probability of finding a pre-collision species 1 particle with $E_1 < E_1'$. For example, in Figure 7-4 the probability of finding a post-collision species 1 particle with an energy of 400 is fairly large: this particle could have come from anywhere within the pre-collision gaussian distribution of species 1. However, the probability of finding a post-collision species 1 with an energy of 250 is very small, since this particle must have originated from the small portion of the pre-collision distribution that lies to the left of 250. Denoting the pre-collision energy distribution of species 1 particles as $f_1(E)$ and the probability of finding a post-collision species 1 particle with energy E_1' as $P_1'(E_1')$ gives

Eqn. 7-3
$$P_1'(E_1') = \int_0^{E_1'} f_1(e) de.$$

As an illustration of this Figure 7-5 shows the pre-collision energy distribution of species 1 particles from Figure 7-4 along with the probability of post-collision species 1 energy calculated according to Eqn. 7-3.

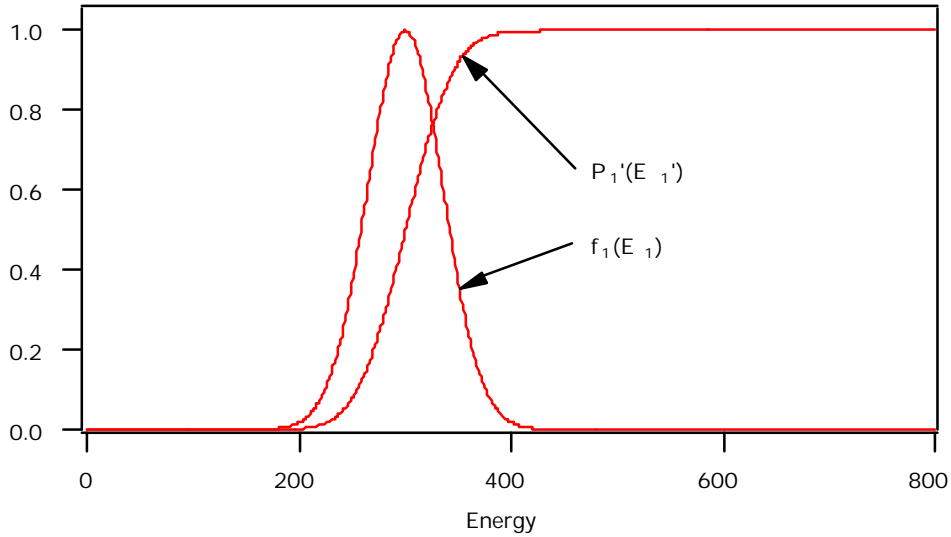


Figure 7-5. Pre-collision energy distribution of species 1 shown with the probability of post-collision velocities for species 1 with a higher energy collision partner.

Figure 7-5 illustrates the effect of the shape of the pre-collision energy distribution on the post-collision energy for particles 1 colliding with a particle 2 of higher energy. However, the final shape of the post-collision energy distribution will also be affected by the distribution of particle 2 energies. Since E_1' must be less than E_2 , a post-collision species 1 particle with energy E_1' must have collided with a species 2 particle with $E_2 > E_1'$. Therefore, analogous to the previous discussion, the probability of finding a post-collision species 1 particle with an energy E_1' is equal to the probability of finding a pre-collision species 2 particle with energy greater than E_1' . Denoting the pre-collision energy distribution of species 2 as $f_2(E)$ yields

Eqn. 7-4
$$P_1'(E_1') = 1 - \int_0^{E_1'} f_2(e) de .$$

The constraint imposed by Eqn. 7-4 is illustrated in Figure 7-6. With these principles it is possible to determine the shape of the resultant energy distribution: the energy distribution of the post-collision species 1 products due to a collision with species 2 is equal to the joint probability that (1) the products will have energy greater than their pre-collision value and (2) the products will have energy less than their species 2 collision partner. Utilizing Eqn. 7-3 and Eqn. 7-4 and denoting the post-collision energy distribution of species 1 as $f_1'(E_1')$:

Eqn. 7-5
$$f_1'(E_1') = \int_0^{E_1'} f_1(e) de \cdot \left[1 - \int_0^{E_1'} f_2(e) de \right].$$

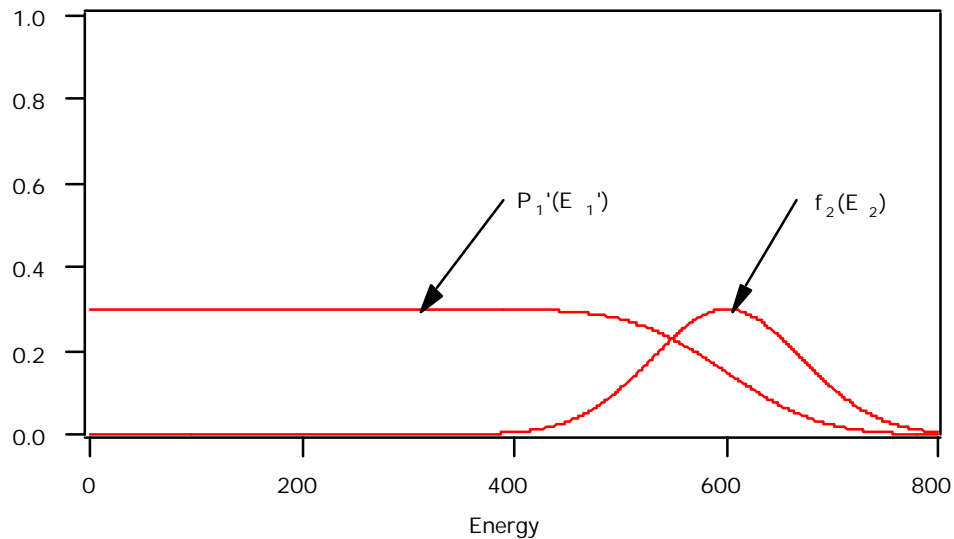


Figure 7-6. Pre-collision energy distribution of species 2 particles shown along with the probability of finding a species 1 particle with post-collision energy of E_1' .

Eqn. 7-5 defines the shape of the energy distribution for the collision products of species 1. Since the collisions are elastic, the exact same mechanism populates the post-collision energy distribution of species 2, therefore $f_1' = f_2'$. Figure 7-7 shows the pre-collision distributions of species 1 and 2 along with the distribution of the post-collision products. The amplitude of the product distribution, which is determined by the cross section, has been chosen arbitrarily in this figure.

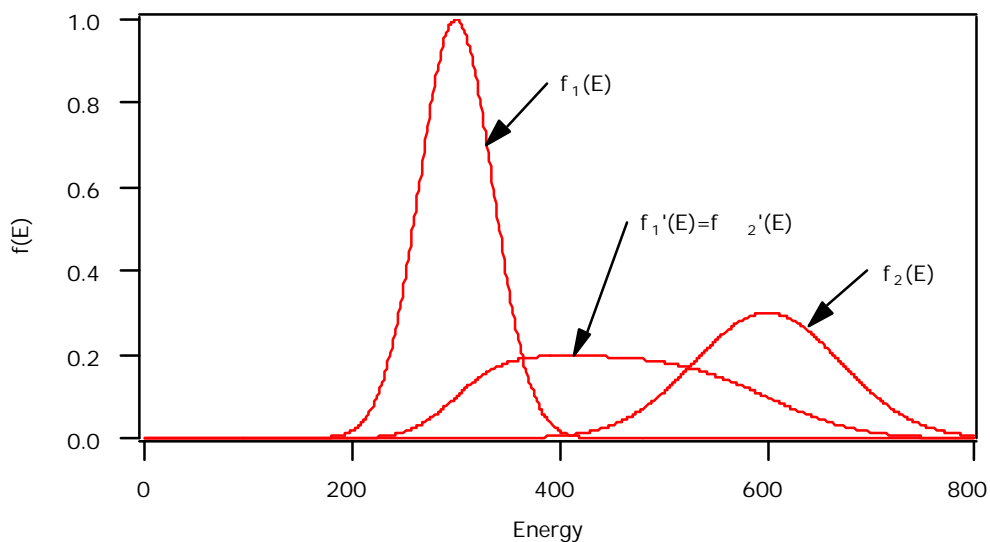


Figure 7-7. Graphical representation of the pre-collision energy distribution of the reactants and the energy distribution of the post-collision products of elastic collisions.

Finally, the resultant energy distribution of all species 1 particles due to elastic collisions with species 2 is the sum of f_1' and the distribution of those species 1 particles that did not suffer a collision (f_1 attenuated for the loss of some particles). Figure 7-8 shows the resulting energy distributions of species 1

and species 2 due to elastic collisions. It is also interesting to consider the pedagogical case of mono-energetic distributions discussed earlier: using Dirac functions to represent the pre-collision distributions as $\delta(E-E_1)$ and $\delta(E-E_2)$ Eqn. 7-5 confirms mathematically that the resultant post-collision distribution is the product of two Heaviside step functions, $H(E-E_1)H(E_2-E)$, as the simplistic conceptual analysis concluded.

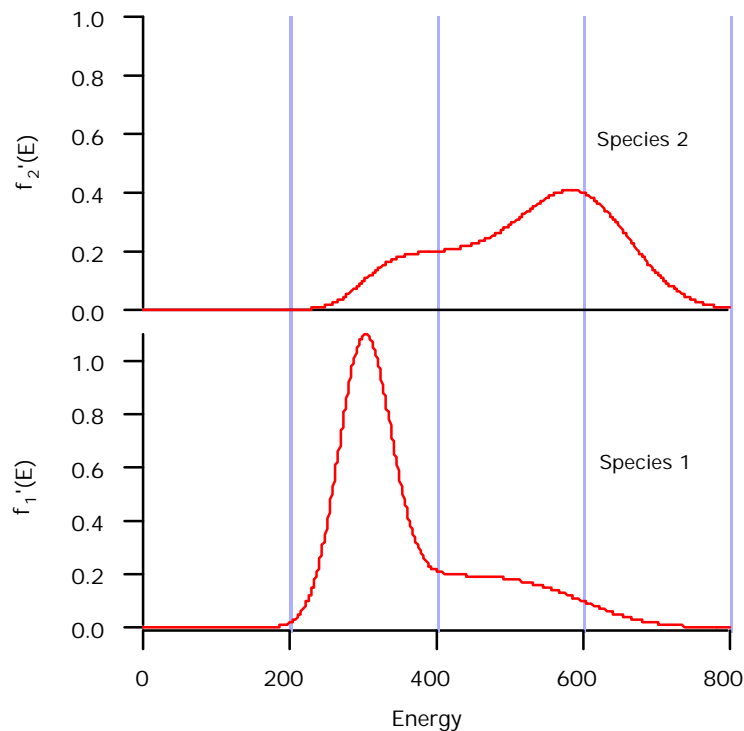


Figure 7-8. Illustration of “tail” formation on pre-collision energy distribution due to elastic collisions.

In the preceding discussion of elastic collisions the magnitude of the collisional interaction, which is defined by the collision cross section, was

unavailable and was assumed arbitrarily for instructive purposes. Fortunately many of the characteristics of the post-collision energy distribution are displayed regardless of the value of the cross section. Indeed, two traits involving the energy distribution function are fundamental: (1) the post-collision distribution for species undergoing elastic collisions is distinguished by a slowly decaying “tail” extending the species 1 distribution towards higher energy and decaying to zero at the maximum pre-collision energy of species 2 (with a similar tail extending to lower energies for species 2); (2) the “tail” decays monotonically and no additional “bumps” (local maxima) arise in the reactant post-collision energy distribution as a result of elastic collisions. Specifically, the post-collision distribution of species 1 does not retain any of the species 2 pre-collision distribution shape (i.e. there is no bump in f_1' corresponding to the most probable energy of f_2).

The elastic collision signatures have been discussed in terms of particle energy, while much of the data reported in this study involves the voltage, or energy/ q distribution. The method of detecting the collision signatures in a voltage distribution follows the same principles with minor considerations; in fact, the initial pre-collision distributions illustrated in Figure 7-4 were constructed with a discussion of the voltage analysis in mind. Consider an ionization and acceleration process within the Hall thruster that produces ions with $q = 1$ according to the energy distribution of species 1 in Figure 7-4. Since the ions are singly charged, the energy axis in the figure is equivalent to the

voltage axis ($V = E/q = E$). At the same time, assume that the thruster produces ions with $q = 2$ in the same physical discharge such that the voltage distribution of the $q = 2$ ions is the same shape as that of the $q = 1$ ions, albeit at a reduced rate such that $f_{q=2} = Af_{q=1}$ where $A < 1$. This voltage distribution is illustrated in Figure 7-9.

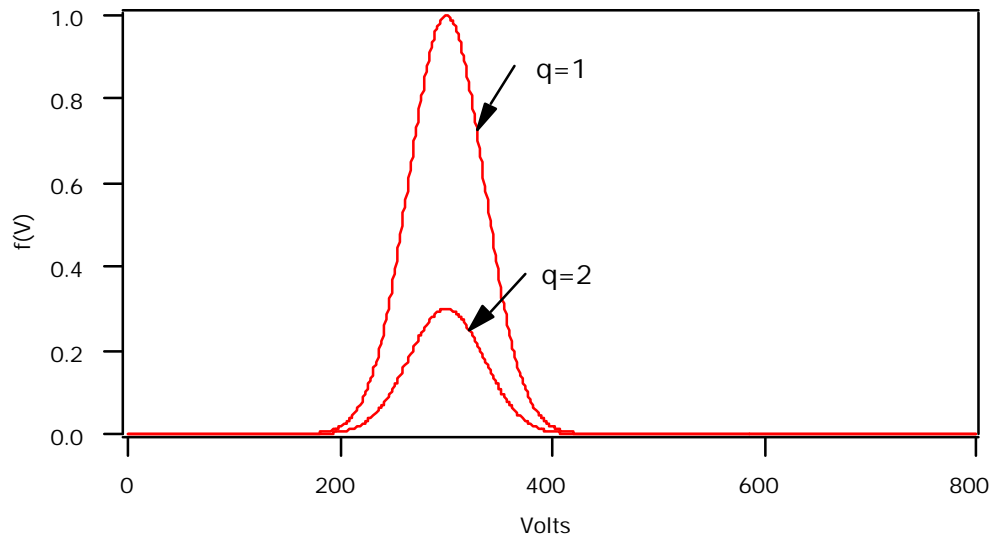


Figure 7-9. Voltage distributions of singly and doubly charged ions formed by identical processes.

In terms of energy, the $q = 2$ ions will have twice the energy of the $q = 1$ ions, therefore the most probable energy for the $q = 2$ ions will be shifted to a location of twice the peak value for $q = 1$, or 600 eV. In addition to a pure translation, in changing from E/q (volts) to E the $q = 2$ distribution will be broadened by a factor of 2 (e.g. the base of the $q = 2$ voltage distribution extends from 200 to 400 volts, therefore the base of the energy distribution will extend from 400 to 800 eV, or twice the width). Thus the resultant energy distribution equivalent to the

voltage distribution in Figure 7-9 is exactly that of Figure 7-4 with species 2 denoting doubly charged ($q = 2$) ions, species 1 representing singly charged ions, and the horizontal axis in units of eV. The shape used for the species 2 distribution in Figure 7-4 is exactly the same shape as that of the species 1 distribution but shifted and broadened by a factor of two. It follows immediately from this fact, then, that the post-collision energy distributions shown as Figure 7-8 can be transformed into post-collision voltage distributions simply by shifting and narrowing the species 2 distribution by a factor of $1/2$. The resultant measured curve of voltage distribution caused by elastic collisions of singly and doubly charged ions is illustrated in Figure 7-10.

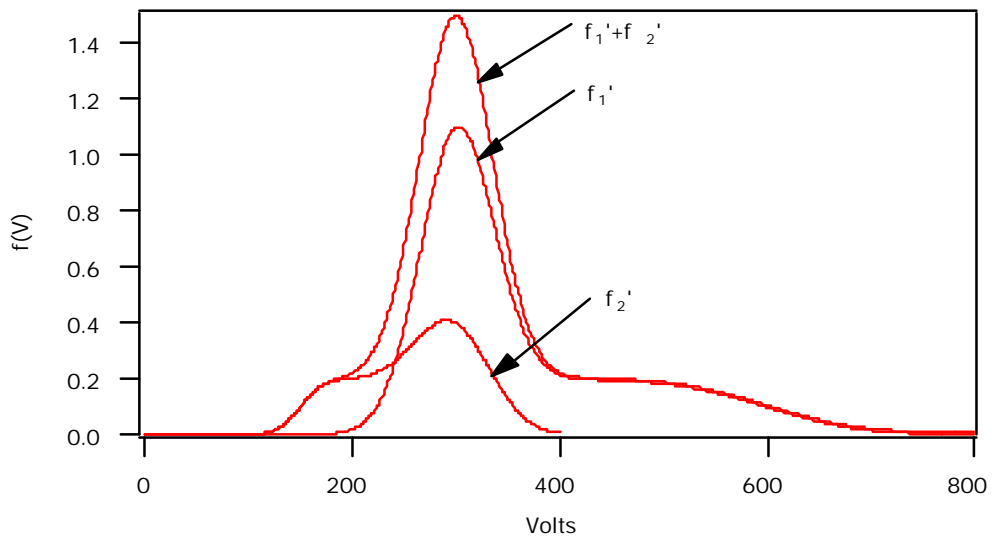


Figure 7-10. Signature of elastic collisions between singly and doubly charged ions as seen in the ion voltage distribution function.

The tell-tale signatures of elastic collisions within the voltage distribution are equivalent to those in the energy distribution: (1) elastic collisions produce a high-voltage “tail” on the singly charged ion voltage distribution that decays to zero at a voltage equal to twice the maximum voltage of the doubly charged ion; (2) elastic collisions produce a low-energy “tail” on the doubly charged ion voltage distribution that decays to zero at a voltage equal to one-half of the minimum voltage of the singly charged ion; and (3) elastic collisions produce tails that decay monotonically such that neither the high- or low-energy tails exhibit “bumps.”

7.1.3. CE Collision Signatures

Consider again the flow composed of species 1 and 2 defined by the equivalent energy and voltage distributions of Figure 7-4 and Figure 7-9 where species 1 has $q = 1$ and species 2 has $q = 2$. The definition of a CE collision is an interaction between two particles during which one or more electrons is transferred with no significant transfer of momentum. When an electron is transferred from a $q = 1$ ion to a $q = 2$ ion the net effect is that the ions “swap” identities: the ion that originated as species 1 with $q = 1$ and energy E_1 is now a species 2 ion with $q = 2$, but with energy still equal to E_1 while the original species 2 ion with $q = 2$ and energy E_2 still has energy E_2 but now has charge $q = 1$ (it is a species 1 ion). Therefore the resultant post-collision energy distributions now appear as indicated in Figure 7-11.

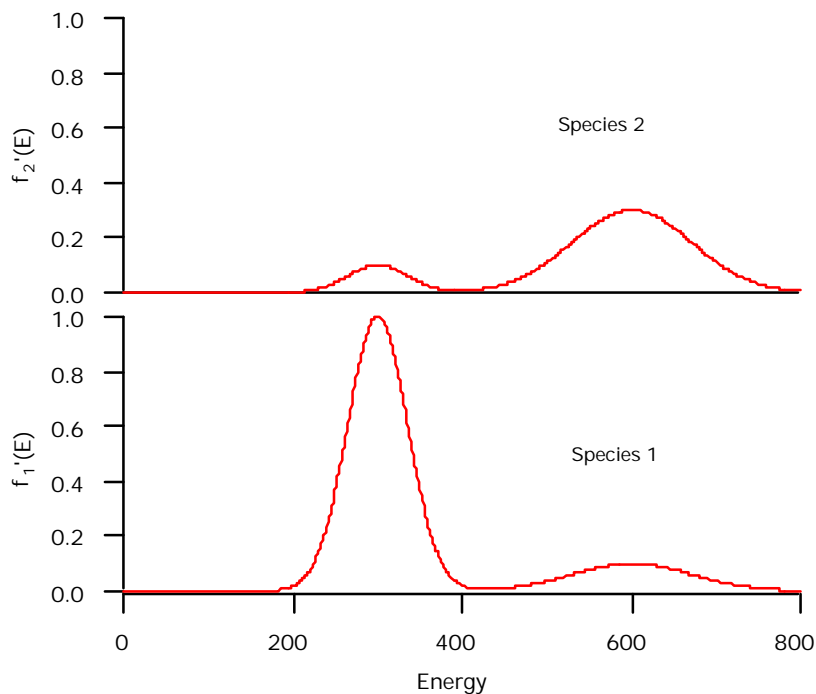


Figure 7-11. Post-CE-collision energy distributions for the interaction of doubly charged ions (species 2) with singly charged ions (species 1) of the same pre-collision voltage distribution.

Thus, rather than producing monotonically decaying “tails” as in elastic collisions, CE collisions produce discrete distributions added on to the pre-collision distribution with “bumps” corresponding to the most probable energy of the collision partner. Indeed, these discrete distributions not only exhibit bumps, instead the shape of the collision partner’s distribution is completely conserved during the CE process (i.e. the “bump” in the tail of species 1 in Figure 7-11 has the same shape as the original pre-collision distribution of species 2).

The CE collision signatures within the voltage distribution can be obtained by scaling the peak energy and width of the $q = 2$ energy distribution

by a factor of 1/2; the resultant voltage distribution of all particles equivalent to the energy distribution of Figure 7-11 is shown as Figure 7-12.

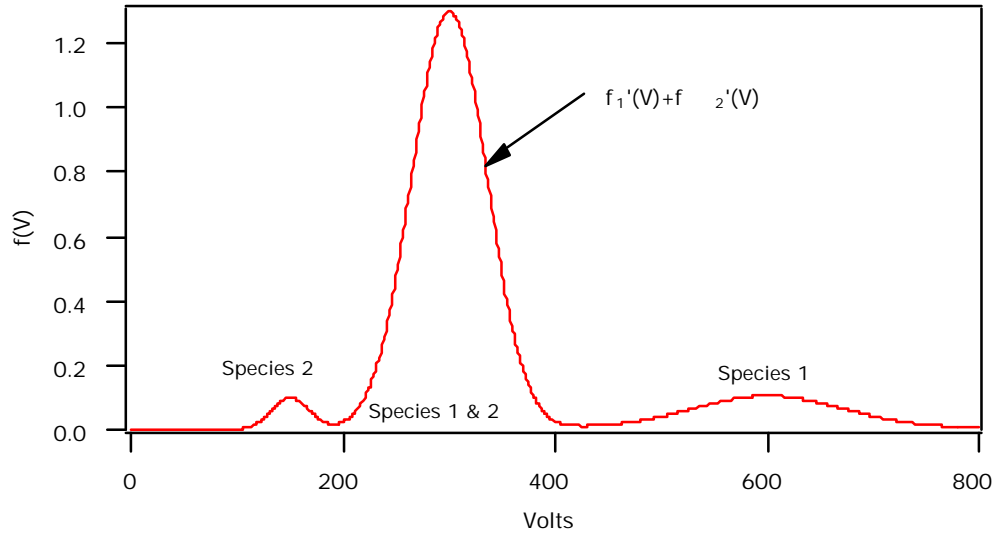


Figure 7-12. Total post-CE-collision voltage distribution function arising from CE collisions between doubly charged ions (species 2) with singly charged ions (species 1).

The analysis of CE collisions between ionic species demonstrates fundamental qualities of the post-collision voltage distribution that can be used as a signature to identify these processes in the data: (1) CE collisions produce tail-like appendages that do not decay monotonically as in the case of elastic collisions; (2) the tails of CE collisions exhibit “bumps” (local maxima) corresponding to the energy distribution of the collision partners; (3) CE collisions completely conserve the shape of the original pre-collision distributions within the bumps of the post-collision tails.

In discussing the effects of both elastic and CE collisions ions with charge $q = 1$ and $q = 2$ were considered. The concepts derived in these analyses can be extended to interactions between ions with different charge states in a straightforward manner. For example, a CE collision involving a two electron transfer between a $q = 3$ ion and a $q = 1$ ion, both with the same voltage $V = E/q$, will produce a $q = 1$ ion with voltage $E/q = 3$ and a $q = 3$ ion with voltage $E/q = 1/3$; the manipulation involved in transferring from an energy to a voltage distribution, then, involves a shifting and narrowing by a factor of $1/3$. The elastic collision analogy for these ions will produce extended tails proportional to the energy difference between the reactants.

In order to easily comprehend the implications of CE reactions it is instructive to consider the Hall thruster plume flow as consisting of two interacting components: (1) high-voltage (on the order of 50-300 V) “beam” ions produced and accelerated within the thruster discharge chamber passing through (2) a “background” gas consisting of very low-energy macroscopically stagnant neutral particles due either to facility pumping limitations or un-ionized propellant. The possible reactions then include collisions between two beam ions and collisions between beam ions and neutrals. Considering all possible reactions between $q = 1, 2,$ and 3 beam ions yields ion products as shown in **Table 7-1** (considering only the formation of ions with $q < 5$) with **Table 7-2** tabulating the possible products of beam ion-neutral collisions. The

MBMS can only detect ions with non-zero voltage, thus the products listed in Table 7-2 are limited to these species.

Reactants at V_b	Ion Products	Electrons transferred
$Xe^{2+} + Xe^+$	$Xe^+ = 2V_b$ with $Xe^{2+} = V_b/2$	1
$Xe^{2+} + Xe^+$	$Xe^{3+} = 2V_b/3$	1
$Xe^{2+} + Xe^+$	$Xe^{3+} = V_b/3$	2
$Xe^{3+} + Xe^+$	$Xe^{2+} = 3V_b/2$ with $Xe^{2+} = V_b/2$	1
$Xe^{3+} + Xe^+$	$Xe^{4+} = 3V_b/4$	1
$Xe^{3+} + Xe^+$	$Xe^+ = 3$ with $Xe^{3+} = V_b/3$	2
$Xe^{3+} + Xe^+$	$Xe^{4+} = V_b/4$	3
$Xe^{3+} + Xe^{2+}$	$Xe^{2+} = 3V_b/2$ with $Xe^{3+} = 2V_b/3$	1
$Xe^{3+} + Xe^{2+}$	$Xe^{4+} = 3V_b/4$ with $Xe^+ = 2V_b$	1
$Xe^{3+} + Xe^{2+}$	$Xe^+ = 3V_b$ with $Xe^{4+} = V_b/2$	2

Table 7-1. Possible reactant and product combinations for CE collisions occurring between two high-energy beam ions, each with voltage V_b .

Reactant ion at V_b with 0 V neutral	Ion products with Energy > 0	Electrons Transferred
$Xe^+ + Xe$	none	N/A
$Xe^{2+} + Xe$	$Xe^+ = 2V_b$	1
$Xe^{3+} + Xe$	$Xe^{2+} = 3V_b/2$	1
$Xe^{3+} + Xe$	$Xe^+ = 3V_b$	2

Table 7-2. Possible reactant-product combinations for the CE collision between a beam ion with voltage V_b and a stagnant background neutral.

7.2. Collision Evidence in SPT-100 Plume

The ion energy distribution functions reported in this study along with previous measurements of ion energy in Hall thrusters have displayed the common feature of a “tail” of ions having voltage greater than that applied to the thruster discharge. Although initially dismissed as an experimental error, this tail has appeared consistently in all probe diagnostics of ion voltage. Data obtained with the MBMS suggested that this tail may be the result of atomic collisions; various potential collision mechanisms to account for this tail are presented in this section.

Initially, consider the near-centerline region of the plume at 0.5 m radius displayed in Figure 5-3 and Figure 5-8. In light of the preceding discussion of collision signatures, these data seem to display the trends associated with elastic momentum transfer collisions: primary central distributions between monotonically decaying tails. Drawing inspiration from the similarity between the post-collision shape displayed in Figure 7-10 and the form of the ion voltage distributions near centerline in Figure 5-3, assume that the measured voltage distribution represents the post-collision form of the situation introduced in Figure 7-9: a pre-collision voltage distribution of singly and doubly charged ions obeying the same shape, but with the doubly charged distribution having an amplitude of some fraction of the singly charged distribution. This situation seems reasonable for the Hall thruster since both ion species are formed and

accelerated within the same region according to the same processes, albeit with the doubly charged ions produced at a reduced rate. Figure 7-13 shows such a supposed case for the ion voltage measured at 0.5 m from the SPT-100 at 5 degrees off centerline with an assumed pre-collision distribution of Xe^+ and Xe^{2+} chosen to match the central shape of the data, with the height of the Xe^{2+} distribution set at 15% of the Xe^+ height. Although there is no physical basis on which to choose a mathematical form for the pre-collision distribution, the nature of the elastic collision process is such that the post-collision distribution largely retains the pre-collision shape with the addition of tails attached to each side. It is therefore reasonable to assume that the 220 to 300 V regime of the measured distribution in Figure 7-13 reflects the same shape as the pre-collision distribution; thus, a gaussian curve-fit was chosen to represent the pre-collision distributions simply on the basis of providing a close mathematical approximation to the center portion of the data.

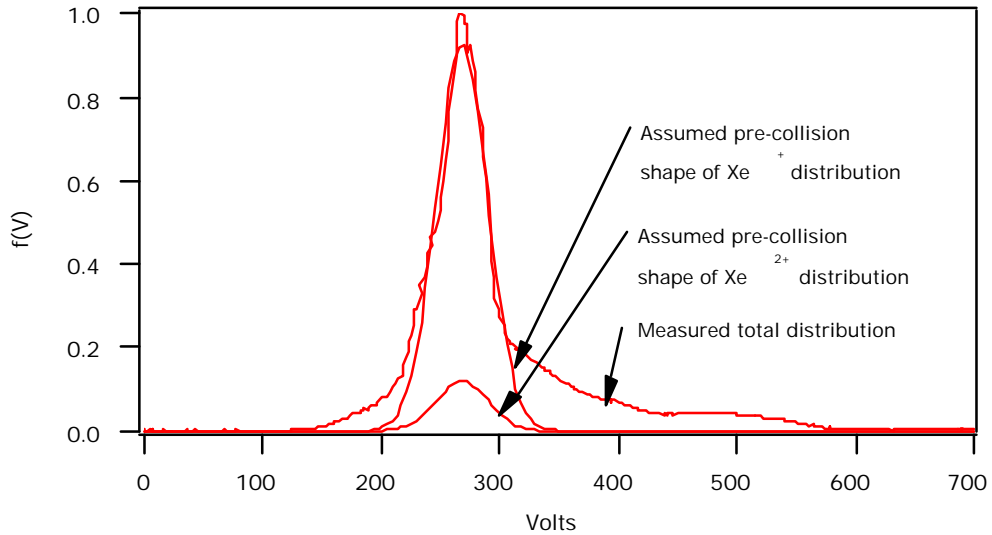


Figure 7-13. Total ion voltage distribution measured at 0.5 m from the SPT-100 at 5 degrees off thruster centerline with proposed forms of the pre-collision distributions of singly and doubly charged ions.

With the proposed pre-collision distributions of singly and doubly charged ions in hand the method of Eqn. 7-5 can be used to convolve the two distributions into their combined post-collision shape. Figure 7-14 shows the results of this convolution along with the sum of the two individual post-collision distributions compared to the MBMS data; in this figure the amplitude of the post-collision product distribution (height of the tail) was chosen arbitrarily to match the tail in the data; physically, this tail height would be a function of the collision cross section.

Even without the value of the elastic cross section between Xe^+ and Xe^{2+} the trends and qualitative behavior in the post-collision convolution of the assumed distribution very closely match the data curve. Specifically, the high-energy tail in the data decays in nearly the same manner as the tail in the

proposed model, falling to a value of zero at the same value of voltage; the shape of the low-energy tails also reach zero at the same voltage. Thus, although the model contains no method by which to set the tail height, the overall width and trends in the proposed convolution closely follow the data.

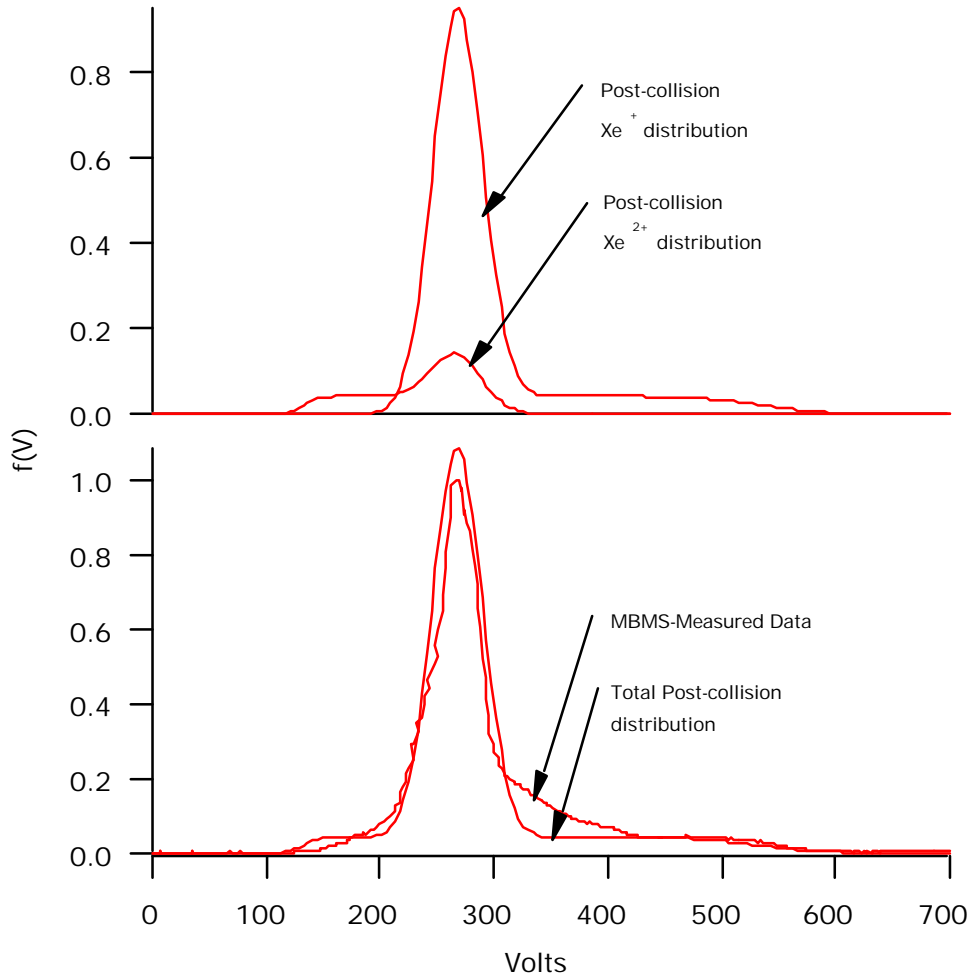


Figure 7-14. Convolution of assumed pre-collision gaussian distributions of Xe⁺ and Xe²⁺ into their combined post-collision shape compared with MBMS-measured data at 0.5 m radius from the SPT-100 and 5 degrees off centerline.

By utilizing the species-dependent data obtained from the MBMS it is possible to evaluate the proposed elastic collision concepts discussed above more extensively. Using the TOF mode of the MBMS the species-dependent voltage distributions were measured at 0.5 m, 5 degrees for Xe^+ , Xe^{2+} , and Xe^{3+} ; these data were presented previously as Figure 6-6. Figure 7-15 shows a comparison between the Xe^+ and Xe^{2+} post-collision distributions derived by convoluting the assumed pre-collision gaussians (as plotted in Figure 7-14) compared with the MBMS-measured voltage distributions of these same species.

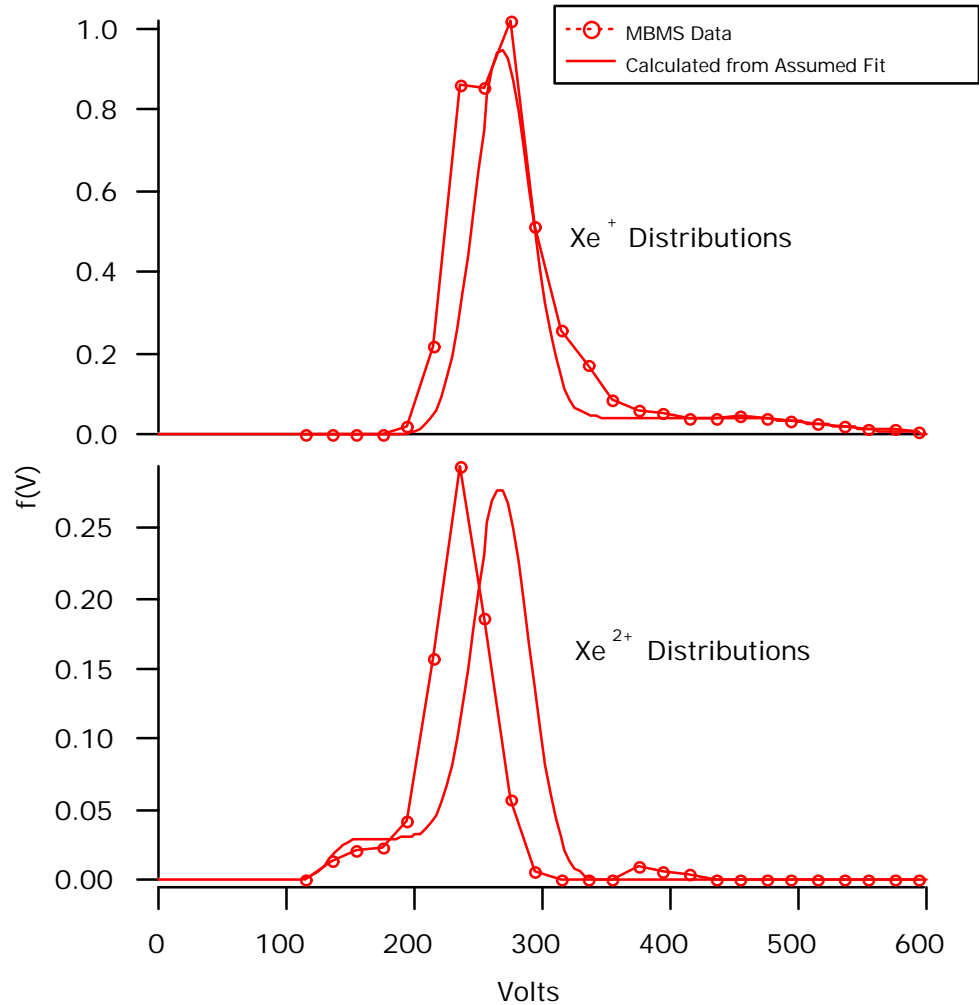


Figure 7-15. Comparison of MBMS data with convolution of proposed pre-collision gaussians for Xe⁺ and Xe²⁺ at 0.5 m from the SPT-100, 5 degrees off centerline.

The similarity between the shapes computed based on the assumed pre-collision distributions convoluted according to elastic collisions and the data is striking: the Xe⁺ distribution data exhibits a high-energy tail that extends and decays to zero nearly identically with the computed curve, while the Xe²⁺ distribution displays the corresponding low-energy tail attributed to elastic collisions with

Xe⁺ that also follows the computed shape. It follows, then, that the ion voltage distribution data at 5 degrees off centerline, 0.5 m from the thruster is consistent with the description of the phenomena attributed to elastic momentum transfer collisions between singly and doubly charged plume beam ions having a gaussian-like pre-collision distribution: the high-voltage tail is formed by singly charged xenon ions that have gained momentum from the higher-energy doubly charged ions, while the low-energy tail is the corresponding appearance of doubly-charged ions which have lost energy to elastic collisions. This explanation seems plausible since the assumed pre-collision distributions shown in Figure 7-13 resemble the intuitive shape of the ion voltage distribution that would be expected to form within the plasma discharge described by the trends shown in Figure 5-27: ion voltages ranging from 200 to 300 V with no ions exceeding the applied discharge voltage. Although the pre-collision distributions of Figure 7-13 exhibit a small population of ions greater than 300 V, it must be remembered that these shapes were simply assumed with no physical justification other than agreement with data. The curve-fit representing the pre-collision shape complied with the data only up to about 290 V: the portion of the pre-collision distribution greater than 300 V is therefore intangible.

The comparisons of Figure 7-15 show exceptional agreement for the singly ionized xenon distributions, whereas the doubly charged distributions display a slight offset. The reason for this disagreement is likely to arise from the acceleration scenario discussed previously in Section 6.3.2 and illustrated in

Figure 6-7: rather than having the same pre-collision shape and location as the Xe^+ distribution as assumed, the doubly-charged ions are likely to be formed further downstream in the thruster acceleration layer and would thus have a pre-collision voltage distribution that was shifted towards lower voltages. This accounts for the offset apparent in Figure 7-15. However, the breadth of the low-energy tail on the Xe^{2+} distribution is determined by the pre-collision voltage distribution of Xe^+ and therefore shows good agreement with the data in spite of the main peak offset.

The discussion of elastic collisions has thus far assumed hard-sphere interactions, such that the differential collision cross section is constant. These hard-sphere interactions serve to demonstrate many important features of the collisions while being conceptually and mathematically simple. In truth, the elastic collision between ions will be described by the differential collision cross section calculated according to the Coulomb inverse power potential. Written in terms of collision scattering angle

Eqn. 7-6
$$S(\mathbf{q}) = \frac{b_0^2}{4 \sin^4 \mathbf{q}/2}$$

where the Landau length is defined as

Eqn. 7-7
$$b_0 = \frac{q_1 q_2 e^2}{4\pi \epsilon_0 m^* u_{\text{coll}}^2} .$$

The differential cross section, which describes the probability of an ion being scattered into an angle θ , can be combined with Eqn. 7-1 describing the energy transferred for a collision of angle θ to predict the distribution of post-collision energy transfer in a binary elastic collision. With ΔE denoting the fraction of the collision energy transferred and recognizing that the Landau length (for identical mass collision partners) can be written as

Eqn. 7-8
$$b_0 = \frac{q_1 q_2 e^2}{4p e_0 E_{\text{coll}}},$$

yields

Eqn. 7-9
$$S(\Delta E) = \frac{q_1^2 q_2^2 e^4}{64p^2 e_0^2 (\Delta E)^2}.$$

Eqn. 7-9 states the probability of a binary Coulombic collision producing an energy transfer of ΔE . The result implies that since the Coulomb differential cross section favors small angle collisions, such interactions are more likely to create products with small energy transfer. This is illustrated in Figure 7-16 which plots the normalized differential cross section ($64S\pi^2\epsilon_0^2/q_1^2q_2^2e^4$) as a function of the normalized energy transfer (i.e. the fraction of total collision energy transferred, or $\Delta E/E_{\text{coll}}$).

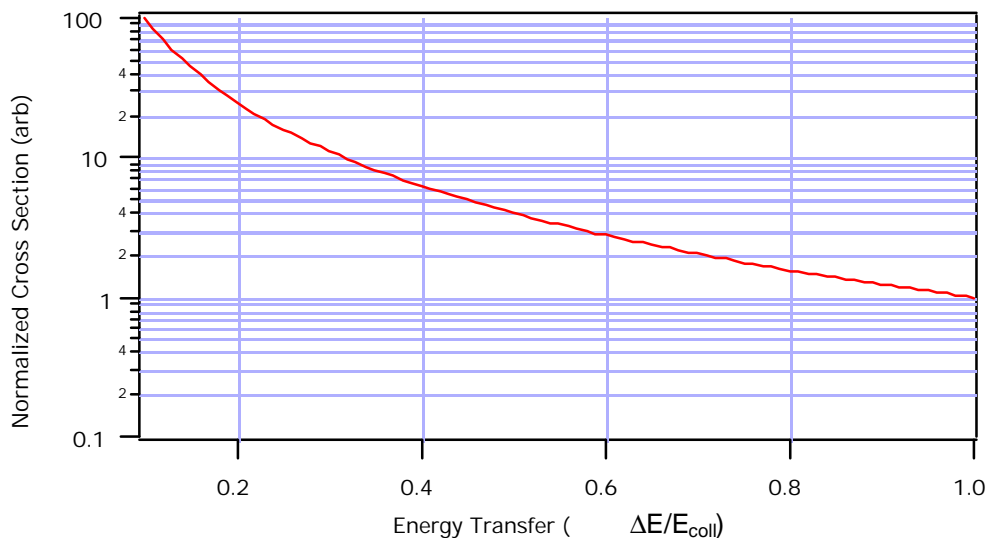


Figure 7-16. Illustration of Coulomb interaction preference for low energy transfer in a binary elastic collision between ions.

The effect of the true Coulomb interaction between ions can be easily understood by examining Figure 7-14. Since the cross section favors collisions with small energy transfer, the effect would be to “fatten” the portion of the post-collision tail of Xe^+ in the 300-to-400 V range and the tail of the Xe^{2+} tail would be amplified in the region near 200 V. Thus, consideration of the true collision dynamics would tend to bring the hard-sphere approximate model in closer agreement with the data.

The measured ion voltage distributions at 0.5 m, 5 degrees demonstrate considerable agreement with an elastic collision explanation for their origin. In addition to the elastic behavior is evidence of CE collision signatures: as can be seen in Figure 7-15 the measured Xe^{2+} distribution displays a well-defined bump at a voltage corresponding to 3/2 of the most probable voltage. An examination

of Table 7-1 and Table 7-2 reveals three possible reactions within the Hall thruster plume that are capable of producing a doubly charged ion with voltage of $3/2$ the beam voltage: (1) a Xe^{3+} beam ion reacting with a Xe^+ beam ion; (2) a Xe^{3+} beam ion reacting with a Xe^{2+} beam ion, or (3) a Xe^{3+} beam ion reacting with a background Xe neutral. The occurrence of the first reaction would require the simultaneous production of a Xe^{2+} ion with voltage of $1/2$ the beam voltage, while the second reaction must produce a Xe^{3+} ion with $2/3$ of the beam voltage. An examination of Figure 6-6 and Figure 7-15 show no evidence of these sibling populations. Thus, the most likely reaction producing the $3/2 V_b$ bump in the Xe^{2+} distribution is the CE collision between a triply charged xenon beam ion with a background neutral. This conclusion is also intuitive: since Xe^{3+} represents the smallest fraction of the plume flow, the most likely reaction involving this ion will occur with the most prevalent species in the flow, i.e. neutral atoms.

The measured ion voltage distributions near centerline at 0.5 m seem to be very consistent with a momentum-transfer elastic collision analysis between plume beam ions, with slight evidence of CE occurrences. An examination of Figure 5-3 through Figure 5-11 reveal that, for increasing angles off centerline, the elastic collision signatures give way to clear CE signatures with distinct bumps in the distribution tails. This trend is condensed in Figure 7-17.

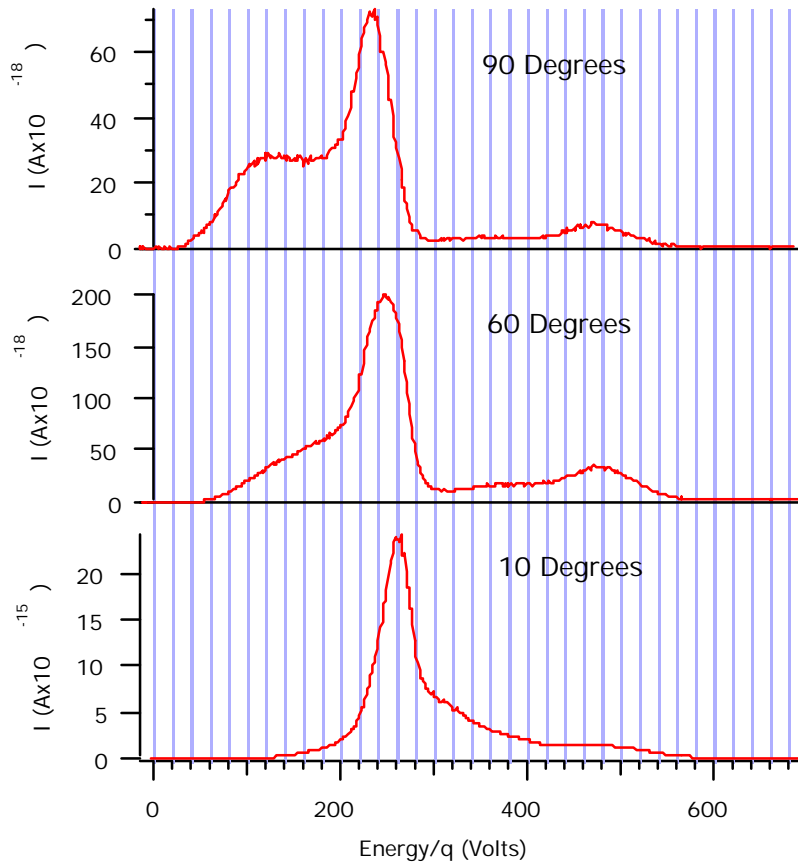


Figure 7-17. Ion voltage distribution at 0.5 m from the SPT-100 from 10 degrees to 90 degrees off centerline showing collision signature evolution from elastic behavior to CE behavior.

The 60 and 90 degree distributions exhibit a “bump on tail” shape, where the voltage of the bump maximum is exactly twice the most probable voltage of the distribution (denoting V_b as the most probable beam voltage, $V_b = 235$ V at 90 degrees with the bump occurring at $V = 470$ V). From Table 7-1 and Table 7-2 the possible reactions creating products with a voltage of twice the main beam voltage are (1) the CE collision between a Xe^+ beam ion with a Xe^{2+} beam ion (2) the CE collision between a Xe^{3+} beam ion and a Xe^{2+} beam ion, and (3) the CE

collision between a Xe^{2+} beam ion with a background neutral. The distribution measured at 90 degrees will be used as a discussion tool to evaluate these collisions.

The second reaction mentioned above involved a collision between two minority species in the plasma. The probability of such a second-order collision is much less than that involving one or more majority species, such as Xe^+ or Xe , therefore either the first or the third reaction seems most likely to be observed. If the reaction responsible for the peak at $2 V_b$ in the 90-degree data is of the first type involving two beam ions, then a sibling bump must occur at a voltage of $V_b/2 = 117 \text{ V}$. The distribution does display a bump near 120 V, however the width of this low-voltage bump is not supported by a CE analysis of the collision between two beam ions. Following the same ideas presented previously in the elastic collision evaluation of the data at 5 degrees, assume that the large central peak in the 90-degree data reflects the pre-collision distribution of Xe^+ and Xe^{2+} . A gaussian curve-fit to this portion of the curve is shown compared with the data at 90 degrees in Figure 7-18.

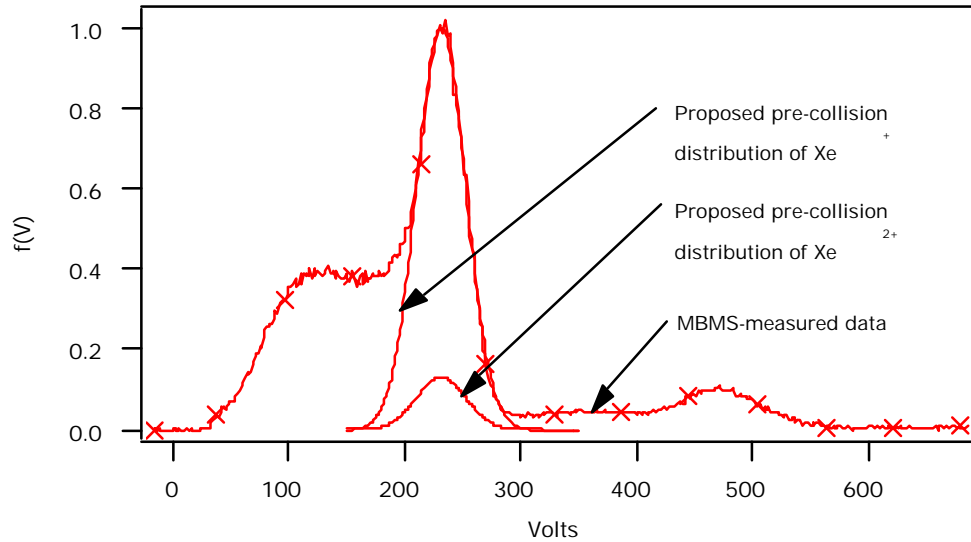


Figure 7-18. Proposed pre-collision gaussian distributions for Xe^+ and Xe^{2+} for the data at 0.5 m from the SPT-100, 90 degrees off axis.

The CE reaction between these two pre-collision distributions of beam ions would then form a resultant post-collision distribution as shown compared with the data in Figure 7-19; in this figure, as previously, the height of the post-collision distributions has been chosen arbitrarily to match the data. The post-collision distribution resulting from the CE collision results in a distribution with the same shape as the pre-collision population shifted and broadened by a factor of two coincidentally with a distribution shifted and narrowed by a factor of 1/2. It is apparent from the figure that even though the shape of the high-voltage bump is well represented, the narrowed product distribution of doubly charged ions does not account for the breadth in the low-voltage portion of the data. Furthermore, arbitrarily choosing the peak height of the post-collision Xe^{2+} distribution to match the data implies that the doubly charged CE products

comprise nearly 50% of the pre-collision ions and hence, that the pre-collision distribution of Xe^{2+} accounted for greater than 50% of the total flow.

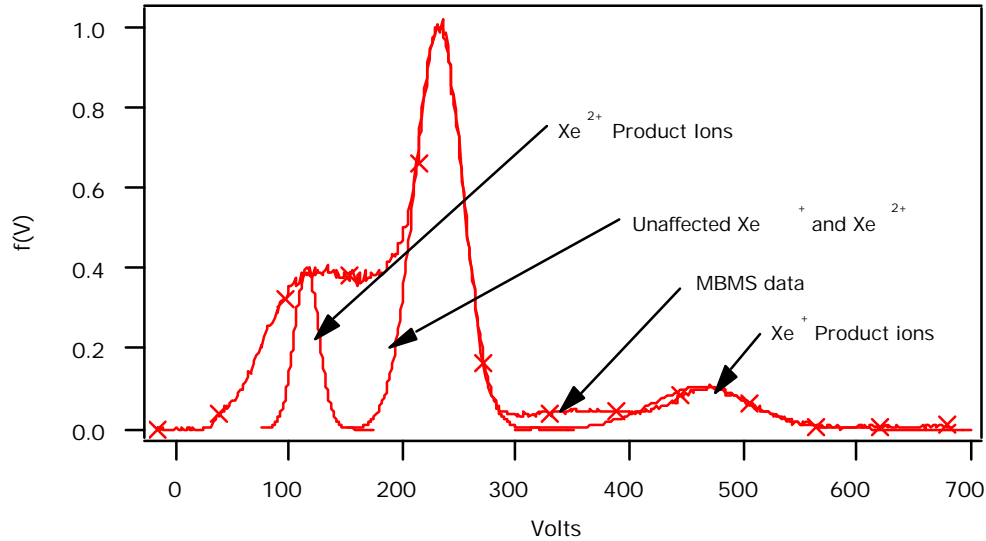


Figure 7-19. Post-collision distribution result of CE reaction between singly and doubly charged beam ions based on assumed gaussian pre-collision distribution.

It is apparent that a CE reaction between two pre-collision gaussian-like distributions of Xe^{+} and Xe^{2+} cannot account for the measured shape of the voltage distribution function at 90 degrees. The other possible reaction producing a bump at $2V_d$ is the collision between a Xe^{2+} beam ion and a background neutral. If the pre-collision distribution of Xe^{2+} was gaussian-like as discussed above, the beam ion/neutral collision would produce only a post-collision distribution centered at $2V_b$. This reaction does not explain the portion of the MBMS data below 200 V nor the portion between 300 V and 400 V (the

resultant post-collision distribution would consist only of the central gaussian and the “bump” on the far right of Figure 7-19).

The trends of the MBMS data suggest another shape for the pre-collision distribution: the high-voltage tail above 300 V in the 90-degree data has a nearly identical shape to the portion of the distribution less than 300 V. With this in mind the following model is proposed. The portion of the 90-degree data curve to the left of 300 V in Figure 7-17 represents the pre-collision distribution of singly and doubly charged xenon created and accelerated in the same region, while the high-voltage tail above 300 V represents Xe^{2+} beam ions which have gained an electron through a CE collision with a background neutral. The pre-collision Xe^{2+} distribution is thus calculated by multiplying the portion of the MBMS data between 0 and 300 V by some fraction. This is shown graphically in Figure 7-20.

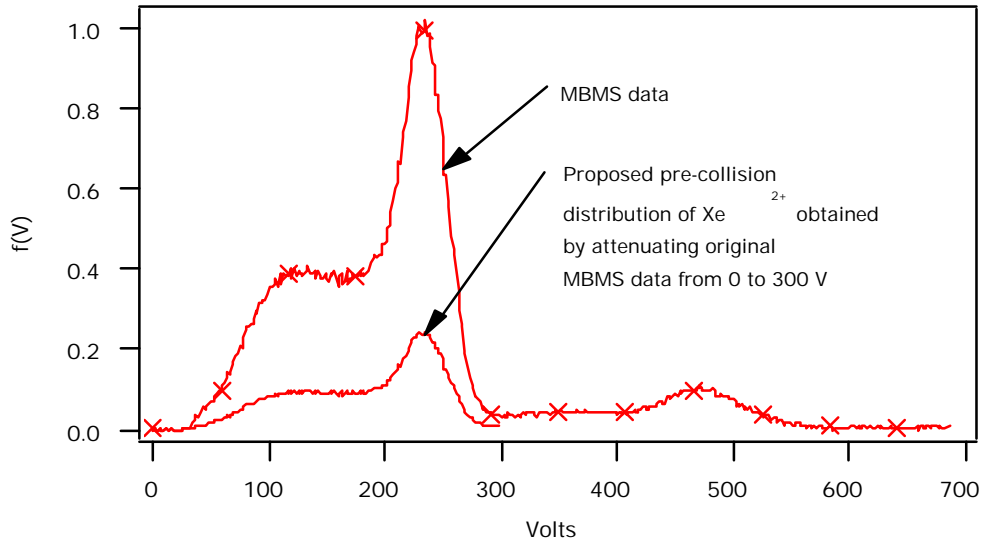


Figure 7-20. Proposed pre-collision distribution of Xe^{2+} computed from the MBMS data at 0.5 m, 90 degrees off axis in the SPT-100. The proposed distribution was calculated as a fraction of the original data between 0 and 300 V.

A CE collision between the doubly charged xenon and background neutral would then produce a distribution of singly charged product ions with the same shape as the pre-collision distribution shifted and broadened by a factor of 2. Figure 7-21 shows the post-collision distribution formed through such a shape-preserving reaction compared with the data. In this plot the height of the post-collision distribution has been chosen to match the data, but the distribution shape was determined by “cutting and pasting” the original data and is thus an exact duplicate of the portion of the curve between 0 and 300 V.

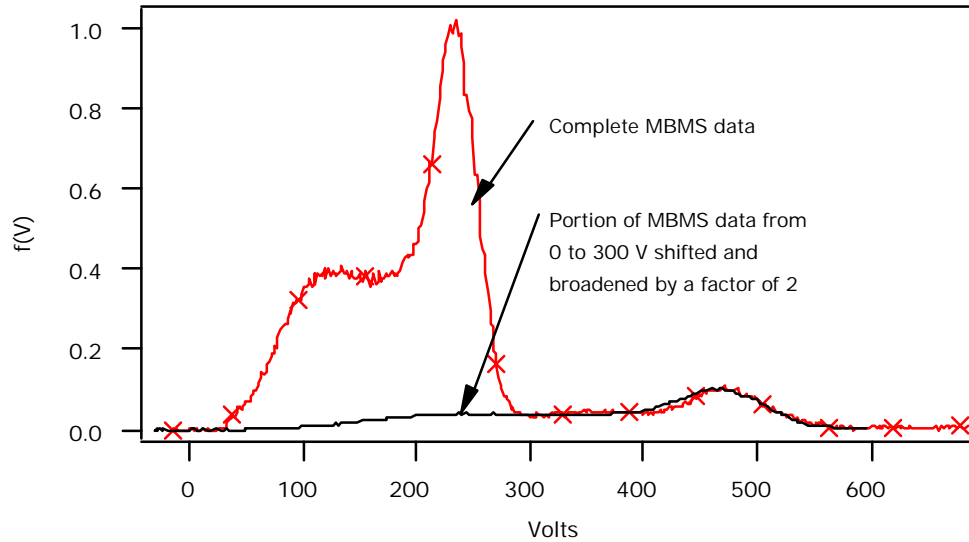


Figure 7-21. Illustration of identical shape in tail and main body of voltage distribution data measured at 0.5 m radius and 90 degrees off centerline in the SPT-100.

It is apparent from an examination of Figure 7-21 that the high-voltage tail in the 90-degree ion voltage distribution is exactly the same as the shape of the curve between 0 and 300 V; such a distribution can be explained through the occurrence of CE collisions between doubly charged xenon ions and ambient background neutrals. This result makes physical sense: the original pre-collision distribution of ions produced in the Hall thruster goes to zero at 300 V and thus does not contain any anomalous ions with voltages greater than that applied to the discharge. The high-voltage portion of the measured distribution function is the result of CE collisions occurring between the different ionic species within the plasma, namely between doubly charged ions and background neutrals.

Discussion of the collision signatures within the plume ion voltage distributions have been confined to the data recorded at 0.5 m radius from the SPT-100 up to this point. The data trends in the 1.0 m data exhibit many of the same tell-tale signatures of collisions, but the angular trends are much more intriguing. Excluding the anomalous zones at 1.0 m between 5 degrees and 20 degrees off axis the data display much of the same angular trends as the 0.5 m case. Referring to Figure 5-12 through Figure 5-18, the centerline voltage distribution exhibits somewhat of a monotonically decreasing tail associated with elastic collisions, with a CE-type signature superimposed. Ignoring, for now, the region between 5 and 20 degrees, the elastic-looking collision signatures evolve into typical CE structures very rapidly with increasing angle from centerline, with a “bump on tail” existing at precisely twice the most probable voltage of the main distribution. Furthermore, the height of these bumps is a larger fraction of the main discharge peak than exhibited in the 0.5 m data.

The voltage distributions measured between 5 degrees and 20 degrees, and -5 degrees and -20 degrees exhibit fascinating structure. These data were presented earlier as Figure 5-19 through Figure 5-22. The voltage distributions of this region are characterized by extremely prominent CE peaks occurring at voltages greater than that which can be considered the “beam” voltage at approximately 260 V. Referring to Table 7-2 it is apparent that this type of signature can arise from collisions between beam ions and background neutrals.

Although there are possible reactions between beam ions that would produce peaks greater than V_b , as can be seen from Table 7-1 these reactions produce sibling products with energies less than V_b simultaneously with the high-voltage peaks. The data do not exhibit any peaks with voltage less than V_b .

Between 5 and 6 degrees and between -5 and -7 degrees the “primary” distribution between 200 and 300 V associated with the thruster discharge acceleration process decays abruptly in magnitude. This decay in the 260 V peak is accompanied by a relative increase in the amplitude of the high-voltage peaks associated with CE collisions. The physics responsible for this process are straightforward. Consider a pre-collision distribution of singly, doubly, and triply charged ions that have been accelerated through the same voltage of V_b . If such a distribution were to pass through an ambient neutral background such that 100% of the ions experienced a CE collision with the background gas, the result would be all of the products listed in Table 7-2; 100% of the reactants would become products and hence the “primary” pre-collision distribution with peak at V_b would completely disappear, with only the product peaks at $3V_b/2$, $2V_b$, and $3V_b$ present in the voltage distribution. If somewhat less of the ions experience a CE collision, say 50%, the peak height of the V_b distribution would be comparable with the high-voltage peaks since an equal number of pre-collision reactants and post-collision products exist. Thus, as the V_b peak decays due to de-populating CE collisions with background gas the product peaks with voltage greater than V_b will experience a simultaneous growth in amplitude.

Furthermore, although the ionization fraction decreases with increasing ion charge state (e.g. there is less Xe^{3+} than Xe^{2+}), the cross section for ion-neutral CE collisions scales according to $q^{1.3}$ so that highly charged ions will demonstrate a disproportionate contribution to the CE signature.^{55,56}

The data between 5 and 20 degrees off axis at 1.0 m display exactly such CE behavior. For convenience, the data presented earlier is reproduced in part here as Figure 7-22. The distribution peaks corresponding to the possible post-collision voltage multiples are clearly visible in the region between -7 and -11 degrees. The peak locations represent all possible products of the reactions considered previously in Table 7-2 along with the original population at $V_b=260$ V. It is apparent, then, that the data at 1.0 m reflect extensive attenuation of the plume ion beam by CE collisions with background neutrals. Subject to this interpretation, the ion voltage data between 5 and 20 degrees reveal a unique insight regarding the species distribution within the plasma. Consider the ion voltage trace taken at 1.0 m, 11 degrees off axis shown in Figure 7-23. In this trace a distribution peak with voltage equal to $4V_b/3$ is clearly evident. The only possible mechanism to account for this peak requires the existence of a quadruply charged ion, i.e. Xe^{4+} exchanging a single electron with a background neutral. This result, then, implies that the electrons within the thruster discharge chamber are hot enough to produce Xe^{4+} ions.

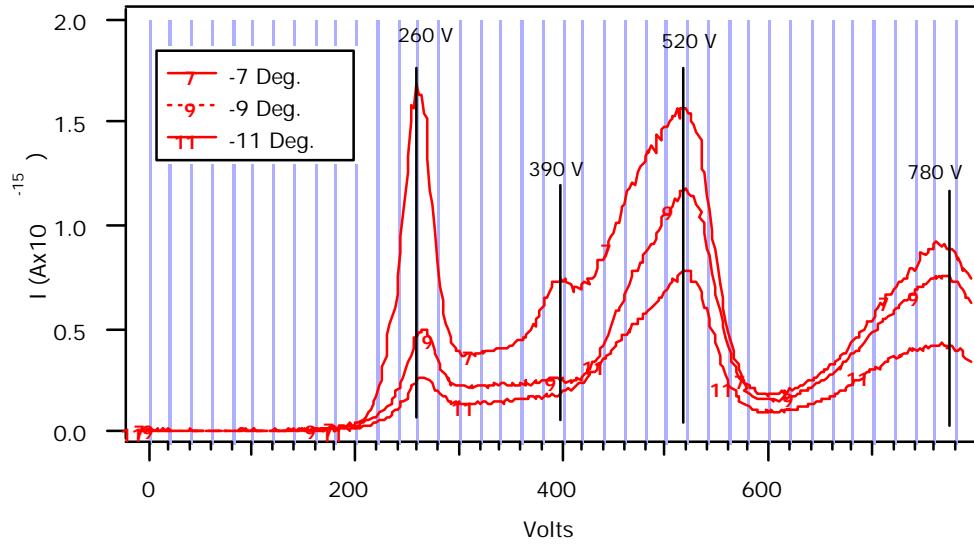


Figure 7-22. Ion energy distribution measured at 1.0 m radius from the SPT-100 for angles at -7, -9, and -11 degrees off thrust axis. Clearly evident are the high-voltage peaks at $3V_b/2$, $2V_b$, and $3V_b$ produced as a result of CE collisions with neutral atoms.

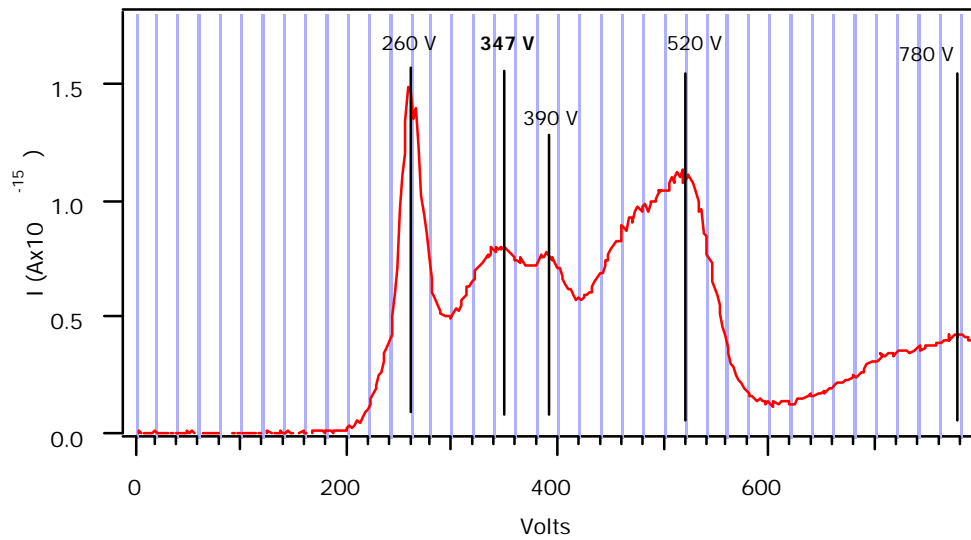


Figure 7-23. Ion voltage distribution at 1.0 m radius from the SPT-100 plume at 11 degrees off axis showing peaks at $4V_b/3$, $3V_b/2$, $2V_b$, and $3V_b$.

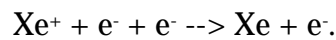
7.3. Ion-Electron Recombination

The analysis of CE collisions within the Hall thruster plume has been predicated on the assumption that the plasma ions acquire one or more electrons from ambient neutral particles, thus reducing their positive charge state and appearing with increased energy-per-charge in the ion voltage distribution. Such behavior could be equally explained by bulk ion-electron recombination within the plasma, where multiply charged ions combine with free electrons to produce an identical effect on the ion voltage distribution.

The balance equation of the free electron density of a decaying plasma can be written as

Eqn. 7-10
$$\frac{dn_e}{dt} = -\alpha n_e^3$$

where α is the generalized recombination coefficient. In a suitably dense plasma α depends on collisions only, so that recombination occurs primarily through the three-body process



The criteria for such collisional recombination is that the plasma must be under local thermodynamic equilibrium (LTE). In terms of the plasma density, this requires⁵⁷

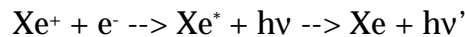
Eqn. 7-11
$$n_e \geq 1.15 \times 10^{14} (q+1)^3 \frac{(E_1 - E_2)^3}{kT_e} \left(\frac{kT_e}{E_1} \right)^{3/2} \frac{2pe^2}{e_0 m_e c^3 h^2}$$

where E_1 is the energy of the ground state and E_2 is the energy of the first excited state. For xenon Eqn. 7-11 can be written as

Eqn. 7-12
$$n_e \geq 1.73 \times 10^{31} \sqrt{kT_e}.$$

From Myers and Manzella²⁵ the electron temperature within the plume in the vicinity of 0.5 m radius from the thruster exit is $T_e = 1$ eV (11,600 K), thus the density must be greater than $7 \times 10^{21} \text{ m}^{-3}$ for LTE to hold. However it was found in the probe-based study reported here that the density was less than $2 \times 10^{16} \text{ m}^{-3}$ and therefore the ion-electron recombination will not be fully collisional.

Since the plasma density is low, the contribution of radiative recombination will be substantial. In this process, a free electron is captured into an excited state of the ion, which then decays to the ground state through the radiation of a photon,



The bulk recombination coefficient, α , can thus be written as the sum of collisional recombination and radiative recombination, $\alpha = \alpha_c + \alpha_r$. Anders gives approximations for the two terms of the collisional-radiative recombination for xenon⁵⁷

Eqn. 7-13
$$\alpha_c = 1.1 \times 10^{-20} T_e^{-9/2}$$

Eqn. 7-14
$$\alpha_r = 3.0 \times 10^{-16} T_e^{-3/4} n_e^{-1}.$$

Considering the plasma plume at 0.5 m radius on the thrust axis, $T_e = 1$ eV and $n_e = 2 \times 10^{16} \text{ m}^{-3}$, so that $\alpha_c = 7 \times 10^{-39} \text{ m}^6/\text{s}$ and $\alpha_r = 1 \times 10^{-35} \text{ m}^6/\text{s}$. It is thus apparent that radiative processes dominate the ion-electron recombination. According to Eqn. 7-10 the decay of the electron density is described by

Eqn. 7-15
$$\frac{1}{n_e^2(t - t_0)} = 2a(t - t_0) + \frac{1}{n_e^2(t_0)}.$$

Defining the recombination time, τ_r , as the time required for the electron density to decay to one-half of its initial value yields

Eqn. 7-16
$$t_r = \frac{3}{2} \frac{1}{an_e^2(t_0)}.$$

For the conditions considered in the Hall thruster plume, $\tau_r > 260$ seconds, while the transit time for an ion to travel 0.5 m in the plume is 30 μs . It is readily apparent, then, that the means by which plume ions obtain electrons is not through bulk recombination with free electrons and must be due to CE with ambient neutrals.

7.4. Discussion of Plume Collisions

A number of various potential collision processes within the Hall thruster plasma have been evaluated. Through this evaluation distinguishing characteristics of each process were identified and used to examine the possible collision evidence within the measured data. Although not significantly quantitative, these collision signatures showed considerable success in

identifying collision products within the MBMS ion voltage distribution measurements as well as the species-specific mass spectrometric studies. Drawing on the vast body of data reported in this study it is possible to infer the probable origins of these collisions.

The near-centerline region of the plume was seen to exhibit considerable evidence of elastic momentum transfer collisions between singly and doubly charged propellant ions. Although these collisions could have occurred anywhere along the path length from the discharge chamber to the MBMS detector, it is most likely that they originated from the region in which the reactant density is greatest, i.e. the thruster discharge chamber. Furthermore, the behavior of the post-collision voltage distributions stipulates that the elastic collisions between Xe^+ and Xe^{2+} must have occurred between high-voltage ions, i.e. these collisions must have occurred downstream of the acceleration zone in order to produce the tail lengths displayed in the data. It follows, then, that the highest probability of elastic collisions between beam ions producing the structure seen in the data will occur immediately downstream of the thruster acceleration zone, or near the thruster exit plane.

The CE collisions involving zero-energy neutrals may have more varied locations of origin. Specifically, there are three possible regions in which these collisions may occur: (1) collisions between ions and un-ionized propellant within the thruster discharge chamber; (2) collisions between beam ions and ambient background neutrals due to facility effects within the plume; and (3)

collisions between beam ions and the neutral “ram cloud” atoms immediately upstream of the MBMS sampling skimmer. This last region is of most concern from a diagnostics standpoint. The sampling skimmer of the MBMS represents an essentially flat-plate obstruction to the high-velocity plasma flow in the Hall thruster plume. Ions impacting this obstruction will neutralize and reflect to form a higher-density “ram cloud” build-up of neutral gas upstream of the skimmer. CE collisions between plume ions and this target layer of neutrals will produce parasitic collision signatures in the data that are not representative of the undisturbed flow, but are instead an artifact of the measurement disturbance. A rough estimate of the magnitude of this ram cloud effect is possible with existing data.

The ion-neutral CE collision that is likely to be most prevalent involves singly ionized xenon with its neutral counterpart. The cross section for this reaction is available via Eqn. 3-6. Although the neutral density of the ram cloud is unknown, approximating the pressure within the ram cloud as being an order of magnitude greater than the ambient vacuum pressure does not seem unreasonable, with the neutral temperature equal to the obstruction surface temperature. It is further assumed that this ram cloud will extend upstream of the skimmer a distance on the order of the transverse dimension of the obstruction, which was a 20-cm-diameter flange holding the skimmer. With these crude approximations it follows that the mean-free-path for ion-neutral charge exchange within the ram layer is 20 times larger than the thickness of the

layer. Employing Eqn. 3-7 reveals that less than 5% of the ionic flow may suffer a CE collision within the ram layer according to this crude approximation.

It seems that the obstruction imposed by the MBMS inlet skimmer does not induce significant perturbation to the measured ion voltage distributions. The data support this conclusion: if the ram cloud obstruction were responsible for CE collisions with the beam ions then the effect would be most pronounced for the highest density region in the plume, for it is this case which would form the most dense, extensive build-up. On the contrary, the highest density point considered in this study (0.5 m radius on thrust axis) shows no evidence of ion-neutral CE collision products, while regions of considerably lower density (1.0 m at 90 degrees from axis) demonstrate considerable ion-neutral CE signatures.

It follows, then, that the ion-neutral CE collisions evidenced in the data occur along the path extending from the downstream end of the thruster acceleration zone to the inlet of the MBMS skimmer. This implies that these collisions are not inherent to the Hall thruster, rather they are due to perturbations associated with an imperfect ground-test environment in the vacuum chamber. The probability of CE collision between a plume ion and a background neutral as a function of path length through the target neutral gas is described by Eqn. 3-7. Thus, the number of CE products detected in the ion voltage distribution should increase with distance from the thruster, since this represents a longer path of travel for the ion during which it has a higher probability of collision. Consider the ion voltage distributions measured at 40

degrees off centerline at both 0.5 m and 1.0 m as displayed in Figure 5-4 and Figure 5-13 as a typical representation of the data. The collision analysis of this chapter strongly suggested that the entire population of ions existing with voltages above 300 V are the products of ion-neutral CE collisions. Therefore the area under the $I(V)$ vs V curve from 0 to 300 V is proportional to the number of “virgin” ions which have not undergone a CE collision with a neutral, while the area under the curve above 300 V is proportional to the number of ions which have suffered a CE collision. Numerically evaluating these integrals reveals that 21% of the total ion population at 0.5 m are products of CE collisions, with CE products accounting for 40% of the total flow at 1.0 m. These estimates agree very well with the earlier prediction of Section 3.3.4 which, based on the available cross section for $Xe^+ - Xe$ and facility background pressure, predicted a 30% collision probability for ions traveling 0.5 m from the thruster and 50% probability in the first 1.0 m of flight.

The estimates of 50% collision probability for the CE reaction between an ion and a neutral at 1.0 m are reflected in the majority of the data sets. The exception is the region at 1.0 m radius between 5 and 20 degrees of centerline. In this region the population of CE products exceeds the “virgin” plume ions for many traces indicating that well over 50% of the flow has suffered a CE collision. Indeed, in many traces the amplitude of the $2V_b$ population is nearly twice that of the original distribution at V_b . Such a large occurrence of CE collisions does not seem to be supported by direct collisions with facility background gas. A

possible explanation for this behavior is the existence of “secondary” CE collisions involving plume ions and the neutral products of the previously discussed “primary” CE collisions.

For instance, CE collisions between plume ions and stagnant background neutrals produce either high-voltage ions (which have been the subject of the discussion to this point) along with zero voltage ions, or high-energy neutrals along with zero voltage ions (e.g. the CE reaction between Xe^+ at V_b and zero-energy Xe produces Xe at V_b with zero-energy Xe^+). Thus a large occurrence of ion-neutral CE collisions would produce a population of high-energy neutrals, as discussed previously in Section 3.3.3. Since these high-energy neutrals were originally plume ions that lost an electron, the density of these neutrals would be greatest in the region of the plume with greatest plasma density, i.e. near thruster centerline. In fact, the probe based study of Chapter 3 concluded that a high-density core of high-energy neutrals existed within 25 degrees of thruster centerline. These neutral products of one CE collision are therefore potential partners for a second CE collision, creating a higher probability of CE collision for a plume ion traveling near centerline than for an ion that travels off centerline through only the background target gas. Furthermore, the cross section for CE is greatest between atoms with zero relative velocity;⁵⁴ therefore a plume ion would have an increased chance of collision with a neutral traveling at the same velocity, such as the fast product of a “primary” CE collision.

The collision analysis of the measured ion energy distributions also provides insight to the thruster acceleration layer behavior. Recall the collision discussion of the ion voltage distribution at 90 degrees off centerline and 0.5 m from the thruster presented earlier in this chapter. This distribution displayed a CE tail with the exact same shape as the portion of the distribution between 0 and 300 V. This suggests that the pre-collision population of ions had the shape displayed in the 0-to-300 V range of the plot, with the high-voltage tail simply a subset of this population conceived through the gain of an electron through CE with a neutral: the conclusion is that the part of the measured distribution below 300 V is not the result of facility interactions, rather a product of the thruster itself. Thus, the thruster discharge produced a bi-modal distribution of ions having a most-probable voltage of $V_b=240$ V with a lesser secondary population having the same width, but centered at $V_b/2=120$ V. This behavior was observed on either side of the thruster near 90 degrees from the thrust axis. The secondary distribution of ions with voltages near $V_b/2$ extend slightly further past the 90-degree direction than the primary distribution. A postulate to explain this behavior is not clear, but the implications are fascinating.

Contrary to the high-angle voltage distributions near 90 degrees, the near centerline data suggest a gaussian-like pre-collision distribution emanating from the thruster discharge. The secondary population at $V_b/2$ begins to become apparent at angles greater than 50 degrees off axis. These gaussian-like shapes near centerline seem to display the evidence of elastic collisions involving

multiply charged plume ions; such collisions are inherent to the thruster operation and plume structure and are not a result of ground-test facility interactions.

As discussed previously in Section 4.1 Manzella utilized a laser technique to measure the Xe^+ ion velocity at the exit plane of the thruster.³⁰ These measurements indicated an ion velocity of 18.8 km/sec. Since the ion species probed had $q = 1$, this equates to an acceleration voltage of 240 V. Indeed, an examination of Figure 5-28 confirms that the most-probable ion voltage measured with the MBMS agrees most convincingly with this result. However, the LIF data implied an ion voltage distribution with a width on the order of 3 V. As can be seen from Figure 5-25 and Figure 5-26 the width of the voltage distribution measured in this study was on the order of 30 V. A means for reconciling this difference is not presently known.

8. CONCLUSIONS

The body of this report represents a large volume of plasmadynamic data. Together these data allow a detailed model of the Hall thruster plasma plume to be constructed. The motivation behind this characterization study was the need for extensive data that is required to quantify the interaction between the Hall thruster plasma and the supporting spacecraft. In gathering these data new diagnostics were developed, while some widely used existing diagnostics were revealed to be inappropriate for Hall thruster plumes. This chapter aims to review the major findings of this study and suggest future research necessary to investigate outstanding issues.

8.1. Overall Hall Thruster Plume Structure

Many quantities related to the heavy-particle flux within the Hall thruster plume were measured using both in-situ probes and the MBMS. These data include most-probable ion voltage, ion temperature, ion density, and neutral particle flux. From these quantities evidence of both elastic collisions between ions and inelastic CE collisions between ions and neutrals were documented.

The overall structure of the Hall thruster plume as defined by these measurements is illustrated in Figure 8-1.



Figure 8-1. Heavy-particle structure of SPT-100 plume. The SPT-100 body outline including the cathode and support structure is drawn to scale with the 0.5 m and 1.0 m radius arcs shown. Azimuthal increments of 10 degrees are indicated. Quantities lying near the inner circle denote those values at 0.5 m radius, while quantities about the outer circle represent 1.0 m radius values.

This figure indicates the evolution of plasmaphysical quantities as a function of both azimuthal position and radial position from the thruster. For example, the ion-voltage distribution was found to have a Gaussian-like shape at 0.5 m from -30 degrees to 30 degrees away from the thrust axis; this structure evolved into a bi-modal distribution existing between 60 and 80 degrees (on the cathode side) and between -70 and -110 degrees (on the non-cathode side) consisting of a dominant peak near 260 V with a second plateau with peak near 120 V. The ion density at 0.5 m varied from a maximum of $2 \times 10^{16} \text{ m}^{-3}$ on centerline to $1 \times 10^{14} \text{ m}^{-3}$ directly behind the thruster. The distribution existing between 110 degrees and -140 degrees at 0.5 m was that of a macroscopically stagnant background plasma with $\tau_i = 5 \text{ V}$. By following the various evolution contours about Figure 8-1 the general trends in the plume can be understood.

8.2. Ion Energy Structure

One of the most interesting contributions of this research was the measurement of the ion energy at angles exceeding 90 degrees off the thrust axis. Although of utmost importance to spacecraft integration, this low-density regime has historically been very difficult to probe. As can be seen by an examination of Figure 8-1, V_m is nearly 260 V for all positions within 100 degrees of the thrust axis at 0.5 m radius, with $V_m = 90 \text{ V}$ extending all the way around to -150 degrees at 1.0 m radius. The mechanism responsible for such high-energy ions extending into the backflow of the plume is not understood. It was

previously believed that such high-energy ions must be formed deep within the thruster discharge chamber, and would therefore not have a direct line-of-sight path to the plume backflow. Since the existence of the force required to produce a trajectory with sufficient curvature to transport ions formed within the discharge chamber into the backflow is not justified, it is likely that these high-energy ions at large angles were formed downstream of the thruster exit plane and accelerated transverse to the thrust axis at voltages comparable to the applied voltage. These data suggest that the structure of the plasma acceleration region downstream of the thruster exit plane is not accurately explained by current models of Hall thruster operation.

A second remarkable finding regarding the ion energy distribution was the discovery of a bi-modal distribution existing in the region of 90 degrees off axis. Near thruster centerline the energy distribution was Gaussian-like with a most-probable voltage near the applied discharge voltage. With increasing angle off axis a secondary “hump” or plateau emerges on the low-energy side of the main peak. This evolution continues such that between 70 and 100 degrees and -70 and -110 degrees the ions possess two fairly distinct voltage distributions: the main distribution centered near the applied discharge voltage, and a secondary distribution of approximately one-half the magnitude of the main peak centered near one-half the applied voltage. With further increases in divergence angle this bi-modal distribution gives way rapidly to a stagnant background population. Although the secondary low-energy population seems

to be centered very near $V_m/2$, a CE analysis of this phenomena does not seem to support the indicated width of the population. It is likely, then, that this distribution shape is a result of the thruster acceleration process and not a facility-induced error.

8.3. Facility Interaction Considerations

This research demonstrated direct documentation of facility perturbances on the Hall thruster plume structure. These parasitic effects were manifested by CE collisions between plume ions accelerated within the thruster and ambient background neutrals due to vacuum pumping limitations. The evidence for such ground-test facility errors was the existence of both reduced-charge ions and a corresponding flux of high-energy neutrals within 20 degrees of the thrust axis. As expected, these effects became more pronounced with increasing distance from the thruster.

The facility pressure during testing was approximately 3×10^{-5} torr, representing a collision probability of 50% at 1.0 m from the thruster for the CE collision between Xe^+ and background Xe. If a facility with an order-of-magnitude improvement in pressure were utilized the collision probability at 1.0 m decreases to 6%. It is apparent, then, that detailed plume characterization in the far-field of Hall thrusters (approaching and exceeding 1.0 m) requiring high-accuracy should be performed at pressures on the order of 1×10^{-6} torr or better

to reduce parasitic signatures and more correctly quantify effects attributed to the thruster.

Some Hall thruster plume characterization will be insignificantly affected by these facility perturbations. For instance, measurements of plume sputtering on sample materials are fairly insensitive to CE collisions. Since the sputtering yield is dependent only on the incident atom energy (and not on the charge state), the charge-changing character of CE collisions will not affect the incident atom energy and the resultant sputtering rate will be unaffected.

8.4. *Plume Asymmetry*

Examination of Figure 8-1 reveals that the plume is not symmetric about the thruster axis. This asymmetry is attributed to the location of the thruster cathode. This asymmetry is most easily seen by an examination of the most-probable ion voltage, V_m . At 1.0 m radius, ion distributions with V_m of greater than 90 V exist from 110 degrees off axis (on the cathode side) to -150 degrees off axis (on the non-cathode side). Similarly, the macroscopically stagnant background population of ions at 0.5 m radius is centered around 165 degrees (to the back left of the thruster) rather than 180 degrees. Conceptually, the overall ion energy structure seems to be rotated to the non-cathode side (clockwise in the figure), with high energy ions existing at larger angles off axis on the non-cathode side. This could possibly be due to a shadow effect of the cathode. The bi-modal structure present in the points near 90 degrees off axis

also extends further past 90 degrees on the non-cathode side. An additional energy manifestation of the asymmetry is the slight depression of the ion temperature on the non-cathode side. A second indication of the plume asymmetry is displayed by the plasma electric field within the plume. This field is much stronger with a magnitude on the order of 10 to 30 V/m in the cathode half-plane than on the non-cathode side where the field is negligible.

Although significant asymmetries were discovered in the plume, it must be noted that the overall ion current flux measured by the Faraday probe was highly symmetric about the thrust axis. This indicates that the cathode-induced asymmetries do not have significant impact on the thrust vector, which should be closely aligned with the thruster axis. The asymmetries seem to be confined mostly to the regions of the plume at large angles from the thruster axis where the ion density is very low; these low-density regions have negligible effect on the direction of the thrust vector.

8.5. Suggestions for Future Work

As in most research, the conclusions of this work seem to leave more questions than answers. This section presents possible directions for future investigations regarding Hall thruster plumes and thruster performance in general. Potentially interesting topics include

- Further investigations into the mechanism causing high-energy ions to be emitted from the thruster at angles up to and greater than 90 degrees off

axis. The discovery of such ions was counter-intuitive and may possibly reveal new insight on the structure of the acceleration zone within the thruster.

- Examination of the bi-modal voltage distributions emitted from the thruster at angles greater than 50 degrees off axis. The existence of a low-energy sub-population of ions with the widths demonstrated in the data is not supported by collisional analysis within the plume. It appears that this bi-modal structure is a result of the ionization and acceleration process within the thruster discharge.
- Extension of LIF techniques to regions in the plume significantly downstream of the thruster exit plane. This would enable a direct comparison between MBMS/RPA type techniques of evaluating ion energy with the LIF method. Although the voltage distributions obtained with the MBMS more closely resemble existent LIF data than previous RPA studies, a gap still separates the two techniques in the determination of ion energy distribution width. It is possible that both MBMS and LIF techniques are recording accurate measurements, albeit at distinctly different regions of the plume.

- Modification of or improvement upon the MBMS system used to obtain plume mass spectra. The instrument constructed and used for this study was hampered by problematic arcing between the beam gate electrodes. Due to this, the gate length was extended beyond the optimum value and, hence, the quantitative evaluation of minority plume products was not possible. Additionally, increasing the ion conservation between the sampling skimmer and the collector would possibly enable the identification of thruster self-erosion products in the mass spectra.

BIBLIOGRAPHY

- 1 Hill, P., and Peterson, C., Mechanics and Thermodynamics of Propulsion, Addison-Wesley Publishing, Massachusetts, 1992.
- 2 Riehl, J., Gefert, L., Myers, R., Pencil, E., McAdams, J., and Kusnierkiewicz, D., "Low power electric propulsion for minor body applications," AIAA-95-2812, 31st AIAA/ASME/SAE/ASEE Joint Propulsion Conference, San Diego, CA, July 10-12, 1995.
- 3 Myers, R., Oleson, S., McGuire, M., Meckel, N., and Cassady, J., "Pulsed plasma thruster technology for small satellite missions," Presented at 9th AIAA/Utah State University Conference on Small Satellites, Sept. 18-21, 1995.
- 4 Dudzinski, L., and Myers, R., "Advanced propulsion benefits to New Millenium class missions," Presented at 9th AIAA/Utah State University Conference on Small Satellites, Sept. 18-21, 1995.
- 5 Caveny, L., Curran, F., and Brophy, J., "Russian electric space propulsion evaluated for use on American satellites," RGC-EP-93-D2-4, 2nd Russian-German Conference on Electric Propulsion Engines and their Application, Moscow, Russia, July 1993.
- 6 Gulczinski, F., and Spores, R., "Analysis of Hall-effect thrusters and ion engines for orbit transfer missions," AIAA-96-2973, 32nd AIAA / ASME / SAE / ASEE Joint Propulsion Conference, Lake Buena Vista, FL, July 1-3, 1996.
- 7 Oleson, S., Myers, R., Kluever, C., Riehl, J., and Curran, F., "Advanced propulsion for geostationary orbit insertion and north-south station keeping," AIAA-95-2513, 31st AIAA / ASME / SAE / ASEE Joint Propulsion Conference, San Diego, CA, July 10-12, 1995.
- 8 Kaufman, H., "Technology of closed-drift thrusters," *AIAA Journal*, Vol. 23, No. 1, Jan. 1985, pp. 78-87.
- 9 Zharinov, A., and Popov, Y., "Acceleration of plasma by a closed Hall current," *Soviet Physics-Technical Physics*, Vol. 12, Aug. 1967, pp. 208-211.

- 10 Morozov, A., Esipchuk, Y., Tilinin, G., Trofimov, A., Sharov, Y., and Shchepkin, G., "Plasma accelerator with closed electron drift and extended acceleration zone," *Soviet Physics-Technical Physics*, Vol. 17, July 1972, pp. 38-45.
- 11 Bishaev, A., and Kim, V., "Local plasma properties in a Hall-current accelerator with an extended acceleration zone," *Soviet Physics-Technical Physics*, Vol. 23, Sept 1978, pp. 1055-1057.
- 12 Shadov, V., Porotnikov, A., Rilov, U., and Kim, V., "Plasma propulsion systems: present state and development," 30th International Astronautical Congress, Sept. 1979.
- 13 The All-Union Conferences on Plasma Accelerators were held in 1971 (Moscow), 1973 (Minsk), and 1976 (Minsk). The subsequent All-Union Conferences on Plasma Accelerators and Ion Injectors were held in 1978 (Moscow), 1982 (Moscow), 1986 (Dnepropetrovsk), and 1989 (Kharkov). (in Russian)
- 14 Artsimovich, L., Andronov, I., Esipchuk, I., Morozov, A., Snarsky, R., et al., "Development of a stationary plasma thruster (SPT) and its testing on the earth artificial satellite 'Meteor'," *Kosmicheskie Issledovania* (a Soviet journal), Vol. 12, No. 3, pp. 451-468. (in Russian)
- 15 Bugrova, A., Kim, V., Maslennikov, N., and Morozov, A., "Physical processes and characteristics of Stationary Plasma Thrusters with closed electrons drift," IEPC-91-079, 22nd International Electric Propulsion Conference, Viareggio, Italy, Oct. 14-17, 1991.
- 16 Brophy, J., et al., "Performance of the Stationary Plasma Thruster: SPT-100," AIAA-92-3155, 28th AIAA / SAE / ASME / ASEE Joint Propulsion Conference, Nashville, TN, July 6-8, 1992.
- 17 Sankovic, J., Hamley, J., and Haag, T., "Performance evaluation of the Russian SPT-100 thruster at NASA LeRC," IEPC-93-094, 23rd International Electric Propulsion Conference, Seattle, WA, Sept. 13-16, 1993.
- 18 Garner, C., Polk, J., Goodfellow, K., and Brophy, J., "Performance evaluation and life testing of the SPT-100," IEPC-93-091, 23rd International Electric Propulsion Conference, Seattle, WA, Sept. 13-16, 1993.

- 19 Garner, C., Brophy, J., Polk, J., and Pless, L., "A 5,730-hr cyclic endurance test of the SPT-100," AIAA-95-2667, 31st AIAA / ASME / SAE / ASEE Joint Propulsion Conference, San Diego, CA, July 10-12, 1995.
- 20 Day, M., Maslennikov, N., Randolph, T., and Rogers, W., "SPT-100 Subsystem qualification status," AIAA-95-2666, 31st AIAA / ASME / SAE / ASEE Joint Propulsion Conference, San Diego, CA, July 10-12, 1995.
- 21 Behrisch, R., Ed., Sputtering by Particle Bombardment, Springer-Verlag Press, New York, 1981.
- 22 Palmer, D.W., Thompson, M.W., and Townsend, P.D., Eds., Atomic Collision Phenomena in Solids, North Holland/American Elsevier Pub. Co., New York, 1970.
- 23 Nastasi, M., Mayer, J.W., and Hirvonen, J.K., Ion-Solid Interactions: Fundamentals and Applications, Cambridge University Press, Cambridge, 1996.
- 24 Absalamov, S., Andreev, V., Colbert, T., Day, M., Egorov, V., Gnizdor, R., Kaufman, H., Kim, V., Korakin, A., Kozubsky, K., Kudravzev, S., Lebedev, U., Popov, G., and Zhurin, V., "Measurement of plasma parameters in the Stationary Plasma Thruster (SPT-100) plume and its effect on spacecraft components," AIAA-92-3156, 28th AIAA / SAE / ASME / ASEE Joint Propulsion Conference, Nashville, TN, July 6-8, 1992.
- 25 Myers, R., and Manzella, D., "Stationary plasma thruster plume characteristics," IEPC-93-096, 23rd International Electric Propulsion Conference, Seattle, WA, Sept. 13-16, 1993.
- 26 Manzella, D., and Sankovic, J., "Hall thruster ion beam characterization," AIAA-95-2927, 31st AIAA / ASME / SAE / ASEE Joint Propulsion Conference, San Diego, CA, July 10-12, 1995.
- 27 Pencil, E., "Preliminary far-field plume sputtering of the Stationary Plasma Thruster (SPT-100)," IEPC-93-098, 23rd International Electric Propulsion Conference, Seattle, WA, Sept. 13-16, 1993.
- 28 Pencil, E., Randolph, T., and Manzella, D., "End-of-life Stationary Plasma Thruster far-field plume characterization," AIAA-96-2709, 32nd AIAA / ASME / SAE / ASEE Joint Propulsion Conference, Lake Buena Vista, FL, July 1-3, 1996.

- 29 Manzella, D., "Stationary plasma thruster plume emissions," IEPC-93-097, 23rd International Electric Propulsion Conference, Seattle, WA, Sept. 13-16, 1993.
- 30 Manzella, D., "Stationary plasma thruster ion velocity distribution," AIAA-94-3141, 30th AIAA / ASME / SAE / ASEE Joint Propulsion Conference, Indianapolis, IN, June 27-29, 1994.
- 31 Baranov, V., Nazarenko, Y., Petrosov, V., Vasin, A., and Yashnov, Y., "Energy model and mechanisms of acceleration layer formation for Hall thrusters," AIAA-97-3047, 33rd AIAA / ASME / SAE / ASEE Joint Propulsion Conference, Seattle, WA, July 6-9, 1997.
- 32 Komurasaki, K., Hirakawa, M., and Arakawa, Y., "Plasma acceleration process in a Hall-current thruster," IEPC-91-078, 22nd International Electric Propulsion Conference, Viareggio, Italy, Oct. 14-17, 1991.
- 33 Grishin, S., Erofeev, V., Zharinov, A., Naumkin, V., and Safronov, I., "Characteristics of a two-stage ion accelerator with an anode layer," Zhurnal Prikladnoi Mekhaniki I Tekhnicheskoi Fiziki, No. 2, pp. 28-36, March-April, 1978.
- 34 Zhurin, V., Kaufman, H., and Robinson, R., "Physics of closed-drift thrusters," IEPC-97-191, 25th International Electric Propulsion Conference, Cleveland, OH, Aug. 24-28, 1997.
- 35 Gallimore, A., Kim, S., Foster, J., King, L., and Gulczinski, F., "Near- and far-field plume studies of a one-kilowatt arcjet," Journal of Propulsion and Power, Vol. 12, No. 1, Jan-Feb 1996.
- 36 Hutchinson, I., Principles of Plasma Diagnostics, Cambridge University Press, Cambridge, 1987.
- 37 Leray, P., Bonnet, J., and Pigache, D., "Spatially resolved emission spectroscopy along a SPT channel. Interpretation by collisional-radiative model," IEPC-97-054, 25th International Electric Propulsion Conference, Cleveland, OH, Aug. 1997.
- 38 Bugrova, A., Desyatskov, A., and Kharchevnikov, V., "Experimental determination of ion energy at the outlet of SPT-ATON," IEPC-95-47, 24th International Electric Propulsion Conference, Moscow, Russia, 1995.

- 39 Marrese, C., Majumdar, N., Haas, J., Williams, G., King, L., and Gallimore, A., "Development of a single-orifice retarding potential analyzer for Hall thruster plume characterization," IEPC-97-066, 25th International Electric Propulsion Conference, Cleveland, OH, Aug. 24-28, 1997.
- 40 Rapp, D., and Francis, W., "Charge exchange between gaseous ions and atoms," *Journal of Chemical Physics*, Vol. 37, No. 11, 1962, pp. 2631-2645.
- 41 Duckworth, H.E., Barber, R.C., and Venkatasubramanian, V.S., Mass Spectroscopy, Cambridge University Press, Cambridge, 1986.
- 42 Reed, R., Ed., Modern Aspects of Mass Spectrometry, Plenum Press, New York, 1968.
- 43 Price, D., and Williams, J.E., Eds., Time-of-Flight Mass Spectrometry, Pergamon Press, Hungary, 1969.
- 44 Cotter, R.J., Ed., Time-of-Flight Mass Spectrometry, American Chemical Society, Washington D.C., 1994.
- 45 Schlag, E.W., Ed., Time-of-flight Mass Spectrometry and its Applications, Elsevier Scientific Publishing Co., Amsterdam, 1994.
- 46 Pollard, J., "Plume angular, energy, and mass spectral measurements with the T5 Ion Engine," AIAA-95-2920, 31st AIAA / ASME / SAE / ASEE Joint Propulsion Conference, San Diego, CA, July 10-12, 1995.
- 47 deZeeuw, W., va der Ven, H., de Wit, J., and Donne, J., "An electrostatic time-of-flight analyzer for simultaneous energy and mass determination of neutral particles," *Rev. Sci. Instrum.* 62 (1), Jan 1991, pp. 110-117.
- 48 Gaus, A, Htwe, W., Brand, T., and Schulz, M., "Energy spread and ion current measurements of several ion sources," *Rev. Sci. Instrum.* 65 (12), Dec. 1994, pp. 3739-3745.
- 49 Esaulov, V., Grizzi, O., Guillemot, L., Huels, M., Lacombe, S., and Vu Ngoc Tuan, "An apparatus for multiparametric studies of ion-surface collisions," *Rev. Sci. Instrum.* 50 (2), Feb. 1979, pp. 210-218.

- 50 Hughes, F.W., Op-Amp Handbook, Third Ed., Prentice Hall, New Jersey, 1993.
- 51 Irvine, R.G., Operational Amplifier Characteristics and Applications, Third Ed., Prentice Hall, New Jersey, 1994.
- 52 Nicholson, D.R., Introduction to Plasma Theory, Krieger Publishing Co., Malabar, Florida, 1983.
- 53 Lide, D.R., Ed., Handbook of Chemistry and Physics, 75th Edition, CRC Press, Ann Arbor, 1994.
- 54 Brown, S.C., Ed., Basic Data of Plasma Physics, American Institute of Physics Press, New York, 1994.
- 55 Kusakabe, T., Horiuchi, T., Nagai, N., Hanaki, H., Konomi, I., and Sakisaka, M., "Charge transfer of multiply charged slow argon, krypton, and xenon ions on atomic and molecular targets. Single-charge transfer cross sections," *Journal of Physics B: Atomic and Molecular Physics*, Vol. 19, 1986, 2165-2174.
- 56 Koding, H., Pinkse, F., and Nibbering, N., "Double-electron transfer from Xe to Xe⁴⁺ at low energies as observed in the trap of a Fourier-transform ion cyclotron resonance mass spectrometer," *Rapid Communications in Mass Spectrometry*, Vol. 7, 1993, pp. 780-783.
- 57 Anders, A., "Recombination of a Xenon Plasma Jet," *Contrib. Plasma Phys.* Vol. 27, No. 5, 1987, pp. 373-398.